PARTICLE BASED TOPOLOGY OPTIMIZATION METHODS FOR ADDITIVE MANUFACTURING TECHNOLOGIES

by
ABDULLAH KENDIBILIR

Submitted to the Graduate School of Engineering and Natural Sciences
in partial fulfilment of
the requirements for the degree of Doctor of Philosophy

Sabancı University
July 2024

DISSERTATION AUTHOR 2024 ©

All Rights Reserved

ABSTRACT

PARTICLE BASED TOPOLOGY OPTIMIZATION METHODS FOR ADDITIVE MANUFACTURING TECHNOLOGIES

ABDULLAH KENDIBILIR

MANUFACTURING ENGINEERING Ph.D. DISSERTATION, JULY 2024

Dissertation Supervisor: Assoc. Prof. ADNAN KEFAL

Keywords: peridynamics, topology optimization, additive manufacturing, crack modelling, fracture toughness

Topology optimization (TO) is a robust design method that generates the best material distribution by improving an objective function (e.g., maximizing stiffness or minimizing strain energy) and satisfying design constraints (e.g., volume constraints, and minimum dimensions). Although TO is increasingly utilized in lightweight designs of various engineering structures, TO designs have usually been criticized for causing complex forms, which makes obtained geometry difficult or even impossible to fabricate by using traditional manufacturing methods such as machining, casting, etc. Additive manufacturing (AM) is an effective approach to fabricating these intricate shapes obtained from topology optimization (TO). However, AM methods, which entail multiple heating and cooling cycles, lead to the formation of concentrated local residual stresses in TO designs. Consequently, this results in diminished material properties in specific areas and increases the possibility of local failures, such as cracks/defects. At this point, a non-local reformulation of classical continuum mechanics, namely Peridynamics (PD), offers a practical way to model discontinuities by only breaking the bonds between particles. The PD method can accurately model the dynamic fracture behavior of the structures including crack branching and coalescence thanks to the utilization of the integral form of balance equations instead of partial derivatives.

Overall, the main motivation of the present thesis is to develop novel 3D topology optimization methods based on peridynamics (i.e., peridynamic topology optimization or PD-TO) to maximize the structural performance of the final designs pro-

duced by AM processes. In this context, three different density-based TO algorithms namely bi-directional evolutionary structural optimization (BESO), optimality criteria (OC), and proportional approach (PROP) are coupled with the PD method for the optimization of three-dimensional structures. The developed methods are extensively validated by performing on various benchmark problems. Afterward, the PD-TO method is utilized for the TO of large-scale engineering structures (ship cross-section design). According to the obtained results, the viability and superior capabilities of the PD-TO methods are revealed. Furthermore, this method is performed with a systematic optimization scheme for increased fracture resistance under the dynamic load by considering a classical continuum mechanics based failure criteria. The comparisons showed the increased fracture resistance on the optimized design by the proposed algorithms against the classical optimization results. Moreover, the PD-TO methods are utilized for decreasing residual stresses occurs on the structures produced by metal AM processes. Thanks to embedding hypotetical cracks in the initial design domain and topologically optimizing via PD-TO, we achieved residual stress minimized light weighted structures and experimentally validated the obtained numerical results.

ÖZET

EKLEMELİ İMALAT TEKNOLOJİLERİ İÇİN PARÇACIK TABANLI TOPOLOJİ OPTİMİZASYON YÖNTEMLERİ

ABDULLAH KENDİBİLİR

ÜRETİM MÜHENDİSLİĞİ DOKTORA TEZİ, TEMMUZ 2024

Tez Danışmanı: Doç. Dr. ADNAN KEFAL

Anahtar Kelimeler: peridinamik, topoloji optimizasyonu, eklemeli üretim, çatlak modellemesi, kırılma dayanımı

Topoloji optimizasyonu (TO), bir amaç fonksiyonunu iyileştirerek (örneğin, rijitlği en üst düzeye çıkarmak veya gerinim enerjisini en aza indirmek) ve tasarım kısıtlamalarını (örneğin, hacim kısıtlamaları ve minimum boyutlar) karşılayarak en iyi malzeme dağılımını üreten güvenilir bir tasarım yöntemidir. Çeşitli mühendislik yapılarının hafifleştirilmiş tasarımlarında giderek daha fazla kullanılmasına rağmen, TO tasarımları genellikle karmaşık formlara neden olduğu için eleştirilir; bu durum, elde edilen geometrinin işleme, döküm vb. gibi geleneksel üretim yöntemleri kullanılarak üretilmesini zorlaştırır hatta bazen imkansız hale getirir. Eklemeli imalat (AM), topoloji optimizasyonundan (TO) elde edilen bu karmaşık şekillerin üretilmesi için etkili bir yaklaşımdır. Ancak birden fazla ısıtma ve soğutma döngüsü gerektiren AM yöntemleri, TO tasarımlarında konsantre yerel kalıntı gerilmelerin oluşmasına yol açar. Sonuç olarak bu, belirli alanlarda malzeme özelliklerinin azalmasına neden olur ve çatlak/kusur gibi yerel bozunmaların olasılığını artırır. Bu noktada, klasik süreklilik mekaniğinin yerel olmayan bir yeniden formülasyonu olan Peridinamik (PD), yalnızca parçacıklar arasındaki bağları kırarak süreksizlikleri modellemenin pratik bir yolunu sunmaktadır. PD yöntemi, kısmi türevler yerine denge denklemlerinin integral formunun kullanılması sayesinde çatlak dallanması ve birleşmesi dahil olmak üzere yapıların dinamik kırılma davranışını doğru bir şekilde modelleyebilir.

Genel olarak, bu tezin ana motivasyonu, AM süreçleriyle üretilen nihai tasarım-ların yapısal performansını en üst düzeye çıkarmak için peridinamiğe dayalı yeni 3B topoloji optimizasyon yöntemleri (yani, peridinamik topoloji optimizasyonu veya PD-TO) geliştirmektir. Bu kapsamda, üç boyutlu yapıların optimizasyonu için çift

yönlü evrimsel yapısal optimizasyon (BESO), optimallik kriterleri (OC) ve orantısal yaklaşım (PROP) olmak üzere üç farklı yoğunluk tabanlı TO algoritması peridinamik yöntemiyle birleştirilmiştir. Geliştirilen yöntemler, çeşitli kıyaslama problemleri üzerinde uygulanarak kapsamlı bir şekilde doğrulanmıştır. Daha sonra büyük ölçekli mühendislik yapılarının (gemi kesit tasarımı) hafifletilmesi için PD-TO yönteminden yararlanılmıştır. Elde edilen sonuçlara göre PD-TO yöntemlerinin uygulanabilirliği ve üstün yetenekleri ortaya çıkarılmıştır. Ayrıca bu yöntem, klasik sürekli ortam mekaniği temelli hasar kriterleri dikkate alınarak dinamik yük altında kırılma direncinin arttırılması için sistematik bir optimizasyon şeması ile birleştirilmiştir. Yapılan karşılaştırmalar, hasar oluşumuna yatkın kritik bölgeleri dikkate alınca, klasik optimizasyon sonuçlarına göre önerilen algoritmalar tarafından optimize edilen tasarımda kırılma direncinin arttığını gösterdi. Bu tezde ayrıca, metal AM prosesleri ile üretilen yapılarda oluşan kalıntı gerilmelerin azaltılması amacıyla PD-TO yöntemlerinden yararlanılmıştır. İlk tasarım alanına varsayımsal çatlakların yerleştirilmesi ve PD-TO aracılığıyla optimizasyon yapılması sayesinde kalıntı gerilimi en aza indirilmiş hafif yapılar elde edilmiştir ve bu sayısal sonuçlar mekanik testler aracılığıyla deneysel olarak doğrulanmıştır.

ACKNOWLEDGEMENTS

I would like to express the first and the biggest thanks to my thesis advisor, Assoc. Prof. Adnan Kefal. What he taught me and what he contributed to me during the long time I spent with him is invaluable. In addition to being a great guide with his academic competence, his help in every subject like a friend was the biggest advantage I had in my PhD period. I am grateful to him for his motivating and supportive behavior, which provides all kinds of support that a graduate student needs. In addition, thanks to the tasks that require great responsibility, he helped me to become a more successful, responsible, and self-confident researcher. Once again, I would like to thank him from the bottom of my heart.

I would also like to thank my best friends and colleagues who supported me during this period. There would be a lot of names to be mentioned but I would spell some of them: Mustafa, Hayrullah, Tolga Abi, Berkan, Emre, Erdem, Aryan, Mahmut, Safa, Sina, Furkan and others.

Most special thanks must go to my family, who undoubtedly supported me in every decision I made. My mother, Hamide Kendibilir, my father, Nasip Kendibilir and my sister and brother, Nuray and Yusuf. I can not ever be thankful enough to have them.

I also have to give a special thank you to my grandmother and grandfather. They hosted me and offered me great comfort throughout my PhD education.

Finally, I would like to thank Sabanci University, SU-IMC (Sabanci University-Integrated Manufacturing Center) and TUBITAK (Scientific and Technological Research Council of Turkey) for their support in allowing me to conduct this research over the past years.

Dedicated to
My family

TABLE OF CONTENTS

LIST OF TABLES ..... **xiv**

LIST OF FIGURES ..... **xv**

1. GENERAL INTRODUCTION **1**
1.1. Introduction 1
1.2. Background and Motivation 1
1.3. Objectives of the Research 3
1.4. Structure of the Thesis 4

2. LITERATURE REVIEW **7**
2.1. Historical Overview of Topology Optimization Algorithms 7
2.2. Topology Optimization for Additive Manufacturing 8
2.3. The Role of Peridynamic Method and its Applications in Topology Optimization and Fracture Modelling Literature 11

3. 3D PERIDYNAMICS TOPOLOGY OPTIMIZATION METHODS **15**
3.1. Introduction 15
3.2. Bond-Based Peridynamic Formulation for Three Dimensional Structures 15
3.3. Crack Implementation in Peridynamics Topology Optimization 24
3.4. Topology Optimization Problem Statement 28
3.5. Bi-directional Evolutionary Structural Optimization Method 29
3.6. Optimality Criteria Method 32
3.7. Proportional Optimization Method 34
3.8. Filter Scheme and Stabilization 36
3.9. Smoothing Operation on the Optimized Solutions 39

4. PD-TO METHODS FOR ENGINEERING STRUCTURES WITH/WITHOUT DISCONTINUTIES **41**

4.1. Peridynamics Topology Optimization of Three-Dimensional Structures with Surface Cracks for Additive Manufacturing 41
4.1.1. Introduction 41
4.1.2. Novelty and Motivation 42
4.1.3. Topology Optimization Examples 43
4.1.3.1. Case I: Three-Dimensional Cantilever Beam with/without Surface Cracks 43
4.1.3.2. Case II: Three-Dimensional L-Shaped Beam with/without Surface Cracks 53
4.1.3.3. Case III: Three-Dimensional Bridge Structures with/without Multiple Surface Cracks 62
4.1.3.4. Case IV: Three-Dimensional Wrench Geometry with a Curved Crack 70
4.1.4. Concluding Remarks 73
4.2. Coupling of Bond-Based Peridynamics and Continuous Density-Based Topology Optimization Methods for Effective Design of Three Dimensional Structures with Discontinuities 76
4.2.1. Introduction 76
4.2.2. Novelty and Motivation 77
4.2.3. Topology Optimization Examples 78
4.2.3.1. Case I: Cantilever Beam 78
4.2.3.2. Case II: Hanger Beam 87
4.2.3.3. Case III: MBB Beam 96
4.2.4. Dynamic Analyses for the Assessment of Fracture Toughness Enhancement 105
4.2.4.1. Dynamic Analysis Setup 105
4.2.4.2. Comparison Strategies 106
4.2.4.3. Numerical Results: Dynamic Behaviour of the Optimized Structures 107
4.2.5. Concluding Remarks 111
4.3. Enhanced Ship Cross-Section Design Methodology Using Peridynamics Topology Optimization 113
4.3.1. Introduction 113
4.3.2. Novelty and Motivation 114
4.3.3. Problem Definition and Design Model 115
4.3.3.1. Initial Bulkhead Geometry 115
4.3.3.2. PD Model and Optimization Parameters 118
4.3.4. Results and Discussions 119

4.3.4.1. Optimum Results for Hogging and Sagging Conditions using PD-PROP and PD-OC Methods 119
4.3.4.2. Alternative Optimum Designs for Different Damaged Scenarios 121
4.3.4.3. Final Designs after Smoothing Process 123
4.3.4.4. Mechanical Assessment of the PD-TO Results against Conventional Web Frame 126
4.3.5. Concluding Remarks 129

5« APPLICATIONS OF PD-TO FOR MINIMIZING RESIDUAL STRESS ARISES FROM AM PROCESSES 132

5.1. A Systematic Fusion of Failure Criteria and Peridynamics Topology Optimization for Enhanced Fracture Resistance 132
5.1.1. Introduction 133
5.1.2. Novelty and Motivation 133
5.1.3. An Algorithm for Failure Criterion Based Crack Definition in PD-TO 134
5.1.4. Numerical Results and Discussions 138
5.1.4.1. Case I: Hanger Beam 140
5.1.4.2. Case II: L-Beam 145
5.1.4.3. Case III: Portal frame 151
5.1.5. Concluding Remarks 154
5.2. On Utilizing Peridynamics Topology Optimization for Residual Stress Minimization in Metal Additive Manufacturing 156
5.2.1. Introduction 156
5.2.2. Novelty and Motivation 156
5.2.3. Numerical Results 157
5.2.3.1. Topology Optimization of L-Beam 157
5.2.3.2. Topology Optimization of MBB-beam Problem 161
5.2.4. Concluding Remarks 164
5.3. Lightweight Engine Bracket Design for Metal Additive Manufacturing: Peridynamics Topology Optimization for Reduction of Thermal Stresses and Improved Structural Performance 164
5.3.1. Introduction 164
5.3.2. Novelty and Motivation 165
5.3.3. Problem Definition for Engine Bracket 166
5.3.4. Particle Model for PD-TO Analyses 167
5.3.5. Sequential Optimization Strategy 167
5.3.6. Numerical Results 168

5.3.7. Manufacturing and Deformation Measurements of Manufactured Parts 172
5.3.8. Experimental Test Setup 173
5.3.9. Experimental Results for Optimized Brackets 174
5.3.10. Concluding Remarks 175

6 GENERAL CONCLUSIONS 178
6.1. Achievements against the Objectives 178
6.2. Gaps and Future Studies 179
6.3. Research Outputs 180

BIBLIOGRAPHY 184

LIST OF TABLES

Table 4.1. Strain energy density comparison around the cracks for different results 61
Table 4.2. Dimensions of the wrench geometry 71
Table 4.3. Mesh-dependency study based on compliance values. 81
Table 4.4. The final compliance values for the cantilever beam without crack. 82
Table 4.5. The final compliance values for the hanger beam without crack. 91
Table 4.6. Mesh-dependency study based on compliance values. 91
Table 4.7. The final compliance values for the MBB beam without crack. . 100
Table 4.8. Maximum displacements on cantilever beam just before the crack propagates. 109
Table 4.9. Maximum displacements on hanger beam just before the crack propagates. 111

Table 5.1. Total, average and maximum strain energy density comparison in the vicinity of the embedded cracks (region of interest as shown in Fig.5.10) between three optimized Hanger-beam structures under static loading condition 143
Table 5.2. Compliance and maximum deformation comparison between three optimized L-beam structures under static loading condition 146
Table 5.3. Total, average and maximum strain energy density comparison in the vicinity of the embedded cracks between three optimized L-beam structures under static loading condition 149
Table 5.4. Dimensions of the portal frame geometry 151
Table 5.5. Comparison of maximum and average residual stresses as well as the number of high stress carrying points inside the interest region for two optimized results: No crack and With crack results 172
Table 5.6. Comparison of the Strains and Strain Energies 175

LIST OF FIGURES

Figure 1.1. Distortions and defects in a twin cantilever beam due to residual stresses after cutting of support.(Buchbinder, Meiners, Pirch, Wissenbach & Schrage (2014)) 2

Figure 2.1. Manufacturability of cantilever structures with decreased overhang angles (Jihong, Han, Chuang, Lu, Shangqin & Zhang (2021)). .. 10
Figure 2.2. The general framework of the particle-based topology optimization methods for topology optimization of structures with discontinuities. From the initial design domain to the rapid prototyping of the obtained results by the proposed PD-TO methods in this thesis. 13

Figure 3.1. Representation of 3D particles in a PD model. 16
Figure 3.2. Two-dimensional illustration of interactions of a PD particle in before and after deformation. 17
Figure 3.3. PD discretization and particle interactions in 3D space. (a) An example of 3D model. (b) Particle-based discretized PD model of the given model. (c) Horizon and interactions of a particle i. (d) Horizon. (e) PD bond between two interacting particles i and j. (f) All the bonds of the particle i. 18
Figure 3.4. Surface crack modelling in a three-dimensional PD domain. (a) PD particles and their interactions before the crack, (b) Intersection points of the bonds and a surface crack, (c) Interactions of the same particles after crack involvement. 25
Figure 3.5. Crack generation algorithm for breaking the intersecting bonds. 25
Figure 3.6. Displacement contours of a simple bending problem (a) without crack, and (b) with crack where the results are 300 times exaggerated for a better representation 27
Figure 3.7. Flowchart of the proposed 3D PD-BESO-TO method. 31
Figure 3.8. Design variable updating algorithm in BESO method. 32
Figure 3.9. Design variable updating algorithm in OC method. 34
Figure 3.10. Design variable updating algorithm in PROP method. 36

Figure 3.11. The general framework of the continuous density based PD-TO methods. 38
Figure 3.12. Examples of the effect of smoothing operation on the final topologies obtained by PD-TO method. 40

Figure 4.1. Design domain for the 3 different scenarios considering (b, c) with and (a) without surface cracks. 43
Figure 4.2. Isometric views of the final topologies for changing parameters: (a) particle resolution, (b) horizon radius. 44
Figure 4.3. The compliance histories for changing parameters: (a) particle resolution, (b) horizon radius. 45
Figure 4.4. The comparison of time costs of one iteration for changing parameters: (a) particle resolution, (b) horizon. These are the relative values based on $60 \times 30 \times 30$ and Delta=3dx in (a) and (b), respectively. 46
Figure 4.5. Final topologies of FEM-TO and PD-TO without crack. 47
Figure 4.6. Comparison of 2-D views of FEM-TO and PD-TO without crack. 47
Figure 4.7. Optimized topologies of Case I for different crack locations. ... 48
Figure 4.8. Comparison of the total displacements (left column) and strain energy densities (right column) of the optimal topologies of Case I. .. 49
Figure 4.9. Final topology of PD back-crack case (a) before and (b) after smoothing operation. 50
Figure 4.10. Comparison of the smoothed geometries for Case I. 50
Figure 4.11. Printed version of optimal topologies made of PLA filament material. 52
Figure 4.12. The iteration histories of the compliance of Case I. 52
Figure 4.13. Design domain of Case II for the 3 different scenarios considering (b, c) with and (a) without surface cracks. 53
Figure 4.14. Comparison of the optimal topologies of Case II for different crack locations. 54
Figure 4.15. Comparison of the optimal topologies for different views (x-y and y-z). 55
Figure 4.16. Comparison of the total displacements (left column) and strain energy densities (right column) of the optimal topologies of Case II... 56
Figure 4.17. Final topology of PD up-crack case (a) before and (b) after smoothing operation. 57
Figure 4.18. Comparison of the smoothed geometries for Case II. 58
Figure 4.19. Printed version of optimal topologies made of PLA filament material. 59

Figure 4.20. The compliance histories of PD-TO results for Case II. 60
Figure 4.21. The dimensions of the region in the vicinity of cracks: (a) up-crack, (b) down-crack. 62
Figure 4.22. Design domain and crack positions of the bridge case (Case III). 63
Figure 4.23. Comparison of the optimal topologies of Case III for different views (Isometric and x-y). 64
Figure 4.24. Comparison of the total displacements (left column) and strain energy densities (right column) of the optimal topologies of Case III. . 65
Figure 4.25. Final topology of PD without crack case (a) before and (b) after smoothing operation. 66
Figure 4.26. Comparison of the smoothed geometries for Case III. 68
Figure 4.27. The compliance histories of PD-TO results for Case III. 68
Figure 4.28. Experimental and numerical comparison of FEM-TO and PD-TO for Case III without crack. 69
Figure 4.29. Design domain and crack features of the wrench geometry. 70
Figure 4.30. Comparison of the optimal topologies of Case III for different views (Isometric and x-y). 71
Figure 4.31. Comparison of the total displacements for the optimal topologies 72
Figure 4.32. Comparison of the strain energy densities for the optimal topologies. 73
Figure 4.33. Smoothed versions of the optimum results for wrench geometry. 74
Figure 4.34. Graphical abstract of the Section 4.2 76
Figure 4.35. Design domain and loading condition of the Cantilever Beam problem for five scenarios in total including with/without crack conditions, namely (a) without crack; (b) back crack; (c) front crack; (d) double parallel crack; (e) double perpendicular crack. Single or multiple cracks are embedded into different locations. Cases (b), and (c) are designed to investigate the location effect of a single crack by positioning at varying distances to the applied force. In cases (d) and (e), we intend to examine the reaction of the optimizers in the existence of multiple cracks in different orientations. 79
Figure 4.36. Compliance values and final topologies obtained by PD-PROP for different discretization options 80
Figure 4.37. Compliance values and final topologies obtained by PD-OC for different discretization options. 81

Figure 4.38. Comparison of the optimal topologies of the Cantilever Beam obtained by PD-TO and FEM-TO represented in two isometric, top and front views in order: (a) PD-TO; (b) FEM-TO. In each division in the figure, the first and second columns represent the PROP and OC results of the relevant method, respectively. 82
Figure 4.39. Optimal material distributions of the Cantilever Beam obtained by PROP, OC, and BESO for all the cases with/ without cracks: (a) without crack; (b) back crack; (c) front crack; (d) double parallel cracks; (e) double perpendicular cracks. Here, the results are presented in an isometric view to show the geometrical details. Note that, for PROP results, the colour scale contains green and blue colours to represent the minimum and maximum values of the design variables, respectively. For the results of OC, yellow corresponds to the minimum value of the design variable whereas red colour represents the solid material where the design variable of the particle is equal to 1. The design variable is equal to 1 for all particles shown in the BESO results. 84
Figure 4.40. Front and top views of the optimal topologies: (a) without crack; (b) back crack; (c) front crack; (d) double parallel crack; (e) double perpendicular crack. In each view section in the figure, the first and second column represents the ROP and OC results of the relevant case, respectively. 85
Figure 4.41. The compliance history of the cantilever beam throughout the optimization process for each case where the red and blue lines refer to the compliance values obtained by PD-OC and PD-PROP, respectively. The initial few iterations, where the compliance values are extremely high, are not plotted in the figure to be able to compare the remaining part of the compliance values. For the sake of clarity, we zoomed into selected zones to show the exact standings. 86
Figure 4.42. Design domain and loading condition of the Hanger problem for five scenarios in total including with/without crack conditions, namely: (a) without crack; (b) back crack; (c) front crack; (d) double crack; (e) triple crack. Single or multiple cracks are embedded into different locations. Cases (b) and (c) are designed to investigate the location effect of a single crack by positioning at varying distances from the applied force. In cases (d) and (e), we intend to examine the reaction of the optimizers in the existence of multiple cracks near the clamping and loading regions. 88

Figure 4.43. Topology evolution of PD-PROP for the case without crack: (a) initial step, (b) step 10, (c) step 20, (d) step 30, (e) step 40, and (f) step 50. 89
Figure 4.44. Topology evolution of PD-OC for the case without crack: (a) initial step, (b) step 10, (c) step 20, (d) step 30, (e) step 40, and (f) step 50. 89
Figure 4.45. Comparison of the optimal topologies of the Hanger obtained by PD-TO and FEM-TO represented in two isometric, front and right views in order: (a) PD-TO; (b) FEM-TO. In each division in the figure, the first and second column represents the PROP and OC results of the relevant method, respectively. 90
Figure 4.46. Final topologies obtained by PD-OC and PD-PROP for varying horizon size. 91
Figure 4.47. Optimal material distributions of the Hanger obtained by PD-PROP and PD-OC for all the cases with/without cracks: (a) without crack; (b) back crack; (c) front crack; (d) double crack; (e) triple crack. Here, the results are presented in two isometric views to show the geometrical details as much as possible. Note that, for PROP results, the colour scale contains green and blue colours to represent the minimum and maximum values of the design variables, respectively. For the results of OC, yellow corresponds to the minimum value of the design variable whereas red colour represents the solid material where the design variable of the particle is equal to 1. 93
Figure 4.48. Right and front views of the optimal topologies: (a) without crack; (b) back crack; (c) front crack; (d) double crack; (e) triple crack. In each view section in the figure, the first and second column represents the PROP and OC results of the relevant case, respectively. 94
Figure 4.49. The compliance history of the Hanger throughout the optimization process for each case where the red and blue lines refer to the compliance values obtained by PD-OC and PD-PROP, respectively. The initial few iterations, where the compliance values are extremely high, are not plotted in the figure to be able to compare the remaining part of the compliance values. For the sake of clarity, we zoomed into selected zones to show the exact standings. 95

Figure 4.50. Design domain and loading condition of the MBB-Beam problem for five scenarios in total including with/without crack conditions namely: (a) without crack; (b) parallel front and back cracks; (c) parallel mid cracks; (d) parallel mid cracks; (e) perpendicular mid cracks. There are two different crack locations and orientations: back and front, mid, parallel, and perpendicular. Identical square-shaped surface cracks are embedded into the relevant positions. 97
Figure 4.51. Filter radius analysis with different Rmin values: (a) Rmin = 2, (b) Rmin = 3, (c) Rmin = 4. The left and right columns contain PD-PROP and PD-OC results, respectively..... 98
Figure 4.52. Comparison of the optimal topologies of the MBB-Beam obtained by PD-TO and FEM-TO represented in isometric, top, and front views in order from top to bottom: (a) PD-TO; (b) FEM-TO. In each division in the figure, the first and second column represents the PROP and OC results of the relevant method, respectively. 99
Figure 4.53. Optimal material distributions of the MBB-Beam obtained by PD-PROP (left column) and PD-OC (right column) for all the cases with/without cracks: (a) without crack; (b) parallel front and back cracks; (c) perpendicular front and back cracks; (d) parallel mid cracks; (e) perpendicular mid cracks. Note that, for PROP results, the colour scale contains green and blue colours to represent the minimum and maximum values of the design variables, respectively. For the results of OC, yellow corresponds to the minimum value of the design variable whereas red colour represents the solid material where the design variable of the particle is equal to 1. 101
Figure 4.54. Top and front views of the optimal topologies: (a) without crack; (b) parallel front and back cracks; (c) parallel mid cracks; (d) parallel mid cracks; (e) perpendicular mid cracks. In each division in the figure, the first and second row represents the PROP and OC results of the relevant case, respectively..... 103
Figure 4.55. The compliance history of the MBB-Beam throughout the optimization process for each case where the red and blue lines refer to the compliance values obtained by PD-OC and PD-PROP, respectively. The initial few iterations, where the compliance values are extremely high, are not plotted in the figure to be able to compare the remaining part of the compliance values. For the sake of clarity, we zoomed into selected zones to show the exact standings. 104

Figure 4.56. The structures utilized in dynamic analysis correspond to the results of (a) OC-without crack (b) PROP-without crack (c) OC-front crack (d) PROP-front crack. Note that, the relevant bonds are broken to introduce the front crack in the given domain before the dynamic load is applied. 106
Figure 4.57. Fracture patterns obtained for the topologies of (a) OC-without crack, and (b) PROP-without crack under dynamic load. Observing the patterns, new cracks are embedded in the initial design domain in (c) and (d) for OC and PROP, respectively. 107
Figure 4.58. Damage plots at the certain time steps for different optimized PD-OC-TO and PD-PROP-TO results during dynamic PD analysis. Note that total displacements are also reflected in these pictures by the magnification factor of 50. 108
Figure 4.59. Maximum displacements for cantilever beam during dynamic analysis. The starting point of crack propagation is clarified by showing up the status of critical regions at relevant time steps. 110
Figure 4.60. Damage plots at the certain time steps for different optimized PD-OC-TO and PD-PROP-TO results during dynamic PD analysis. Note that total displacements are also reflected in these pictures by the magnification factor of 10. 110
Figure 4.61. Maximum displacements for the hanger during dynamic analysis. The starting point of crack propagation is clarified by showing up the status of critical regions at relevant time steps. 111
Figure 4.62. Problem definition with (a) dimensions of the initial design domain of a reference bulkhead; (b) location of the fixed points in the structures. 116
Figure 4.63. Representation of different loading conditions; (a) Typical illustration of hogging condition: wave crest amidships; (b) Typical illustration of sagging condition: wave through amidships, (c) Distribution of force vectors acting on PD particles for hogging condition, (d) Distribution of force vectors acting on PD particles for sagging condition. 117
Figure 4.64. (a) Particle based PD model of the design domain as a point cloud; (b) fixed PD particles to employ the boundary conditions; (c) passive particles which bound the design domain. 118
Figure 4.65. Isometric view of the final topologies under hogging condition. Four different volume fractions are considered by PD-OC (a, b, c, and d) and PD-PROP (e, f, g, and h). 119

Figure 4.66. Isometric view of the final topologies under sagging condition. Four different volume fractions are considered by PD-OC (a, b, c and d) and PD-PROP (e, f, g, and h). 121
Figure 4.67. (a) Crack dimension and positions in the design domain; (b) List of the cracked scenarios with relevant crack numbers which are included in the design domain. 122
Figure 4.68. (a) Initial optimum design without crack; Alternative designs and diversified regions for various cracked scenarios: (b) Case 1; (c) Case 2; (d) Case 3; (e) Case 4; (f) Case 5; (g) Case 6; (h) Case 7; (i) Case 8. 124
Figure 4.69. (a, c) PD-TO results for the hogging condition; (b, e) smoothed web-frame designs; (c, f) particle model of the smoothed designs (Volume fraction of these results are 0.4 and 0.5, from top to bottom, respectively). 125
Figure 4.70. (a) Conventional web frame design; (b) particle-based PD discretization of the design given in (a). 126
Figure 4.71. Total displacement contours of (a) reference design consisting of 60% material of initial domain; (b) optimized and smoothed design with 50% material; (c) optimized and smoothed design with 40% material. 127
Figure 4.72. Strain energy density distribution for the same energy level, (a) reference design with 60% material of initial domain; (b) optimum design with 50% material; (c) optimum design with 40% material. 128
Figure 4.73. Total strain energy (i.e., compliance) values for: reference with 60% volume; optimum design with 50% volume; and optimum design with 40% volume (from left to the right, respectively). 129
Figure 4.74. The main dimensions of the hole shapes in the (a) reference web frame and, (b) optimum design with 50% volume. 129
Figure 4.75. 3D model of the midship compartment consisting of bulkheads and optimized web-frame designs for the hogging condition and 50% volume fraction. 130

Figure 5.1. Graphical abstract of the Section 5.1 132
Figure 5.2. The workflow of the proposed failure criterion based crack definition framework. 135

Figure 5.3. (a) Example of a 3D solid body. (b) Illustration of particle and element-based models with the same discretization density. (c) Finite element discretization consisting of eight noded solid elements. (d) PD discretization consisting of equally distanced uniform particles. (e) The center of each PD particle corresponds to the center of each finite element. 136
Figure 5.4. Surface crack positioning. (a) Blue balls are the PD particles, and the pink sphere represents the horizon. (b) FEM elements around particles, transparent cubes are the meshes. (c) Mesh around the horizon. (d) Stress transformation to obtain principal stress. (e) Creating the surface crack (green surface) around the location of maximum stress by using the principal stress (red arrow) direction. 137
Figure 5.5. Surface crack positioning on the optimized L-beam structure, (a) FEM mesh around point clouds. (b) von-Mises stress distribution. (c) The embedded surface crack (green surface) according to principal stresses (red arrows) around the location of maximum stress. 138
Figure 5.6. (a) Problem domain for the hanger beam geometry. (b) PD discretization of the given geometry and selected particles for applying the loading condition. 139
Figure 5.7. Crack positions on hanger-beam geometry for (a) 2dx cracks, and (b) 4dx cracks according to critical von Mises stresses. 139
Figure 5.8. From top to bottom, the particle-based topology optimization results are transformed into 3D closed meshes utilizing voxel elements, and a final smoothing operation is performed to obtain ready-to-print designs. 141
Figure 5.9. Strain energy distribution comparison on particularly cracked regions. 141
Figure 5.10. (a) Extracting the strain energy density values under static loading for the particles inside the interest region of Hanger-beam problem. There are 94, 82, and 44 particles inside the critical region on the optimized structures for the scenario of (b) No crack, (c) 2dx cracks, and (d) 4dx cracks, respectively. 143
Figure 5.11. (a) Maximum displacements during dynamic analyses on Hanger-beam designs. (b) The damage contours and the failed regions in three designs when the crack starts to propagate. 144
Figure 5.12. (a) Problem domain for the L-Beam geometry, (b) PD discretization of the given geometry and selected particles for applying the loading condition. 145

Figure 5.13. Crack positions on L-Beam geometry for (a) 2dx cracks, and (b) 4dx cracks according to critical von Mises stresses. 146
Figure 5.14. The effect of crack inclusion in PD model. (a) Exaggerated displacement contours before crack. (b) Crack location on structure. (c) Exaggerated displacement contours after crack is modeled. 147
Figure 5.15. Final designs of L-beam before and after cracks. (a) Strain energy distribution over the designs. (b) Left view. (c) Top view. (d) Ready-to-print smoothed versions of point cloud results. 148
Figure 5.16. (a) The particles inside the interest region that covers embedded cracks of L-beam problem. There are 118, 120, and 134 particles inside the critical region on the optimized structures for the scenario of No crack, 2dx cracks, and 4dx cracks, respectively. (b) Top view of these particles. 149
Figure 5.17. (a) Maximum displacements during dynamic analyses on L-beam designs. (b) The damage contours and the failed regions in three designs when the crack starts to propagate. 150
Figure 5.18. (a) Problem domain for the Portal frame geometry. (b) Quarter part of the portal frame for symmetric modelling. (c) PD discretization of the quarter part. 151
Figure 5.19. (a) The optimum result of portal frame geometry without considering cracks. Locations of the multiple (b) 2dx cracks and (c) 4dx cracks in design domain. 152
Figure 5.20. Final designs of Portal frame before and after cracks. (a) Different plane views. (b) Ready-to-print smoothed versions of quarter point cloud results. 153
Figure 5.21. The damage contours and the failed regions from some of the selected important time steps in three designs. 154
Figure 5.22. The problem definition of the L-beam. 158
Figure 5.23. Optimum topology for the L-beam problem after the initial optimization without considering cracks. (a) Isometric view of the final geometry, (b) Plane views. 158
Figure 5.24. Crack locations on the optimized L-beam geometry. (a) Isometric view and (b) plane views are given for the better understanding of location and direction of the surface cracks. 159
Figure 5.25. Optimum topology for the L-beam problem considering crack (a) Isometric view of the final geometry, (b) Plane views. 160
Figure 5.26. The problem definition of the MBB-beam 161

Figure 5.27. Optimum topology for the MBB-beam problem after the initial optimization without considering cracks. (a) Isometric view of the final geometry, (b) Plane views. 162
Figure 5.28. Crack locations on the optimized MBB-beam geometry. (a) Isometric view and (b) plane views are given for the better understanding of location and direction of the surface cracks..... 162
Figure 5.29. Optimum topology for the MBB-beam problem considering cracks. (a) Isometric view of the final geometry, (b) Plane views..... 163
Figure 5.30. Demonstration of fixture assembly, loading and boundary conditions (a) Right view (b) Front view (c) Isometric view. 166
Figure 5.31. (a) Particle model of the bracket geometry. (b) Selected particles for boundary conditions. (c) Passive particles during topology optimization process. 167
Figure 5.32. Sequential optimization strategy framework..... 168
Figure 5.33. PD-TO result without considering any imaginary defects in (a) Isometric, (b)Top, (c) Right, (d) Front views. 169
Figure 5.34. (a) Location of the multiple cracks involved in the initial design domain. (b) Dimensions of a square-shaped crack, (c) Top, (d) Right, (e) Front views of the design domain with cracks..... 170
Figure 5.35. PD-TO result considering imaginary defects in (a) Isometric, (b) Top, (c) Right, (d) Front views. 171
Figure 5.36. Smoothed holes. (a) PD-TO result considering cracks, (b) The final state of the design given in (a) with smoothed holes. 171
Figure 5.37. The critical region where the residual stress values obtained by thermo-mechanical analyses for two optimized designs are compared. 171
Figure 5.38. Additively manufactured parts. (a) Initial design. (b) PD-TO result without considering crack. (c) PD-TO optimized considering cracks. 173
Figure 5.39. Strain-load plots of the specimens..... 175

1. GENERAL INTRODUCTION

1.1 Introduction

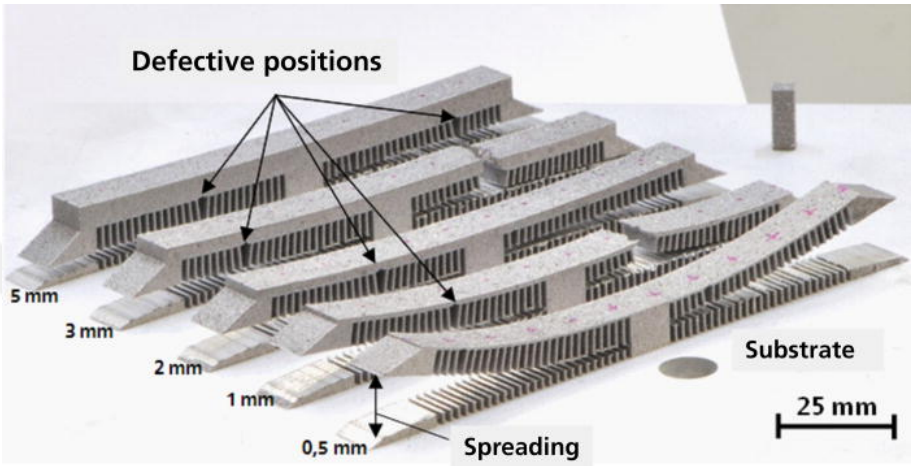
This chapter includes the background, motivation, objectives and novelties of the research presented in this thesis. The chapter is divided into four following sections. Section 1.2 provides the fundamental background regarding topology optimization (TO) and peridynamics (PD) methods with the recent state of the art. This section also discusses the necessity of the coupling of PD and TO methods and proposing three-dimensional TO system which is called as peridynamics topology optimization (PD-TO). Afterwards, Section 1.3 provides the objectives and potential utilization areas of the PD-TO methods. Finally, the structure of the thesis is described in the Section 1.4

1.2 Background and Motivation

Topology optimization (TO) is the process of identifying the most efficient arrangement of material and connections within a specified design domain to achieve the best possible performance. This involves determining the optimal placement and distribution of material to meet specific design criteria and constraints. As a powerful structural design method, TO has been mostly utilized for improving critical engineering structures in the automotive and aerospace industries where the weight and stiffness of the structures are crucial factors (Briot & Goldsztejn (2018); Cavazzuti, Baldini, Bertocchi, Costi, Torricelli & Moruzzi (2011); Li, Liu, Zhang, Du & Guo (2021); Maute & Allen (2004); Xu, Chen, Tang & Cao (2012); Yang & Chahande

(1995); Zhu, Zhang & Xia (2016)). TO method mainly focuses on minimizing an objective function (i.e., compliance) while satisfying the problem constraints such as volume fraction, stress, and minimum dimensions (Deaton & Grandhi (2014); Rozvany (2009); Wu, Sigmund & Groen (2021)). However, reducing the weight of geometries while minimizing compliance or stress leads to a considerable decrease in manufacturing simplicity.

Figure 1.1 Distortions and defects in a twin cantilever beam due to residual stresses after cutting of support.(Buchbinder et al. (2014))



Due to the geometrical complexities emerging from TO processes, additive manufacturing (AM) technologies have been mostly preferred for the fabrication of optimized structures (Belhabib & Guessasma (2017); Gibson, Rosen, Stucker, Khorasani, Rosen, Stucker & Khorasani (2021); Jihong et al. (2021); Li, Qin, Xu, Zhou & Chen (2022); Liu, Gaynor, Chen, Kang, Suresh, Takezawa, Li, Kato, Tang, Wang & others (2018); Nejat, Changizi, Tootkaboni & Asadpoure (2021); Xu, Gao, Xiao, Gao & Li (2020)) since AM has ability to produce any components layer-by-layer which significantly reduces the geometric complexity limitations. Therefore, AM can take full advantage of the freeform structural development enabled by TO. On the other hand, additive manufacturing of those complex structures has been criticized for having residual stress concentrations (Allaire & Jakabčin (2018); Cheng, Liang, Bai, Chen, Lemon & To (2019); Misiun, van de Ven, Langelaar, Geijselaers, van Keulen, van den Boogaard & Ayas (2021)). Residual stress can lead to distortion of an additive manufacturing (AM) part once it is removed from the build platform, (Figure 1.1). Additionally, residual stresses can result in cracking and negatively impact the fatigue resistance of the part.(Becker, Kumar & Ramamurty (2021); Leuders, Thöne, Riemer, Niendorf, Tröster, Richard & Maier (2013); Yang, Xie, Zhao, Qin, Wang & Wu (2022); Zerbst, Bruno, Buffiere, Wegener, Niendorf, Wu, Zhang, Kashaev, Meneghetti, Hrabe & others (2021))

Most of the proposed topology optimization approaches utilize mesh-based methods such as the finite element method (FEM) to conduct structural analysis during the optimization. However, these methods bring out limitations in presence of structural discontinuities such as the need for re-meshing and elimination of elements to embed cracks in a design domain. As a result, they lead to higher computational complexity and become prone to inaccurate results in case of structural discontinuities. Therefore, several studies have been conducted to overcome the limitations of mesh-based methods in fracture modeling (Guidault, Allix, Champaney & Cornuault (2008); Kang, Liu & Li (2017); Kim, Pereira & Duarte (2010); Lazarus (2011); Pereira, Kim & Duarte (2012); Stazi, Budyn, Chessa & Belytschko (2003); Talebi, Silani, Bordas, Kerfriden & Rabczuk (2013)).

On the other hand, since the additive manufacturing processes involve heating and cooling repeatedly, topologically optimized structures with complex shapes have concentrated local residual stresses during manufacturing and result in poor material properties in corresponding regions (Bartlett & Li (2019); Mercelis & Kruth (2006); Parry, Ashcroft & Wildman (2016); Prabhakar, Sames, Dehoff & Babu (2015); Shiomi, Osakada, Nakamura, Yamashita & Abe (2004); Vrancken, Cain, Knutsen & Van Humbeeck (2014); Zaeh & Branner (2010)). This issue causes local failures such as cracks in the structures after 3D printing processes. Therefore, considering embedded cracks in those regions at the optimization stage would be crucial to improve the designs and prevent residual stress concentrations during manufacturing. At this point, non-local methods such as Peridynamics (PD) proposed by Silling (Silling (2000)) have the potential to practically overcome the issues related to mesh in presence of structural discontinuities without any additional special methods of fracture mechanics. The PD is discretizing structures with particles and utilizes integrodifferential equations while the classical continuum mechanics methods use partial derivatives which result in singularity in case of structural discontinuities.

1.3 Objectives of the Research

The main objective and novelty of the current thesis are developing a novel 3D topology optimization method based on peridynamics and utilizing the primary advantages of this method. Hence, all the following method development and implementation ideas of the research efforts provided in this thesis listed as:

- Density-based TO algorithms namely bi-directional evolutionary structural optimization (BESO), optimality criteria (OC), and proportional approach (PROP) will be coupled with peridynamics method for the optimization of three-dimensional structures.
- These methods will be developed with in-house MATLAB codes and comprehensively validated by solving various benchmark problems. We can embed crack/cracks into the initial design domain and optimize the initial structure once more to achieve more reliable designs against the designs obtained by classical FEM based TO methods. After the methods are developed, we will extend the utilization of the proposed TO methods by specific applications and frameworks:
- PD-TO methods can be performed on large-scale engineering structures by simulating their most critical loading conditions and avoiding crack formations in some regions via apriori knowledge of damaged regions.
- Furthermore, the PD-TO method can also be performed with thermo-mechanical AM simulations to decrease the residual stresses on the manufactured structures by metal AM processes.
- Additionally, the PD-TO method would systematically be performed by working with a CCM based failure criteria to increase the fracture toughness of the lightweight structures. In this situation, PD model can include many smaller cracks that are aligned according to first principle directions to reflect the mode-1 cracks in the initial design domain.
- Eventually, the precise crack modeling ability of PD-TO would enable the optimizer to create a final design with decreased strain energy over the full domain thereby providing more load-bearing capacity under the same boundary conditions.

1.4 Structure of the Thesis

This thesis is constituted by the following six chapters:

- **Chapter 1.** This chapter presents a basic introduction to the methods utilized in this thesis. In this context, topology optimization method (TO), additive

manufacturing (AM) and peridynamics (PD) are defined to emphasize the background and motivation of this thesis. Moreover, objectives of PD-TO research are listed, and finally the organization of the thesis are provided in this chapter.

- **Chapter 2.** This chapter starts with a historical overview of the TO algorithms and their limitations in modelling of discontinuities via existing local CCM methods. Afterwards, the relation between TO and AM processes is presented by providing the recent studies published which aim to increase the efficiency of the AM processes in manufacturing of the designs created by TO methods. Finally, the chapter provides the recent advances in non-local methods and applications of PD in TO field.

- **Chapter 3.** This chapter provides a detailed explanation of the mathematical foundations for three-dimensional peridynamic-based topology optimization (PD-TO) methods, named as PD-BESO-TO, PD-OC-TO, and PD-PROP-TO. It includes relevant equations, algorithms, and frameworks. All these TO algorithms are density-based, but BESO uses discrete density values, whereas OC and PROP use continuous density values that can vary between 0 and 1. The author has implemented these formulations and algorithms as in-house MATLAB codes. The numerical and experimental results from these 3D PD-TO methods are thoroughly discussed in the following chapters.

- **Chapter 4.** This chapter presents the novel applications of the three-dimensional PD-TO methods described in the previous chapter. Performing various benchmark TO cases, the numerical and experimental verification of three different proposed PD-TO methods are extensively demonstrated. In Section 4.1, 3D PD-BESO-TO method results are given via four cases and an experimental comparison between PD-TO and FEM-TO is performed to show the viability of the proposed method. Moreover, Section 4.2 shows the obtained TO results by PD-OC-TO and PROP-PD-TO methods for three case studies which have different crack position scenarios. The results showed that locating hypothetical cracks into the critical regions inside the initial design domain can increase the fracture toughness of the TO results obtained by proposed methods (PD-OC-TO and PD-PROP-TO). In Section 4.3, a large scale TO application of the PD-TO methods is performed by optimizing a ship-cross section.

- **Chapter 5.** This chapter presents a novel PD-TO strategy and its applications on minimizing the residual stress arises from AM processes due the repeated cooling and heating cycles. Section 5.1 proposes a systematic fu-

sion of failure criteria and PD-TO for enhanced fracture resistance of the light weighted engineering structures designed by TO methods. Moreover, Section 5.2, utilizes the proposed strategy in Section 5.1 to decrease the residual stresses on the final product fabricated by metal AM process. Finally, Section 5.3 deals with design, optimization and manufacturing of an engine mounting bracket via the proposed strategy and PD-TO method to increase the structural performance of the lightweighted and produced design by metal AM process thanks to minimized residual stresses.

- **Chapter 6.** This chapter outlines the achievements against research objectives, discusses gaps, and suggests future works. The final section provides the research outputs of this thesis.

2. LITERATURE REVIEW

2.1 Historical Overview of Topology Optimization Algorithms

Topology optimization (TO) is a robust design method that generates the best material distribution by improving an objective function such as minimizing strain energy and satisfying design constraints. Unlike size and shape optimization, TO serves as a freeform material distribution method that allows for the creation, merging, and splitting of interior discretized solid or void parts of the design domain while the optimization process thereby leading much larger design space and great structural performance. Thanks to the continuous development of classical TO methods and the introduction of promising new methods, TO has become the most attractive research topic in structural optimization over recent years.

Among the myriad of TO methods, a homogenization-based method (Bendsøe & Kikuchi (1988)) is one of the first studies followed by many researchers (Sigmund & Maute (2013)). Considering the homogenization method is one class of TO method, the other approaches can be classified (Rosen (2016)) as the level-set-based methods (Sethian & Wiegmann (2000); Van Dijk, Maute, Langelaar & Van Keulen (2013); Wang, Wang & Guo (2003)) and the solid isotropic material with penalization (SIMP) (Bendsøe & Sigmund (1999); Bendsoe & Sigmund (2013); Rozvany, Zhou & Birker (1992)) based methods. In the SIMP approach, design variables correspond to the elemental densities where a density value of 1 and 0 represent solid material and void, respectively. This model utilizes the so-called power-law scheme to update the material properties (elastic modulus) of the elements by a penalization factor (Bendsoe & Sigmund (2013)). Thus, the SIMP method enables TO iterations by changing the material properties of each element according to the design variables.

Utilizing the SIMP as the material interpolation scheme, several discrete density-

based TO algorithms are proposed such as simulated annealing optimization (Bureerat & Limtragool (2008)), evolutionary structural optimization (ESO) (Huang & Xie (2010b); Xie & Steven (1993)), and bi-directional evolutionary structural optimization (BESO) (Huang & Xie (2010a); Huang, Xie & Burry (2007); Querin, Young, Steven & Xie (2000); Yang, Xie, Steven & Querin (1999)) as an improved version of ESO, where the design variables only take binary values. Until the volume constraint is satisfied, the materials with low strain energy are removed in each iteration of the ESO approach whereas BESO can both eliminate/add those elements during the optimization. Besides, continuous density-based TO methods were proposed, providing less computational cost and higher efficiency than discrete density-based algorithms, and allowing intermediate densities in TO process (Svanberg & Werme (2007)).

Optimality criteria (OC) is a popular continuous density-based TO approach (Bendsøe (1995); Hassani & Hinton (1998); Sigmund (2001)). Instead of direct optimization of an objective function, pre-defined analytical criteria are satisfied during the OC process. The algorithm uses the material interpolation scheme of the SIMP and utilizes sensitivities in every iteration (Sigmund (2001)). Thus, the design variables are not updated using only the strain energy of elements, but the relative change of the elemental compliances with respect to densities. The sensitivities and previous elemental densities are incorporated with a bi-section algorithm in the inner loop of the OC to update the design variables (Hassani & Hinton (1998)). Another important TO approach based on SIMP is the proportional topology optimization algorithm (Biyikli & To (2015)). This method calculates the strain energy proportion of each element to the whole domain at the beginning of each iteration. Then, the desired amount of density is allocated to the elements based on their calculated proportion value. This increases computational efficiency by excluding the sensitivities. Both OC and PROP allow intermediate densities by utilizing continuous design variables and achieve optimal topologies with the integration of filtering schemes.

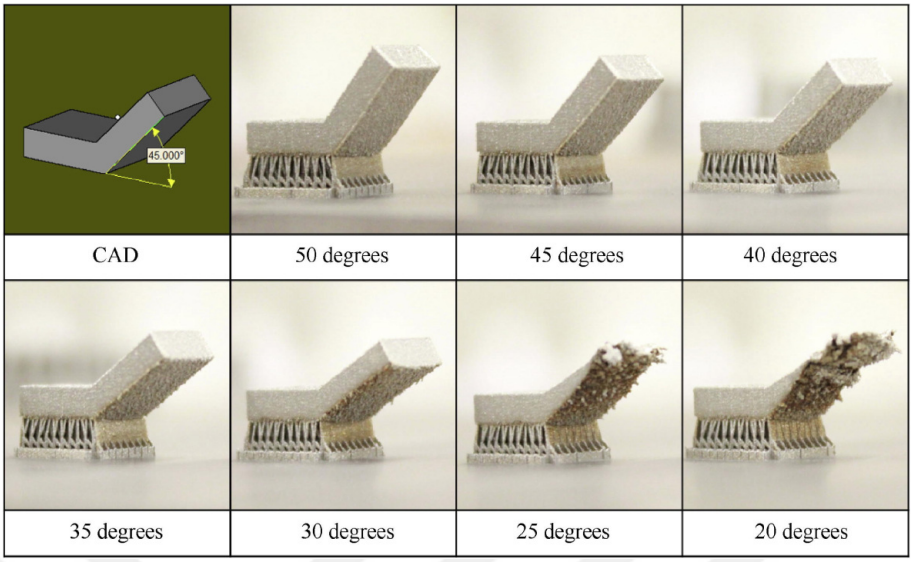
2.2 Topology Optimization for Additive Manufacturing

Although TO is increasingly utilized in lightweight designs of various engineering structures, TO designs have usually been criticized for causing complex forms, which makes obtained geometry difficult or even impossible to be fabricated by using traditional manufacturing methods such as machining, casting, etc. Additive manu-

facturing (AM) is a computer-controlled layer-by-layer process that provides an unrivaled capability to produce these intricate geometries obtained from TO, thereby transforming optimization methods from a conceptual design method into a practical and widely used design tool (Fernandez, Ayas, Langelaar & Duysinx (2021); Gibson et al. (2021); Joshi & Sheikh (2015); Tay, Panda, Paul, Noor Mohamed, Tan & Leong (2017)). The AM process enables producing more complex geometries without large increases in production time and cost. Despite these benefits, AM has its own set of manufacturing process-induced constraints that must be considered while developing topology optimization methods. Although TO can enhance the applicability and usage of AM for rapid/serial prototyping, most existing TO approaches do not consider the manufacturing limitations related to the AM practice. To resolve these issues during the topology optimization process, various research studies have been dedicated to studying overhang limitations (Allaire, Dapogny, Estevez, Faure & Michailidis (2017); Gaynor & Guest (2016); Guo, Zhou, Zhang, Du, Liu & Liu (2017); Langelaar (2017); Qian (2017); Wang, Gao & Kang (2018); Zhang, Cheng & Xu (2019)), minimum length scale control (Allaire, Jouve & Michailidis (2016); Liu & Ma (2018); Liu, Zheng, Ahmad, Tang & Ma (2019); Mohan & Simhambhatla (2019); Zhou, Lazarov, Wang & Sigmund (2015)), error control (Guo, Zhang & Zhang (2013); Schevenels, Lazarov & Sigmund (2011); Sigmund (2009)), and residual-stress-induced failures (Allaire & Jakabčin (2018); Cheng et al. (2019); Wildman & Gaynor (2017)). Besides, general problems and opportunities of leveraging TO algorithms for AM were elaborated in Brackett, Ashcroft & Hague (2011).

One of the most notable limitations can be considered as the presence of overhangs, which are not supported in downward-facing regions. Langelaar (2016) introduced a novel topology optimization formulation that considers AM fabrication model, which excludes the unprintable geometries from the design space. High-resolution meshing strategies were implemented for 3D-TO by considering the exclusion of overhangs (Zhang & Cheng (2020)). Besides, Fu, Rolfe, Chiu, Wang, Huang & Ghabraie (2019) implemented and experimentally validated Langelaar's method for the self-supported topologies. The term self-supporting means that the structure has no additional supporting material and has downward-facing surfaces, which exceed a certain overhang angle (Figure 2.1). Moreover, Mezzadri, Bouriakov & Qian (2018) conducted a study to optimize self-supporting structures and reduce the undesired effect of overhang regions. Further, Liu & Ma (2015) employed the level-set method to solve TO problems as a machining feature-based approach. Besides, the BESO-based design method was proposed to create periodic lattice structures to be manufactured by AM (Tang, Kurtz & Zhao (2015)).

Figure 2.1 Manufacturability of cantilever structures with decreased overhang angles (Jihong et al. (2021)).



In addition, various periodic truss-lattice cells for AM were analyzed and their performances were compared by experimental measurements (Li, Lei, Zhang, Zhang, Zhou, Wang & Fang (2020)). Most recently, a natural evolution method, that concurrently applies local reinforcement and searches density distribution, was proposed for the topology optimization of 3D continuous fiber-reinforced structures and their 3D printing (Safonov (2019)). In addition to overhang constraint, thermal residual stress is another undesired issue in metallic additive manufacturing processes. An electron or laser beam, as a heat source, is utilized in the layer-by-layer AM process (Bartlett & Li (2019); Cotteleer & Joyce (2014); Gu, Meiners, Wissenbach & Poprawe (2012); Sames, List, Pannala, Dehoff & Babu (2016); Zhou, Shen, Liu, Du, Jin & Lin (2022)), therefore different parts of the workpiece are heated and cooled repeatedly. Thus, the residual stress and distortion in additively produced components are caused by the spatially variable heat cycles. When a built structure is removed from its support, it can cause substantial deformations or even permanent damage, fracture, or delamination of the subsequent layers. As a result, predicting thermal residual stress and avoiding its negative effects are critical concerns. Many experimental and numerical studies for measuring thermal residual stress have been recently published (Fergani, Berto, Welo & Liang (2017); Gusarov, Yadroitsev, Bertrand & Smurov (2009); Heigel, Michaleris & Reutzel (2015); Megahed, Mindt, N'Dri, Duan & Desmaison (2016); Schoinochoritis, Chantzis & Salonitis (2017); Van Belle, Vansteenkiste & Boyer (2013)). There were detailed and simplified models proposed for numerical studies. The detailed models are computationally expensive due to their multi-physics/scale nature whereas simplified models are useful for macroscopic scale thanks to relevant homogenization techniques. Recently,

the inherent strain method was proposed using multi-scale modeling to predict the residual stresses during AM process (Chen, Liang, Hayduke, Liu, Cheng, Oskin, Whitmore & To (2019); Keller & Ploshikhin (2014); Li, Fu, Guo & Fang (2016); Liang, Cheng, Chen, Yang & To (2018); Neugebauer, Keller, Ploshikhin, Feuerhahn & Köhler (2014); Ueda & Yuan (1993)), and this method was used to reduce the residual stress-induced failures during the topology optimization process (Zhang, Ibhadode, Ali, Dibia, Rahnama, Bonakdar & Toyserkani (2020)). However, none of these studies can model any discontinuity (e.g., cracks) in the structure considering large-scale failures during the AM process.

2.3 The Role of Peridynamic Method and its Applications in Topology Optimization and Fracture Modelling Literature

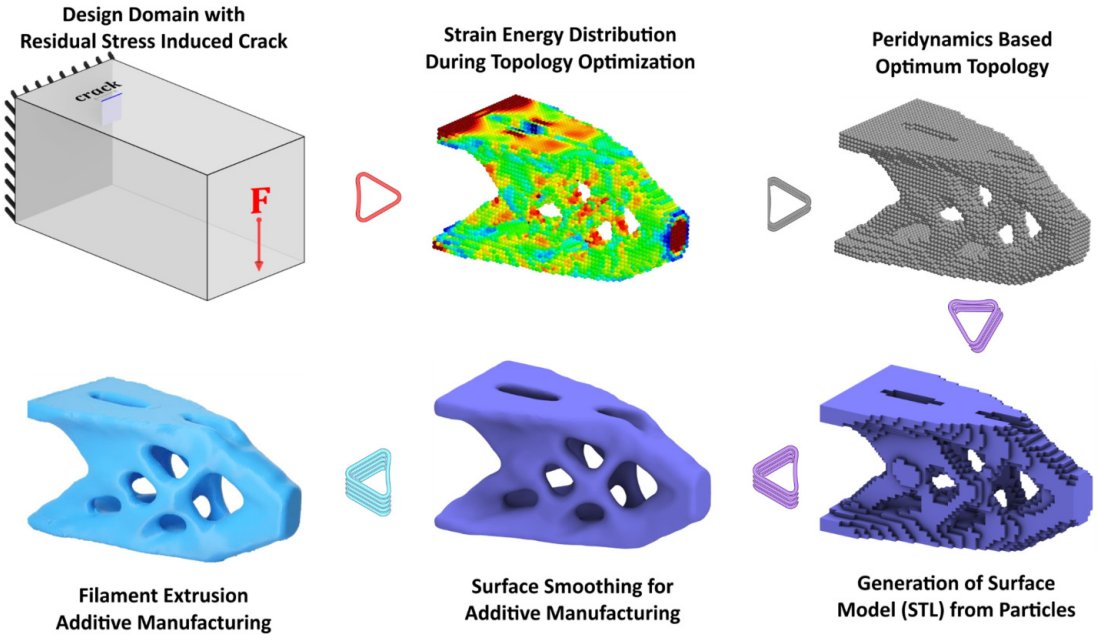
For modeling fracture problems, crack paths are influenced by the mesh edges in a finite element context. To address the issue of mesh dependency, Moës, Dolbow & Belytschko (1999) developed the X-FEM to implicitly represent cracks. Sharma & Maute (2018) presented a level set topology optimization approach that incorporates X-FEM for robust stress computation and uses a constraint agglomeration technique to enhance stress constraint handling. Very recently, Habashneh & Rad (2024) presented a structural topology optimization method that integrates fatigue crack propagation analysis using X-FEM and the Paris model, effectively optimizing material distribution under various crack conditions. However, tracking the evolution of complex fracture surfaces is still challenging, leading to recent research focusing on the phase-field fracture model, which treats material damage as a diffusive process rather than a discrete one.

Due to their ability to model structures with cracks/damages and analyze their growth more easily, meshless methods (Atluri & Zhu (1998); Belytschko, Lu & Gu (1994); Liu, Jun & Zhang (1995); Monaghan (2012)) have recently become popular for solving TO problems of cracked structures. The effects of pre-existing material discontinuities (i.e., cracks/damages) on 2D structures were investigated by employing the phase-field method in a mesh-dependent solution domain (Burger & Stainko (2006)). According to this study, initial material discontinuity can alter the final optimum topology such that neglecting them in the TO process may result in partially inaccurate topologies, especially in the vicinity of the damaged/cracked regions. Despite the proven significance of the initial discontinuities, among the existing topol-

ogy optimization studies, Xia, Da & Yvonnet (2018) investigated the effect of an initially embedded crack on quasi-brittle composites to increase its fracture resistance. Zhang, Liu, Nguyen-Thanh, Li, Li & Zhou (2024) developed an adaptive isogeometric–meshfree method using the phase field approach to efficiently enhance fracture resistance and reduce computational costs in topology optimization. Moreover, Wu, Fang, Zhou, Zhang, Sun, Steven & Li (2020) proposed a level-set-based topology optimization procedure combined with a phase-field fracture model to enhance fracture resistance in multimaterial composite structures, effectively addressing crack initiation and propagation. Wu, Yvonnet, Li & He (2022) proposed a topology optimization framework that combines the phase field method and SIMP to enhance dynamic fracture resistance by minimizing fracture energy during dynamic loading.

On the other hand, among the meshless approaches, a non-local reformulation of classical continuum mechanics proposed by Silling, namely Peridynamics (PD) (Silling (2000); Silling & Askari (2005); Silling, Epton, Weckner, Xu & Askari (2007)), offers a practical way to model discontinuities. PD method basically creates a particle-based discretization of the problem geometry and integrates the forces acting on each particle due to the non-local interactions. Hence, the PD method can accurately model the dynamic fracture behavior of the structures including crack branching and coalescence thanks to the utilization of the integral form of balance equations instead of partial derivatives. A crack can be involved in the structure by only breaking the necessary bonds between the particles. Horizon diameter determines the extent of interactions between the particles and must be constant in primary peridynamic formulations (bond-based peridynamics (BB-PD), ordinarystate-based peridynamics (OSB-PD), and non-ordinary state-based peridynamics (NOSB-PD)) to prevent erroneous wave reflections and ghost forces. Nevertheless, varying horizon dimensions can improve computational efficiency. Therefore, a PD formulation that involves changing horizon sizes and precisely satisfies the linear and angular momentum balances, named dual-horizon peridynamics (DH-PD) was introduced by Ren, Zhuang, Cai & Rabczuk (2016); Ren, Zhuang & Rabczuk (2017a). Further, Rabczuk & Ren (2017) provided a DH-PD formulation for fracture in granular and rock-like materials. Moreover, DH-PD is introduced for ductile fracture (Ren, Zhuang & Rabczuk (2017b)). Recently, to solve partial differential equations, Rabczuk, Ren & Zhuang (2019); Ren, Zhuang & Rabczuk (2020) suggested a nonlocal operator method (NOM). The traditional differential operators are generalized in the nonlocal operator. Because the nonlocal operator is defined by integral form, it is still applicable in fields where there is discontinuity.

Figure 2.2 The general framework of the particle-based topology optimization methods for topology optimization of structures with discontinuities. From the initial design domain to the rapid prototyping of the obtained results by the proposed PD-TO methods in this thesis.



Kefal, Sohouli, Oterkus, Yildiz & Suleman (2019) first proposed a novel PD-TO coupled approach conducting topology optimization of structures with embedded cracks where a discrete density-based TO method, BESO, is used. Then, the approach is extended to consider continuous density-based algorithms namely optimality criteria (OC) and proportional approach (PROP), while optimizing the cracked structures (Sohouli, Kefal, Abdelhamid, Yildiz & Suleman (2020)). Moreover, the multi-material TO of cracked structures was performed in Habibian, Sohouli, Kefal, Nadler, Yildiz & Suleman (2021). Furthermore, a comparative study between FEM-TO and PD-TO was conducted by Lahe Motlagh & Kefal (2021), where the advantages of the PD-TO approach were demonstrated in modelling cracks during the TO of two-dimensional structures. The PD-TO approach was also utilized to investigate the effect of micro-cracks in topology optimization (Motlagh, Kendibilir, Koc & Kefal (2021)). These PD-TO approaches are presented in 2D and showed that the cracked structures can be modeled easily without any re-meshing and eliminating particles. Overall, these present efforts advance the current state-of-the-art of the PD-TO research.To the best of author's knowledge, there is no study in the literature that proposes 3D PD-TO methods for optimizing the structures having structural discontinuities. In this regard, the current thesis majorly focuses on 3D modelling those local damages effectively utilizing state-of-the-art nonlocal theory,

peridynamics (PD), as pre-defined surface cracks before optimization and investigation of their effects on the optimized topologies (2.2). Accordingly, the proposed TO algorithms aim to decrease the residual stresses and defects on the final products produced by AM processes. Moreover, the fracture resistance and dynamic behaviour of the TO designs against possible damages under static/dynamic loads would be enhanced via PD-TO methods.

3. 3D PERIDYNAMICS TOPOLOGY OPTIMIZATION METHODS

3.1 Introduction

In this chapter, the mathematical background of the three-dimensional peridynamic based topology optimization methods namely PD-BESO-TO, PD-OC-TO, and PD-PROP-TO are extensively explained by providing relevant equations, algorithms and frameworks. Althouh all TO algorithms utilized in this thesis are density based frameworks the difference between them is that the BESO algorithm uses discrete density values whereas OC and PROP algorithms utilize continous density values which can take any value between 0 and 1. All these formulations and algorithms are implemented by the author as in-house MATLAB codes. Moreover, the obtained results by the developed 3D PD-TO methods are comprehensively discussed in Chapter 4 and Chapter 5.

3.2 Bond-Based Peridynamic Formulation for Three Dimensional Structures

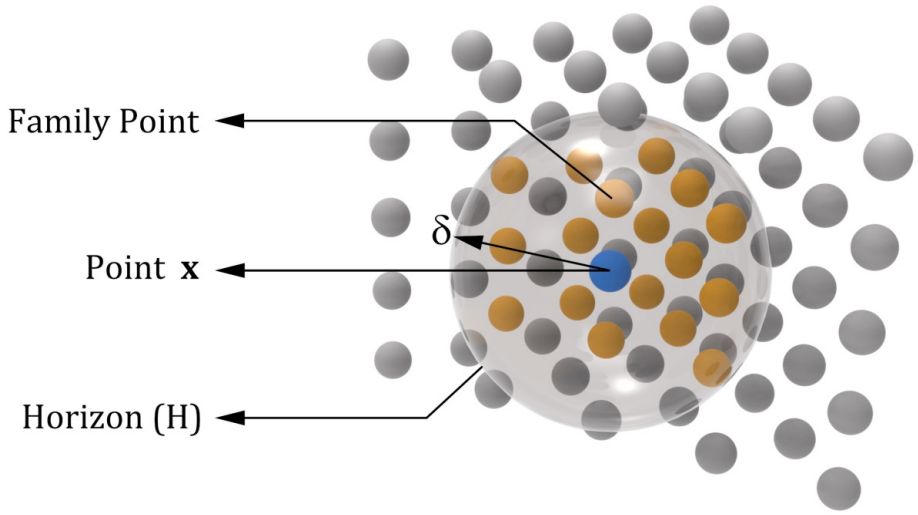
According to the classical continuum mechanics, the conservation of linear momentum yields the equation of motion as given in Equation 3.1, and angular momentum is locally satisfied by the symmetry of stress tensor, $\sigma = \sigma^{\mathbf{T}}$.

$$\rho \ddot{\mathbf{u}}(\mathbf{x},t) = \nabla \cdot \sigma + \mathbf{b}(\mathbf{x},t) \tag{3.1}$$

In Equation 3.1, $\mathbf{b}$ is the body force, $\ddot{\mathbf{u}}$ is the acceleration, ρ is the density, and $\mathbf{x}$ is the position vector of the material point. The divergence of the stress tensor may cause difficulties in the presence of discontinuities as it becomes singular at the position of cracks. The peridynamic theory, however, has the capability to eliminate such issues using non-locally written continuum mechanics formulation.

Peridynamics (PD), a non-local reformulation of classical continuum mechanics (CCM) was first proposed by Silling (2000) to provide a well-suited solution framework to fracture problems. This recent theory of solid mechanics, utilizes integral equations as an alternative to partial differential equations in the classical continuum mechanics formulation, which gained high potential for effective modelling of discontinuities in computational mechanics. The PD method uses integration instead of differentiation to calculate the force on a material particle. Therefore, the PD equations remain valid at points or surfaces of discontinuity without the use of spatial derivatives. As a result, the structural discontinuities become a part of the PD solution, not a problem that requires extra attention. In a three-dimensional domain, peridynamic theory may be considered a continuum form of molecular dynamics considering the non-local interactions between the material particles (Figure 3.1).

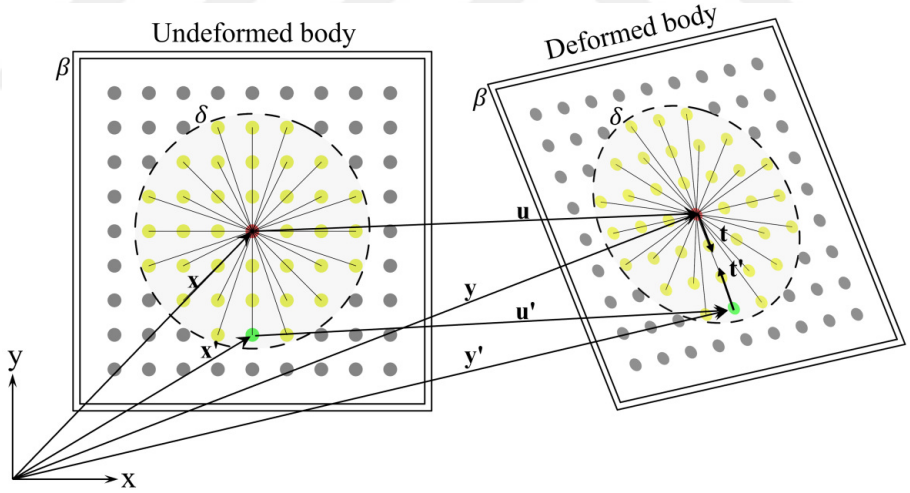
Figure 3.1 Representation of 3D particles in a PD model.



Currently, three peridynamics formulations have been proposed: bond-based (BB-PD), ordinary state-based (OSB-PD), and non-ordinary state-based (NOSB-PD)

peridynamic formulations. The original peridynamics began with the bond-based formulation (BB-PD) in which the bonds act as independent springs. BB-PD is limited to representing materials in 2D with a Poisson's ratio of one-third, and one-fourth in 3D. To surpass this limitation, the state-based peridynamics (SB-PD) has been brought forth, whereby the bond deformation is influenced by the overall deformation of other bonds. The SB-PD was expanded to include the OSB-PD and NOSB-PD types. In OSB-PD, the bond force direction is aligned with the bond, whereas it can have any orientation in NOSB-PD. Due to its straightforward implementation, the BB-PD is utilized in the solution steps of the TO process without losing any accuracy in the results. The force density vector which has opposite direction but equal magnitude according to BB-PD in a deformed state for two interacting points as shown in Figure 3.2. Peridynamics, is adopted in this study for performing topology optimization of three-dimensional geometries with/without structural discontinuities such as surface cracks or defects. The coupling of the PD and TO was originally implemented for the topology optimization of 2D geometries by Kefal et al. (2019) and is extended herein for three-dimensional analysis.

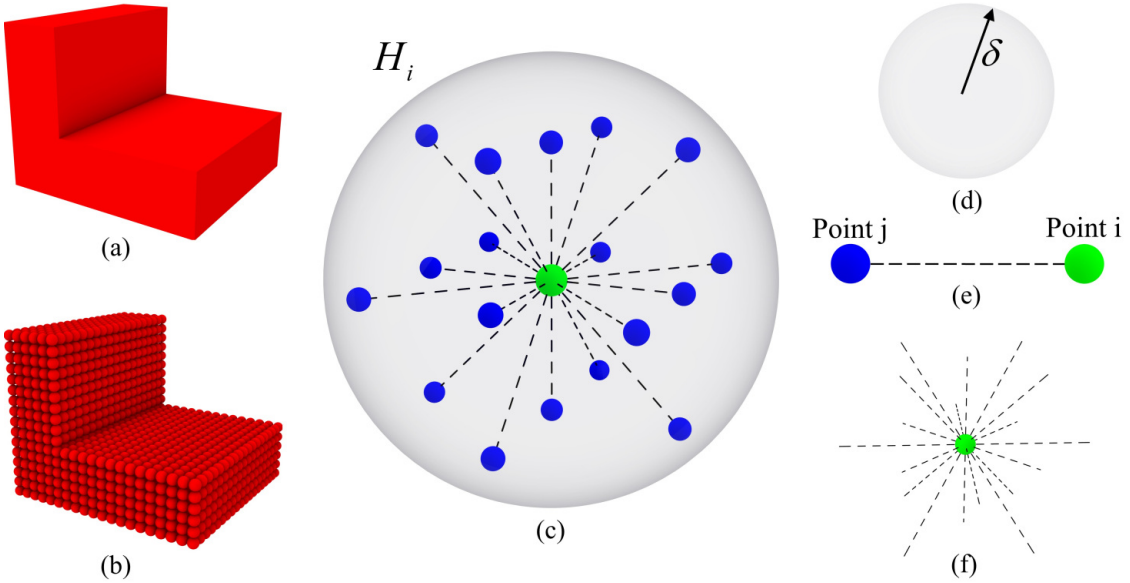
Figure 3.2 Two-dimensional illustration of interactions of a PD particle in before and after deformation.



In PD, material particles can be considered as an ensemble of infinitely small volumes. In this context, equally distanced particles form the solid geometry (Figure 3.3a, b) and these particles interact with each other as long as the distance between two interacting points is less than a pre-defined horizon size as depicted in Figure 3.3(c, d).The extent of these interactions is limited by a sphere for 3D space. As shown in Figure 3.3, each particle interacts with its neighbor (family) particles in a non-local sense, referred to as peridynamic bonds (Figure 3.3f), within a compactly supported domain called as the horizon, H_i, which can be a circle or sphere with a radius of δ for a 2D/3D domain, respectively. The PD equation can be considered

as an integral expression of the linear momentum balance in CCM.

Figure 3.3 PD discretization and particle interactions in 3D space. (a) An example of 3D model. (b) Particle-based discretized PD model of the given model. (c) Horizon and interactions of a particle i. (d) Horizon. (e) PD bond between two interacting particles i and j. (f) All the bonds of the particle i.



The PD equation of motion for a material point located at point $\mathbf{x}$ in reference configuration at the time t can be written as:

$$\rho(\mathbf{x})\,\ddot{\mathbf{u}}(\mathbf{x},t) = \mathbf{L}_u(\mathbf{x},t) + \mathbf{b}(\mathbf{x},t) \quad \forall x \in \beta,\ t \geq 0 \tag{3.2}$$

$$\mathbf{L}_u(\mathbf{x},t) = \int_H \left(\mathbf{t}\left(\mathbf{u}'-\mathbf{u},\mathbf{x}'-\mathbf{x}\right) - \mathbf{t}'\left(\mathbf{u}-\mathbf{u}',\mathbf{x}-\mathbf{x}'\right)\right) dH \tag{3.3}$$

where β represents the reference configuration of the body, $\mathbf{u}$ is the displacement vector. $\mathbf{L}_u$ corresponds to the internal force density per unit volume that is applied on a particle $\mathbf{x}$ by other material points. Another term given in Equation 3.3, $\mathbf{t}$, is the force density vector which has opposite direction but equal magnitude according to bond-based PD in a deformed state for two interacting points $\mathbf{x}$ and $\mathbf{x}'$ in two-dimensional space as depicted in Figure 3.2. Here, the force density vector can be given as follows:

$$\mathbf{t} \equiv \mathbf{t}(\eta, \xi) = \frac{1}{2} f \frac{\mathbf{y}' - \mathbf{y}}{|\mathbf{y}' - \mathbf{y}|} \tag{3.4}$$

$$\mathbf{t}' = \mathbf{t}'(-\eta, -\xi) = -\frac{1}{2} f \frac{\mathbf{y}' - \mathbf{y}}{|\mathbf{y}' - \mathbf{y}|} \tag{3.5}$$

where the magnitude of pairwise force density is represented by f. Here, η and ξ define the relative displacement and position vectors of two particles as:

$$\eta = \mathbf{u}' - \mathbf{u} \tag{3.6}$$

$$\xi = \mathbf{x}' - \mathbf{x} \tag{3.7}$$

When we add the initial position vector and displacement vector together, we reach the final position vector of the relevant particle. Therefore, the final position vectors can be written as $\mathbf{y}' = \mathbf{x}' + \mathbf{u}'$ and $\mathbf{y} = \mathbf{x} + \mathbf{u}$. Considering that $\mathbf{t}'(-\eta, -\xi) = -\mathbf{t}(\eta, \xi)$ satisfies the conservation rule of linear and angular momentum, the general PD equation of a motion can be rewritten in terms of the pairwise force density vector as:

$$\rho(\mathbf{x})\, \ddot{\mathbf{u}}(\mathbf{x}, t) = \int_H \mathbf{f}(\eta, \xi)\, dH + b(\mathbf{x}, t) \tag{3.8}$$

where the pairwise force density function is equal to:

$$\mathbf{f}(\eta, \xi) \equiv \mathbf{f} = f \frac{\mathbf{y}' - \mathbf{y}}{|\mathbf{y}' - \mathbf{y}|} = cs \frac{\xi + \eta}{|\xi + \eta|} \tag{3.9}$$

where s is the stretch and c is the bond constant that defines the strength of the direct physical interaction of the material points which can be considered as spring in the elastic region. The stretch between two body points and bond constant for

elastic material can be calculated as given in Equation 3.10 and Equation 3.11, respectively:

$$s = \frac{|\mathbf{y}' - \mathbf{y}| - |\mathbf{x}' - \mathbf{x}|}{|\mathbf{x}' - \mathbf{x}|} = \frac{|\xi + \eta| - |\xi|}{|\xi|} \tag{3.10}$$

$$c = \frac{12E}{\pi \delta^4} \tag{3.11}$$

It is important to remind that the interactions are non-local but restricted by a predefined horizon size, δ, thus it follows:

$$\mathbf{f}(\eta, \xi) = 0 \;\; \forall \eta \;\; \text{whenever} \;\; |\xi| > \delta \tag{3.12}$$

which says that a particle $\mathbf{x}$ cannot communicate with a point beyond its horizon. In the next step, we can formulate the micro-potential between two interacting points, and thus, the total strain energy density of a point at $\mathbf{x}$ can be written by integrating all the micro-potentials exerted from its neighborhood (H) as follows:

$$w(\eta, \xi) = \frac{1}{2}\mathbf{f}(\eta, \xi)(|\xi + \eta| - |\xi|) \equiv \frac{1}{2} c s^2 |\xi| \tag{3.13}$$

$$W(\mathbf{x}, t) = \frac{1}{2} \int_H w(\eta, \xi)\, dH \tag{3.14}$$

Consequently, one can calculate the compliance (i.e., total strain energy) of the structure by integrating the strain energy densities of the particles over the whole domain β as:

$$C = \int_\beta W(\mathbf{x}, t)\, d\beta \tag{3.15}$$

At this point, general formulations should be written in explicit forms for computational implementation purposes. Then, the PD equation of motion can be written in an explicit form as:

$$\rho(\mathbf{x}_i)\,\ddot{\mathbf{u}}(\mathbf{x}_i,t) = \sum_{j=1}^{N_f} \mathbf{f}_{ij} V_j + \mathbf{b}(\mathbf{x}_i,t) \tag{3.16}$$

Here, i is the index of the particle located at $\mathbf{x}$ which has the interactions between j points with the total number of N_f. The summation term on the right-hand side in Equation 3.16 calculates the total PD force acting on the point i, whereas the second term is the body force acting on the same point. V_j is the volume of a material point. Linearization of PD force density is possible to perform a direct solution approach. The linearized version of force density for the point i is given as:

$$\mathbf{f}_{ij} \equiv \mathbf{f}(\eta_{ij},\xi_{ij}) = \frac{c_{ij}}{|\xi_{ij}|}\mathbf{T}_{ij}\eta_{ij} \tag{3.17}$$

The pairwise force density vector and transformation matrix are represented by $\mathbf{f}_{ij}$ and $\mathbf{T}_{ij}$ in the above equation, respectively. The use of a transformation matrix is here necessary for mapping the relative displacement from the bond direction to the direction of the global axes in the initial configuration. For a three-dimensional space, the transformation matrix and direction of cosines can be written as:

$$\mathbf{T}_{ij} = \begin{bmatrix} n_x n_x & n_x n_y & n_x n_z \\ n_y n_x & n_y n_y & n_y n_z \\ n_z n_x & n_z n_y & n_z n_z \end{bmatrix} \tag{3.18}$$

$$n_\chi = \frac{\chi_j - \chi_i}{|\xi_{ij}|} \;\; (\chi = x, y, z) \tag{3.19}$$

We can define the ξ_{ij} , η_{ij} vectors, as well as $\mathbf{x}_\chi$, and $\mathbf{u}_\chi$ vectors for the position and deformation vectors of two body points in the global orthogonal cartesian coordinate (x, y, z) system as:

$$\xi_{ij} = \mathbf{x}_j - \mathbf{x}_i \tag{3.20}$$

$$\eta_{ij} = \mathbf{u}_j - \mathbf{u}_i \tag{3.21}$$

$$\mathbf{x}_\chi = [x_\chi \ y_\chi \ z_\chi]^T \ (\chi = i, j) \tag{3.22}$$

$$\mathbf{u}_\chi = [\bar{u}_\chi \ \bar{v}_\chi \ \bar{w}_\chi]^T \ (\chi = i, j) \tag{3.23}$$

Considering the changing material properties of the particles during the optimization process, the bond constant, c_{ij}, and harmonic averaged elastic modulus, E_{ij}, of the interactions should be calculated by:

$$c_{ij} = \frac{12 E_{ij}}{\pi \delta^4} \tag{3.24}$$

$$E_{ij} = \frac{2 E_i E_j}{E_i + E_j} \tag{3.25}$$

Now, one can perform quasi-static analysis by setting resultant zero acceleration. Then, the general PD equation can eventually be written in compact matrix-vector form explicitly:

$$\sum_{j=1}^{N_f} \frac{c_{ij} V_j}{|\xi_{ij}|} [\mathbf{T}_{ij} \ \ -\mathbf{T}_{ij}] \begin{Bmatrix} \mathbf{u}_i \\ \mathbf{u}_j \end{Bmatrix} = \begin{Bmatrix} b_x \\ b_y \\ b_z \end{Bmatrix}_i \tag{3.26}$$

$$\mathbf{s}_i \mathbf{d}_i = \mathbf{b}_i \tag{3.27}$$

$$\mathbf{s}_i = \left[\sum_{j=1}^{N_f} \mathbf{T}_{ij} \frac{c_{ij} V_j}{|\xi_{ij}|} \quad -\mathbf{T}_{i1} \frac{c_{i1} V_1}{|\xi_{i1}|} \quad -\mathbf{T}_{i1} \frac{c_{i2} V_2}{|\xi_{i2}|} \quad ... \quad -\mathbf{T}_{iN_f} \frac{c_{iN_f} V_n}{\left|\xi_{iN_f}\right|} \right] \tag{3.28}$$

$$\mathbf{d}_i = \begin{bmatrix} \mathbf{u}_i & \mathbf{u}_1 & ... & \mathbf{u}_{N_f} \end{bmatrix}^T \tag{3.29}$$

$$\mathbf{b}_i = \begin{bmatrix} b_x & b_y & b_z \end{bmatrix}_i^T \tag{3.30}$$

In Equation 3.28 and Equation 3.29, the stiffness matrix and displacement vector of a body-point, $\mathbf{s}_i$ and $\mathbf{d}_i$, are given in the explicit form. Moreover, $\mathbf{b}_i$ is the force vector of a particle and includes the body force components along the x, y and z axes. Note that, the displacement vector $\mathbf{d}_i$, contains all the displacement vectors of the family points of i. The displacement vector of a family member is then represented by, $\mathbf{u}_i$, which consists of three components of the displacement in the cartesian coordinate system as:

$$\mathbf{u}_i = \begin{bmatrix} u_x & u_y & u_z \end{bmatrix}_i \tag{3.31}$$

Since a set of equations has been established on a single point, one can construct a single compact matrix-vector equation for the entire domain, β, by the given assembly process, $\cup$, for the global stiffness matrix, displacement and force vectors $\mathbf{S}$, $\mathbf{D}$, and $\mathbf{B}$:

$$\mathbf{SD} = \mathbf{B} \tag{3.32}$$

$$\mathbf{S} = \bigcup_{i=1}^{N} \mathbf{s}_i, \ \mathbf{D} = \bigcup_{i=1}^{N} \mathbf{d}_i, \ \mathbf{B} = \bigcup_{i=1}^{N} \mathbf{b}_i \tag{3.33}$$

N is the total number of particles in the domain. In this system, we can solve a quasi-static problem by applying the relevant boundary and loading conditions. In PD, it is crucial to apply the forces as body force density on each particle in the desired layer. Moreover, the relevant points should be constrained according to the given boundary conditions. Consequently, the PD problem can be directly solved by performing a similar procedure as the conventional finite element does. In this way, taking the inverse of the reduced global stiffness matrix and solving the system results in the displacements of all particles. Hence, the strain energy densities that are needed by the optimization process can be calculated particle-wise as:

$$W_i = \frac{1}{2} \sum_{j=1}^{N_f} \frac{c_{ij}(|\xi_{ij} + \eta_{ij}| - |\xi_{ij}|)^2}{2\,|\xi_{ij}|} V_j \tag{3.34}$$

To calculate the objective function (compliance) at the beginning of each TO iteration, a summation of the energy densities can be taken as:

$$C = \sum_{i=1}^{N} W_i V_i \tag{3.35}$$

which can be used to define the design variables of the particles in the topology optimization process to be elaborated in the proceeding section.

3.3 Crack Implementation in Peridynamics Topology Optimization

In the proposed three-dimensional PD-TO algorithm, we generated all the surface cracks by breaking the relevant PD bonds which are intersecting with a crack. For this purpose, we scan all interactions and evaluate them geometrically to understand whether they are intersecting with the crack or not. In this respect, the crack

implementation procedure is schematically explained in Figure 3.4. Additionally, a pseudo-code of this procedure is shown in Figure 3.5. In the given algorithm, N and N_f are representing the total number of particles in the domain and the number of family members for each material point, respectively. This process can also be investigated visually from Figure 3.4. As shown in the illustration, 8 particles are interacting with the total number of 28 PD bonds before a crack (Figure 3.4a). Then, the embedded crack cuts some of these interactions (8 bonds) from the intersecting points (Figure 3.4b). In the final state, as depicted in Figure 3.4c, the remaining bonds continue to play a role in the PD model.

Figure 3.4 Surface crack modelling in a three-dimensional PD domain. (a) PD particles and their interactions before the crack, (b) Intersection points of the bonds and a surface crack, (c) Interactions of the same particles after crack involvement.

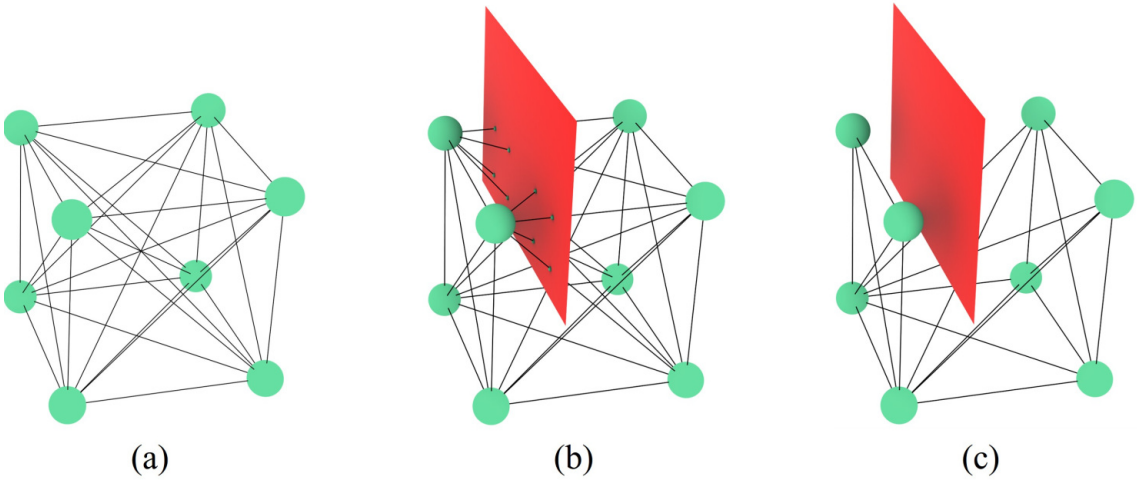


Figure 3.5 Crack generation algorithm for breaking the intersecting bonds.

Algorithm 1: Pseudo-code of the crack implementation in PD-TO

```
procedure Update the failure function by checking intersections
    for i = 1 to N do
        for j = 1 to N_f (i) do
            Create a line between two interacting material points
            if intersection between line and crack surface = true then
                Assign the failure value as: fail (i, j)=0
            end if
        end for
    end for
end procedure
```

A scalar-valued failure function defining the failure parameter γ_{ij} between points and j can be defined explicitly as:

$$\gamma_{ij} = \begin{cases} 0 & \text{if } s_{ij} > s_c \\ 1 & \text{otherwise} \end{cases} \tag{3.36}$$

where 0 and 1 values correspond to a broken or unbroken bond, respectively. Thus, to involve the failure in the PD model, the failure parameter of the relevant interactions should be updated to zero. In addition, the critical stretch value, s_c, is the decisive parameter that defines a critical stretch limit in a dynamic PD analysis to break the bond when a stretch value between two points, s_{ij}, exceeds the pre-defined limit. The critical stretch can be calculated for three-dimensional bodies as:

$$s_c = \sqrt{\frac{5G_c}{6E\delta}} \tag{3.37}$$

Here, G_c, is the critical energy release rate which is a characteristic of materials related to fracture behaviour. Moreover, the damage parameter, ϕ_i, represents the amount of damage at a material point which can be utilized to monitor crack propagation in time. The damage is associated with the failure function in a way that an increasing number of broken bonds leads the damage value to converge 1 as:

$$\phi_i = 1 - \frac{\sum_{j=1}^{N_f} \gamma_{ij} V_j}{\sum_{j=1}^{N_f} V_j} \tag{3.38}$$

Finally, to obtain converged results in the dynamic PD analysis, the time step size is calculated by utilizing the standard von Neumann stability analysis (Lapidus & Pinder (1999)) as:

$$dt = 0.8\sqrt{\frac{\rho}{2\pi b \delta^3}} \tag{3.39}$$

where b is one of the PD parameters for three-dimensional analysis

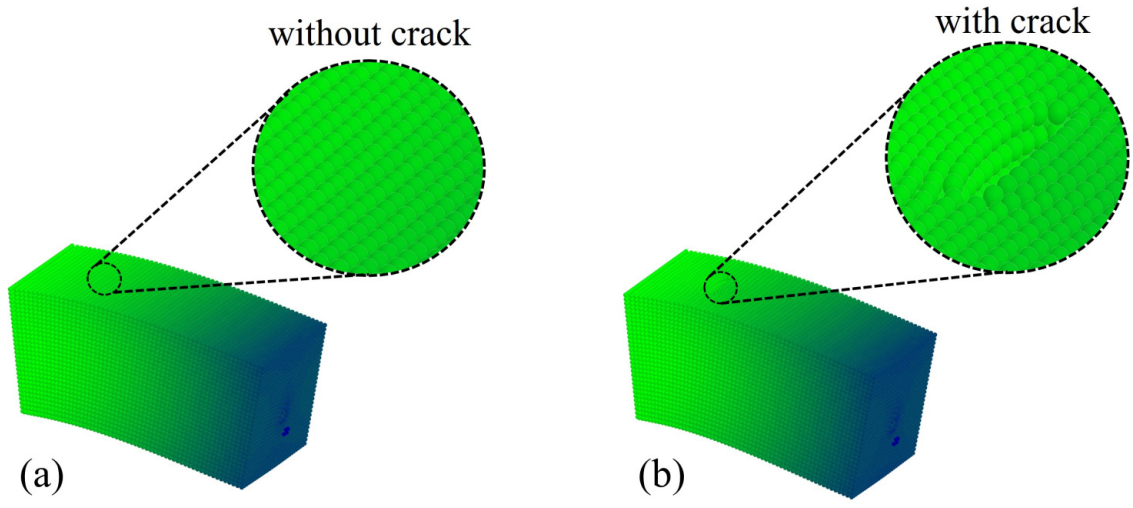
(3.40) $$b = 15\mu \Big/ 2\pi\delta^5$$

which is related to the engineering material constant of shear modulus. Additionally, shear modulus, μ, can be calculated as

(3.41) $$\mu = E/2(1+v)$$

by using Poisson's ratio value of $v = 1/4$ for 3D BB-PD. Elimination of the PD bonds in the cracked region gives rise to the relevant particles the chance of moving independently. To reveal this mechanical effect, the total displacements of a cantilever beam problem are given in Figure 3.6. It is observed that the particles in the zoomed region are aligned in a regular arrangement in a crack-free state (Figure 3.6a) whereas these particles are looking separated in the cracked model (Figure 3.6b).

Figure 3.6 Displacement contours of a simple bending problem (a) without crack, and (b) with crack where the results are 300 times exaggerated for a better representation



3.4 Topology Optimization Problem Statement

This chapter presents the essential principles of the topology optimization process, elucidating the mathematical foundation underlying the employed algorithms for updating material density. Here, our objective is to explore the optimal material distribution across the design domain while satisfying a specified volume constraint on the material. Minimizing compliance stands out as the most selected objective function within the topology optimization literature. This framework involves assessing the structural response iteratively throughout the optimization process. Considering that the mean compliance (strain energy) of the structure is an inverse indicator of stiffness, the objective function is formulated to minimize the mean compliance. As a result, utilizing the strain energy values calculated by PD, the compliance of the structure can be minimized with the following scheme:

$$\min_{\kappa_i} C(\kappa_i) \;\; s.t. \begin{cases} \mathbf{SD} = \mathbf{B} \\ \sum_{i=1}^{N} \kappa_i V_i = \bar{V} \sum_{i=1}^{N} V_i \\ \kappa_{min} \leq \kappa_i \leq 1 \end{cases} \tag{3.42}$$

Each PD particle has a design variable, κ_i, that determines its density and thereby its material property. The design variable can take a value between 0 and 1, continuously. Therefore, a particle in the design domain can be placed as void, solid, or even as a material with an intermediate density. Material properties are updated using the SIMP which depends on elastic moduli of solid and void material in addition to the design variable as:

$$E_i \equiv E_i(\kappa_i) = E^v + (\kappa_i)^p (E^s - E^v) \tag{3.43}$$

Here, solid and void materials have the elastic moduli of E^s and E^v, respectively. The power of the design variable, penalization parameter, p, is used to achieve distinct values. Setting the elastic modulus of void material to $E^v = 0$, simplifies Equation 3.41 into:

$$E_i = (\kappa_i)^p E^s \tag{3.44}$$

A minimum value of the design variable can be defined in the range of $0 < \kappa_{\min} < 10^{-3}$ which ensures that the elastic modulus of void material is not equal to zero. Moreover, the penalty parameter can be selected in between $1 \leq p \leq 5$. We adjust the optimization parameters as $\kappa_{\min} = 10^{-3}$ and $p = 3$ in this thesis.

3.5 Bi-directional Evolutionary Structural Optimization Method

The BESO algorithm adds and removes particles based on their sensitivity numbers until the objective volume fraction is attained. The structure's initial volume is set to the total percentage of the design domain; as a result, it should be steadily reduced at each iteration until the target volume fraction is achieved. Therefore, the target volume for the $(k+1)^{th}$ iteration can be defined as:

$$V_{k+1}^{tar} = V_k^{tar}(1 - ER) \tag{3.45}$$

ER is the evolutionary volume ratio and it determines the percentage of the decrease in the structure volume. When the computed volume for the following step is less than the target volume, then V_{k+1}^{tar} is fit to be target volume. The design variables are reset for all the particles according to their sensitivity numbers using the Optimality Criteria (OC). In each iteration, for solid particles, the design variable is switched from 1 to $\kappa_{\min}$ if:

$$\alpha_i \leq \alpha_{th} \tag{3.46}$$

and for void particles, the design variable is switched from $\kappa_{\min}$ to 1 if:

$$\alpha_i > \alpha_{th} \tag{3.47}$$

where α_{th} is the threshold of the sensitivity number. The optimization process stops when the target volume and the following convergence criterion are satisfied.

$$error = \frac{\left| \sum_{m=1}^{M} (C_{k-m+1} - C_{k-M-m+1}) \right|}{\sum_{m=1}^{M} C_{k-m+1}} \leq \tau \tag{3.48}$$

where M is an integral number, which is selected as 5 here, and τ is an allowable convergence error. The general framework of the computational method is summarized in Figure 3.7. Moreover, to clarify the computation sensitivity threshold and assignment of design variables for solid/void particles, a pseudo-code is given in Figure 3.8.

Figure 3.7 Flowchart of the proposed 3D PD-BESO-TO method.

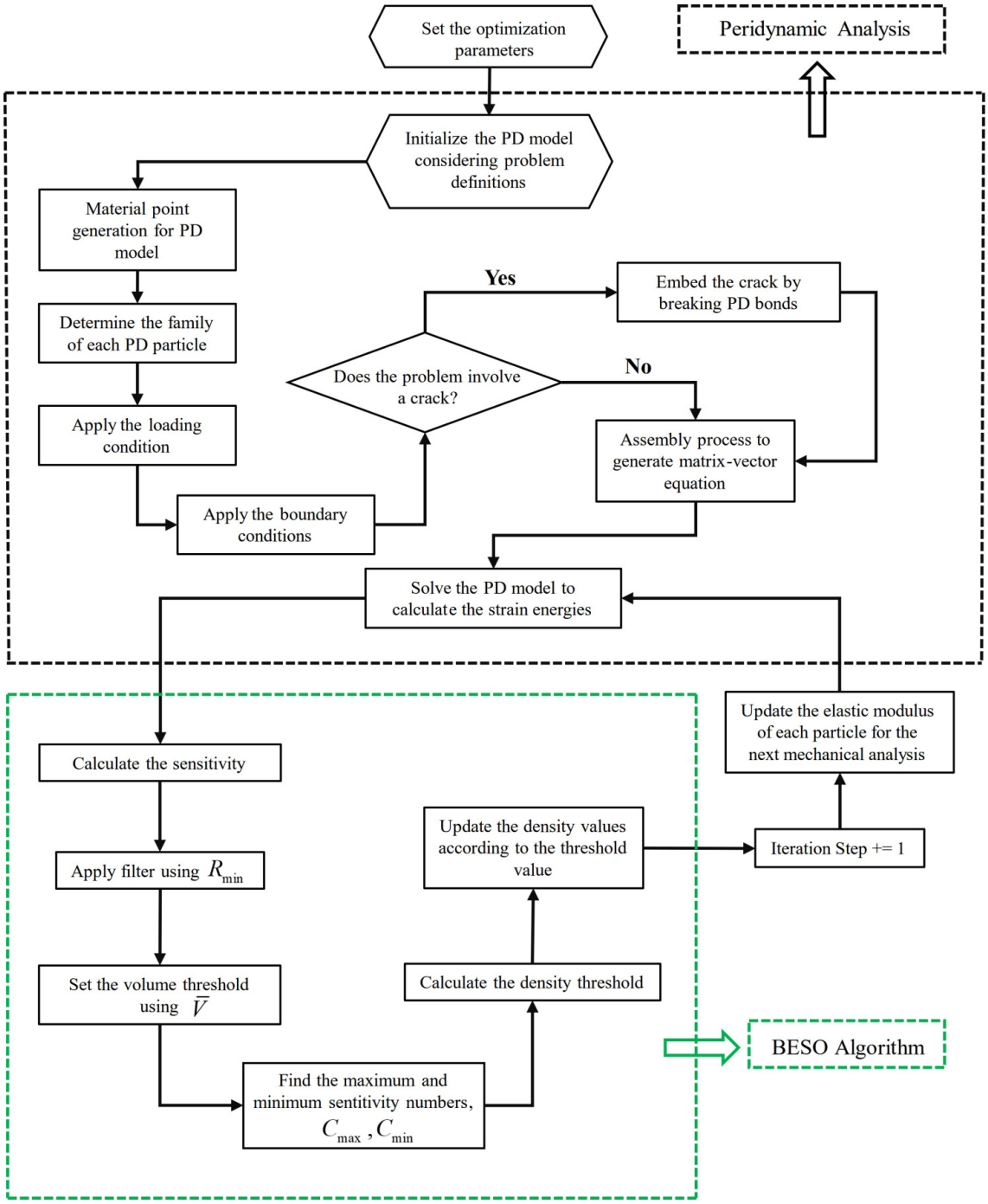


Figure 3.8 Design variable updating algorithm in BESO method.

Algorithm 2: Pseudo-code of the sensitivity threshold and design variable update.

procedure Update the design variables
  Find the minimum and maximum strain energies: $C_{\min} = \min(C)$, $C_{\max} = \max(C)$
  while $\left((C_{\max} - C_{\min}) / C_{\max}\right) > 10^{-5}$ **do**
    Calculate the threshold of the sensitivity number: $\alpha_{th} = \left(C_{\max} + C_{\min}\right) / 2$
    for $i = 1$ to N **do**
      if $\alpha_i > \alpha_{th}$ **then**
        Assign the design variable as: $\kappa_i = 1$
      else
        Assign the design variable as: $\kappa_i = \kappa_{\min}$
      end if
      if $sum(\kappa_i) - \overline{V} > 0$ **then**
        Assign the threshold sensitivity as minimum: $C_{\min} = \alpha_{th}$
      else
        Assign the threshold sensitivity as maximum: $C_{\max} = \alpha_{th}$
      end if
    end for
  end while
end procedure

3.6 Optimality Criteria Method

Optimality criteria (OC), a sensitivity-based topology optimization approach, is used to solve the described optimization problem. The method utilizes the filtered sensitivities to distribute the elemental densities and provides intermediate densities by continuous design variables. The method updates the design variables based on the following equation:

$$\kappa_i^{new} = \begin{cases} \max(0,\ \kappa_i - mv) & \text{if} \quad \kappa_i B_i^{0.5} \leq \max(0,\ \kappa_i - mv) \\ \min(1,\ \kappa_i + mv) & \text{if} \quad \kappa_i B_i^{0.5} \geq \min(1,\ \kappa_i + mv) \\ \kappa_i B_i^{0.5} & \text{otherwise} \end{cases} \tag{3.49}$$

where the move limit (mv) is defined as 0.2 and B_i is computed with the optimality

condition:

$$B_i = \frac{-\frac{\partial C(\kappa_i)}{\partial \kappa_i}}{\lambda \frac{\partial V(\kappa_i)}{\partial \kappa_i}} \tag{3.50}$$

where λ is a Lagrangian multiplier which is found by a bi-sectioning algorithm. The sensitivity of a compliance value, ω_i, can be calculated as follows:

$$\omega_i = \frac{\partial C\left(\kappa_i\right)}{\partial \kappa_i} = -p(\kappa_i)^{p-1} C_i \tag{3.51}$$

where the compliance of any particle is represented by C_i. It can be calculated using Equation 3.35.

$$error = \frac{\left| \sum_{m=1}^{M} (C_{k-m+1} - C_{k-M-m+1}) \right|}{\sum_{m=1}^{M} C_{k-m+1}} \leq \tau \tag{3.52}$$

The pseudo-code of the OC method is given in Figure 3.9. The method starts with using the current strain energies and previous design variables to calculate the sensitivity of each element which is the key factor to determine the new elemental densities. Then, the sensitivity values are filtered by weighted local averaging within a sphere horizon with radius to prevent checkerboard patterns and instabilities in the optimized topologies. The algorithm continues with initializing the volume threshold, lower and upper bounds, and move limits that will be used in the inner loop while updating the elemental densities. The inner loop uses the lower and upper bounds for the termination criterion and starts with calculating the middle value between the bounds. Afterward, the algorithm recalculates the densities using Equation 3.49. At the end of each inner loop iteration, the bounds are updated with the bi-sectioning algorithm. Finally, when the inner loop terminates, the design variables are assigned to the calculated densities.

Figure 3.9 Design variable updating algorithm in OC method.

Algorithm 3: Pseudo code of the optimality criteria

```
procedure Update the design variables
    Calculate the sensitivities
    Apply filter to sensitivities
    Set the volume threshold, V_thr = V̄N
    Set lower and upper bounds for the bi-section algorithm, l_1 = 0, l_2 = 10^5, mv = 0.2
    while (l_2 − l_1)/(l_1 + l_2) > 10^−4 do
        Calculate the middle of the bounds: l_mid = (l_1 + l_2)/2
        Update the densities using Eq. (41)
        if Σ κ_i^new > V_thr then
            Update the lower bound: l_1 = l_mid
        else
            Update the upper bound: l_2 = l_mid
        end if
    end while
    Update the design variables for the next iteration
end procedure
```

3.7 Proportional Optimization Method

Proportional topology optimization algorithm (PROP), originally introduced in Biyikli & To (2015), a non-sensitivity approach, distributes material in a given domain by assigning the design variables to particles proportionally to their compliance value. Unlike optimality criteria (OC), sensitivity calculations are not included in this method, so it is both a computationally cheaper approach and prevents the complexities related to the incorporation of sensitivities. In addition, similar to OC, PROP employs continuous density variables resulting in intermediate densities and enhanced search performance during the optimization. PROP distributes the densities according to the strain energy of the particles as follows:

$$\kappa_i{}^{opt} = \frac{R_m}{\sum_{i=1}^{N} \left(C\left(\kappa_i\right) V_i\right)^q} C(\kappa_i)^q \tag{3.53}$$

R_m is the amount of remaining material, ${\kappa_i}^{opt}$ corresponds to optimal particle densities in the current iteration, and q represents the proportion exponent. The actual material distributed to the particles is calculated after applying the filter on ${\kappa_i}^{opt}$. Then, the design variables are updated for the next iteration as follows:

$$ {\kappa_i}^{new} = \alpha {\kappa_i}^{prev} + (1-\alpha)\, {\kappa_i}^{opt} \tag{3.54} $$

${\kappa_i}^{new}$, particle densities in the next iteration, is calculated here by linearly blending the ${\kappa_i}^{opt}$ and, ${\kappa_i}^{prev}$ design variables from the last iteration. The history coefficient, α, is utilized to control the impact of the last iteration on the current one.

The pseudo-code of the PROP method is given in Figure 3.10. After the structural analysis and strain energy calculation, the algorithm starts with the determination of the target volume (desired total volume), and the remaining volume (target volume - actual volume) is set to the target volume initially. Then, the algorithm calculates the proportional compliance of each element so that the available volume can be distributed to the elements accordingly. These values are used at the beginning of each inner loop iteration to distribute the remaining material and this loop continues until there is no remaining volume. The distributed densities are filtered through weighted local averaging using a prescribed R_{min} (minimum filter radius) distance and the density limits $\left(10^{-3}, 1\right)$ are enforced. At the end of the inner loop, the current volume obtained after the distribution, filtering, and density limits is subtracted from the target volume to update the remaining volume used for redistribution. Finally, outside of the inner loop, the elemental densities are updated by linearly mixing the design variables computed at the current iteration and the ones from the previous iteration.

Figure 3.10 Design variable updating algorithm in PROP method.

Algorithm 4: Pseudo code of the proportional approach

procedure Update the design variables
  Define the history coefficient, $\alpha = 0.5$
  Set the target volume, $V_{\text{tar}} = \bar{V}N$
  Set the remaining volume, $V_{rem} = V_{\text{tar}}$
  Initialize new design variable vector for update scheme, $\kappa_{new} = 0$
  Calculate the compliance proportion of each particle, $C_i^{prop} = C_i / C_{total}$
  while $V_{rem} > 10^{-3}$ **do**
    Distribute densities to the elements proportional to their compliance
    Apply filter to κ_i^{opt}
    Add the distribution to the design variable vector, $\kappa^{new} = \kappa^{new} + \tilde{\kappa}^{opt}$
    Enforcing the material density limits, $\kappa^{new} = \max\left((\min(\kappa^{new}, 1), 10^{-3}\right)$
    Update the remaining volume, $V_{rem} = V_{tar} - \sum \kappa^{new}$
    Update the upper bound: $l_2 = l_{mid}$
  end while
  Update the design variables for next iteration
end procedure

3.8 Filter Scheme and Stabilization

The main numerical instabilities to consider in the optimization process are the checkerboard pattern and mesh dependency. In OC, the filter is employed for the sensitivities, whereas PROP filters the particle densities to eliminate these numerical difficulties. To identify the nearby particles inside this sub-domain, a circular domain with a set radius, $R_{\min}$, is specified at the center of the material point i^{th}. The modified sensitivity number in OC, $\tilde{\omega}_i$, and the filtered density in PROP, $\tilde{\kappa}_i^{opt}$, can be calculated by:

$$\tilde{\omega}_i = \frac{\sum_{j=1}^{N_i} \psi(R_{ij})\omega_j}{\sum_{j=1}^{N_i} \psi(R_{ij})} \tag{3.55}$$

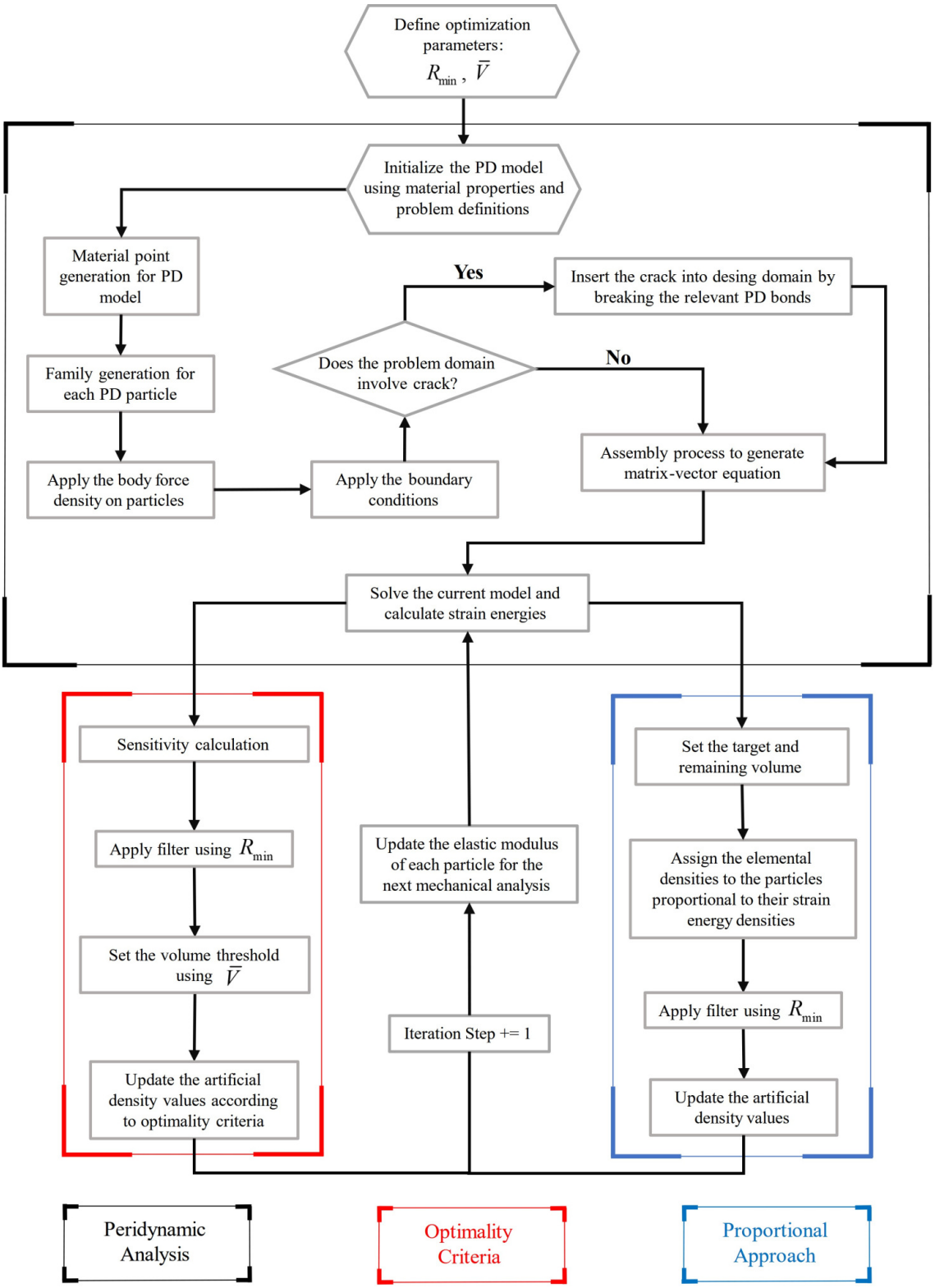
$$\tilde{\kappa}_i^{opt} = \frac{\sum_{j=1}^{N_i} \psi(R_{ij})\, {\kappa_j}^{opt}}{\sum_{j=1}^{N_i} \psi(R_{ij})} \tag{3.56}$$

where N_i represents the total number of particles in the horizon of the particle i,$R_{ij} = |\mathbf{x}_j - \mathbf{x}_i|$ is the distance between the particle i and j, and $\psi(R_{ij})$ is a weight factor given as:

$$\psi(R_{ij}) = \begin{cases} R_{\min} - R_{ij} & if \quad R_{ij} \leq R_{\min} \\ 0 & if \quad R_{ij} > R_{\min} \end{cases} \tag{3.57}$$

The mathematical formulations of the methods are introduced. A general framework of the both continuous density based TO methods namely PD-PROP-TO and PD-OC-TO methods are given in Figure 3.11.

Figure 3.11 The general framework of the continuous density based PD-TO methods.

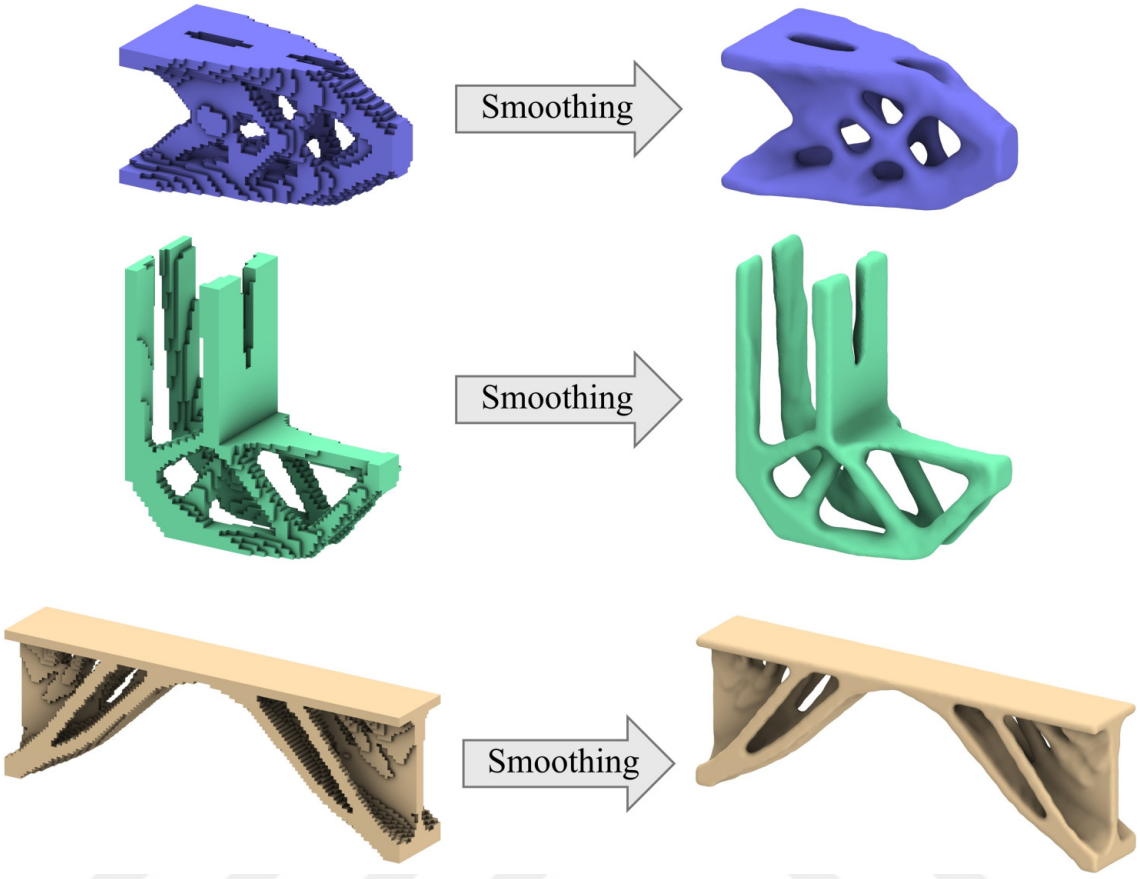


3.9 Smoothing Operation on the Optimized Solutions

Although the topology optimization algorithms can provide the optimum structure in terms of compliance and strength, the attained structures are not generally suitable for direct production. For this reason, it is always desirable to perform smoothing operations on the optimum geometries without altering their compliance whilst making them suitable for AM production. At this point, the objective of the smoothing process is to achieve a final geometry that is more producible than the obtained geometry from 3D TO, considering real-life structures. Since .stl is a widely used file format for printing a geometry in the field of additive manufacturing, a general in-house code is developed that generates the .stl file from the output of the peridynamics-based 3D TO algorithm.

Basically, the optimization algorithm only provides the design variables for each material point representing a 3D volume in the spatial domain. Utilizing the center point of this volume and design variable of each particle, 3D geometries with closed outer surfaces are produced in .stl format. This .stl file represents the direct outcome of the TO algorithm with sharp geometric features of the structure, thus requiring an adequate smoothing application. To this end, .stl files are imported in ANSYS Workbench software and the smoothing process is performed for the optimum topology utilizing the SpaceClaim interface, i.e., computer-aided design software built-in ANSYS. For this operation, a specified shrinking parameter is defined in SpaceClaim based on an element/particle spacing size of Δx, and this operation is performed twice to ensure the high-fidelity smoothness of the external surface. Subsequently, the shrinking parameter is defined again as $\Delta x/2$ and the smoothing process is repeated one last time to provide superior smoothness of the bounding surfaces. Hence, the entire sharpness of the final/optimum topology is remarkably reduced as can be clearly seen in Figure 3.12.

Figure 3.12 Examples of the effect of smoothing operation on the final topologies obtained by PD-TO method.



In the numerical example section, the advantage of the smoothing operation is clearly conveyed for each case study being presented herein. Note that smoothed geometries are more suitable than obtained geometries by 3D-TO to be produced and utilized as engineering structures. Thus, .stl files of given smoothed geometries are prepared to be employed as an input of additive manufacturing for producing them. In the final step, we produce these smoothed geometries by filament-based 3D printing using polylactic acid (PLA) material.

4. PD-TO METHODS FOR ENGINEERING STRUCTURES WITH/WITHOUT DISCONTINUTIES

4.1 Peridynamics Topology Optimization of Three-Dimensional Structures with Surface Cracks for Additive Manufacturing

4.1.1 Introduction

Additive manufacturing (AM) is an effective approach to fabricating intricate shapes obtained from topology optimization (TO). However, it may cause undesired manufacturing-induced defects/cracks due to high thermal residual stresses. This section provides a PeriDynamics-enabled three-dimensional Topology Optimization method (PD-TO) for designing structures by considering surface cracks for the AM processes. The PD-TO approach employs a bi-directional evolutionary structural optimization method and uses particle discretization of geometry for mechanical analysis. Crack surfaces are generated by breaking three-dimensional nonlocal interactions of the particles, and thus, during the optimization process, complex multiple structural discontinuities can be diligently modeled. First, the proposed approach is validated by solving benchmark problems without cracks. For each benchmark geometry, the PD-TO analysis is then performed by considering different positions and numbers (single/multiple) of cracks. These analyses extensively investigate and demonstrate the effects of a priori knowledge of residual stress-induced damages/cracks on the optimum topology for additive manufacturing. Besides, the smoothing operation is applied to the optimum designs to transform voxel shapes into AM-friendly smooth surfaces. These geometries are manufactured by an extrusion-based AM process to demonstrate the practical engineering application

of the proposed method. Finally, the comparison of numerical results is also supported by the experimental tests conducted on the optimized topologies. Overall, it is confirmed that the PD-TO approach is a viable and accurate optimization tool for additive manufacturing considering possible process-induced damages. Finally, the provided results in this section is also published in the journal of Computer Methods in Applied Mechanics and Engineering (Kendibilir, Kefal, Sohouli, Yildiz, Koc & Suleman (2022)).

4.1.2 Novelty and Motivation

This section presents the TO results of a novel 3D topology optimization framework that can optimize the initial structure considering the existence of any process-induced surface defects/cracks and voids using non-local PD formulation. To our best knowledge, there is no reported study concerning 3D topology optimization of structures involving possible surface cracks by using the PD-TO algorithm as well as its experimental verification. Such a study is believed to be very crucial in the fields of additive manufacturing because 3D-printed structures unavoidably possess critically high stress–concentration regions due to non-uniform heating and cooling within the part, which might be associated with the complexity of the part geometry, the variable wall thickness of the part, and laser size and speed used in manufacturing. Although these critical regions are in essence formed at the micro-level, their proximity and coalescence may create an effect (i.e., reducing the material stiffness) analogous to that induced by pre-existing damage/crack surfaces at the macro level. To address such issues at the design stage, this study presents the first development and implementation of the three-dimensional PD-TO method for engineering structures with or without structural discontinuities (e.g., voids, damages, etc.). As such, the computational domain is discretized into peridynamic material points, and the topology optimization problem is solved by coupling three-dimensional bond-based PD formulation and the BESO approach. In the current PD-TO analysis, the compliance (strain energy density) minimization, the relative densities, and the volume fraction of the structure are respectively the objective function, design variables, and constraint. The capabilities of the proposed method are demonstrated by optimizing various three-dimensional design problems.

The remainder of this section is structured as follows. In Section 4.1.3, various well-known topology optimization examples are selected from the TO literature and proposed BESO-PD-TO algorithm is performed on these problems. The optimized

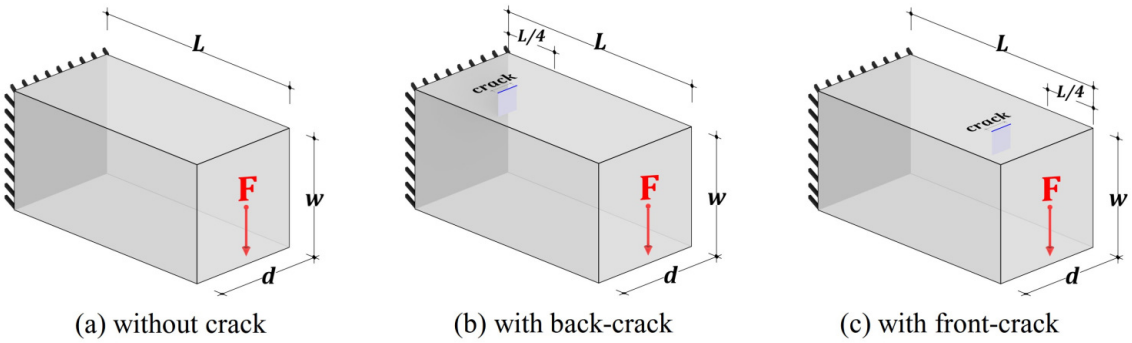
results are extensively discussed and compared with the existing FEM-TO results available in literature. Finally, concluding remarks are provided in Section 4.1.4.

4.1.3 Topology Optimization Examples

4.1.3.1 Case I: Three-Dimensional Cantilever Beam with/without Surface Cracks

A simple case study is investigated to compare the results obtained from PD and FEM analysis. A cantilever beam is clamped at the left end and a concentrated load F = 100 kN is applied along the vertical direction at the center of the right end as shown in Figure 4.1. The dimensions of the beam are as follows: L = 2 m, w = 1 m, d = 1 m. The Poisson's ratio and the elastic modulus of the material are $v = 0.25$ and E = 200 GPa, respectively. The target volume fraction is set to be 25%, the evolutionary volume ratio is equal to 0.02, and the minimum filtering radius value is assumed to be 3. Initially, this case study is solved without any crack as a benchmark case to validate the implementation of 3D PD-TO with respect to the FEM-based TO (FEM-TO) solutions. Then, the effect of crack location is examined for two crack positions (a = l/4, a = 3l/4) as illustrated in Figures 4.1(b, c). For easy referral, cracks located at a = l/4 and a = 3l/4 are named as back and front crack cases, respectively. For both cases, the edge length of the square-shaped crack is 0.2 m.

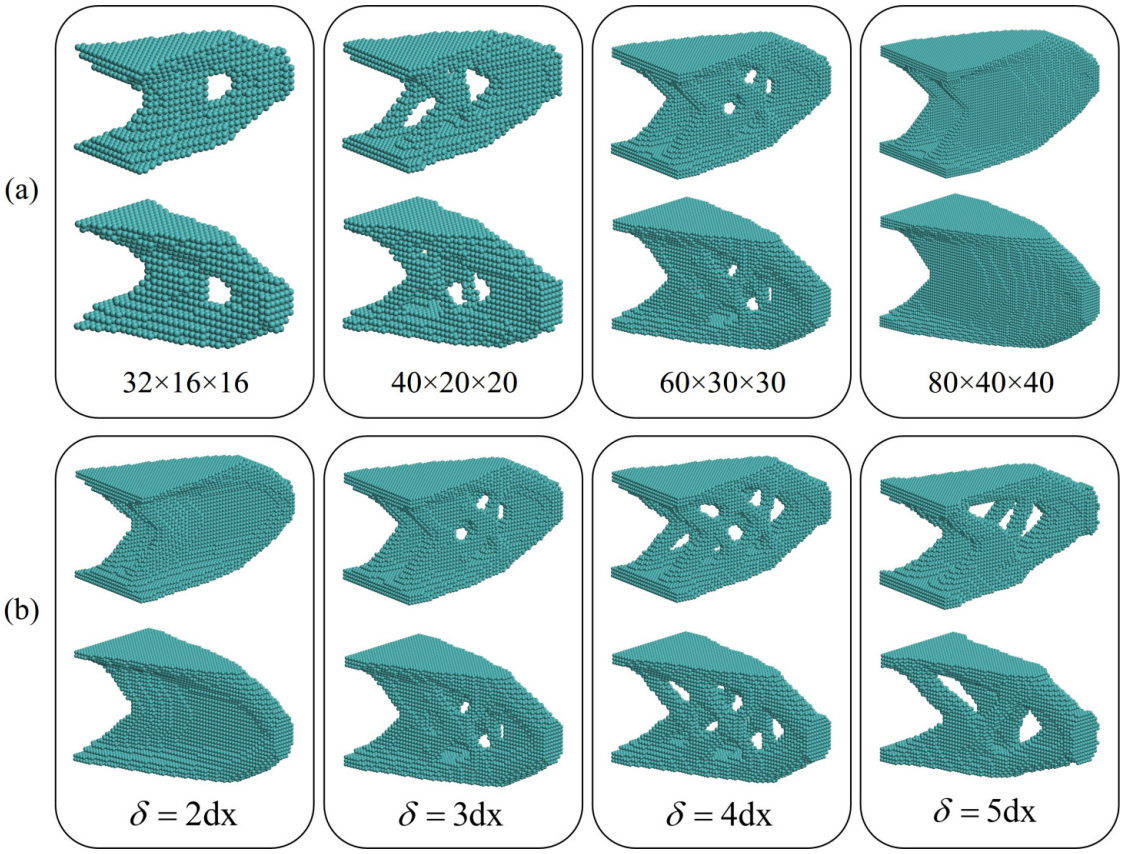
Figure 4.1 Design domain for the 3 different scenarios considering (b, c) with and (a) without surface cracks.



(a) without crack (b) with back-crack (c) with front-crack

Before choosing the main parameters of PD-TO such as particle resolution and horizon size, we performed several analyses by changing the value of horizon radius and particle resolution. In this regard, increasing particle resolution ($32 \times 16 \times 16$, $40 \times 20 \times 20$, $60 \times 30 \times 30$, and $80 \times 40 \times 40$) and horizon radius ($\delta = 2dx$, $\delta = 3dx$, $\delta = 4dx$, and $\delta = 5dx$) options were determined. The obtained final material distributions by PD-TO for these scenarios are given in Figure 4.2.

Figure 4.2 Isometric views of the final topologies for changing parameters: (a) particle resolution, (b) horizon radius.



It can be observed that both parameters affect the geometrical features in the optimum solutions. Moreover, it is shown in Figure 4.3a that compliance values are converged for each discretization after a certain number of iterations. However, utilizing the coarser resolution may not be reliable for different problems. Therefore, time cost becomes the most vital parameter to choose the convenient discretization for the remaining analysis. Here, we intended to keep the time consumption to an acceptable limit by comparing each other. The average time consumption of an iteration is measured for all cases as shown in Figure 4.4. Note that, these values correspond to the ratio between $60 \times 30 \times 30$, and other resolutions as given in Figure 4.4a. Similarly, proportions of $\delta = 3$dx and other options are calculated for

making a clear assessment of time incremental as shown in Figure 4.4b. Visual inspections revealed that the hole numbers in the structure increased up to 60 × 30 × 30 resolution, however, the scenario with the finest resolution has no hole between the structural components. Afterward, comparing time costs showed that increasing the resolution becomes much more expensive while the final distributions are considered. Especially, time demand rises more than four times between 60 × 30 × 30 and 80 × 40 × 40 even if compliance value is not affected remarkably. After these comparisons, choosing the most sensible option, the problem domain is discretized into 60 × 30 × 30 particles. The discretization is the same for FEM and PD analysis, namely, the design domain consists of 60, 30, and 30 elements/particles aligned in the length, width, and height direction, respectively. The particles are uniformly distributed in the design domain for PD analysis.

On the other hand, when the horizon size is increased from $\delta = 3dx$ to $\delta = 4dx$, there is no considerable difference between them as depicted in Figure 4.2. In parallel, the time cost is scaled up by 2.5. It is revealed that an increased horizon demands such a large amount of time that it is difficult to choose. Hence, throughout this study, the horizon size is chosen as δ = 3dx, where dx is the particle spacing, considering a trade-off between the computational time and the optimal topologies.

Figure 4.3 The compliance histories for changing parameters: (a) particle resolution, (b) horizon radius.

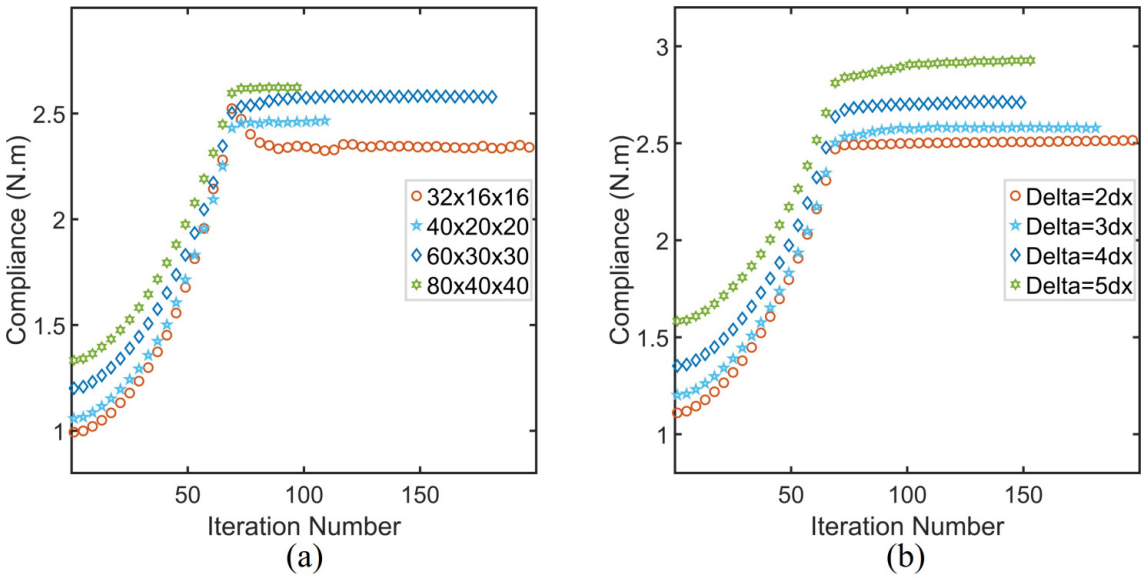
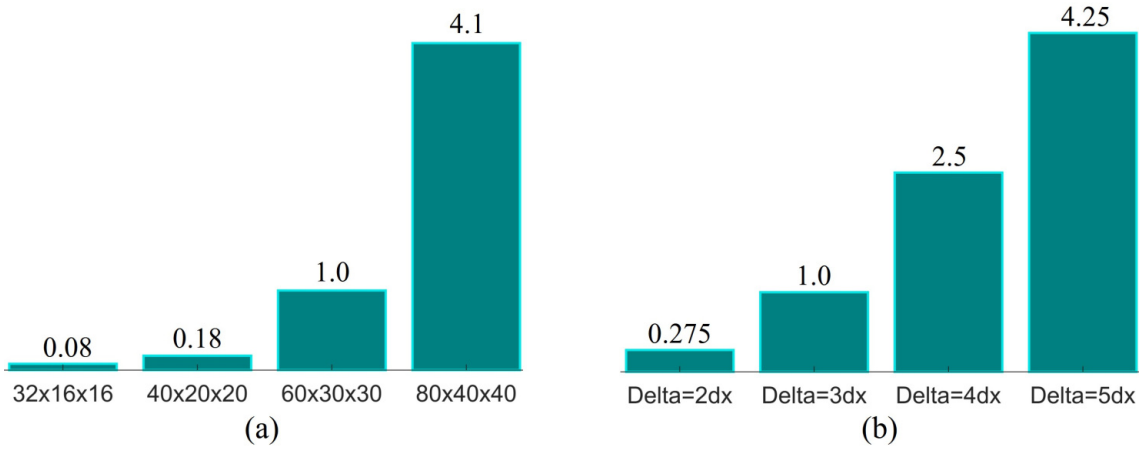


Figure 4.4 The comparison of time costs of one iteration for changing parameters: (a) particle resolution, (b) horizon. These are the relative values based on 60 × 30 × 30 and Delta=3dx in (a) and (b), respectively.



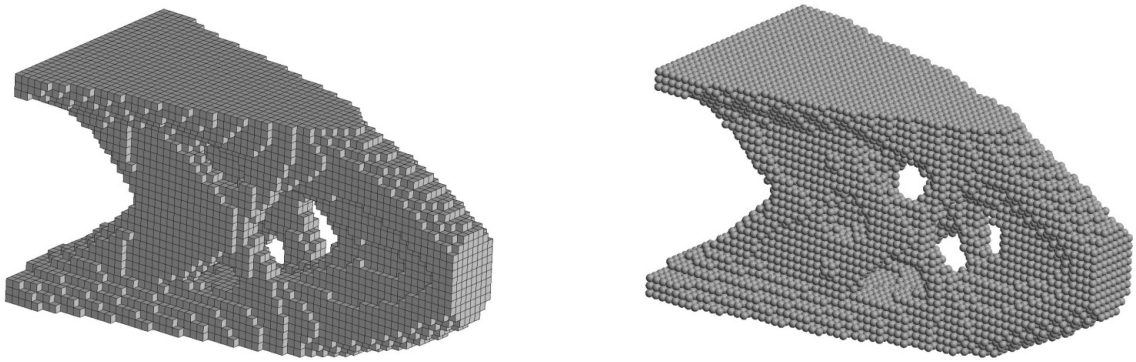
To find out which topology is more optimal, the topologies obtained by both PD-TO and FEM-TO (Figures 4.5 and 4.6) are imported to the ANSYS environment and then analyzed under the same boundary conditions to calculate their strain energies. In fact, given that FEM-TO is a local approach based on classical continuum mechanics whereas the PD-TO is a nonlocal approach, the comparison of strain energies obtained from these methods might be erroneous. Therefore, the utilization of the same computational platform (ANSYS) is necessary for prudently comparing the strain energies (compliances) of the optimum topologies achieved by PD-TO and FEM-TO analyses. Accordingly, the total compliances of the optimal topology based on PD-TO and FEM-TO methods are computed to be 2.901 and 2.891, respectively, by ANSYS. These results indicate that both methods can deliver almost the same accuracy in finding the optimum topology except for a slightly better topology obtained by FEM-TO, i.e., 0.34% less strain energy.

Having proven the reliability of the PD-TO with respect to the FEM-TO, the advantage of the PD-TO methodology would be obvious in modeling and optimizing structures with discontinuities. The optimal results of back and front crack cases are shown in Figure 4.7, which reveals that changing the crack location significantly alters the optimal topology. The PD-TO approach distributes materials depending on whether the crack is located in the high strain energy region or not. In other words, as shown in Figure 4.7, the material may be removed from or added to the vicinity of the crack location based on the proximity of the crack to high-stress gradient regions.

To be specific, the material is removed nearby the crack location as the crack is

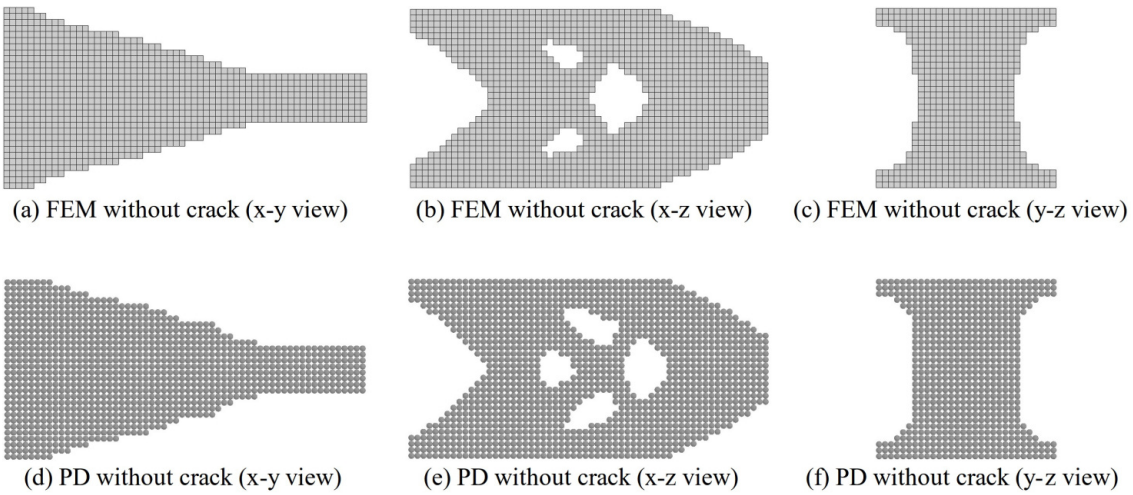
close to the loading edge, where strain energy is relatively smaller than the clamped region for the front-crack case, as depicted in Figure 4.7b. In the result of back-crack case in Figure 4.7a, the materials are distributed more in the vicinity of the crack tips since the location of the crack corresponds to the high strain energy region because of the clamping boundary condition. Therefore, the location of the cracks changes the strain energy distribution within the structure and the optimizer can find the topology with the least-strain energy. To further elaborate on present the difference in material distribution for the cracked structures, the x-z views of the optimal topologies are also compared in Figures 4.7(c, d).

Figure 4.5 Final topologies of FEM-TO and PD-TO without crack.



(a) FEM (Isometric view) (b) PD without crack (Isometric view)

Figure 4.6 Comparison of 2-D views of FEM-TO and PD-TO without crack.



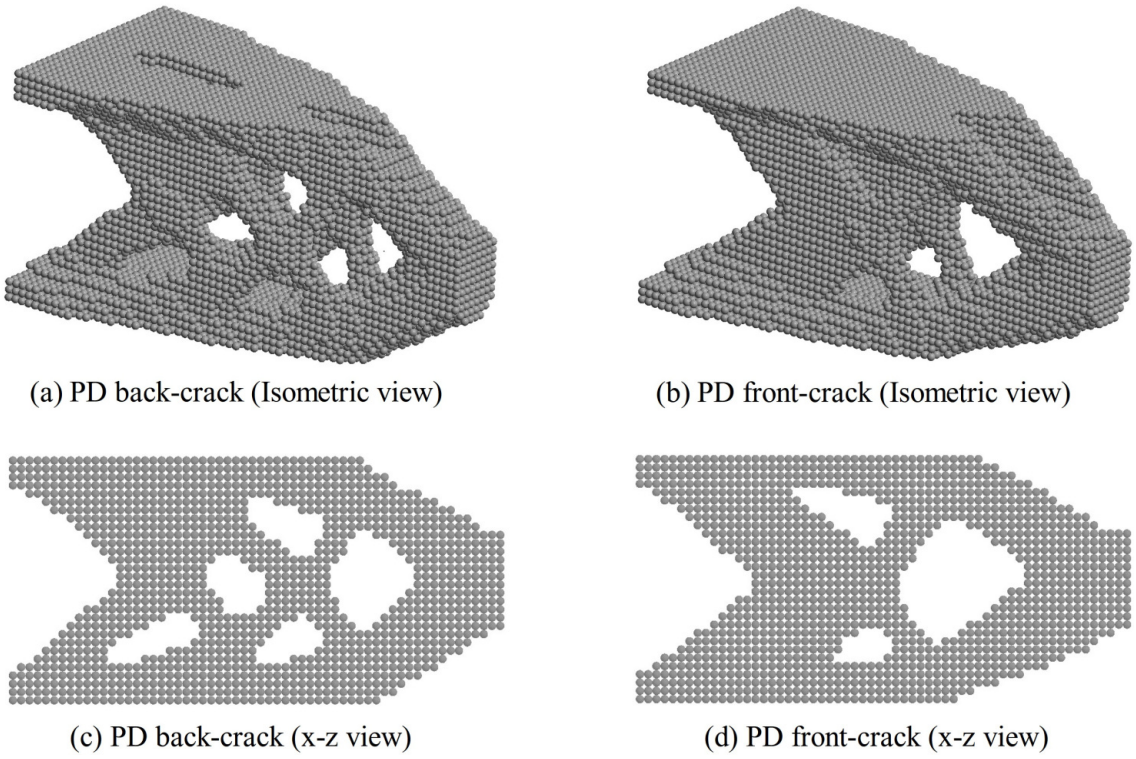
(a) FEM without crack (x-y view) (b) FEM without crack (x-z view) (c) FEM without crack (y-z view)

(d) PD without crack (x-y view) (e) PD without crack (x-z view) (f) PD without crack (y-z view)

Additionally, Figure 4.8 shows the comparisons for the distributions of the strain energy density and the total displacement. It can be investigated from the figure that the crack location modifies the displacement and energy distributions. The geometry

with the back-crack case has the highest total displacement in comparison to those without cracks and with front-crack cases. This behavior is attributed to the fact that since the volume constraint is identical for all cases, the optimizer distributes available materials more towards the position of crack tips while providing more slender geometrical features in the direction of the loaded tip. Moreover, it is noted that the optimizer deposits more material points to the regions where the crack is going to propagate along the width direction of the block (y-axis).

Figure 4.7 Optimized topologies of Case I for different crack locations.



(a) PD back-crack (Isometric view)

(b) PD front-crack (Isometric view)

(c) PD back-crack (x-z view)

(d) PD front-crack (x-z view)

Given that there is no deformation on the mid-plane surface of the crack during its opening under the current loading condition, the strain energy reaches its minimum value therein and maximum value on its side edges (crack tip edges). This phenomenon can be clearly observed from the strain energy density contours plotted over the optimum topologies in Figures 4.8(b, d, f). Since strain energy is minimum in the direction normal to the crack surface, the optimizer removes the material along the normal direction of the crack region in the optimized body. An important conclusion can be drawn from these results that if the crack orientation concerning applied load enables crack opening mode, then topology is created in a way that promotes crack closure. Such a crack closure is created by the BESO optimizer by rotating the crack surface roughly 90 degrees from the initial crack surface. This point can be observed for both crack configurations albeit being more obvious in

the back-crack case as seen in Figures 4.8(c, d). Note that such observation can be only possible if the 3D model is utilized during the topology optimization, as such highlighting the importance of the 3D PD-TO method.

Figure 4.8 Comparison of the total displacements (left column) and strain energy densities (right column) of the optimal topologies of Case I.

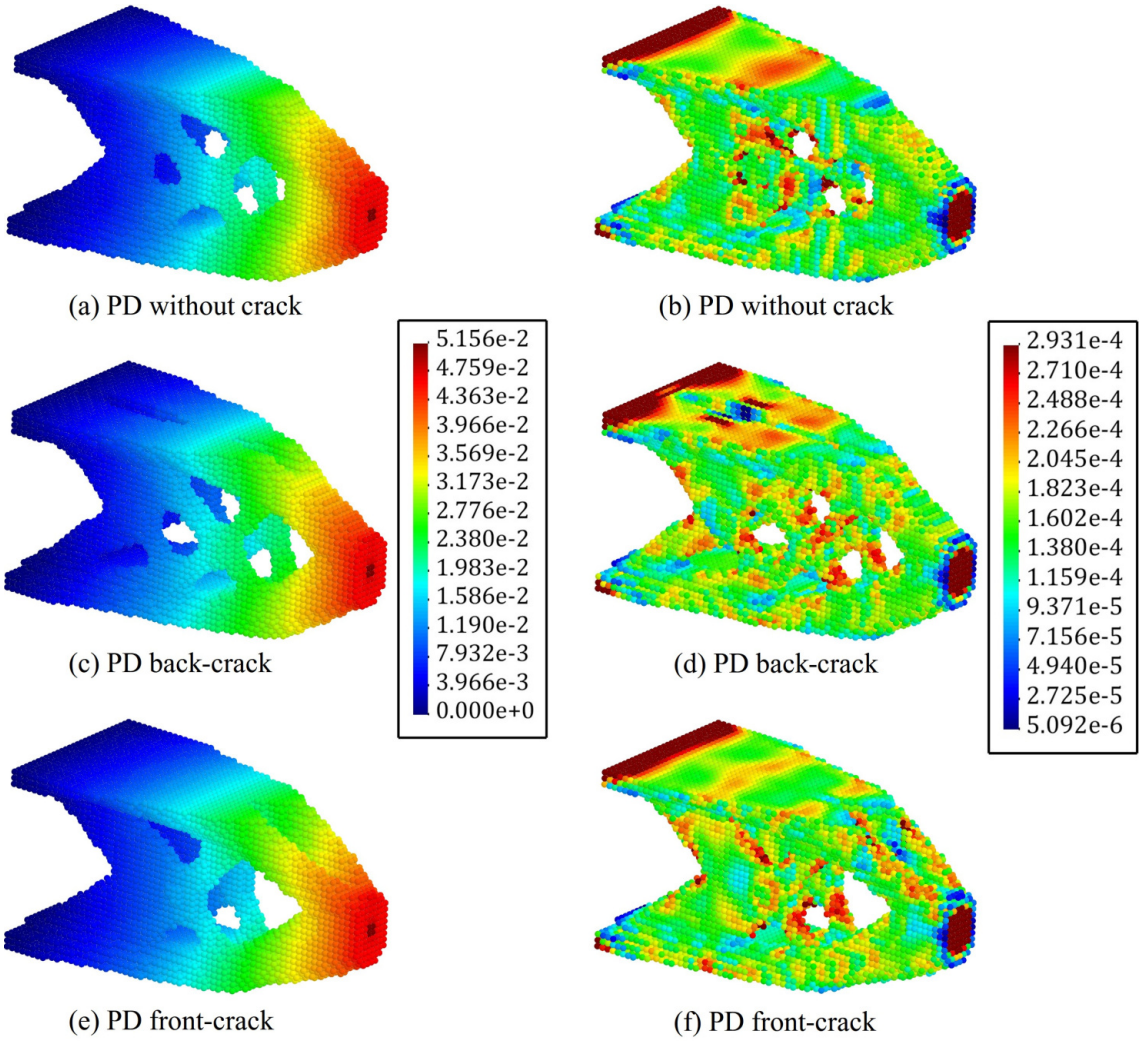
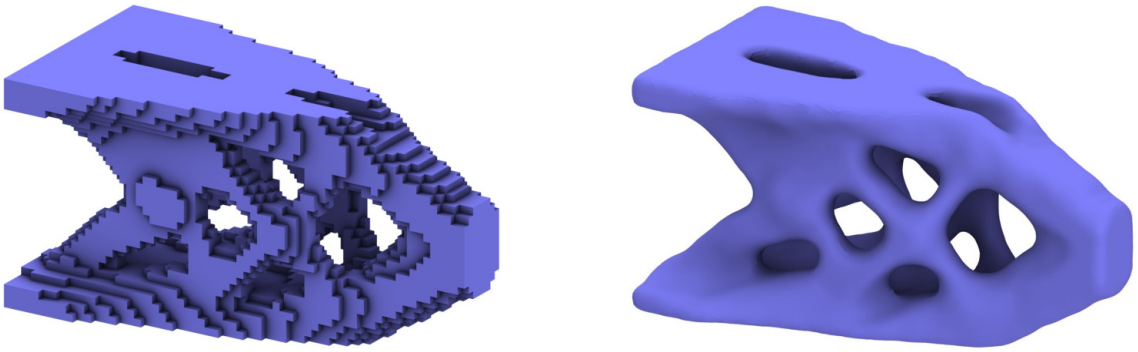
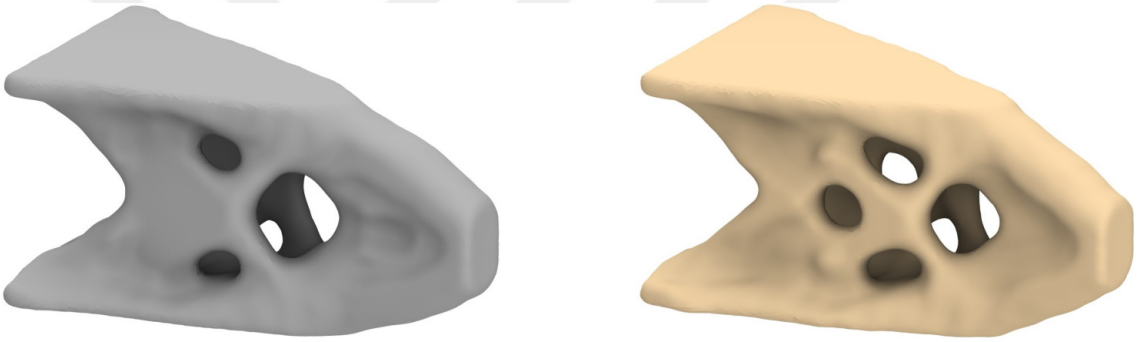


Figure 4.9 Final topology of PD back-crack case (a) before and (b) after smoothing operation.

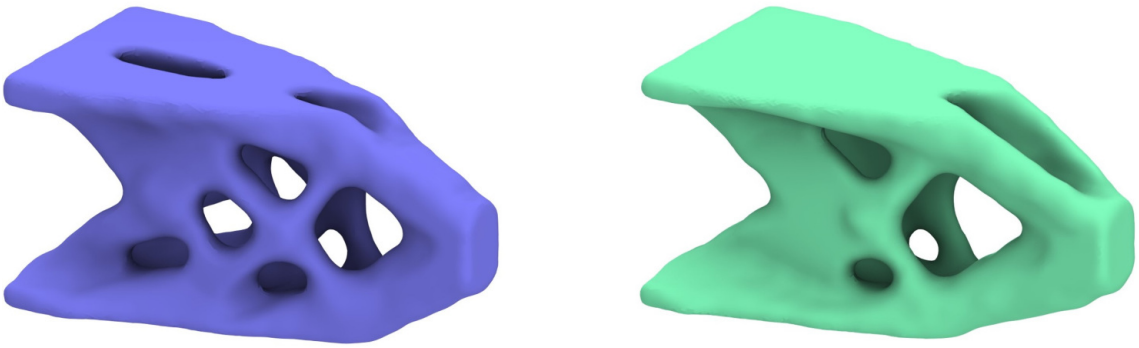


(a) Before smoothing (b) After smoothing

Figure 4.10 Comparison of the smoothed geometries for Case I.



(a) FEM without crack (b) PD without crack

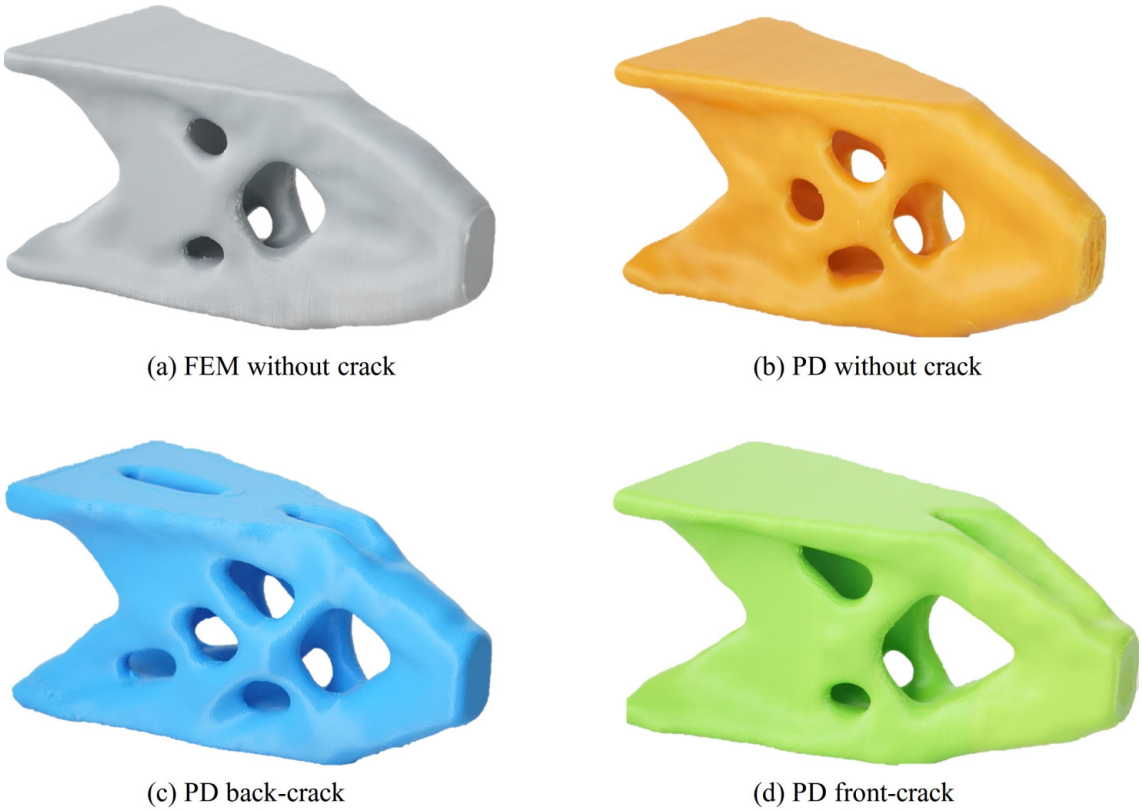


(c) PD back-crack (d) PD front-crack

Thus far, direct optimum material depositions attained by FEM/PD-TO analyses are scrupulously compared with each other. These particles/elements can cause intricate sharp edges and orthogonal surfaces in the final geometry (Figure 4.9a), thereby leading to undesirable designs for manufacturing purposes. Accordingly, the 'posteriori' smoothing process is performed for all the final topologies. This

operation intends not only to generate more manufacturable geometries but also to eliminate non-essential local geometric features that may lead to high-stress concentration. To demonstrate these advantages of smoothing operation, Figure 4.9 presents the final topology of the PD back-crack case at the stage before and after smoothing. It can be observed that smoothed topology (Figure 4.9b) is a more convenient geometry to be produced and utilized in realistic applications. In addition to the single example shown in Figure 4.9, the smoothed optimum geometries for all cases are illustrated in Figure 4.10. Furthermore, Figure 4.11 shows the printed version of these smoothed geometries, which demonstrates the rapid prototyping of these geometries using the additive manufacturing technique (i.e., filament-based 3D printing using polylactic acid (PLA) material). Figure 4.12 shows the compliance histories for all cases optimized by PD-TO. The compliance of topologies increases in the beginning due to the material removal in the BESO approach. Once the volume fraction is satisfied (roughly at iteration number 80), the material removal stops, and the compliance of the structure decreases slightly and/or stabilizes until reaching a convergence point. It is clear from this figure that the compliance of the optimal topology without a crack has the minimum value while the optimal topology with back-crack has the maximum compliance. This result proves that the crack/defect close to the clamping region brings about an optimum topology with higher compliance due to high strain/stress intensification nearby the clamped boundary (Figures 4.8d, 4.10c, 4.11c, 4.12).

Figure 4.11 Printed version of optimal topologies made of PLA filament material.



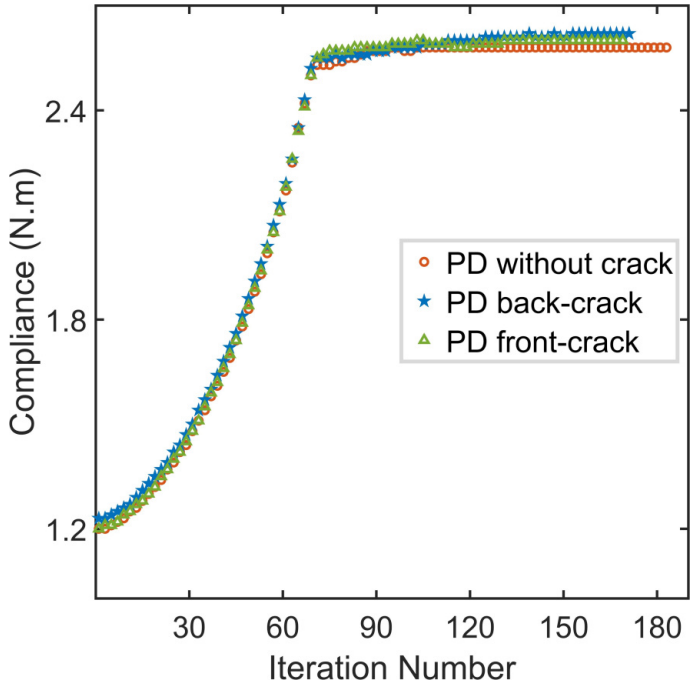
(a) FEM without crack

(b) PD without crack

(c) PD back-crack

(d) PD front-crack

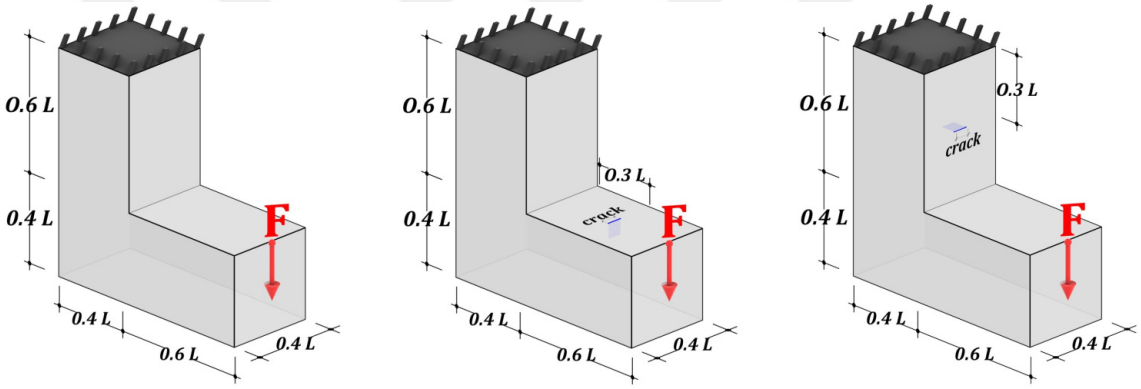
Figure 4.12 The iteration histories of the compliance of Case I.



4.1.3.2 Case II: Three-Dimensional L-Shaped Beam with/without Surface Cracks

To further indicate the robustness and accuracy of the proposed method, in this case study, one of the widely used geometry in the literature, the L-shaped beam, is modeled within three different crack conditions regarding including embedded crack or not (Figure 4.13). In the first scenario, the surface crack is not embedded into the structure to validate the proposed method by comparing it with the available FEM-TO method. Besides, the remaining two models involve embedded cracks in the middle of different faces as illustrated in Figures 4.13(b, c). The geometrical dimensions of the L-beam are adjusted by a length parameter, L = 1 m.

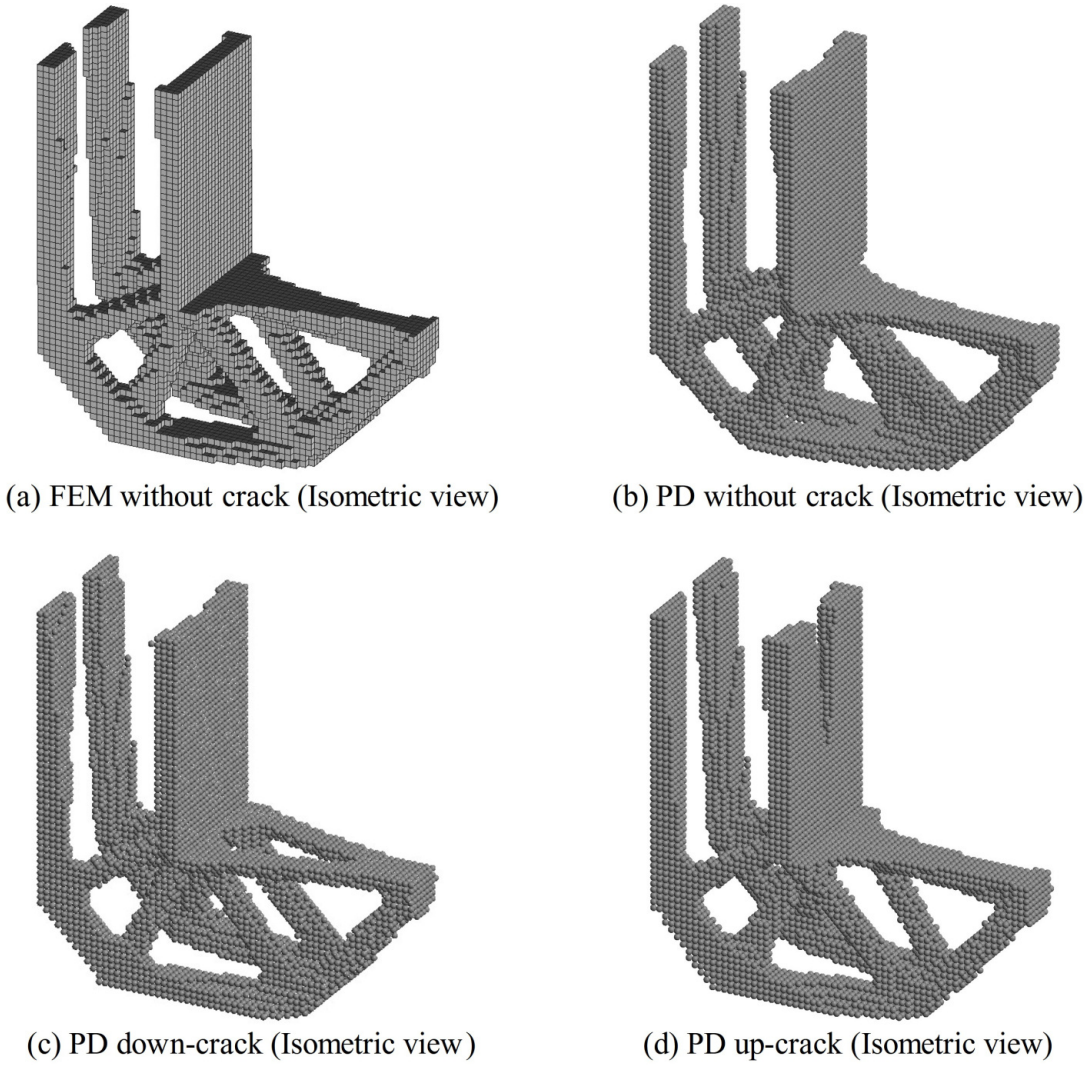
Figure 4.13 Design domain of Case II for the 3 different scenarios considering (b, c) with and (a) without surface cracks.



(a) without crack (b) with down-crack (c) with up-crack

The loading condition and design domain are also illustrated in Figure 4.13. The top edge of the structure is clamped where a downward force is loaded on the middle of the upper edge of the leading face with a magnitude of F = 50 kN. For this problem, the volume constraint is adjusted to 20%, the elastic modulus is 200 GPa, and the Poisson ratio is $v = 0.25$. The discretization is the same for FEM and PD analysis: 36 elements/particles for 0.6L, thus it means that 60 elements/particles are aligned along the length of L. The optimization parameters (R_{min}, ER) are kept the same as in Case I. The length of the square-shaped crack surface is 66 mm. Two cases with an embedded crack are named as down-crack and up-crack as presented in Figures 4.13b and 4.13c, respectively. The distance between the down-crack and right end is 0.3L, and the up-crack is 0.3L away from the top (clamped) edge of the structure.

Figure 4.14 Comparison of the optimal topologies of Case II for different crack locations.



(a) FEM without crack (Isometric view)

(b) PD without crack (Isometric view)

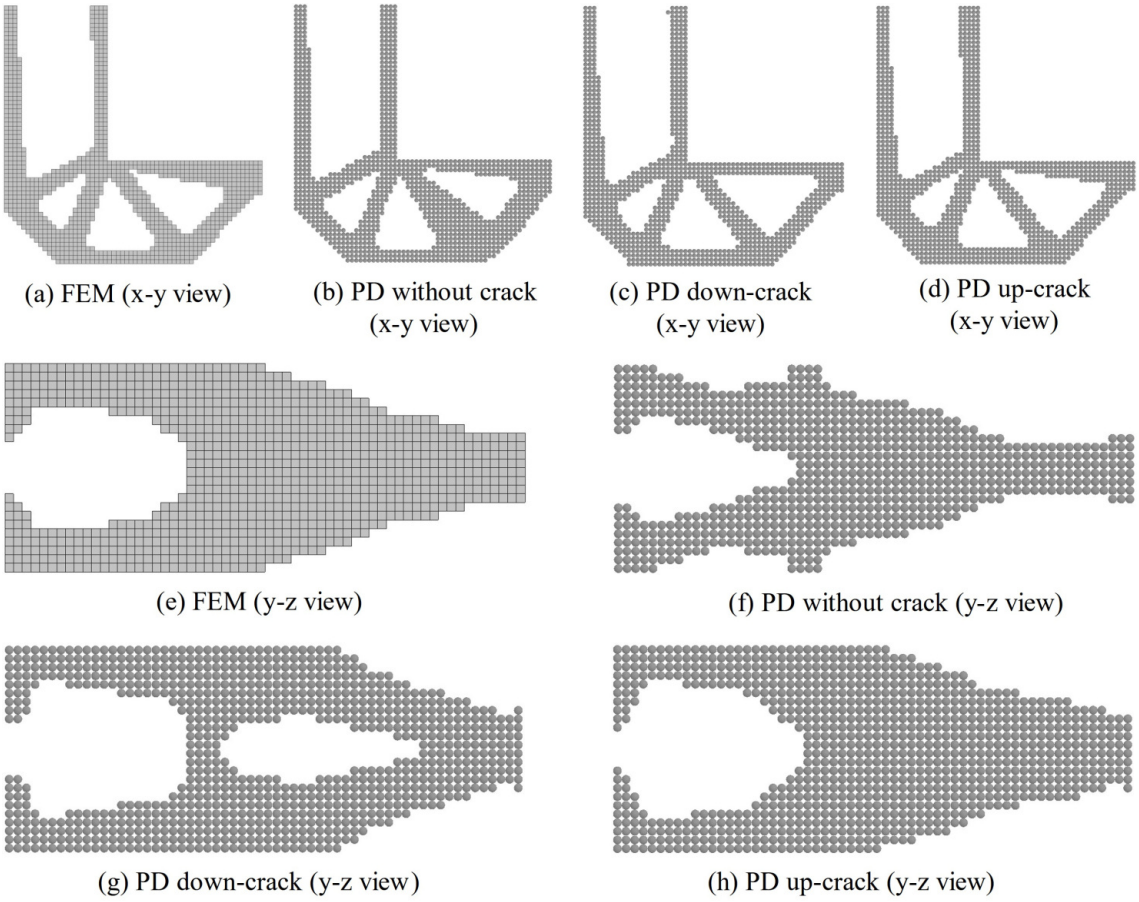
(c) PD down-crack (Isometric view)

(d) PD up-crack (Isometric view)

First, the optimized geometries of the L-shaped beam without crack are compared for the FEM and PD approaches in Figures 4.14(a, b), which proves that the optimal result obtained using FEM is similar to the optimized structure achieved using the PD based TO. However, as a minor difference here, it is noticed that the support in the lower region, which supports the right end region at the loading position, sprouts as a single support arm (Figure 4.14b) from the center which differs from the double support arms shown in the FEM result (Figure 4.14a). It brings about an implication that PD-TO and FEM-TO generate similar but not identical results for the same topology optimization problems. Additionally, by comparing the total compliance of the optimal topologies without a crack in the FEM environment, the topology obtained by FEM gives about 0.07% better compared to the proposed PD approach, which can be interpreted as a very negligible difference. Hence, when considered with

the results of Case I, this case study (without crack) strongly demonstrates that the 3D PD-TO is a credible technique to be utilized as a topology optimization method for additive manufacturing applications.

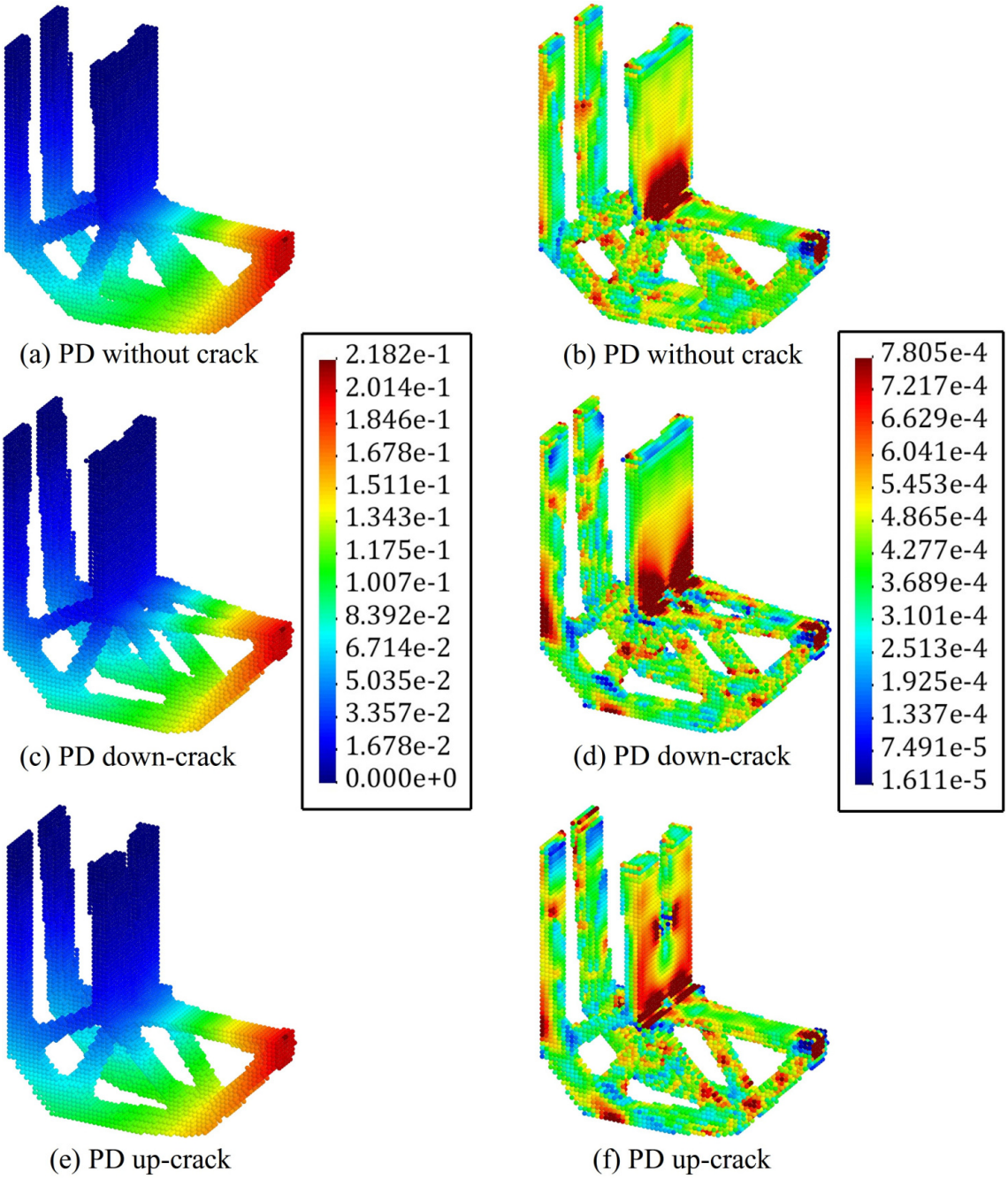
Figure 4.15 Comparison of the optimal topologies for different views (x-y and y-z).



In the next step, the effect of two cracks is investigated in different locations as illustrated in Figures 4.14(c, d). Figure 4.14 depicts the isometric views of the optimal topologies for two crack locations, whereas 2-D plane views of these optimal topologies are shown in Figure 4.15 to demonstrate the geometrical dissimilarities more easily. Figures 4.15(a–d) demonstrate that x-y views are practically the same for each topology except the final topology of the PD without crack has relatively thicker support which goes to the right bottom corner. On the other hand, by examining the y-z plane views, Figures 4.15(e–h) present detailed geometrical variations between the optimized structures. Although material distributions are substantially similar for FEM, PD down-crack, and PD up-crack cases, one important dissimilarity that can be marked is that the down crack case includes considerable space in the vicinity of the crack. Moreover, the final topology of the PD without crack case has remarkable distribution concerning all the other results in the y-z view due to

the nonlocality of the PD theory.

Figure 4.16 Comparison of the total displacements (left column) and strain energy densities (right column) of the optimal topologies of Case II.

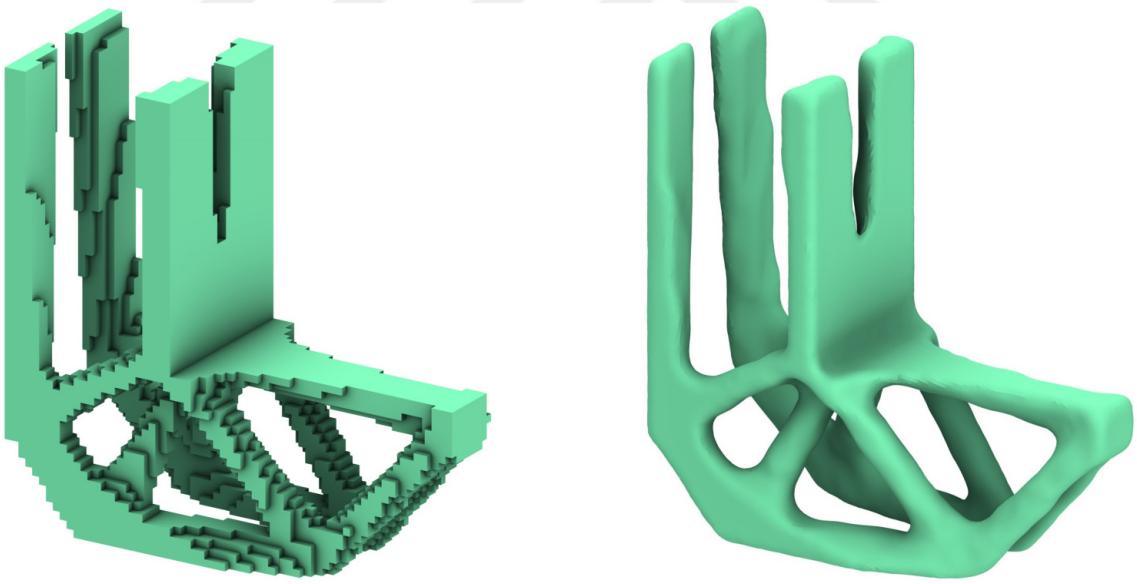


From these figures (Figures 4.14, 4.15), it is true to indicate that crack location has a significant impact on the final topologies for this case study as well. Remarkably, the proposed topology optimization approach distributes or removes the materials close to the crack location according to the critical crack location. For the down-crack case, one can see that the materials close to the crack location are removed,

whereas there is more material assigned at the crack location for the up-crack case. However, in detail, the most conspicuous evolvement in the optimization of the cracked structure is that, in the normal direction of the induced crack, the strain energies of the particles are relatively lower and thus materials in these regions are removed in both cases (Cases I–II).

The comparison of the total displacement distributions can be seen in Figures 4.16(a, c, e). Besides, the distributions of the strain energy density are compared in Figures 4.16(b, d, f). According to these figures, high spots of the energy accumulations are mainly evolved at the tips of the crack surfaces, which further supports our conclusions presented in the above paragraph. Namely, the high strain energy densities at the crack locations change the optimal topologies compared to the topology of the structure without a crack. Moreover, it can be concluded that the optimizer attempts to evenly distribute the strain energy within the structure. The high strain energy accumulation can only be seen at the turning point of the L beam structure due to its geometry.

Figure 4.17 Final topology of PD up-crack case (a) before and (b) after smoothing operation.

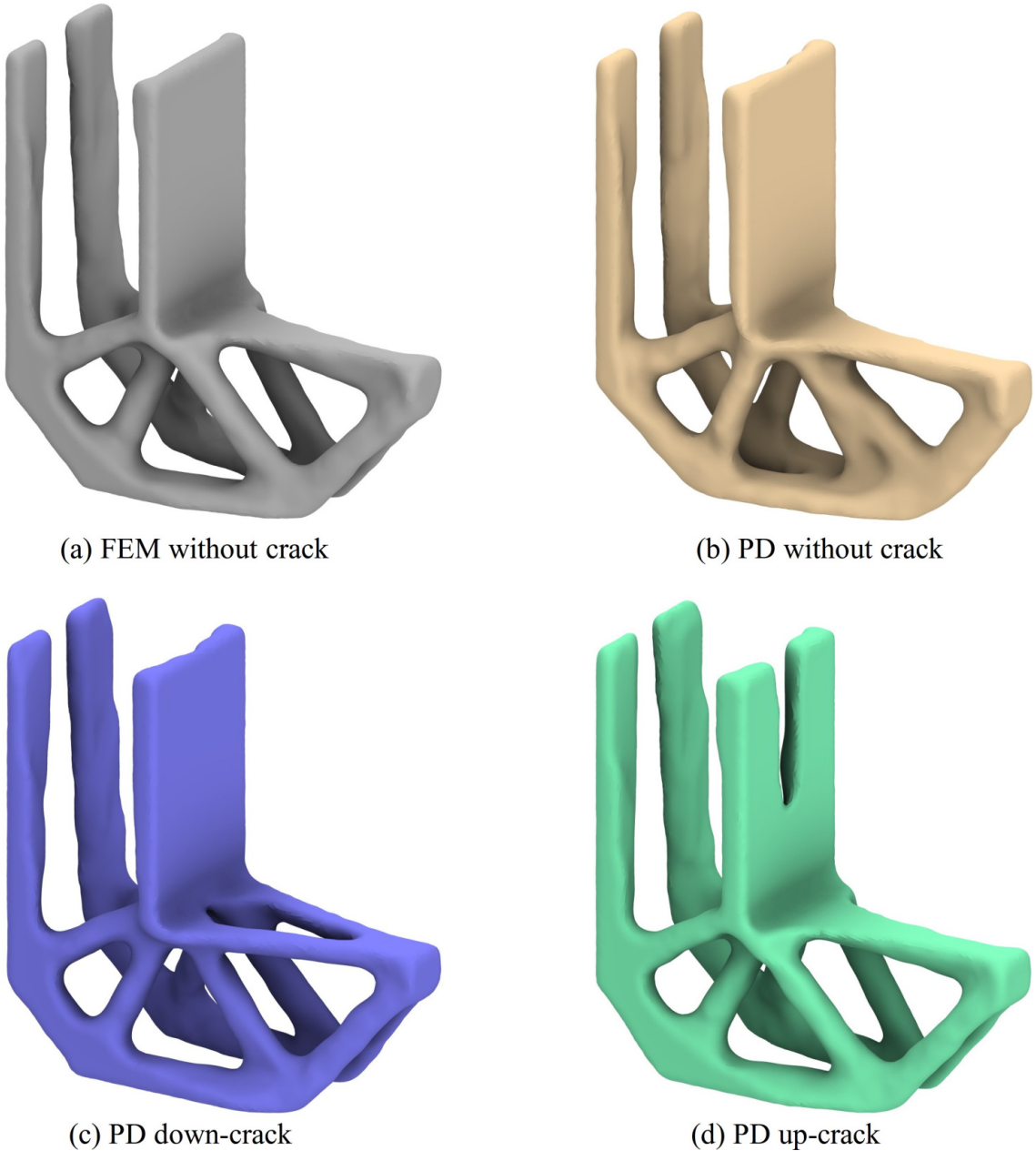


(a) Before smoothing (b) After smoothing

Due to the existence of the high strain energy region on the turning point of the L shape, in the up-crack case, materials are removed from the crack to the top surface of the geometry. Based on this, it can be discovered that the distance between crack and hot spot regions (accumulation of particles with high strain energy) has also a significant effect on the optimum topologies. Therefore, it shows that the crack

location has an important role in removing particles but is not enough to determine the direction or size of this emptied region. Another common consequence that can be drawn for Cases I–II is that the optimized results for the structures with cracks demonstrate that the solid material points agglomerate to circumvent crack propagation. In other words, the material is deposited in the crack tip regions which have high strain energy thus preventing crack propagation through the tips. Thanks to this intention, the proposed PD-TO method can be extremely beneficial to prevent potential crack initiation and propagation when the possible damage scenarios are known for a structure.

Figure 4.18 Comparison of the smoothed geometries for Case II.



(a) FEM without crack

(b) PD without crack

(c) PD down-crack

(d) PD up-crack

Figure 4.19 Printed version of optimal topologies made of PLA filament material.



(a) FEM without crack

(b) PD without crack

(c) PD down-crack

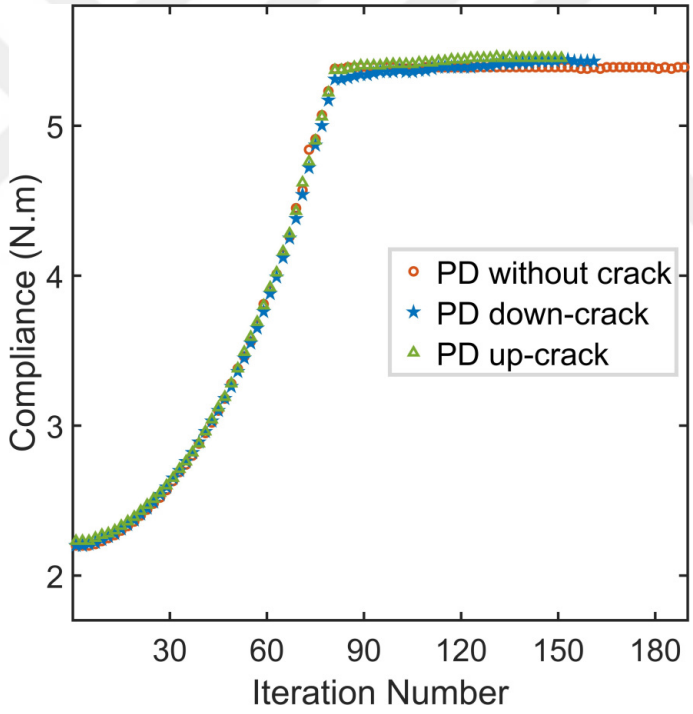
(d) PD up-crack

As we performed in Case I, the smoothing operation have created fine-shaped topologies for this case as well. The difference between before and after the operation can be examined in Figure 4.17. Furthermore, Figure 4.18 depicts the smoothed version of the whole optimal topologies for this case. From these figures, the optimal shapes can be easily examined and hence the influence of the embedded cracks would also be observed in comparison with the previous figures. Smoothed geometries are produced by additive manufacturing method using PLA filament as seen in Figure 4.19. Comparing Figures 4.18 and 4.19, the smoothed geometries are almost identically manufactured, which can be attributed to the 3D PD-TO optimization

algorithms' performance in terms of distributing material points as even as possible during topology optimization.

Finally, the compliance histories of the PD-TO results can be observed in Figure 4.20, in which the compliance value increases till the target volume is satisfied. After that, it converges smoothly, when the volume is stabilized. Although there are no large differences between compliance results, geometries with embedded surface crack have slightly larger total strain energy internal to the structure due to the damage condition posed by cracks. Moreover, by comparing the compliance values at the last iterations, it can be observed that the structure with up-crack has the highest one, thereby indicating that the closer the crack is to the clamping region, the higher the total energy will be during optimization. All in all, the results provided in this case study strongly indicated the important effect of crack implementation on the TO of three-dimensional structures.

Figure 4.20 The compliance histories of PD-TO results for Case II.



As known from classical fracture mechanics, the more the strain energy (compliance) is, the higher the possibility of crack propagation will be. Therefore, compliance is one of the key parameters for defining the fracture resistance of the structure under a given condition. In this regard, we compared compliance of the final topologies optimized with and without cracks in the vicinity of the crack tips. This way, one can make sure that the fracture toughness of the structure in that region is increased with the use of PD-TO. The cracks (up and down) are introduced into the final topologies of the case with up/down-crack and without crack. Applying

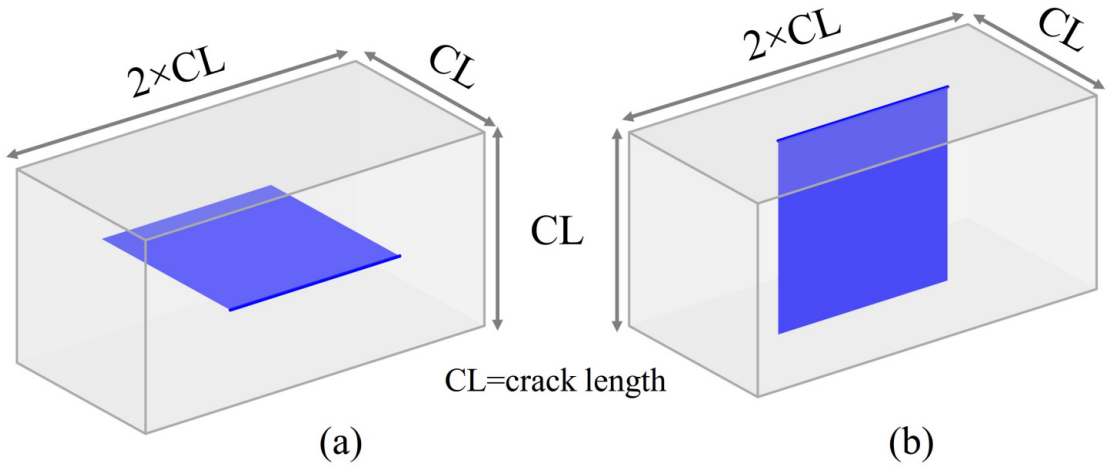
the boundary and loading conditions same as defined before, we performed one step static analysis and measured the strain energy density all over the body. After that, an imaginary region which can be considered as a rectangular prism that covers the vicinity of the crack is utilized as a horizon to select the relevant particles as illustrated in Figure 4.21.

Table 4.1 Strain energy density comparison around the cracks for different results

Crack position	Placed in	Average strain energy density [N/m^2]	Reduction (%)
Down Crack	Without crack result	174	40.8
	Down crack result	103	
Up Crack	Without crack result	156	27.5
	Up crack result	113	

The dimensions of the prism are equal to the crack length in two axes. On the third axis which corresponds to the crack alignment, the prism lies double of crack length to be able to capture the most important particles located at the crack tips. In Table 4.1, we listed the average strain energy density value of the particles in the vicinity of the involved cracks. It is found that the final topologies obtained by cracked scenarios provide less strain energy in the critical region than the result of the crack-free case. For instance, when we introduce pre-defined down-crack into the without crack result (Figure 4.14b) and down-crack result (Figure 4.14c), the average value of the strain energy density around the crack is decreased by 40%. This reduction is 27.5% for the other crack position. Eventually, it can be revealed that the proposed method significantly reduces the strain energy in a region that is pre-defined as a “hot-spot region”, thus effectively enhancing the fracture resistance against crack propagation in the topology optimized with crack.

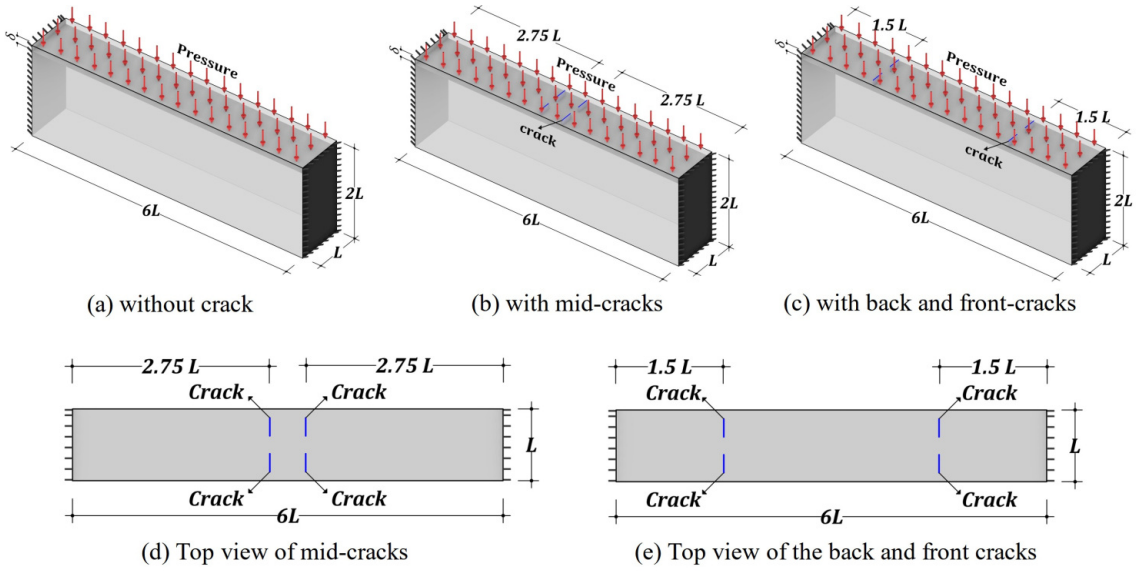
Figure 4.21 The dimensions of the region in the vicinity of cracks: (a) up-crack, (b) down-crack.



4.1.3.3 Case III: Three-Dimensional Bridge Structures with/without Multiple Surface Cracks

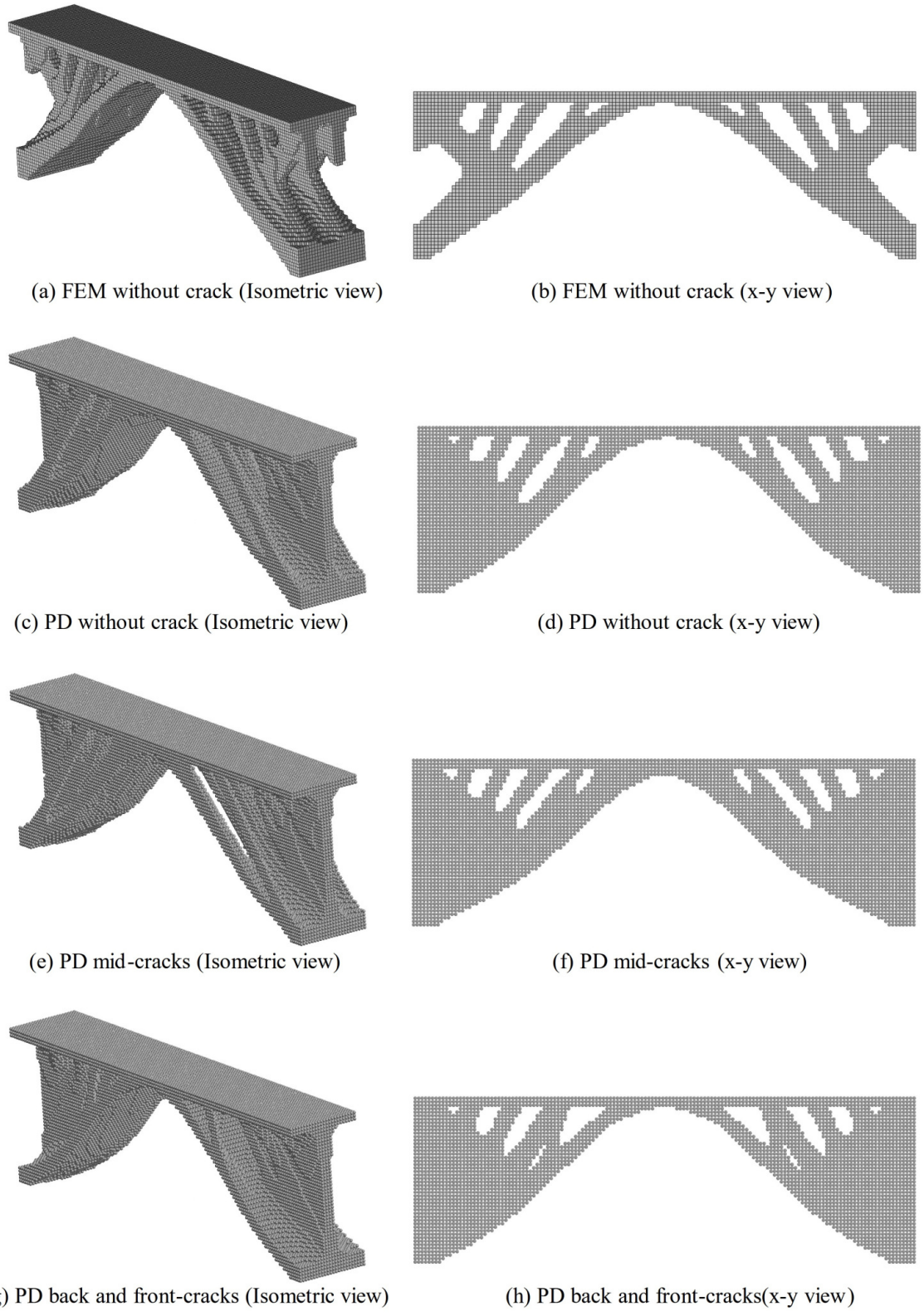
As another case study, structural optimization of a long rectangular prism is performed utilizing the proposed 3D PD-TO algorithm to obtain a bridge-like structure. The length-to-height ratio of the bridge is 3:1 with the exact prism dimensions of $60 \times 20 \times 10\ m^3$ (Figure 4.22). The right and left surfaces of the prism are fully constrained in all directions and uniform pressure of P = 800 MPa is applied on the top surface of the prism along the negative y-axis as shown in Figure 4.22. Material properties and optimization parameters are selected as same as the ones used in the previous case studies. The volume constraint of the optimization problem is set to 0.25. The design domain is uniformly discretized into $144 \times 48 \times 24$ particles along length, height, and width, respectively. For investigating the effect of multiple cracks in the design domain, we have created 3 scenarios with and without cracks. In the case of the prism with surface cracks, the cracks are embedded at the top side and two different crack alignments are considered as depicted in Figures 4.22(b–e).

Figure 4.22 Design domain and crack positions of the bridge case (Case III).



The case with the four cracks being close to each other in the middle of the structure is called the mid-cracks (Figure 4.22b) whereas the other multiple crack scenario is referred to as back and front-cracks (Figure 4.22c). Mid-cracks and the back and front-cracks are located 2.75L and 1.5L far from the left and right ends of the geometry as shown in Figures 4.22(d, e), respectively. These alternative crack positions are intentionally designated to assess the effect of multiple cracks' positions (away from clamped surfaces) on the optimal topologies. Each crack surface has a square shape with an edge size of 2.5 m. Design variables are kept as 1 (the solid particles) at the top side of the bridge within predefined a fixed layer. The thickness of this layer is the same as the dimension of the horizon size, δ, being equal to the size of 3 particles along the height direction as illustrated in Figure 4.22(a–c).

Figure 4.23 Comparison of the optimal topologies of Case III for different views (Isometric and x-y).



(a) FEM without crack (Isometric view)

(b) FEM without crack (x-y view)

(c) PD without crack (Isometric view)

(d) PD without crack (x-y view)

(e) PD mid-cracks (Isometric view)

(f) PD mid-cracks (x-y view)

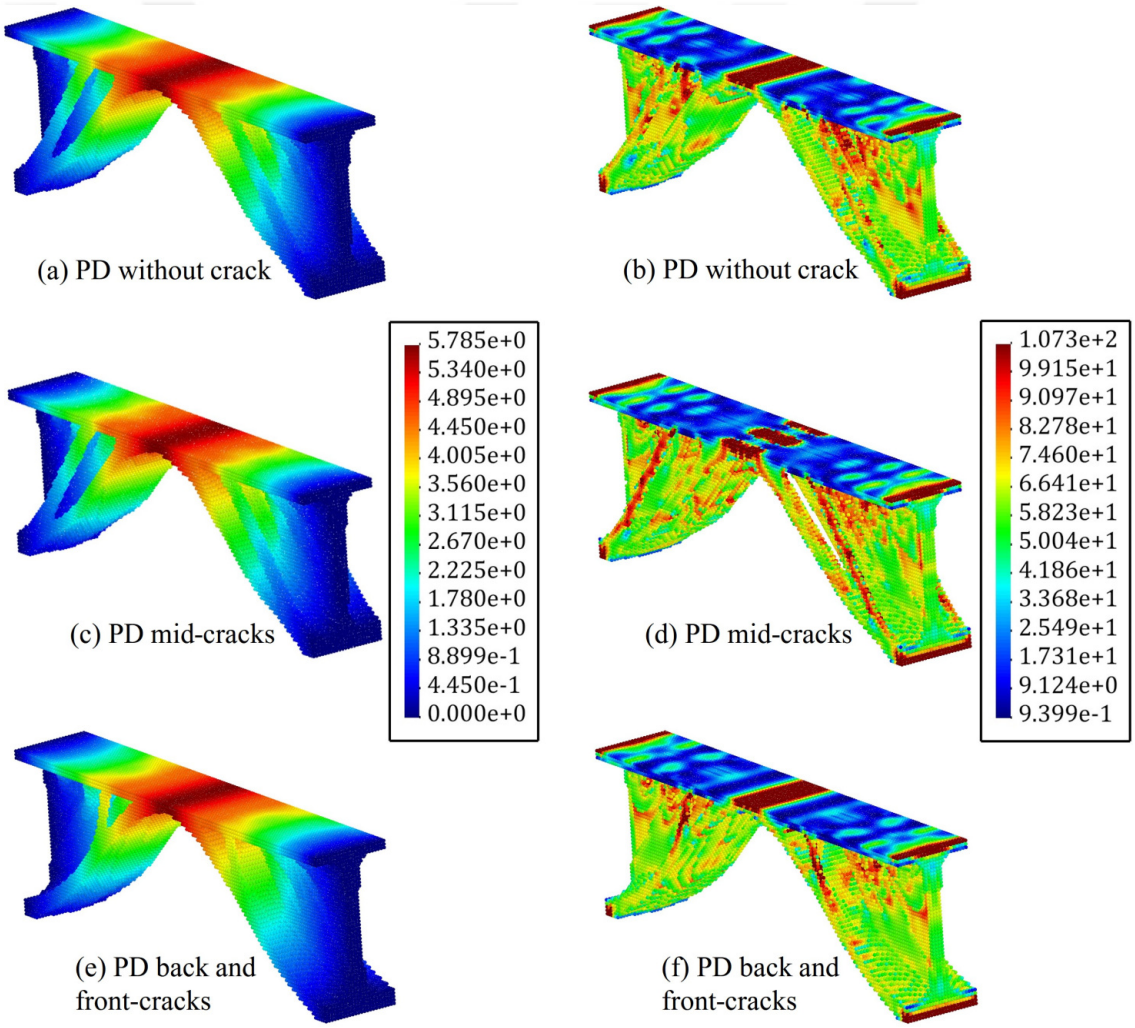
(g) PD back and front-cracks (Isometric view)

(h) PD back and front-cracks(x-y view)

Various plane and isometric views of the optimal results are shown in Figure 4.23

to compare the differences in optimum material deposition for bridges with/without cracks. The most visible geometrical difference is observed on the topologies without cracks. The FEM solution has two discrete supports along the width direction of the bridge as presented in Figures 4.23(a, b). On the contrary, the PD-TO analysis provides one centered continuous support (along height direction) at the right and left sides of the structure as illustrated in Figures 4.23(c, d). In addition, the effect of the multiple cracks can be particularly scrutinized by examining the results of the PD-TO approach from Figures 4.23(e–h). It is apparent from the 2-D views that the thickness of the supporting legs increases near the crack surface (Figures 4.23f, h) as compared to the ones without cracks (Figure 4.23d).

Figure 4.24 Comparison of the total displacements (left column) and strain energy densities (right column) of the optimal topologies of Case III.

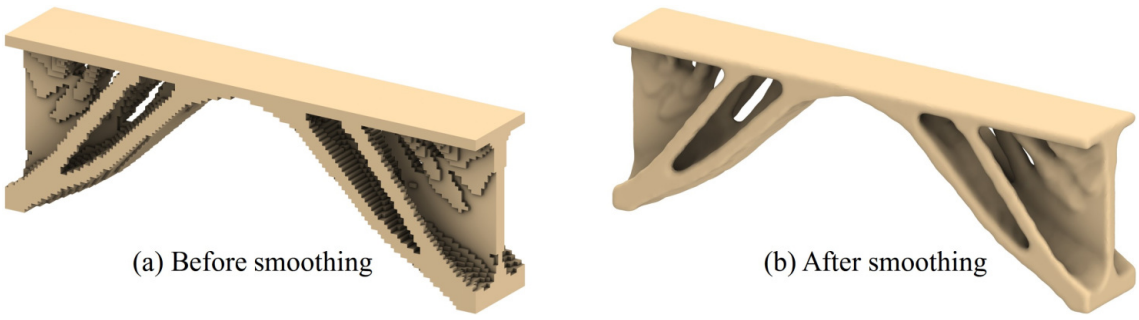


Moreover, the total number of holes between these legs is more or less the same. Besides, these holes possess almost identical shapes when the optimum topology

of the mid-cracks case is compared with one without cracks. On the other hand, moving the cracks near the clamping regions alters the material deposition of the bridge without cracks more distinctly (Figures 4.23g, h). Furthermore, the case with mid-cracks is more likely to conserve more material points in the middle of the bridge as compared to the case with back and front-cracks (Figures 4.23e–h). Additionally, the PD-TO optimizer remarkably deposits more material along the boundary of the crack surface (especially at the crack tips). These reinforced crack tip regions can increase the ultimate strength of the bridge, thereby leading to an optimum bridge less prone to crack opening mode failure. This phenomenon reveals that PD-TO is a reliable method for optimizing 3D structures with embedded cracks.

Strain energy and total displacement distributions of PD-TO analyses are depicted in Figure 4.24. Note that these results correspond to the final step of the optimization process. Although the displacement variations are similar in general as observed from Figures 4.24(a, c, e), the presence of more than one crack and the effect of crack position on the optimum results bespeak in the strain energy contours as given in Figures 4.24(b, d, f). Namely, in the best topology of the bridge with mid-cracks, strain energy increases in the vicinity of cracks and decreases at the center of the cracks along the length of the bridge as observed in Figure 4.24d. Instead, the cracks in the back and front regions yield increased strain energy at the topside position of the feet generated by the PD-TO optimizer to support the upper body of the bridge due to cracks as seen in Figure 4.24f. Additionally, these supporting legs grow much thicker than the other crack case to reinforce the multiple cracks close to the clamping regions.

Figure 4.25 Final topology of PD without crack case (a) before and (b) after smoothing operation.



As depicted in Figure 4.25, we have applied the smoothing process to the final topology to obtain a more realistic and manufacturable optimal bridge geometry. Repeating this process for other cases, the net shapes of all designed bridges are achieved as illustrated in Figure 4.26. These net shapes clearly reflect the geo-

metrical differences between the cases. For instance, the major differences in the supporting legs between FEM-TO and PD-TO results can be inspected by comparing Figures 4.26(a, b). Moreover, one can observe from Figures 4.26(c, d) that locating the cracks closer to the clamping surfaces enables the PD-TO optimizer to create thicker supporting legs in the final geometry. Furthermore, the variation of the compliance is plotted for the 3 cases analyzed using PD-TO in Figure 4.27. Here, it is noticed that the total strain energy accumulated in the structure tends to stabilize after 70–80 iteration steps. Comparison of compliance results implies that the case with mid-cracks has the highest compliance in the optimum geometry. This result can be attributed to the location of the mid-cracks in the structure being close to the region of critical strain energy concentration as compared to back and front-cracks. Hence, allocating cracks/defects in the high strain energy regions results in higher compliance during optimization, thereby providing a lower rigidity as compared to the crack-free case.

At the final step of this case study, the experimental performance of the optimum topologies is evaluated by conducting a mechanical test on the direct outcomes of the FEM-TO and PD-TO analyses. To this end, the nonsmoothed crack-free bridge geometries are manufactured by filament-based additive manufacturing method as shown in Figures 4.28(a, b). For visibility of the sample within the test setup in Figure 4.28c, the front surface of the specimen is painted with a thin white layer. As seen in this figure, the mechanical test fixtures on the right and left sides of the sample ensure the simply supported condition of the bridge structure. The mechanical test is load-controlled, and the maximum load is set to 5 kN. During the experiment, the total displacement of the head of the universal test machine is measured for each incremental load.

The experimental measurements obtained from the load cell and displacement of the head are plotted for each sample of FEM-TO and PD-TO in Figure 4.28d. Here, one can evaluate the total strain energy (i.e., compliance) of the structures stored within the samples during the experiment by computing the areas under the force–displacement curve. Accordingly, it is found that the optimum topology obtained with PD-TO retains approximately 15% less strain energy than the geometry optimized by FEM-TO analysis.

Figure 4.26 Comparison of the smoothed geometries for Case III.

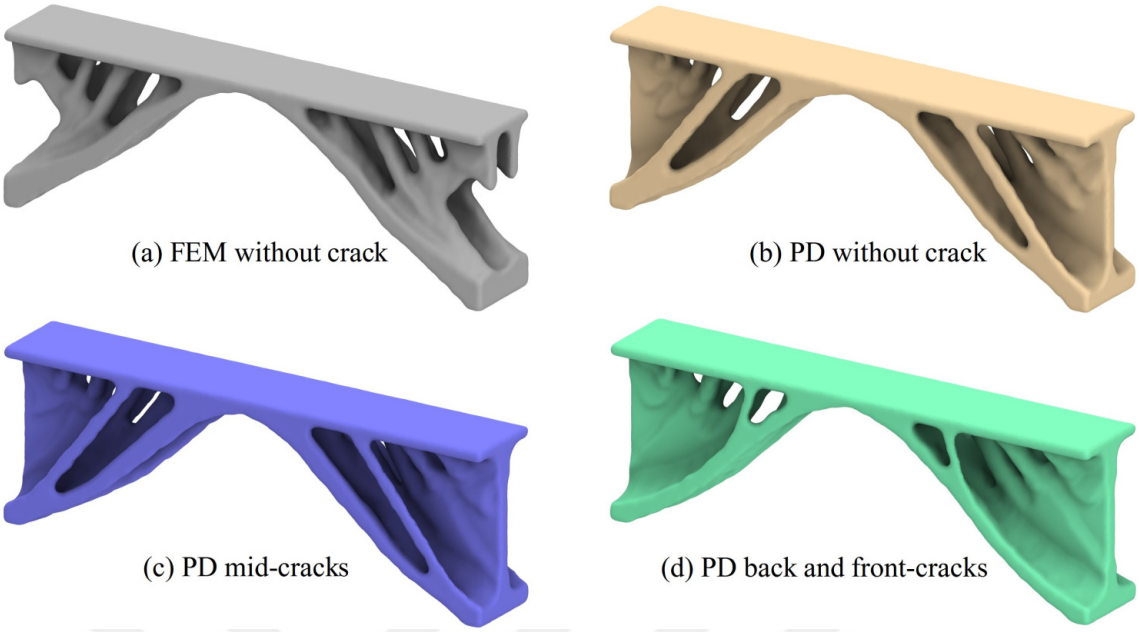
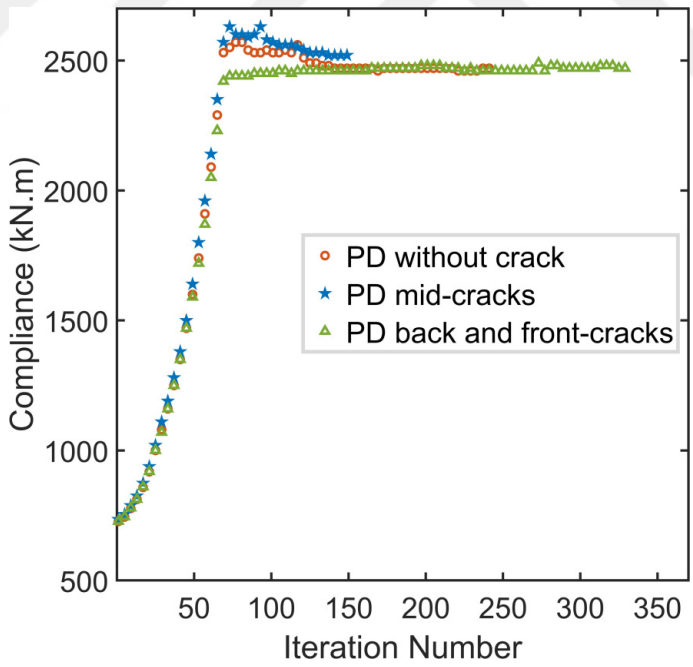


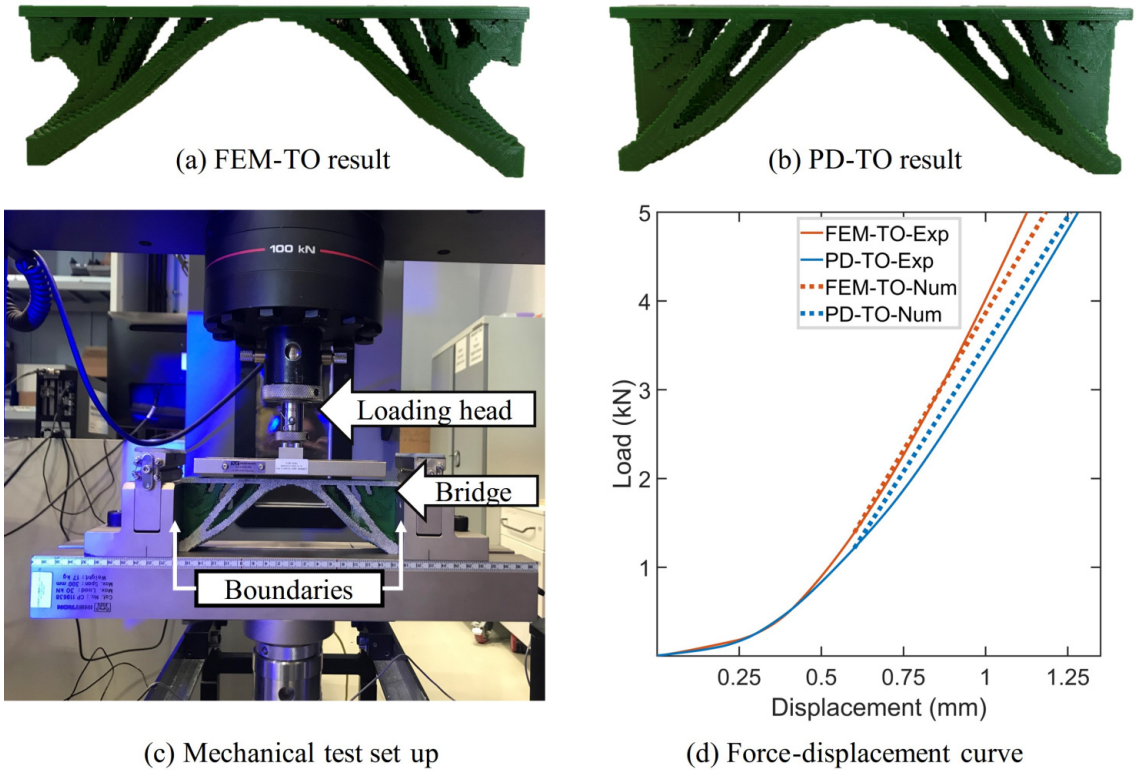
Figure 4.27 The compliance histories of PD-TO results for Case III.



In addition to the experimental application, we also compared the methods numerically as shown in Figure 4.28d. The dotted lines represent the numerical results while the solid lines represent the experimental data. Since the printed geometry is made of PLA material, we selected a proper material property considering the experiments (Travieso-Rodriguez, Jerez-Mesa, Llumà, Traver-Ramos, Gomez-Gras

& Roa Rovira (2019)) available in the literature. After that, to ensure the same conditions as the experiments, the final geometries obtained by FEM-TO and PD-TO are scaled down to the printed ones. The printed geometry has the dimensions of $180 \times 60 \times 30\ mm^3$. Each geometry is modeled and analyzed by the PD theory. For the discretization, the particle number of the problem domain is kept the same as we utilized in the PD-TO optimization. The point, where the displacement equals 0.6 mm, is chosen as the base point, ignoring the entrance region where non-linear deformation is caused by the initial backlash of the loading head of the experimental test machine. Therefore, we shifted the numerical displacement results considering this base point and reached the dotted lines shown in Figure 4.28d. As a result, it can be observed that the following region is quite linear and numerical results are highly compatible with the experimental results in that region. According to the numerical results obtained for FEM-TO and PD-TO, it is found that PD-TO provides 11.5% less strain energy than FEM-TO which is close to the difference observed in experimental results. These results prove the high competence of the non-local PD-TO method for both experimental application and numerical analysis of topology optimization. Overall, it can be concluded that the PD-TO methodology is a viable design tool for optimizing three-dimensional topologies with/without cracks, thus it can be effectively used in applications of additive manufacturing.

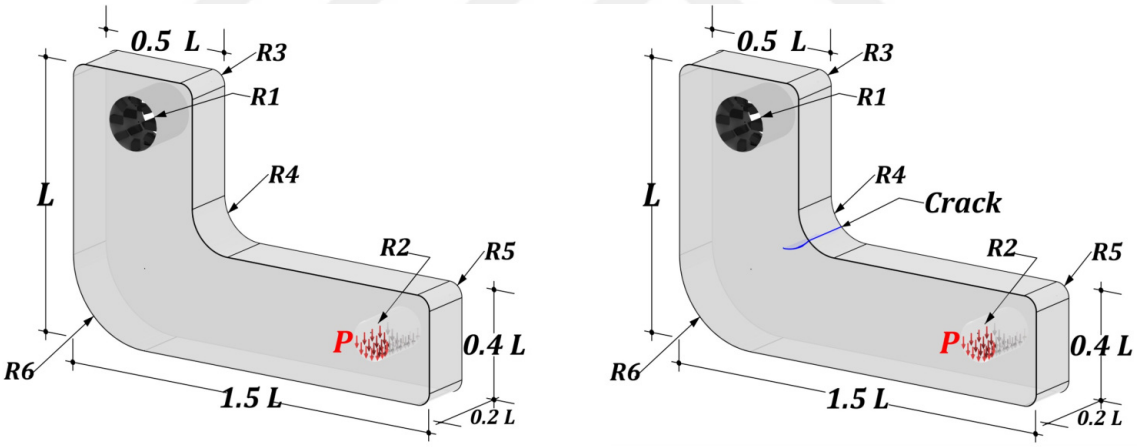
Figure 4.28 Experimental and numerical comparison of FEM-TO and PD-TO for Case III without crack.



4.1.3.4 Case IV: Three-Dimensional Wrench Geometry with a Curved Crack

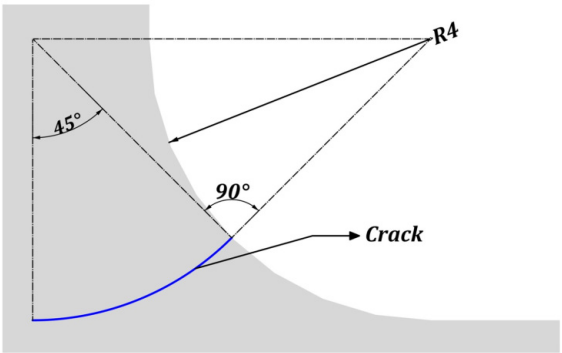
To show the extensive capacity of our methodology, we performed a final case with a complex design domain and curved crack. Appropriately, wrench geometry which is a widely known industrial element used in different applications is modeled. The design domain and the boundary conditions are illustrated in Figure 4.29. A uniform pressure load is applied on half of the small hole, while the bigger hole is fully fixed. The main dimensions can be observed in Figure 4.29, where L = 1 m. Moreover, other dimensions related to the corners are given in Table 4.2. A curved surface crack is embedded in the wrench with a length of 0.4 cm. Figure 4.29c shows the curved shape crack in detail. The length of the curved crack is approximately 118 mm and the crack lies along the width of the wrench in the transverse direction. The wrench is uniformly discretized where the distance between the particles is equal to 0.0125 mm. This results in a distribution of 153600 particles within the design domain. The volume fraction constraint of the problem is set to 0.3.

Figure 4.29 Design domain and crack features of the wrench geometry.



(a) Without crack

(b) With a curved crack



(c) Crack position and shape

Table 4.2 Dimensions of the wrench geometry

Name	L	R1	R2	R3	R4	R5	R6
Dimension [mm]	1000	100	75	50	150	50	300

Figure 4.30 Comparison of the optimal topologies of Case III for different views (Isometric and x-y).

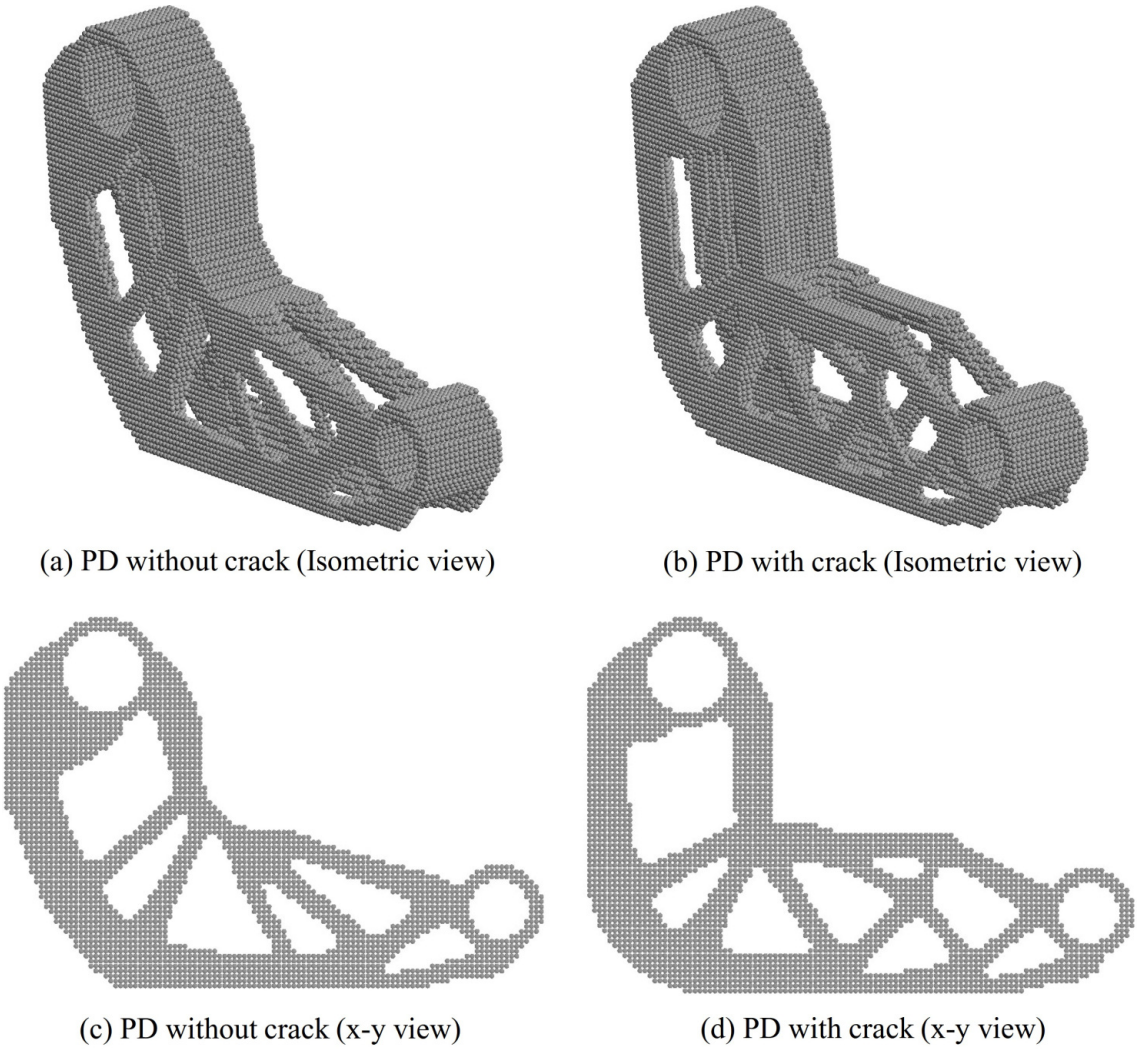
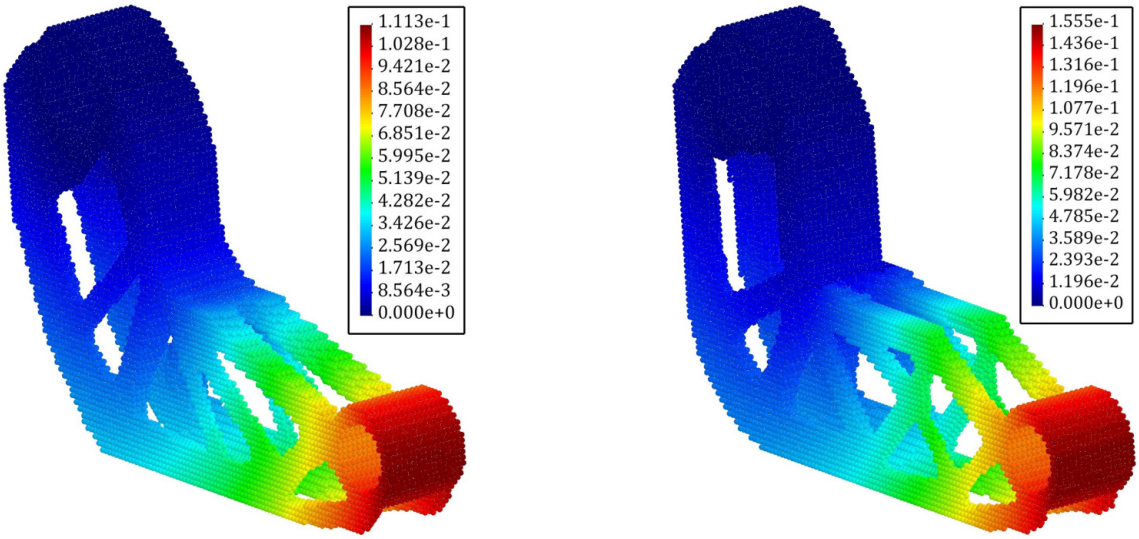


Figure 4.30 shows the optimal topologies for the design domain with and without the crack. It is apparent that the crack presence leads to a very different topology. The x-y view of the optimal topologies is illustrated in Figures 4.30(c, d) which shows a better comparison of the optimal results. The embedded crack changes the optimal result, and the materials are distributed more in the crack location. After the crack is involved, the arm extending from the cracked region lies in a straight form whereas the result without a crack has an inclined arm as depicted in

Figure 4.30. For this reason, some other links are formed between the main bearing elements. Consequently, this material distribution enhances the structure to prevent crack propagation according to this boundary condition.

Figure 4.31 depicts the comparison of the total displacements of the optimal topologies for this example. Furthermore, the distributions of the strain energy density are shown in Figure 4.32, which shows the high strain energy regions. One can see the maximum displacement of the structure is increased significantly by embedding the crack in the structure. It is because the existence of a crack in the more critical region results in more compliance or displacement in the optimized structure. In fact, the location and size of the crack created in this problem were specially chosen to prove this result. Considering the boundary and loading conditions, it is estimated that the region of rotation collects a high amount of strain energy. This result is also seen in the strain energy distribution of the final topology obtained in the crack-free condition, as in Figure 4.32a. There is a region where strain energy is highly accumulated relative to the remaining of the body. Instead, as shown in Figure 4.32b, the strain energy distribution is more balanced throughout the structure. This is a significant indicator of being avoided from possible damage initiation. Therefore, it can be revealed that the fracture toughness of the structure is increased for possible damages that may happen in the region where we embedded the crack.

Figure 4.31 Comparison of the total displacements for the optimal topologies

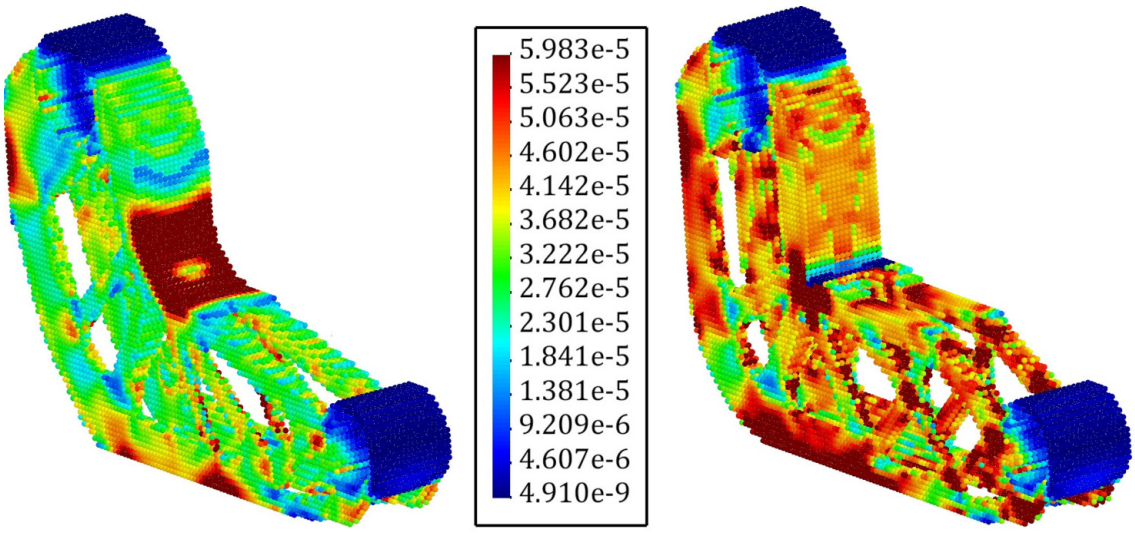


(a) PD without crack (b) PD with crack

The topology of this cracked case may be optimized using FEM-based approaches; however, they cannot handle the crack in a straightforward manner so much as

what PD can offer and requires very complex algorithms to do so. Therefore, the main advantage of our proposed approach for 3-D structures is the crack/damage modeling during the topology optimization of the structural geometry without any special algorithms such as mesh refinement, and crack front tracking, among others. These topologies are smoothed to manufacture by 3D printing as shown in Figure 4.33.

Figure 4.32 Comparison of the strain energy densities for the optimal topologies.

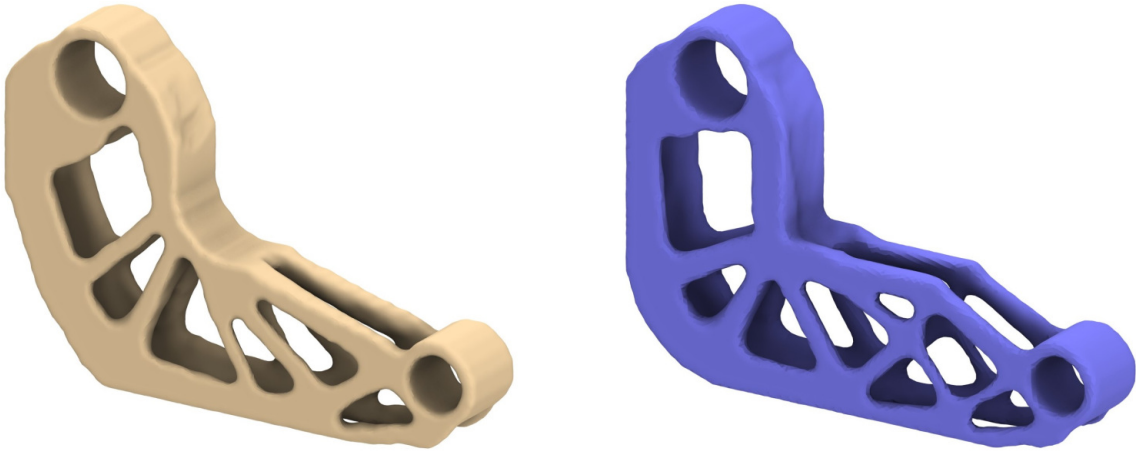


(a) PD without crack (b) PD with crack

4.1.4 Concluding Remarks

In this section of the thesis, a novel three-dimensional PD-TO method is developed to optimize the structures with single/multiple surface cracks for AM applications. A discrete-density-based algorithm, BESO, is employed as the optimizer whereas a bond-based peridynamics is implemented due to its straightforward coding application. This new approach has no special treatments to handle TO problems involving large deformations and/or structural discontinuities (i.e., damage/crack/defect). Leveraging this feature of the PD-TO algorithm, the effect of possible surface cracks with several orientations/sizes representing process-induced large-scale damages/defects that may occur during AM process is investigated for 3D topology optimization.

Figure 4.33 Smoothed versions of the optimum results for wrench geometry.



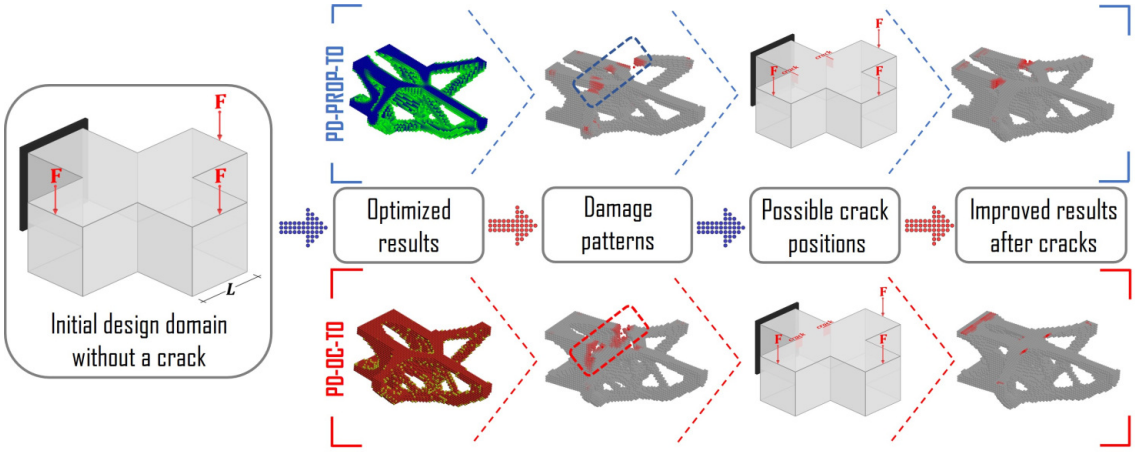
(a) PD without crack (b) PD with crack

Initially, the PD-TO method is applied to various 3D geometries without cracks, and the PD-TO results are extensively validated with the reference solutions obtained from FEM-TO. Comparisons of total strain energy results demonstrate that both methods provide almost identical compliance for the same geometry and discretization without damage/defect but may generate remarkably different optimum topologies (e.g., Figures 4.10a–4.10b, 4.18a–4.18b, 4.26a–4.26b), which can be attributed to the non-local nature of the PD theory. Then, to integrate the AM-induced damages into the TO process, the benchmark problems are optimized by considering different crack configurations (positions, orientations, and single or multiple cracks) and utilizing the 3D PD-TO method. The results of 3D geometries with cracks demonstrate that the involvement of a crack in a structure naturally affects the optimized topology, and the crack location has a significant effect on the optimal topologies. The material distribution critically alters with the basic intention of preventing crack propagation in the existence of cracks. Therefore, the most common finding can be indicated that the material is distributed with more support at the crack tips as compared to the normal direction of the crack. Accordingly, closer regions to the crack tips are thickened by the PD-TO optimizer, thus avoiding crack growth in this direction. Consequently, the residual stress can be reduced in these hot-spot regions due to an increase in the surface area, hence exhibiting the functionality of the proposed method for performing topology optimization for AM applications. In other words, the outcomes of these analyses prove that the PD-TO optimizer can automatically find where the material should be accumulated to reduce the undesired effects of thermal residual stresses during AM process.

Further, the final topologies optimized by PD-TO are smoothed by applying surface

smoothing methods to obtain print-ready designs for fabrication using additive manufacturing. Afterward, smoothen geometries are successfully 3D printed by using extrusion-based AM with PLA material. As a final contribution, a wrench geometry is optimized to reveal the superior capabilities of the proposed method. In this problem, we generated a more sophisticated structure and crack geometry to prove that the proposed method can be utilized in the optimization of real-life engineering structures. In addition to the numerical comparisons, the results of FEM-TO and PD-TO for the bridge problem without crack are experimentally compared by conducting a mechanical test. The experimental results show that PD-TO provides an optimized structure that stores 15% less total strain energy than those optimized by FEM-TO under the same loading condition. Hence, this enhanced strain energy distribution reveals that the PD-TO is a viable optimization scheme for designing 3D structures even without considering defects. All in all, the current PD-TO method can be a promising future technology with superior modeling, analysis, and optimization capability for industrial applications of 3D structures, especially, considering probable defects due to AM processes.

Figure 4.34 Graphical abstract of the Section 4.2



4.2.1 Introduction

This section of the thesis presents continuous density-based three-dimensional TO approaches developed by coupling the PD with optimality criteria (OC) and proportional approach (PROP). These frameworks, abbreviated as PD-OC-TO and PD-PROP-TO, can be practically utilized to enhance the fracture toughness of the structures during the optimization process by taking critical regions into account as pre-defined cracks. Breaking the non-local interactions (bonds) between relevant PD particles enables us to readily model cracks. Utilizing this advantage, we solve several benchmark optimization problems including different numbers, positions, and alignments of the cracks. The major differences between the proposed methods are examined by comparing optimum topologies for various cracked scenarios. Moreover, the mechanical behaviour of the optimized structures is investigated under dynamic loads to prove the significant improvements achieved by the present approach in the final designs. The results of dynamic analyses reveal the viability of both PD-TO methods for increasing the fracture toughness of the structure in the optimization stage. Overall, the proposed approach is confirmed as a superior

design and optimization tool for future engineering structures. Worth noting that the provided results in this section is also published in the journal of Engineering with Computers (Kendibilir, Bilgin & Kefal (2024)).

4.2.2 Novelty and Motivation

Fracture toughness is one of the most important design criteria for the high-performance engineering structures utilized in the automotive and aerospace industries which are subjected to dynamic boundary conditions due to their operation load types. Increasing fracture resistance would enhance the lifetime of engineering components and decrease the likelihood of damage under given loading conditions, thereby reducing overall maintenance and renovation costs in such industries. One can improve the fracture toughness of the topologically optimized structures by utilizing the proposed continuous density-based peridynamics topology optimization framework. To the best of our knowledge, there is not any reported study in the literature that performs 3D PD-TO with continuous density-based topology optimization methods. Investigating the performance of OC and PROP algorithms with PD for the 3D structures involving surface cracks for the first time in the literature is one of the motivations and novelty of the present study. The capabilities of the proposed approach are presented by optimizing various 3D structures involving different crack scenarios with both offered methods which are named PD-OC-TO and PD-PROP-TO. Another significant novel contribution of this study is to enhance the fracture toughness of TO designs utilizing PD-TO methods. To this end, the locations of the surface cracks on the optimized structures are detected under dynamic loads for the first time. Then, the optimization procedure is performed once more to create tougher structures against the same load. Therefore, this framework can be performed in the preliminary design stage to assess the performance of topologically optimized designs and improve the toughness under operation loads. In addition, this study can be utilized in the design of additively manufactured structures, where the residual-stress-induced defects can be minimized in the TO process.

The remainder of this section is structured as follows. Numerical examples are presented in Section 4.2.3 for four different crack scenarios. Results of dynamic PD analyses are provided in Section 4.2.4 to compare the load-bearing capacity of optimized structures with/without cracks. In the end, the concluding remarks of this section are included in Section 4.2.5.

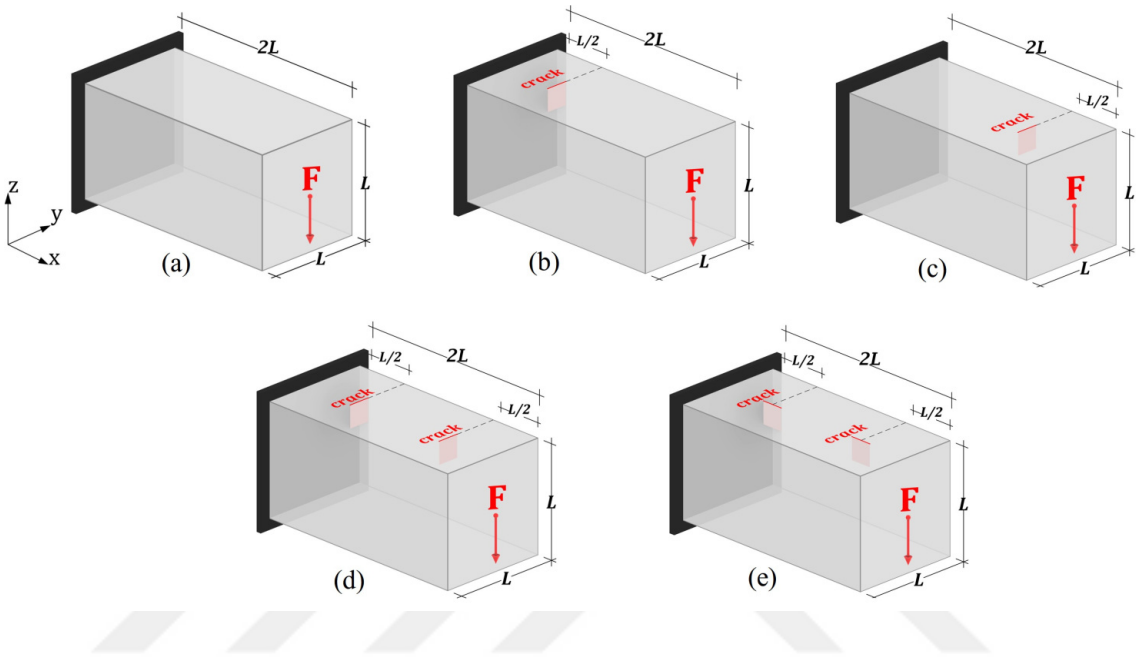
4.2.3 Topology Optimization Examples

In this chapter, we first optimize well-known examples of TO problems from the literature to prove the accuracy and abilities of the proposed optimization methods. Initially, the PD-TO results are compared with the reference FEM-TO solutions considering a crack-free domain for each problem for validation. Additionally, several crack-involving domain scenarios are created to examine the location and orientation effect of crack/cracks. At this stage, to utilize the superior advantages of the PD in modeling discontinuities such as crack, void, or damages, we only perform the developed PD-PROP-TO and PD-OC-TO frameworks for the optimization of crack-involving case scenarios. All the numerical results are generated by an in-house MATLAB code. Unless otherwise stated, the Poisson's ratio and modulus of elasticity of the material are $v = 0.25$ and E = 200 GPa, respectively. Additionally, the minimum filter radius and PD horizon size kept remained as $R_{min} = 3dx$ and $\delta = 3.015dx$ for all the optimization problems in this study. In the design variable updating scheme, the penalization parameter is set to 3.

4.2.3.1 Case I: Cantilever Beam

The most famous benchmark problem in topology optimization literature, the 3D cantilever beam, is chosen as the first case study. Figure 4.35 presents the five scenarios including several crack conditions where the length $L = 1m$. Particle spacing is chosen as $dx = L/30$ which results in a discretization of 54000 particles in total ($60 \times 30 \times 30$ along x, y, and z axes). Applied boundary and loading conditions are clamping on the left face and a concentrated downward load of $F = 100kN$ divided into 4 PD particles at the center of the right face, respectively. The total volume of this geometry during the optimization process is constrained to 25% of the initial volume. The embedded square-shaped cracks are formed with an edge length of 0.2L .

Figure 4.35 Design domain and loading condition of the Cantilever Beam problem for five scenarios in total including with/without crack conditions, namely (a) without crack; (b) back crack; (c) front crack; (d) double parallel crack; (e) double perpendicular crack. Single or multiple cracks are embedded into different locations. Cases (b), and (c) are designed to investigate the location effect of a single crack by positioning at varying distances to the applied force. In cases (d) and (e), we intend to examine the reaction of the optimizers in the existence of multiple cracks in different orientations.



The crack-involving scenarios are designed in a way that they serve the investigation of location, quantity, and orientation effects in comparison to the crack-free case and each other. Firstly, a single surface crack is embedded into regions L/2 distant from the clamped face (back crack) and L/2 away from the load face (front crack) as shown in Figure 4.35b and Figure 4.35c, respectively. Note that, the crack is aligned parallel to the clamped face in both cases. Since the location of the crack is the only variable between these two scenarios, the purpose of their comparison is to observe how the PD-PROP and PD-OC solvers lead the final topologies when the same crack is close to the fixed support or applied load. Furthermore, the defined single crack cases are combined as presented in Figure 4.35d to examine their combined effect as a double crack with equal distances to the clamping and loading faces. Finally, Figure 4.35e depicts that the orientations of the embedded surface cracks in the double parallel crack case are changed to be perpendicular to their previous alignment. The goal of the last scenario is to observe whether the same double crack causes a different topology by changing only their orientations. The computational simulations involving numerical discretization are usually subjected to mesh dependency studies to show that the result obtained by the proposed method

does not depend on the discretization size. Therefore, we created four different models with the discretization of the domain as $32 \times 16 \times 16$ (coarse discretization), $40 \times 20 \times 20$ (medium discretization), $60 \times 30 \times 30$ (fine discretization), and $80 \times 40 \times 40$ (finest discretization) to select the optimum resolution in terms of accuracy and computational cost. Our objective function (compliance) results with the final material distributions obtained by the PD-PROP and PD-OC methods are illustrated in Figure 4.36 and Figure 4.37, respectively. It is clear from these figures that the result depends on the particle size up to a certain limit of the resolution. Especially, coarse and medium discretizations lead to considerably higher compliance values as compared to the fine and finest discretization for both methods. For the sake of clarity, their relative differences among varying resolutions are listed in Table 4.3. Here, it is obvious that the lowest difference between two sequential resolutions has been found between fine and finest discretization. That is why we selected the domain which includes 54000 ($60 \times 30 \times 30$) particles as the suitable resolution for our analysis by considering both the optimum result and computational efforts. Even though mesh dependency analyses are not explicitly given for further cases, we determine their discretization sizes with the same methodology.

Figure 4.36 Compliance values and final topologies obtained by PD-PROP for different discretization options

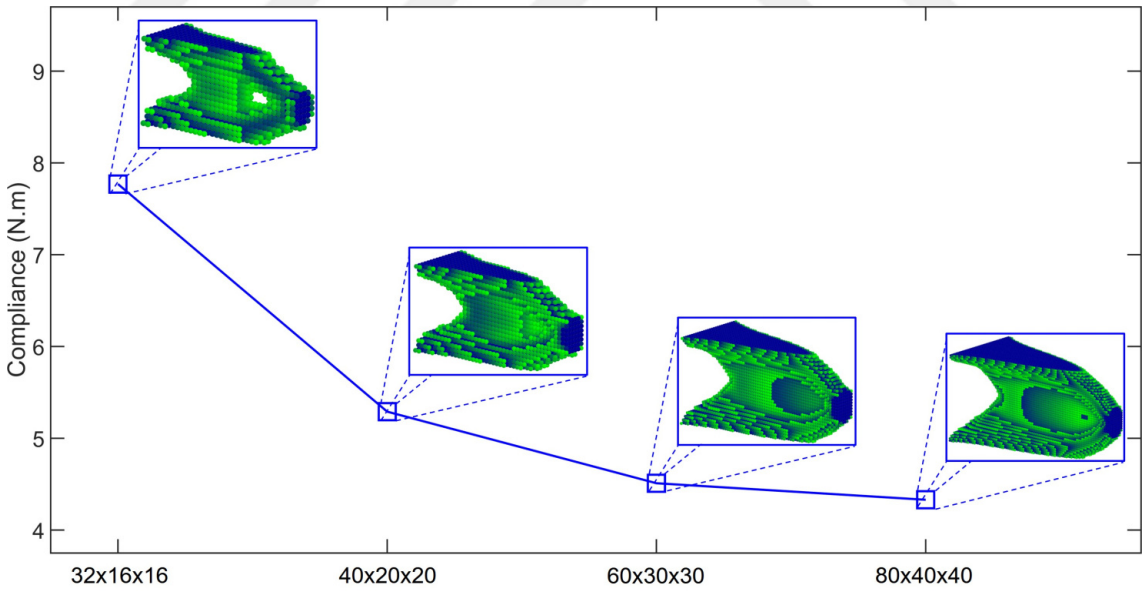


Figure 4.37 Compliance values and final topologies obtained by PD-OC for different discretization options.

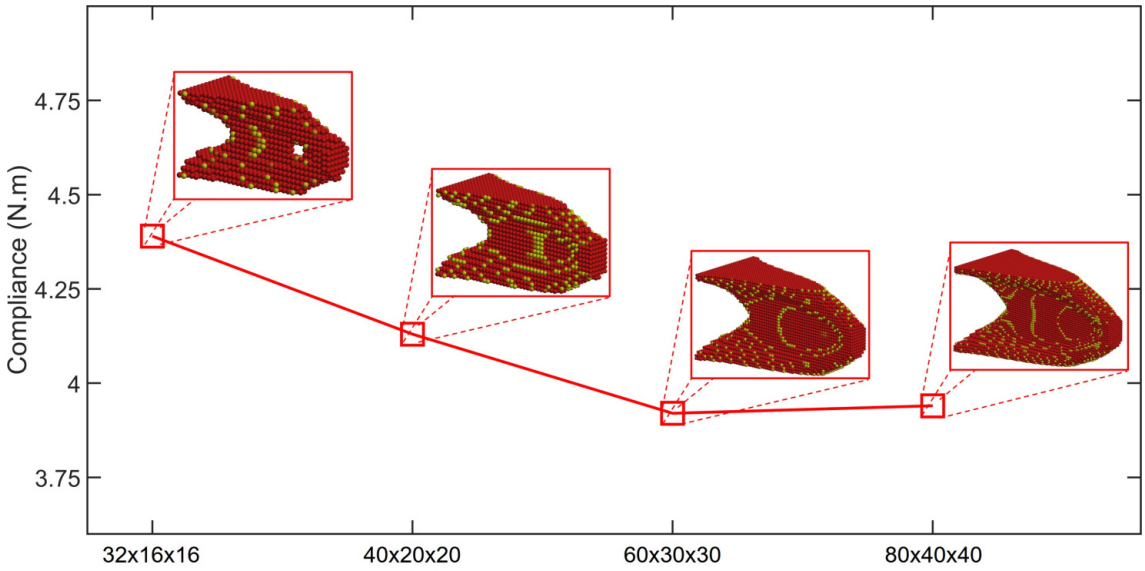


Table 4.3 Mesh-dependency study based on compliance values.

Discretization	Coarse to Medium		Medium to Fine		Fine to Finest	
Approaches	PD-PROP	PD-OC	PD-PROP	PD-OC	PD-PROP	PD-OC
Difference (%)	31.92	5.92	14.74	5.08	3.99	-0.51

Figure 4.38 demonstrates the results of the problem without embedded crack obtained by PD-TO and FEM-TO in both PROP and OC methods. It is clear that the two approaches generated similar material distributions with no considerable geometrical distinction in both PROP and OC algorithms as revealed in the given isometric and plane views. Concerning that FEM is a local approach while the PD is a non-local method, their final compliance values obtained by MATLAB code are not sensible to compare with each other. Instead, Ansys, as a common environment, is chosen to analyze the final topologies under the same conditions. Therefore, the design variables achieved by PD-TO in the final step are utilized to model a finite element mesh in Ansys. Since our FEM-TO code utilizes the hexahedral elements, we created uniform eight-noded elements assuming that the coordinates of each PD particle correspond to the center of the relevant element in Ansys. Consequently, the final compliance values of the resulting FEM-TO and PD-TO topologies are given in Table 4.4.

Figure 4.38 Comparison of the optimal topologies of the Cantilever Beam obtained by PD-TO and FEM-TO represented in two isometric, top and front views in order: (a) PD-TO; (b) FEM-TO. In each division in the figure, the first and second columns represent the PROP and OC results of the relevant method, respectively.

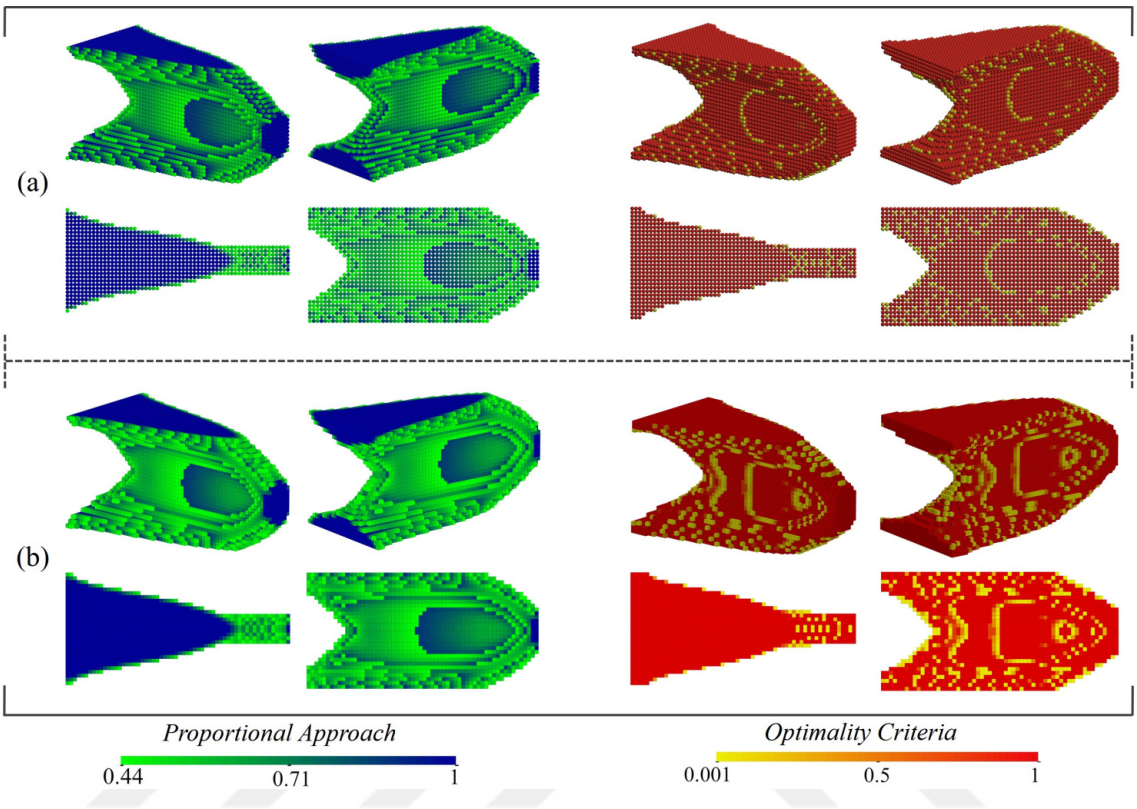


Table 4.4 The final compliance values for the cantilever beam without crack.

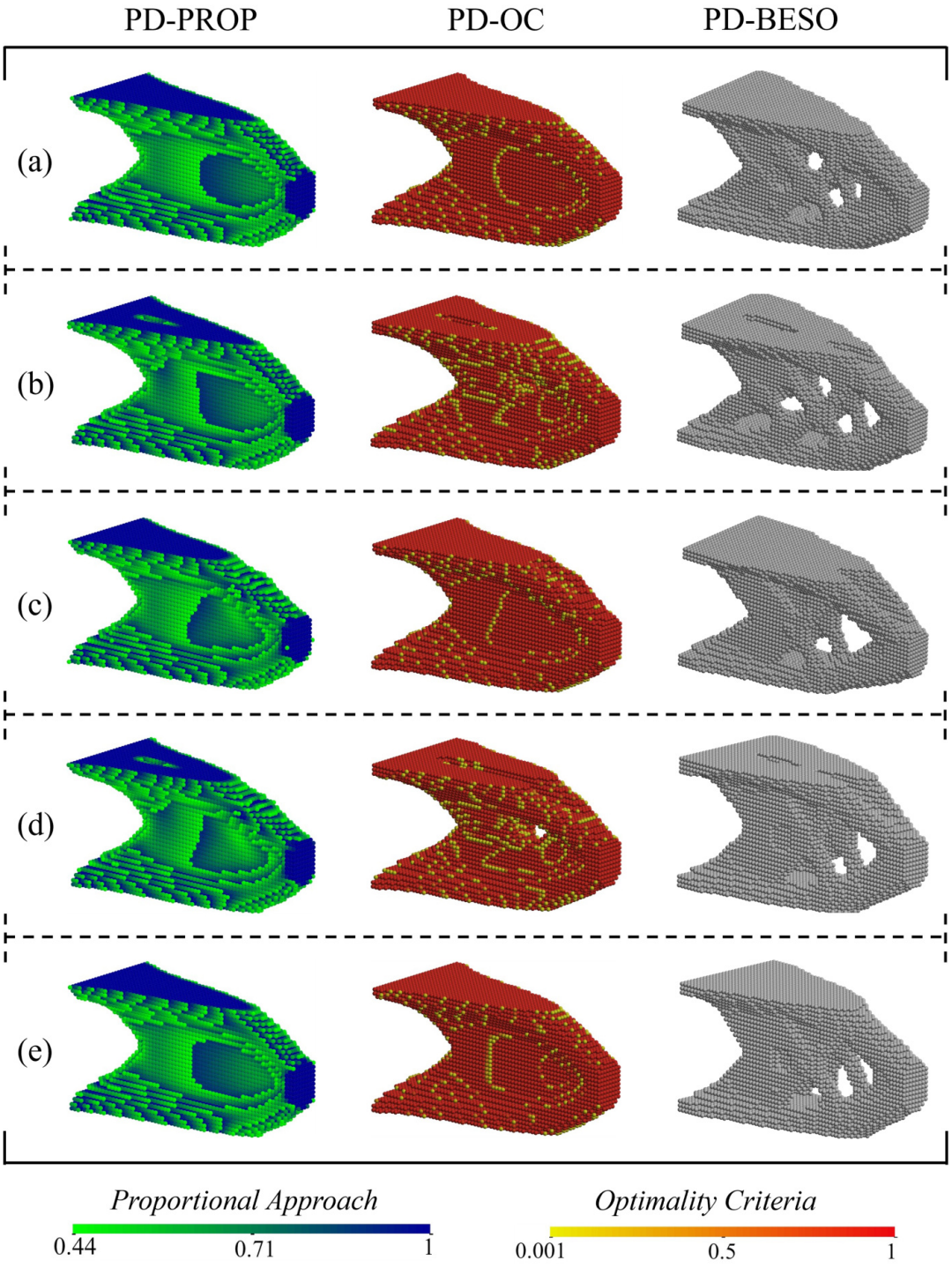
	FEM (reference)	PD	Difference (%)
OC	2.8	2.811	0.39
PROP	3.263	3.27	0.21

After the PD-TO approaches are validated with FEM results of the crack-free case, aforementioned crack-involved problems are solved with both PD-PROP and PD-OC. The optimum designs obtained by PD-PROP and PD-OC with the results of reference PD-BESO (Kendibilir et al. (2022)) are presented in Figure 4.39 (isometric view). Here, there are remarkable geometric differences observed between the optimum design of continuous (PROP, and OC) and discrete (BESO) density-based approaches. This comparison is made to reveal the difference between the proposed methods and the previously published method in Kendibilir et al. (2022). In the remainder of the section, only the results of the two proposed methods will be compared. For the back crack case, both optimization methods displayed a similar

reaction creating a hole in the normal direction while preserving material at the crack tips. As depicted in Figure 4.39c, PROP and OC maintained material at the back like the crack-free scenario, but more material accumulated in the width around the cracked regions (front). The hole at the back crack region and increased width of the front crack region can be observed in PROP result (Figure 4.39d). Likewise, by removing material from the normal direction of the cracks and accumulating the materials in the crack tips, a combination of back and front crack cases is revealed in optimum OC design (Figure 4.39d). Changing only the orientation resulted in totally different topologies as compared to the double parallel case. However, as seen in Figures 4.39(a, e), double perpendicular case results are like the first case as if there is no crack at all. The results of these scenarios are presented along with the case without a crack in plane views (Figure 4.40). When the back crack case is investigated, it is observed that both optimization methods gave the same reaction by opening a hole in the normal direction and leaving material at the tips of the crack. Similarly, as seen in Figure 4.40b, both PROP and OC strengthened the back of the beam by accumulating material in favor of the cracked region's width.

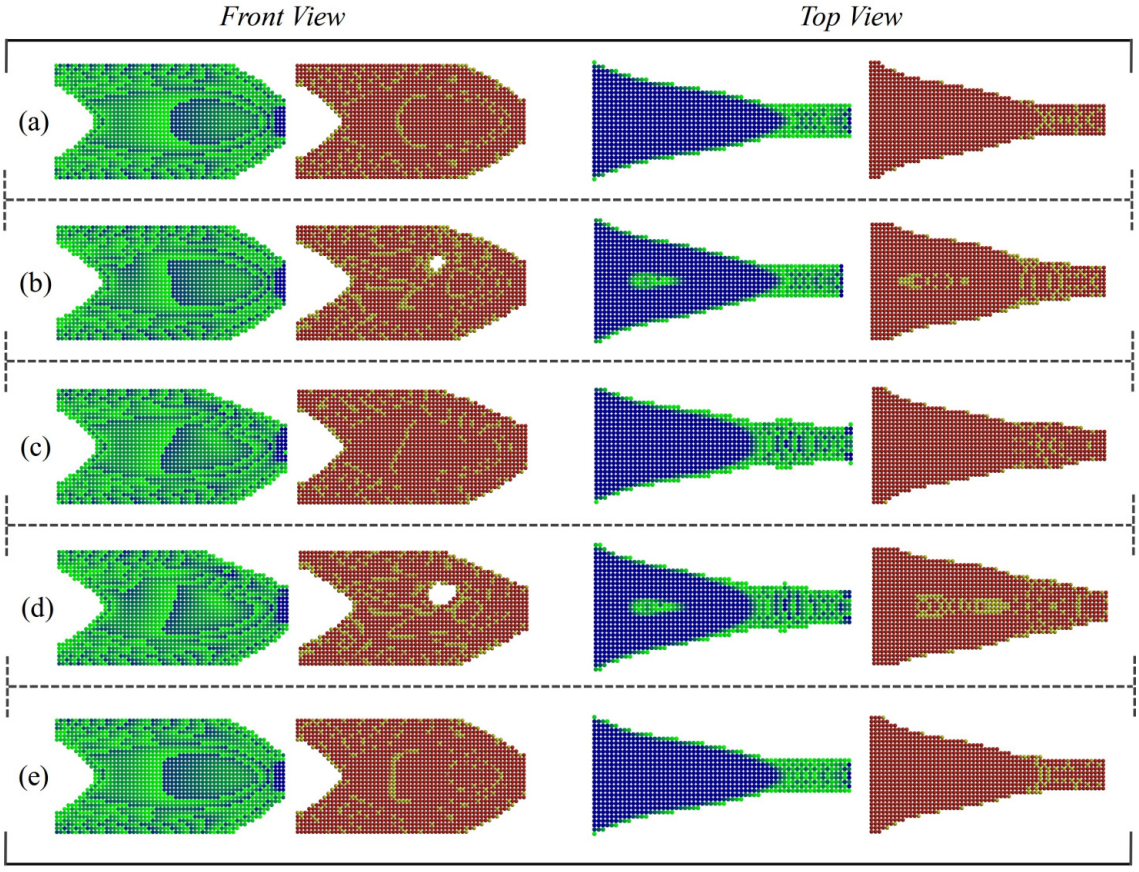
Moreover, when it is compared to the crack-free case in the front view, OC created another hole in the front part, which can be attributed to the need for additional material at the back of the beam due to the crack. On the other hand, the front crack case showed that the location of the structural discontinuities is a significant factor for both methods. In detail, as Figure 4.39c demonstrates both PROP and OC did not open holes and the back part of the domain remained the same in comparison to the case without crack, unlike the previous scenario. However, the top views in Figure 4.40c showed that the methods again accumulated material and resulted in a considerable increase in the width of the part around the cracked regions. Therefore, it proves that although the same crack is embedded in the same orientation, its location influences the reactions of the utilized TO methods.

Figure 4.39 Optimal material distributions of the Cantilever Beam obtained by PROP, OC, and BESO for all the cases with/ without cracks: (a) without crack; (b) back crack; (c) front crack; (d) double parallel cracks; (e) double perpendicular cracks. Here, the results are presented in an isometric view to show the geometrical details. Note that, for PROP results, the colour scale contains green and blue colours to represent the minimum and maximum values of the design variables, respectively. For the results of OC, yellow corresponds to the minimum value of the design variable whereas red colour represents the solid material where the design variable of the particle is equal to 1. The design variable is equal to 1 for all particles shown in the BESO results.



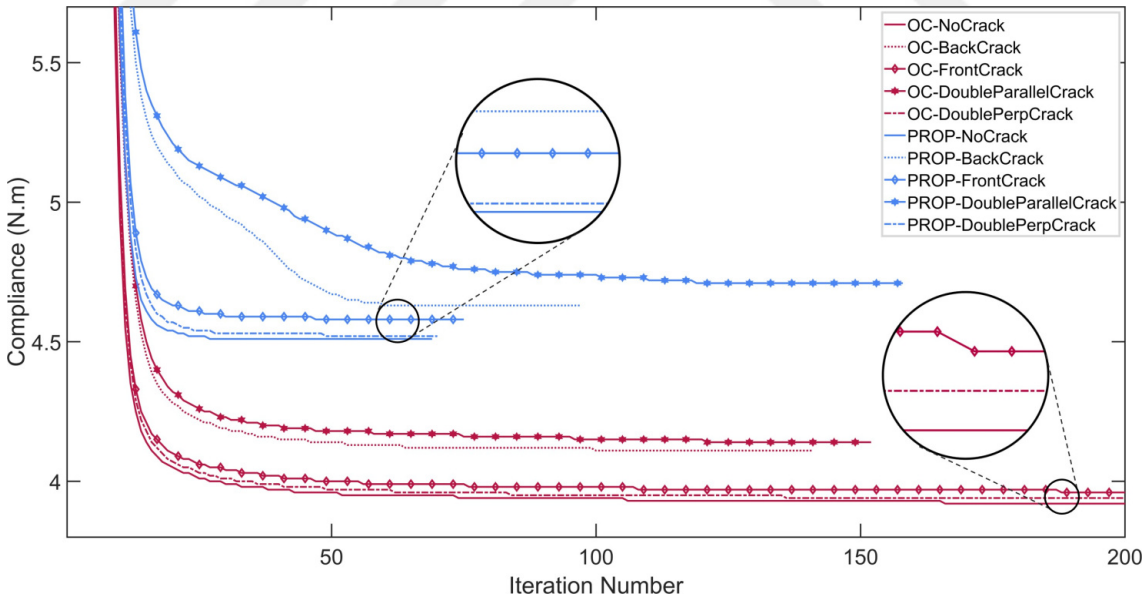
As mentioned in the problem definition, the double parallel crack case is constructed to see if it shows an effect of the back and front crack cases together. As expected, both methods provided results that seem to be combinations of the first two cases. PROP opened the same hole at the back crack region and increased the width of the front crack region as shown in Figures 4.39d and 4.40d, respectively. Likewise, OC also reacted by combining its results of back and front crack cases by removing material from the normal direction of the cracks and accumulating in the crack tips. However, OC results contain additional features unlike the PROP results of the double parallel crack scenario. For instance, if it is compared with an imaginary combination of front and back crack results, OC results of double parallel crack additionally involved a long path of removed material between the crack regions and the hole in the front view became much larger in this case. One of the potential reasons for this effect could be that OC incorporates sensitivities during the optimization process unlike PROP, so is much more responsive to the changes.

Figure 4.40 Front and top views of the optimal topologies: (a) without crack; (b) back crack; (c) front crack; (d) double parallel crack; (e) double perpendicular crack. In each view section in the figure, the first and second column represents the ROP and OC results of the relevant case, respectively.



Even though the results of the final crack case (double perpendicular crack) are almost identical to the results of the crack-free state, it revealed another significant effect of the structural discontinuities. The cracks from the previous case are placed in the same region but perpendicular orientation to the clamped face in this scenario. Changing only the orientation resulted in totally different topologies as compared to the double parallel case. However, as seen in Figures 4.39(a, e) and Figures 4.40(a, e), double perpendicular case results are similar to the first case as if there is no crack at all. As a result, this problem showed that the perpendicular cracks cannot easily propagate in this loading condition and thus do not lead to a considerable increase in strain energy. As a result, this problem shows that the perpendicular cracks cannot easily propagate in this loading condition and thus do not lead to a considerable increase in strain energy. Therefore, it can be inferred that the TO methods do not react to such cracks that are not creating any moment with the applied force.

Figure 4.41 The compliance history of the cantilever beam throughout the optimization process for each case where the red and blue lines refer to the compliance values obtained by PD-OC and PD-PROP, respectively. The initial few iterations, where the compliance values are extremely high, are not plotted in the figure to be able to compare the remaining part of the compliance values. For the sake of clarity, we zoomed into selected zones to show the exact standings.



Compliance values during the optimization can be seen in Figure 4.41 to compare the effect of various cracks embedded into the initial domain. First, it can be revealed that the PD-OC method provides better optima as compared to the PD-PROP method in all crack scenarios. Moreover, one can observe that crack involvement

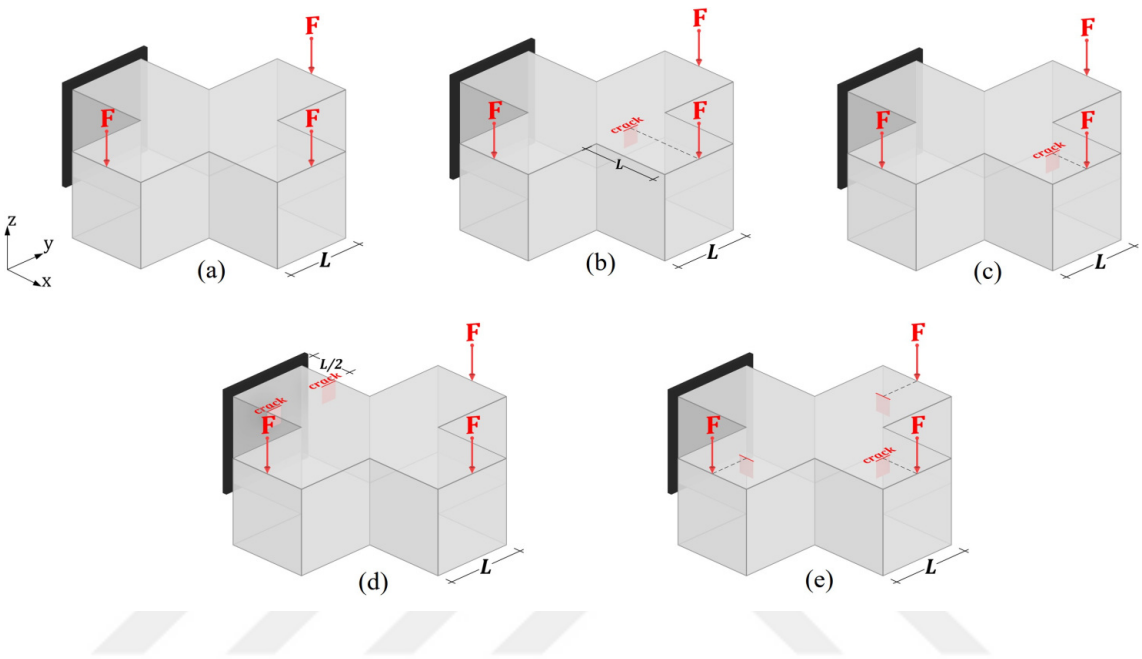
brings about higher strain energy accumulation in the structure. Furthermore, comparing the compliance of the cracked cases shows that double parallel crack led to the highest value among all others. Notedly, in both optimizers, double parallel crack is followed by back crack, front crack, double perpendicular crack, and no crack cases in descending order in terms of their compliance values. From this, a conclusion can be drawn about which crack location and orientation has a more critical effect. Compliance values of PD-PROP analyses at the final iteration are ranging between 4.51 - 4.71 Nm whereas the PD-OC method provides lower compliance values between 3.92 - 4.14 Nm. Accordingly, the average difference between the compliances obtained by OC and PROP is 12% in favor of the OC method.

4.2.3.2 Case II: Hanger Beam

In this problem, a 3D domain shaped like a hanger is modelled as depicted in Figure 4.42 where all the edges have the same length of $L = 60mm$. The model is discretized into 69120 particles with a uniform particle diameter of $dx = 2.5mm$. The hanger is fully clamped on its back whereas a concentrated downward load $F = 500N$ is applied on the edges shown in Figure 4.42. This load is distributed to 4 PD particles located in the middle of the upper edges. The target volume is set to 15% . All the square-shaped surface cracks have an edge length of L/6.

To investigate the effect of crack location on the optimized topologies, a single crack is embedded into different locations. These scenarios are named back (Figure 4.42b) and front (Figure 4.42c) crack cases with respect to their locations. The distance between the back crack and applied force is where the front crack is L/2 closer than the back crack to the load. Note that, the middle of the surface crack and force are in the same alignment in these cases. Furthermore, double surface crack (Figure 4.42d) is generated and located on the left and right sides of the clamping arm where the longitudinal distance between the double crack and clamping region is L/2. Here, the main motivation of this scenario is to examine the closeness effect of any possible defect to the clamping region which is attributed to a critical condition. In the final scenario, triple crack is embedded into the same position in each free hanger arm as clarified in Figure 4.42e. Each of these cracks is located L/2 away from the loading point. In this wise, the cracks at similar locations are examined to see which of them causes a more significant change in the final topology.

Figure 4.42 Design domain and loading condition of the Hanger problem for five scenarios in total including with/without crack conditions, namely: (a) without crack; (b) back crack; (c) front crack; (d) double crack; (e) triple crack. Single or multiple cracks are embedded into different locations. Cases (b) and (c) are designed to investigate the location effect of a single crack by positioning at varying distances from the applied force. In cases (d) and (e), we intend to examine the reaction of the optimizers in the existence of multiple cracks near the clamping and loading regions.



The topology evolution of case without crack can be investigated in Figures 4.43 and 4.44 for PD-PROP and PD-OC, respectively. These topologies correspond to the results at the iteration steps: 0^{th}, 10^{th}, 20^{th}, 30^{th}, 40^{th}, and 50^{th} step with respect to the given order starting from the center and going to the end of the maze. Dynamic changes in the continuous density variable are clearly seen in Figures 4.43 and 4.44. Moreover, it is shown that the material distribution is not seriously changed after a certain amount of iteration steps. Hence, it can be revealed that the first 30 - 40 steps are more critical to determining the main structure of a problem domain under the TO process.

Figure 4.43 Topology evolution of PD-PROP for the case without crack: (a) initial step, (b) step 10, (c) step 20, (d) step 30, (e) step 40, and (f) step 50.

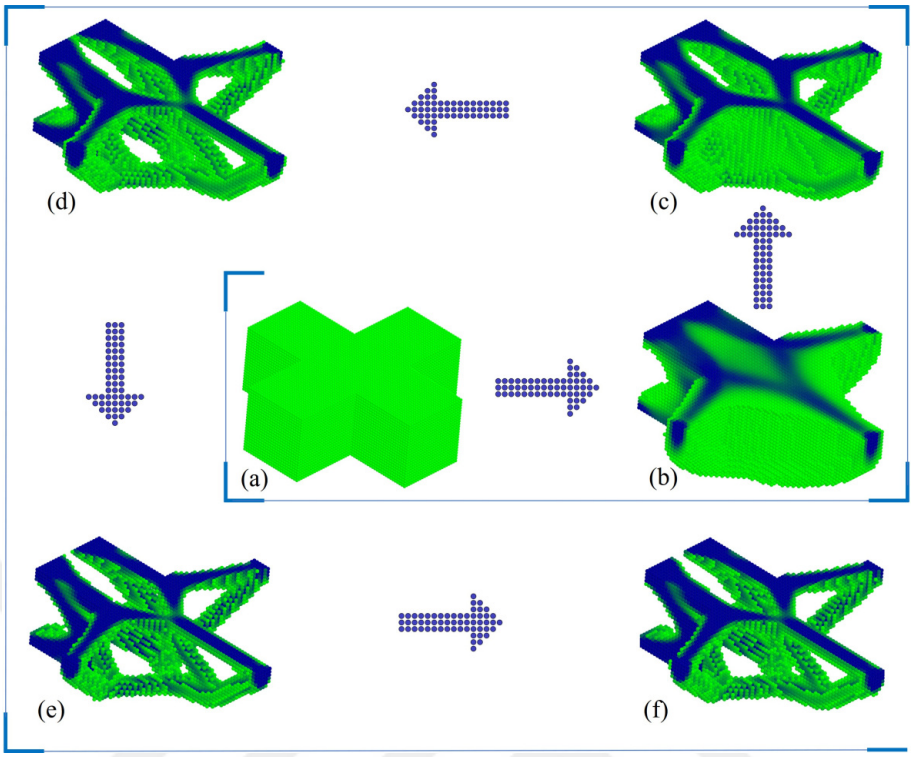
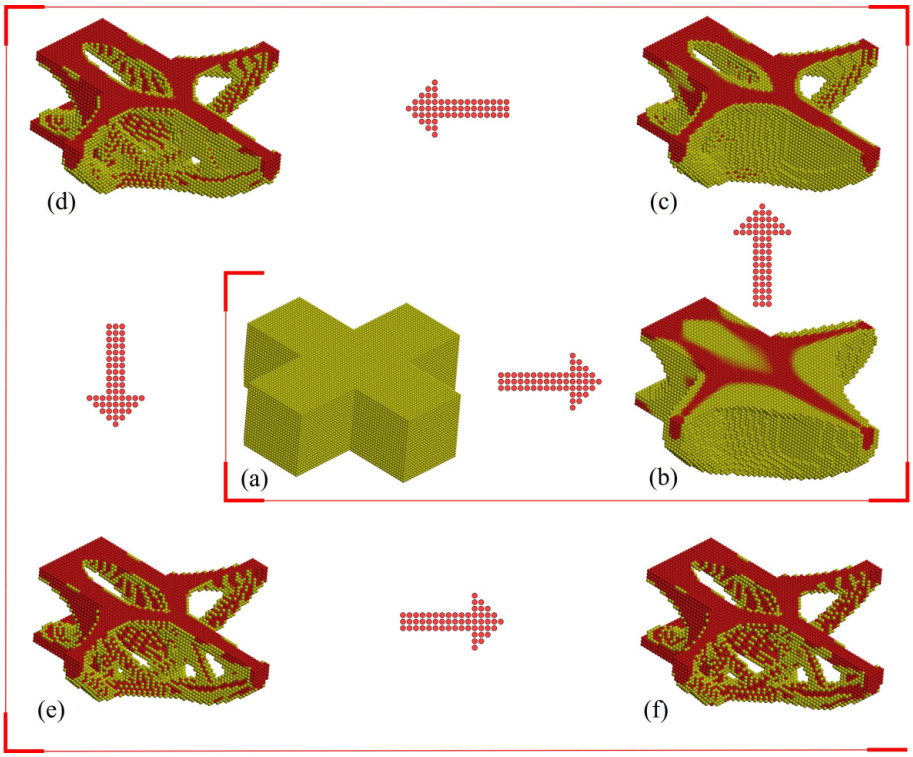


Figure 4.44 Topology evolution of PD-OC for the case without crack: (a) initial step, (b) step 10, (c) step 20, (d) step 30, (e) step 40, and (f) step 50.



The comparison between the optimal topologies obtained by PD-TO and FEM-TO in the crack-free state of the problem is presented in Figure 4.45. The results are given for two different isometric views along with the right and front views for clarity. Commonly, PD-TO and FEM-TO achieved quite similar topologies with the PROP method as clearly seen in all views. Also, the OC method concluded with high similarities between PD-TO and FEM-TO. However, in this case, there are slight geometrical differences observed in PD-TO results such as the additional thin arm from the bottom towards the middle, and the size of the hole at the top region of the topology obtained by the OC method. It can be revealed that OC is more sensitive to the structural analysis method as compared to the PROP method for this problem. In Table 4.5, the total strain energy values of the optimized topologies are listed. Since the final geometries are matching, compliance results are very close to each other as predicted. Considering both the final compliance and topologies, the PD-TO approach has proven to be as useful and capable as the conventional method FEM-TO.

Figure 4.45 Comparison of the optimal topologies of the Hanger obtained by PD-TO and FEM-TO represented in two isometric, front and right views in order: (a) PD-TO; (b) FEM-TO. In each division in the figure, the first and second column represents the PROP and OC results of the relevant method, respectively.

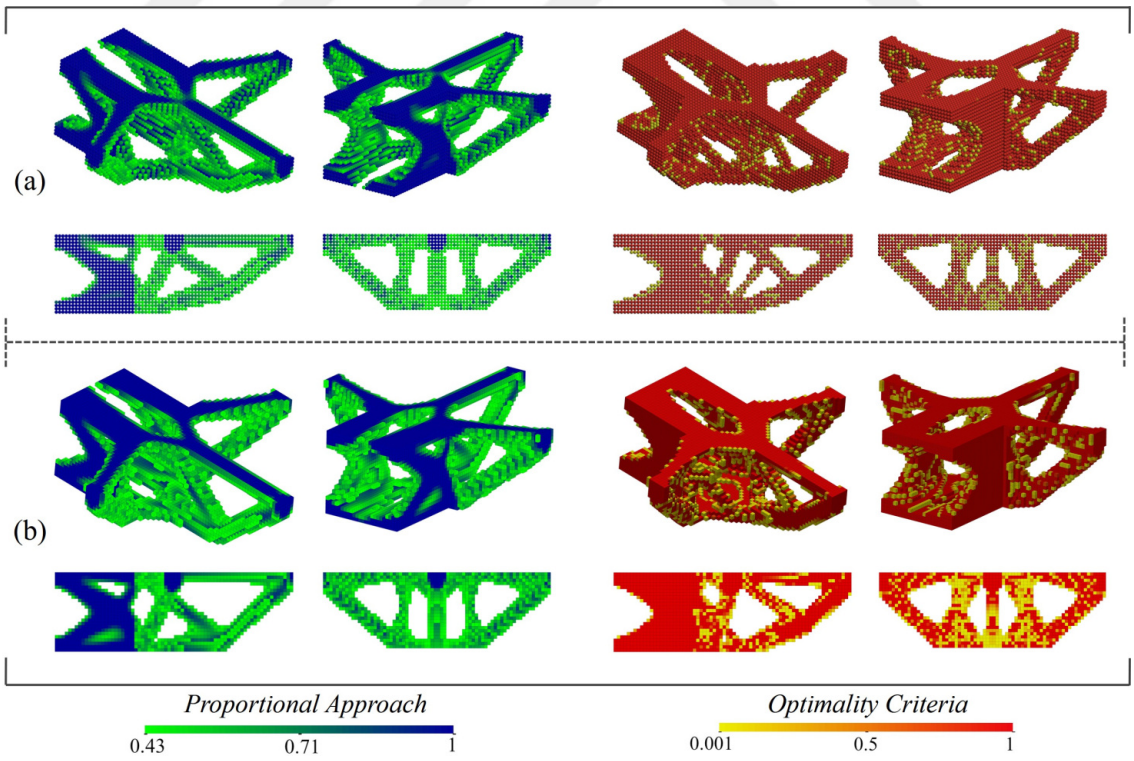


Table 4.5 The final compliance values for the hanger beam without crack.

	FEM (reference)	PD	Difference (%)
OC	0.0134	0.0141	5.22
PROP	0.0191	0.0196	2.61

The horizon radius is an important PD parameter that limits the extent of interactions between two particles. Therefore, the horizon size affects the solution in various aspects such as optimum material distribution, time cost, compliance, and so on. The optimized topologies obtained for four different horizon sizes are presented in Figure 4.46. Average time consumption for a solution step and total strain energy are listed for both methods in Table 4.6. The elapsed time for each optimization analysis is achieved using a workstation having Intel(R) Xeon(R) Silver 4215R CPU 3.20 GHz with 16 cores. The average time can be considered the most influenced parameter as the increasing horizon radius causes high computational costs. Compliance also increases as the horizon is expanded. Decreasing the radius causes thinner sub-branches in the final designs which certainly leads to difficulties in the manufacturing step. Consequently, 3dx, is utilized as the optimum size of the horizon radius in this study.

Figure 4.46 Final topologies obtained by PD-OC and PD-PROP for varying horizon size.

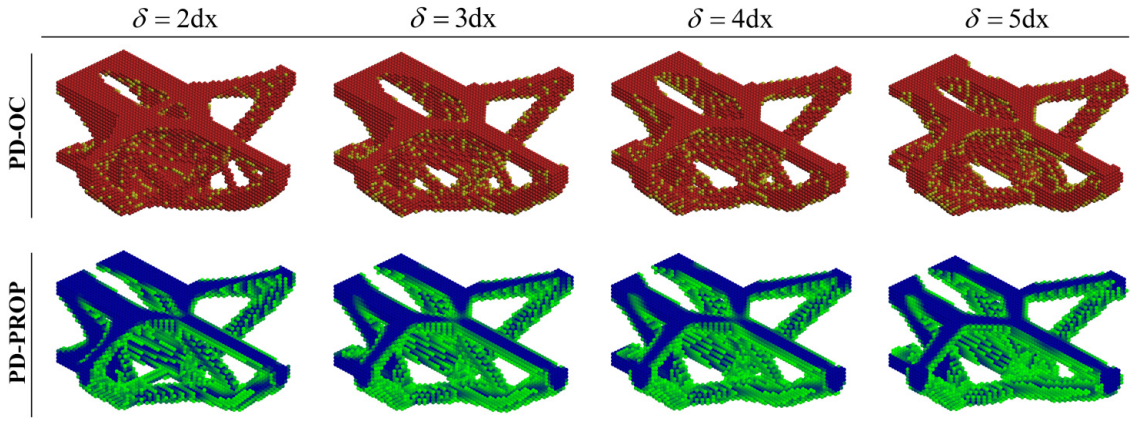


Table 4.6 Mesh-dependency study based on compliance values.

Methods	PD-OC				PD-PROP			
Horizon size (dx)	2	3	4	5	2	3	4	5
Av. time (min/step)	1.7	5	10	15	1.7	5	11	15
Compliance (N.m)	0.0124	0.0133	0.0138	0.0139	0.013	0.0137	0.0139	0.0145

In addition to the crack-free validation study, we then performed PD-TO analyses of the cracked scenarios to utilize the superior advantages of the PD approach. Figure 4.47 presents the optimum topologies obtained by PD-PROP and PD-OC in two different isometric views. Results show that the presence of the crack/cracks gives rise to the optimizer to generate alternative final material depositions. When these alternative distributions are criticized, it can be revealed that the regions close to the crack tips are strengthened. Although the back crack and front crack cases resulted in similar distributions in the clamping region, the front part of the hanger has changed its shape as compared to the crack-free state. PROP and OC results are quite similar for the back crack scenario as depicted in Figure 4.47b. Contrarily, the reactions of the proposed methods in the front crack case (Figure 4.47c) differ in a way that OC opened a hole in the normal direction of the crack whereas the PROP stacked material directly into the crack position. Hence, it can be concluded that although both methods update the geometry in the existence of a crack, they do not have to generate similar topologies.

In the next crack scenario (double crack), the material distribution in the cracked region is affected by the left and right cracks by removing the particles. Accordingly, it can be seen in Figure 4.47d that the PROP method enlarged the existing hole in this region, likewise, OC opened a new hole at the same location. Additionally, the PROP method brought the separate arms together in the clamping region. Another change appearing on the top side of the back part is the shrinkage of the large hole in the middle.

In the other case (triple crack), which can be considered as the extended version of the front crack case, we embedded two additional cracks into similar positions at the other blocks of the hanger. That is why the results of the triple crack case are compared with those of the front crack case, and an interesting discrepancy between OC and PROP is discovered in this comparison. While the PROP results seem almost identical, the OC method alters the geometry with recognizable dissimilarities as can be observed in Figures 4.47(c, e) and 4.48(c, e). This discrepancy can be explained by the main methodological difference between OC and PROP: the incorporation of sensitivities in the design variable updating scheme. In the PROP method, all the design variables directly depend on the strain energy density of the particles, while the OC method calculates and utilizes the variation of energy with respect to design variables in each step to update the design variables. This feature automatically makes the OC method more susceptible than PROP to structural changes during the TO process. Moreover, PROP results indicate that the strain energy distribution has not changed notably after the involvement of two additional cracks due to their positions.

Figure 4.47 Optimal material distributions of the Hanger obtained by PD-PROP and PD-OC for all the cases with/without cracks: (a) without crack; (b) back crack; (c) front crack; (d) double crack; (e) triple crack. Here, the results are presented in two isometric views to show the geometrical details as much as possible. Note that, for PROP results, the colour scale contains green and blue colours to represent the minimum and maximum values of the design variables, respectively. For the results of OC, yellow corresponds to the minimum value of the design variable whereas red colour represents the solid material where the design variable of the particle is equal to 1.

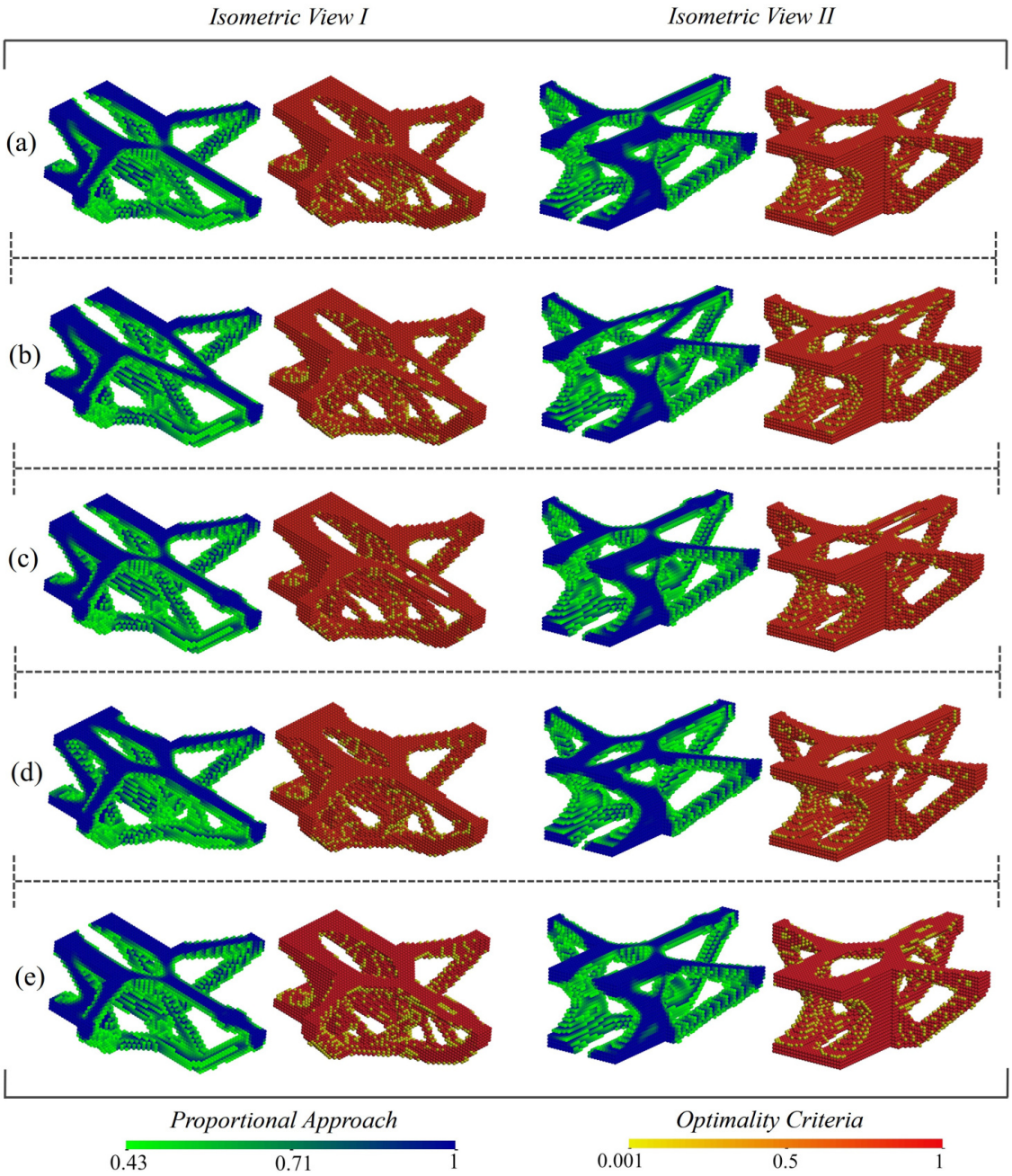
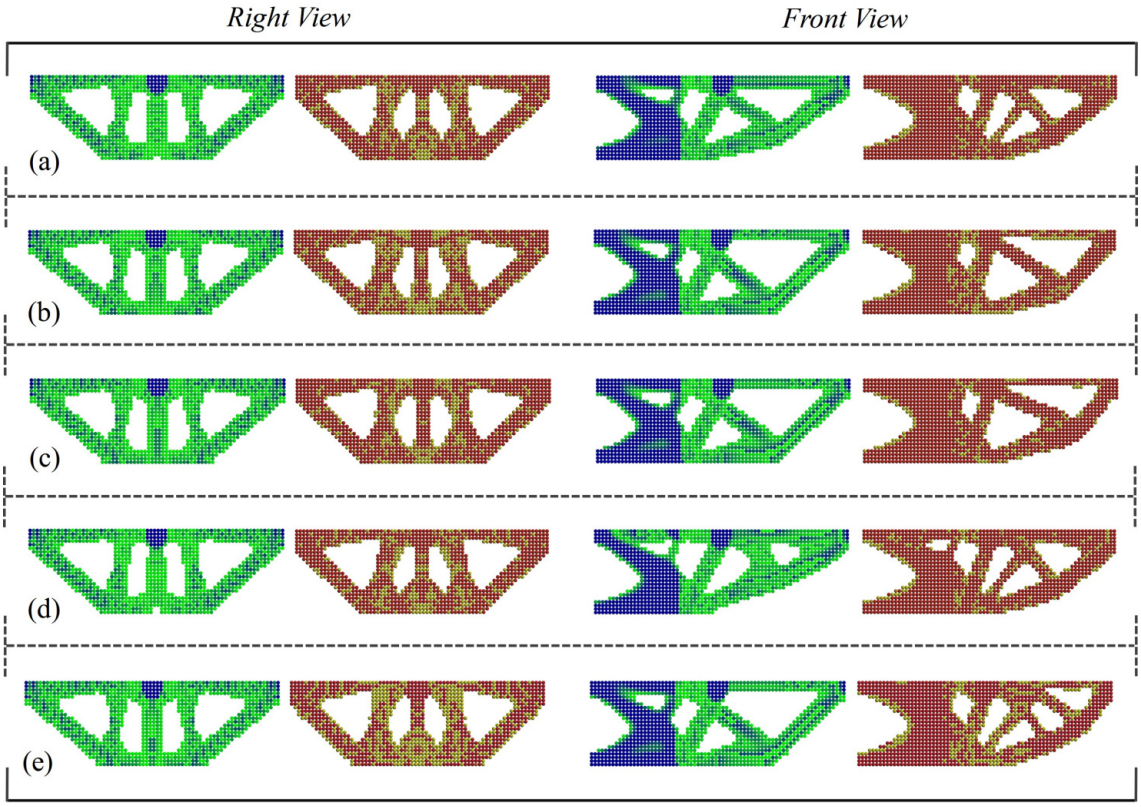
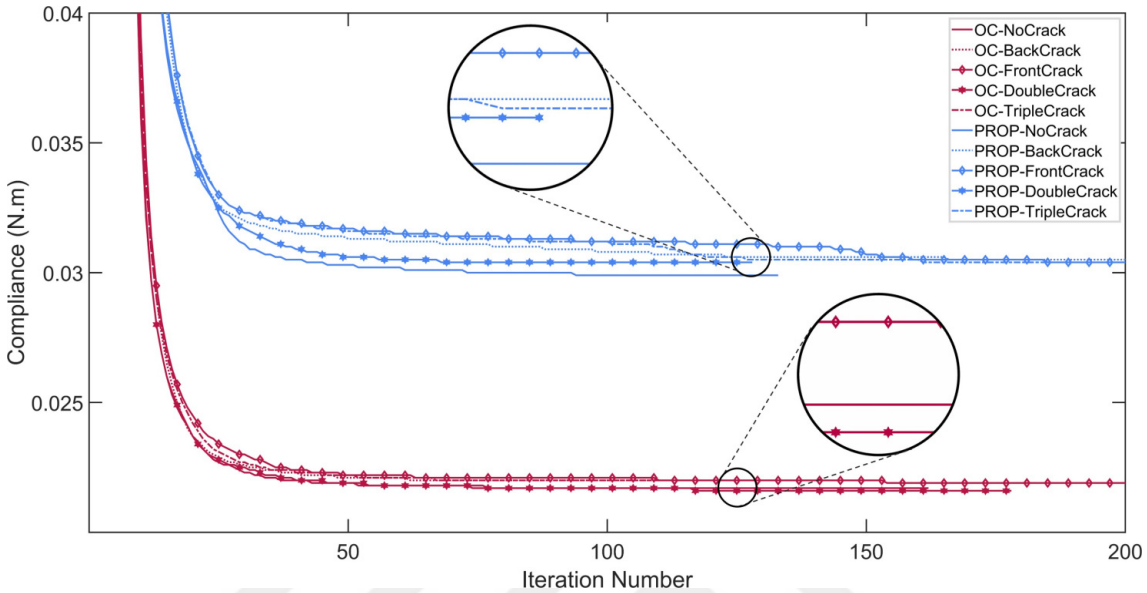


Figure 4.48 Right and front views of the optimal topologies: (a) without crack; (b) back crack; (c) front crack; (d) double crack; (e) triple crack. In each view section in the figure, the first and second column represents the PROP and OC results of the relevant case, respectively.



When all the PROP results are compared in front views from Figure 4.48, it can be observed that back, front, and triple crack cases include a longer base plate along the bottom side, whereas without crack and double crack cases have an arm rising from the bottom early. A potential reason for this effect could be that the cracks closer to the loading points (front, back, and triple crack) were more affected by tension in the upper portion, the PROP method changed the bottom side to prevent the crack-opening at the top.

Figure 4.49 The compliance history of the Hanger throughout the optimization process for each case where the red and blue lines refer to the compliance values obtained by PD-OC and PD-PROP, respectively. The initial few iterations, where the compliance values are extremely high, are not plotted in the figure to be able to compare the remaining part of the compliance values. For the sake of clarity, we zoomed into selected zones to show the exact standings.



The compliance values with respect to the iteration step for all scenarios are plotted in Figure 4.49. In general, the cases with cracks have more strain energy in the structure at the final state. In particular, the cracks closer to the force (front, back, and triple crack) cause higher compliance as shown in Figure 4.49. On the other hand, the OC method created a topology having less compliance even than the crack-free state for the double crack case. Regarding this, we can infer that it is possible to reach a stiffer result even if the structure involves crack/cracks. Moreover, it is clear from Figure 4.49 that OC provides better topologies in terms of compliance values. The total strain energy values of the PROP results are between 0.0299 - 0.0305 Nm while the OC method provided less energy in the range of 0.0216 - 0.0220 Nm considering all the scenarios. Calculating the average difference between the final compliances of PROP-PD and OC-PD indicated that the topologies obtained by OC are stiffer about 28% than those created by PROP.

4.2.3.3 Case III: MBB Beam

One of the most popular benchmark problems in TO literature, the Messerschmitt-Bölkow-Blohm (MBB) beam problem, is studied by considering four different crack-involving design domains as well as a crack-free scenario. The MBB beam has the dimensions of $6 \times 1 \times 1\ m^3$, in three-dimensional space as illustrated in Figure 4.50a. A point force is applied on the center of the top surface with a magnitude of $F = 400kN$ by distributing into 4 PD particles existing in this region. Due to the symmetric feature, the problem is analyzed by modeling one-fourth of the whole structure. The quarter part of the problem domain is discretized into $120 \times 20 \times 40$ particles in x-y-z directions, respectively. Thus, the entire geometry is represented by 384000 particles/elements in total. During the material removal operation, the optimizer is set to reach the predefined volume constraint of 15%.

Initially, the crack-free state of the design domain is optimized with a reference FEM-TO solver to validate the accuracy of the proposed 3D PD-TO optimization methods. After that, by utilizing the continuous density-based PD-OC and PD-PROP methods, the MBB beam is topologically optimized with four different crack scenarios to observe the effect of both the locations and the orientations of the square-shaped surface cracks. These embedded cracks with an edge length of L/6 are sequentially 1.5L (front-back) and 2.5L (mid) distance far from the supporting regions along the x-axis. The effect of varying location (1.5L or 2.5L) and orientation (parallel or perpendicular to the left and right faces) is to be extensively captured. Accordingly, the crack scenarios generated by cross-joining the distance and orientation options, are named the following: 1) parallel front and back cracks (Figure 4.50b), 2) perpendicular front and back cracks (Figure 4.50c), 3) parallel mid cracks (Figure 4.50d), and 4) perpendicular mid cracks (Figure 4.50e). Note that, the structure domain involves four surface cracks in each scenario.

Figure 4.50 Design domain and loading condition of the MBB-Beam problem for five scenarios in total including with/without crack conditions namely: (a) without crack; (b) parallel front and back cracks; (c) parallel mid cracks; (d) parallel mid cracks; (e) perpendicular mid cracks. There are two different crack locations and orientations: back and front, mid, parallel, and perpendicular. Identical square-shaped surface cracks are embedded into the relevant positions.

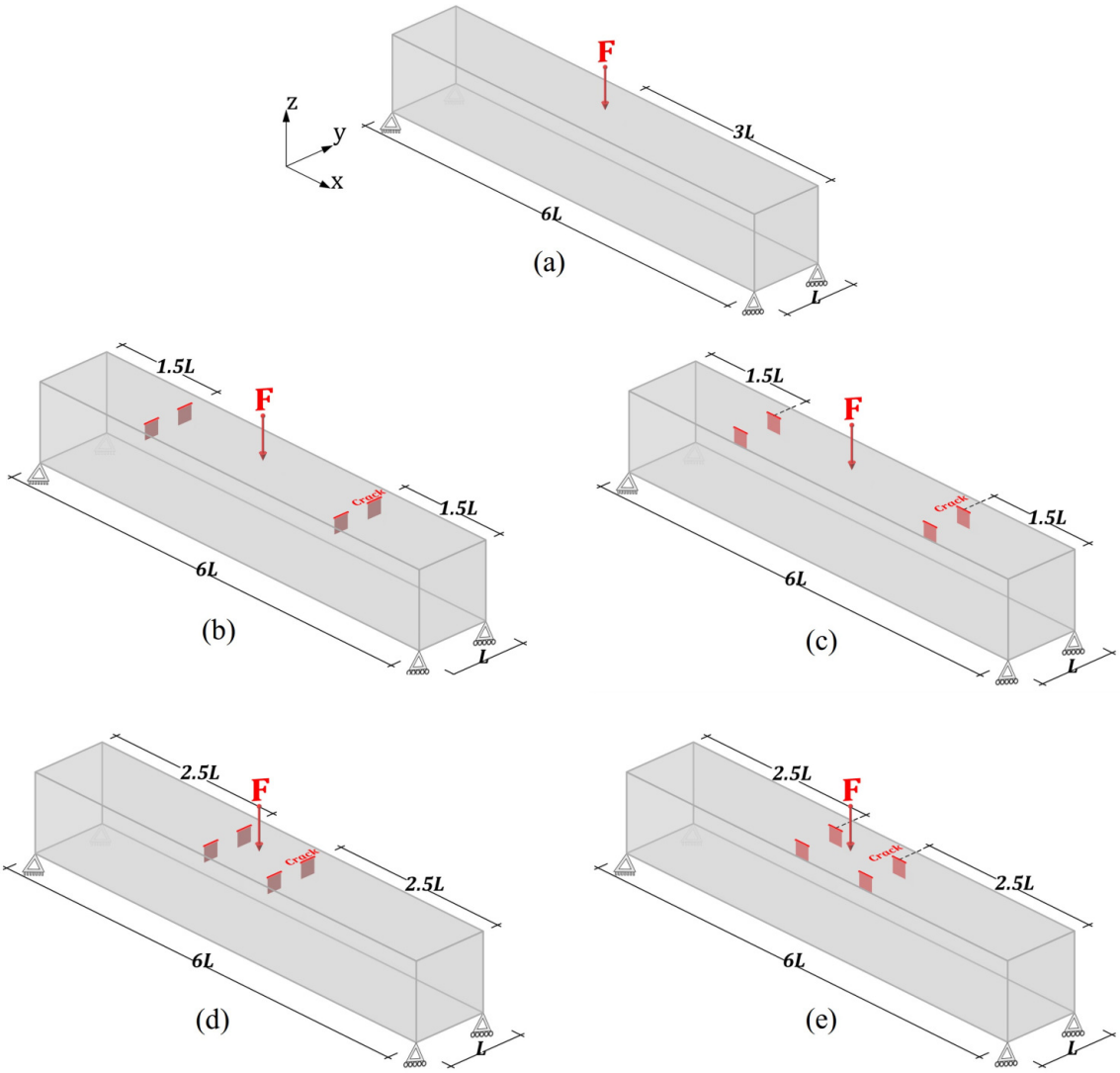
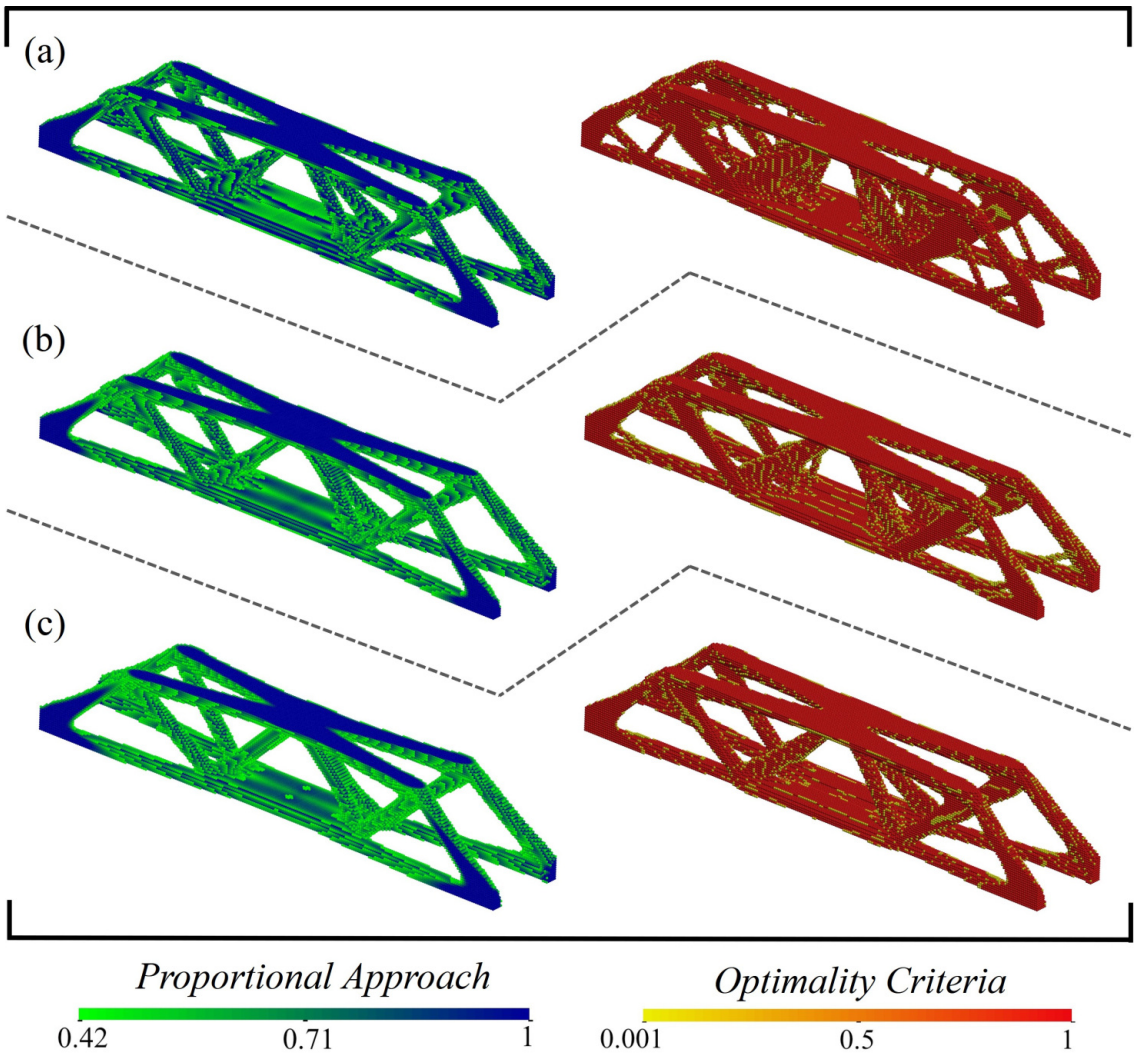


Figure 4.51 Filter radius analysis with different Rmin values: (a) Rmin = 2, (b) Rmin = 3, (c) Rmin = 4. The left and right columns contain PD-PROP and PD-OC results, respectively.



The effect of the filter radius (R_{min}) on the optimized results is researched by performing three different analyses for the same discretization. The final geometries are given in Figure 4.51 for both methods where R_{min} is equal to $2dx$, $3dx$, or $4dx$, respectively. It is observed that the filtering radius is more effective in distributing the material in an OC-based optimizer due to its sensitive nature. Reducing the filter radius from 4 to 2 increases the geometrical links and decreases the thickness of the support arms as clearly shown in OC results. On the other hand, PROP results are almost identical except for negligible differences among them. It can be concluded that changing the filter radius does not force to generation or removal of additional geometrical links in the results obtained by PD-PROP. This effect can be attributed to being a non-sensitive method of the PROP approach. The only distinction is the closer supports that lie down from the center of the top surface.

Increasing the filter radius led to thicker arms by getting them closer as much as possible. Consequently, we evaluated $R_{min} = 3dx$ as an optimum one by considering geometric features and thus we utilized this value in all problems throughout the paper as we declared at the beginning of the numerical examples section.

Figure 4.52 Comparison of the optimal topologies of the MBB-Beam obtained by PD-TO and FEM-TO represented in isometric, top, and front views in order from top to bottom: (a) PD-TO; (b) FEM-TO. In each division in the figure, the first and second column represents the PROP and OC results of the relevant method, respectively.

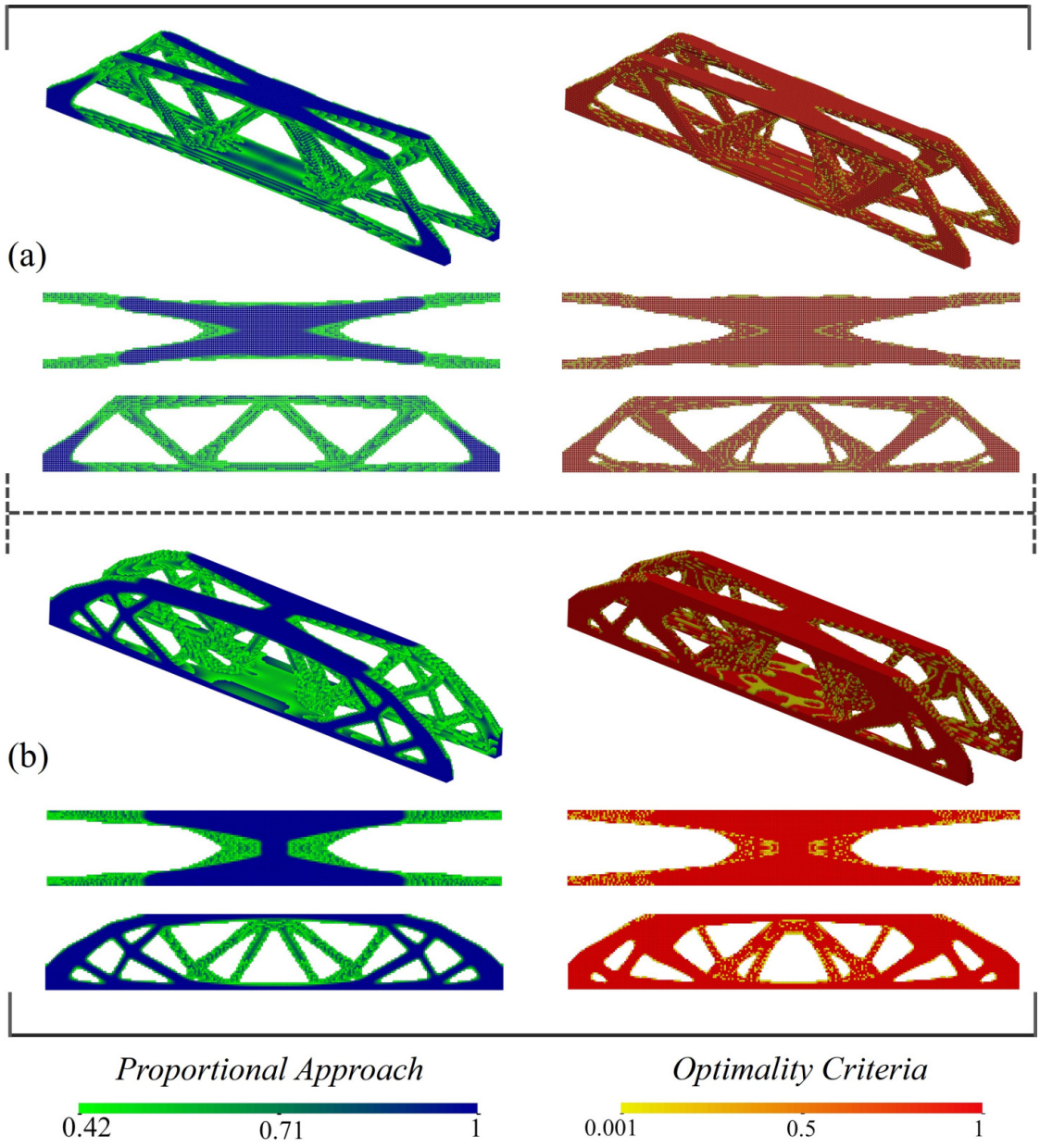


Table 4.7 The final compliance values for the MBB beam without crack.

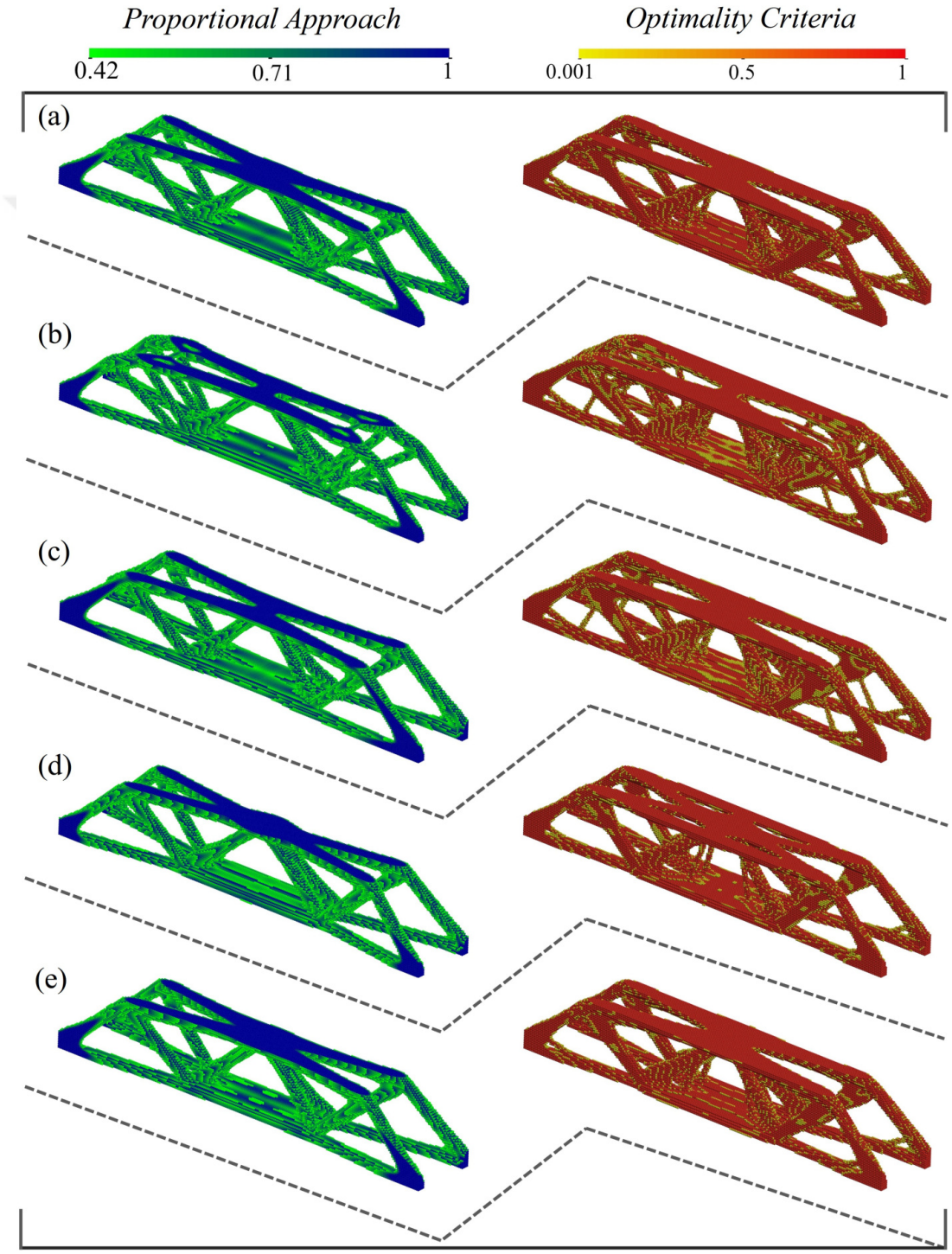
	FEM (reference)	PD	Difference (%)
OC	139.652	145.548	4.22
PROP	168.512	178.032	5.64

The results of the PD-TO approach are compared with that of FEM-TO, using both PROP and OC algorithms, for the problem without crack as shown in Figure 4.52. As revealed in the isometric and plane views the PD-TO and FEM-TO optimizers are considerably differentiated from each other in terms of their resulting geometries in both OC and PROP algorithms. Distinctly, FEM-TO exhibits more tendency to create sub-branches than PD-TO in both topology optimization methods. It can be noticed in the front views (Figure 4.52) that the number of the total support arms has approximately tripled and doubled in the FEM-PROP results and FEM-OC results, respectively.

Moreover, as seen in isometric and top views, PD-TO accumulates more material towards the center of the domain while FEM-TO endeavors to preserve the boundaries of long edges. Compliance results are listed and compared in Table 4.7. FEM-TO provides less strain energy and the PD-TO method results in considerably less geometrical complexity. Although the FEM-TO optimizer constructs more complex and intricate shapes with several supporting branches which are not favorable in manufacturing processes, the compliance difference between the two methods is not remarkable enough. Hence, it can be concluded that the PD-TO method would be a perfect alternative to the conventional FEM-TO method for the optimization of structures without cracks.

The optimal topologies of five cases obtained by PD-PROP (left column) and PD-OC (right column) are demonstrated in Figure 4.53. In general, it is seen that every single final topology is distinct from the others in terms of its geometrical features such as holes, support arms, etc. For example, it is observed that the OC method is more prone to branching than the PROP method. Evidently, only the fundamental thick support arms are encountered in the PROP results whereas the OC method brings about thinner sub-branches to support the main load-bearing arms. However, these thin sub-branches increase the complexity of the final geometry which may result in remarkable difficulty in manufacturing processes. On the other hand, both optimizers more or less construct the same structural skeleton as can be seen explicitly in the front-view comparison.

Figure 4.53 Optimal material distributions of the MBB-Beam obtained by PD-PROP (left column) and PD-OC (right column) for all the cases with/without cracks: (a) without crack; (b) parallel front and back cracks; (c) perpendicular front and back cracks; (d) parallel mid cracks; (e) perpendicular mid cracks. Note that, for PROP results, the colour scale contains green and blue colours to represent the minimum and maximum values of the design variables, respectively. For the results of OC, yellow corresponds to the minimum value of the design variable whereas red colour represents the solid material where the design variable of the particle is equal to 1.

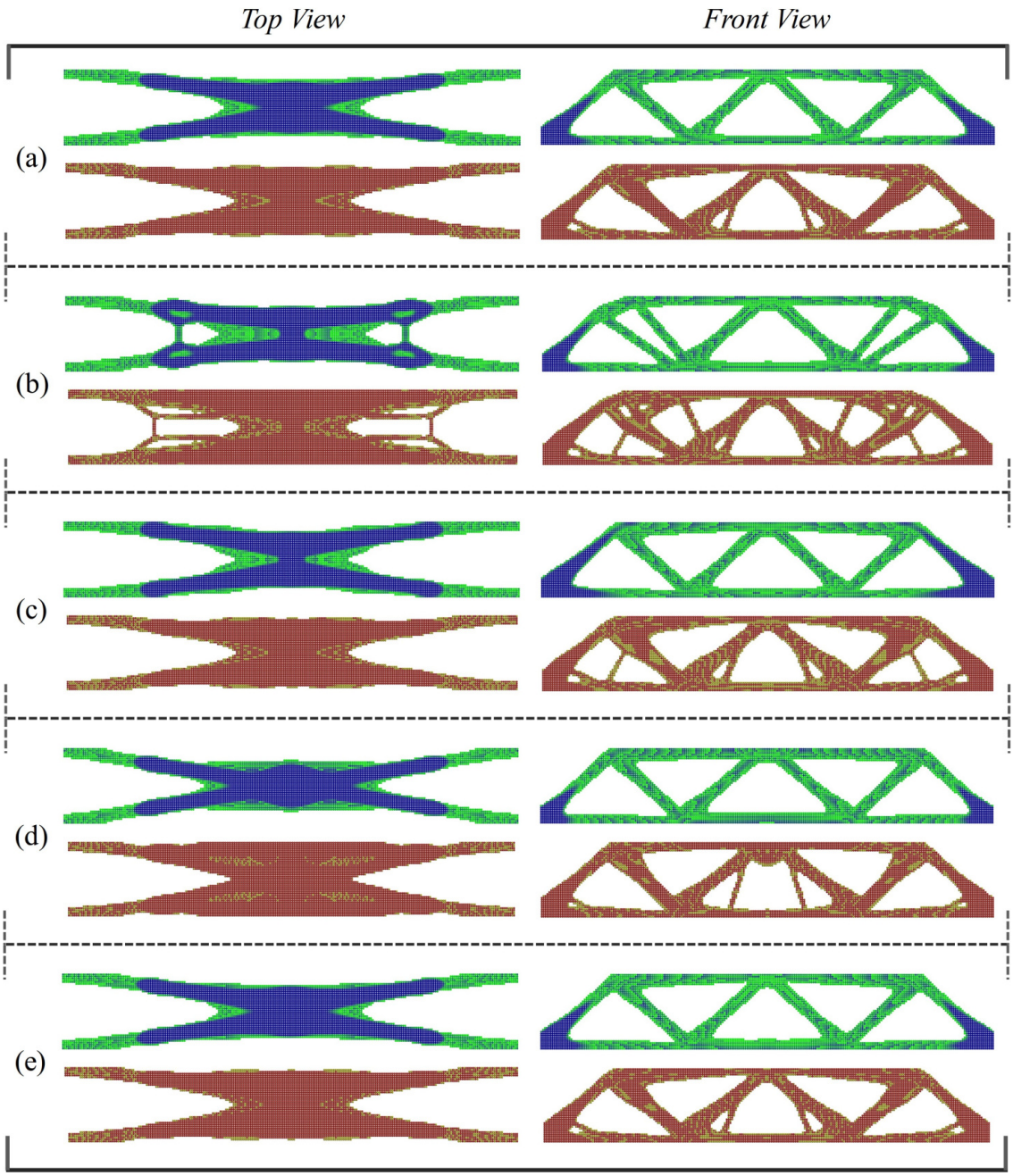


As can be seen in Figure 4.54, the PROP method created two support arms extending to the top region in the right and left faces of the structure, and the OC optimizer expanded the two-sided support arm to assist the same critical location which is close to the embedded surface cracks. Moreover, the other crack scenarios exhibit similar behavior between the two optimization methods.

Both optimizers showed a sensitive reaction to the crack involvement and these reactions should be explained clearly. For instance, in the case of parallel front and back cracks, Figure 4.53b depicts that both optimizers opened holes along the normal direction of the four individual cracks to prevent crack propagation. Therefore, the thickness of the structural element in this region is increased as compared to the crack-free condition. When we change the orientation of the cracks by rotating 90 degrees in the same location (perpendicular front and back cracks), the optimizer does not make a noticeable change around the crack this time as seen in Figure 4.53c. As we mentioned in Case I, the main reason could be the less displacement in the normal direction of the cracks which does not lead to propagation at the crack tips, and an increase in the strain energy in this region as much as parallel front-back cracks scenario.

Observing Figure 4.53e reveals that there is no significant effect on the crack edges as in Figure 4.53c, where the crack orientation is still perpendicular to the left and right faces. Nevertheless, the noticeable difference in material accumulation in the loading region proves that the crack location also affects the overall material distribution significantly. In the PROP results, the region in the center of the upper portion showed a tendency to spread toward the ends as the crack moved in the same direction. Moreover, OC results have shown a difference with a thin support involvement in Figure 4.54c as compared to Figure 4.54e. This sub-branching occurred in a region close to the crack in the longitudinal direction whereas mid-cracks do not yield any additional branches. Hence, the effect of crack location has been demonstrated even when the crack orientation is constant.

Figure 4.54 Top and front views of the optimal topologies: (a) without crack; (b) parallel front and back cracks; (c) parallel mid cracks; (d) parallel mid cracks; (e) perpendicular mid cracks. In each division in the figure, the first and second row represents the PROP and OC results of the relevant case, respectively.



When parallel mid cracks and perpendicular mid cracks cases are examined together, it is observed that OC opens holes in the vicinity of the parallel mid cracks (Figure 4.53d) to avoid crack propagation with a similar reaction as in Figure 4.53a. PROP instead, in the presence of parallel cracks, provided support to the mentioned region by material accumulation in the region close to the crack as shown in Fig. 18d.

However, in the case of perpendicular mid cracks (Figure 4.53e), there is no apparent change in the structure, resulting in almost the same geometry as the crack-free state. This could be caused by that the location of the cracks is already well-supported in the crack-free state, and perpendicular crack orientation does not cause crack opening and high strain energy concentration. Comparing the two parallel crack cases in Figures 4.53(b, d) which are more prone to crack propagation, shows that both optimizers pile up material around the crack regardless of their positions. It is conspicuous in the results of the OC method that the normal directions are cleaned out from materials at the same time the crack tips are strengthened with these materials. On the other hand, PROP distributed the materials in a different way by accumulating more material in the central region. One of the general dissimilarities between PD-OC and PD-PROP can be seen in Figures 4.53 and 4.54 that the PROP method tends to decrease the width by accumulating more material in the central regions along the y-axis while OC preserves the width of the top and bottom plates.

Figure 4.55 The compliance history of the MBB-Beam throughout the optimization process for each case where the red and blue lines refer to the compliance values obtained by PD-OC and PD-PROP, respectively. The initial few iterations, where the compliance values are extremely high, are not plotted in the figure to be able to compare the remaining part of the compliance values. For the sake of clarity, we zoomed into selected zones to show the exact standings.

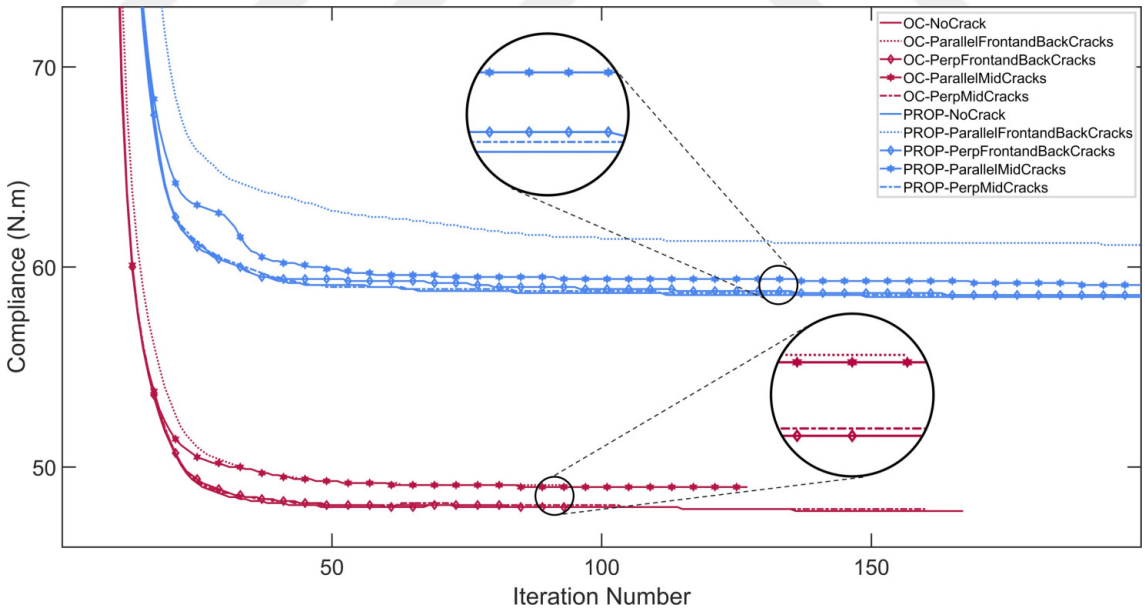


Figure 4.55 shows the comparison of compliance history between all cases and methods. Parallel front and back cracks led to the most compliant structure that supports the previous inference regarding crack location and orientation effects. Associated with it, we can state two significant reasons: parallel crack is more prone to crack

propagation and front-back locations are farther to applied force than mid-cracks. Furthermore, the parallel mid cracks condition is the second-highest scenario among them. Hence, it can be concluded that orientation is the dominant parameter causing more compliance as compared to the location for such a problem. In addition to crack-based comparisons, when we make a method-based comparison, it is obvious from Figure 4.55 that OC provides better topologies in terms of compliance which is the objective function of our optimization problem. The total strain energy values of the PROP results are between 58.5 - 61.1 Nm while the OC method provided less energy in the range of 47.8 - 49.1 Nm considering all the scenarios. Calculating the average difference between the final compliances of PROP-PD and OC-PD indicated that the topologies obtained by OC are stiffer about 20% than those created by PROP.

4.2.4 Dynamic Analyses for the Assessment of Fracture Toughness Enhancement

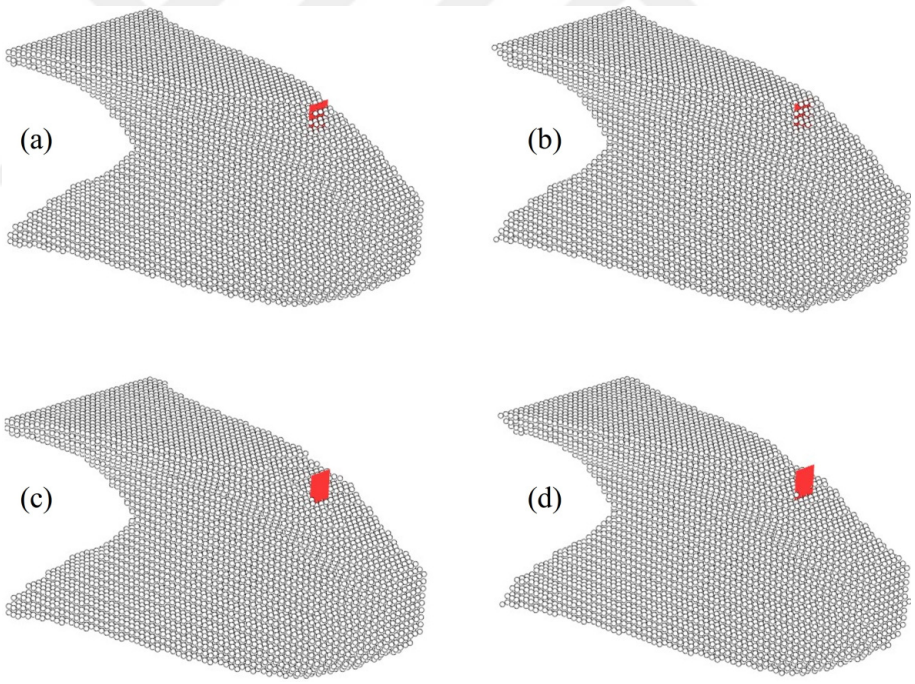
4.2.4.1 Dynamic Analysis Setup

In the previous section, two benchmark geometries have been optimized for various crack locations to assess the effect of the crack numbers/locations and alignments utilizing the proposed PD-TO methods. The final shapes are compared with each other mostly in their shapes under static loading conditions. However, one may desire to know the dynamic behaviour of these structures where the major concern is crack modelling. Therefore, we here conduct a comparison study between the final topologies under the same dynamic loads. This comparison would be effective to reveal whether the fracture toughness of the geometry is increased in the cracked region or not. For the dynamic analysis, we apply the displacement boundary condition to the loading points defined in the previous section for the cantilever beam and hanger problem. The loading points have a velocity of $v = 2m/s$ in the negative z-direction for both problems. The size of a time step is calculated as $dt = 6.53e-6s$, and $dt = 4.90e-7s$ using Equation 3.39 for the cantilever beam and hanger geometries, respectively. Additionally, critical stretch values are determined by Equation 3.37.

4.2.4.2 Comparison Strategies

We determine two different strategies for the comparison of the dynamic behaviour of the optimized structures. The first strategy is the initiation of the crack as defined in Section 4.2.3.1. After that, the structures obtained for the case of with and without cracks are analysed under dynamic load. Here, we selected the front crack for crack initiation and compare the dynamic behaviour and damage patterns of the structure. To be clear, Figures 4.56(a, b) represent the placement of the front crack into the optimized topologies without an initial crack for OC and PROP, respectively. Moreover, in Figures 4.56(c, d), we consider the topologies optimized with the pre-defined front crack and embed this crack into these topologies for dynamic analysis.

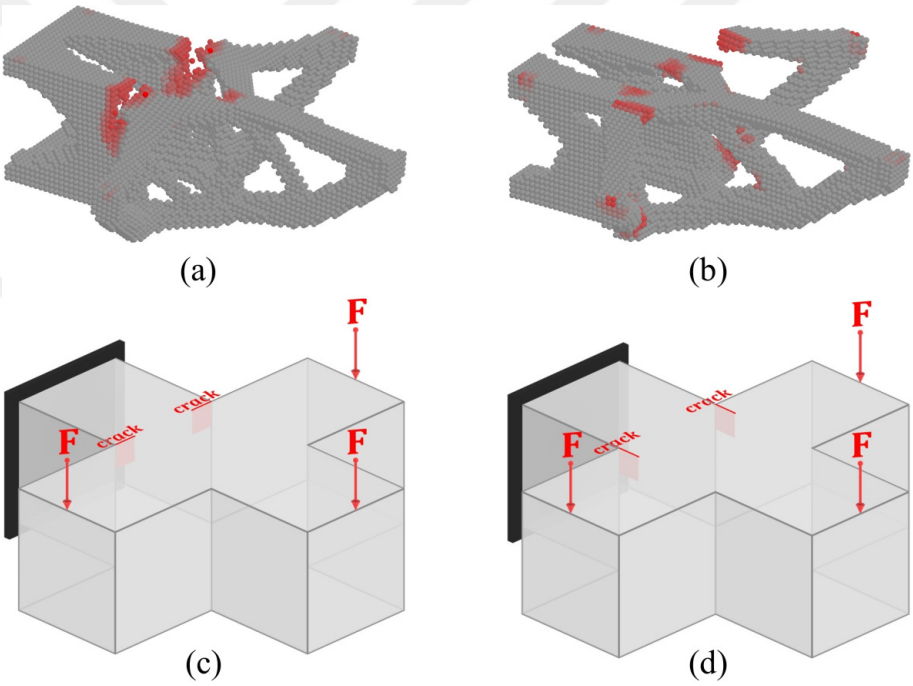
Figure 4.56 The structures utilized in dynamic analysis correspond to the results of (a) OC-without crack (b) PROP-without crack (c) OC-front crack (d) PROP-front crack. Note that, the relevant bonds are broken to introduce the front crack in the given domain before the dynamic load is applied.



For the second strategy, we perform dynamic analysis for a topology without initiating any discontinuities in the structure. An optimized structure is first dynamically loaded until it is broken thus the fracture pattern can be tracked. Hence, the knowledge of possible cracked regions because of operating conditions can be achieved. The following stage herein is to initiate necessary cracks in the initial domain into the regions where the fracture begins. Then, the structure containing these cracks should be re-optimized by the PD-TO methods. Thereafter, the dynamic behaviour

of the initial topology (once optimized) and re-optimized topology (optimized considering possible cracks) can be widely compared to search the fracture toughness enhancement. In this regard, we employ the second strategy on the hanger geometry as depicted in Figure 4.57. Here, Figures 4.57(a, b) show the fracture patterns of the optimized topologies (without crack) of OC-TO and PROP-TO, respectively, which are obtained under dynamic load. Then, we determine the possible crack regions from Figures 4.57(a, b). Finally, the new cracks are embedded in these locations for the next optimization. In this respect, Figures 4.57(c, d) depict the design domain with possible cracks for the second optimization to strengthen the critical regions by the proposed TO methods.

Figure 4.57 Fracture patterns obtained for the topologies of (a) OC-without crack, and (b) PROP-without crack under dynamic load. Observing the patterns, new cracks are embedded in the initial design domain in (c) and (d) for OC and PROP, respectively.

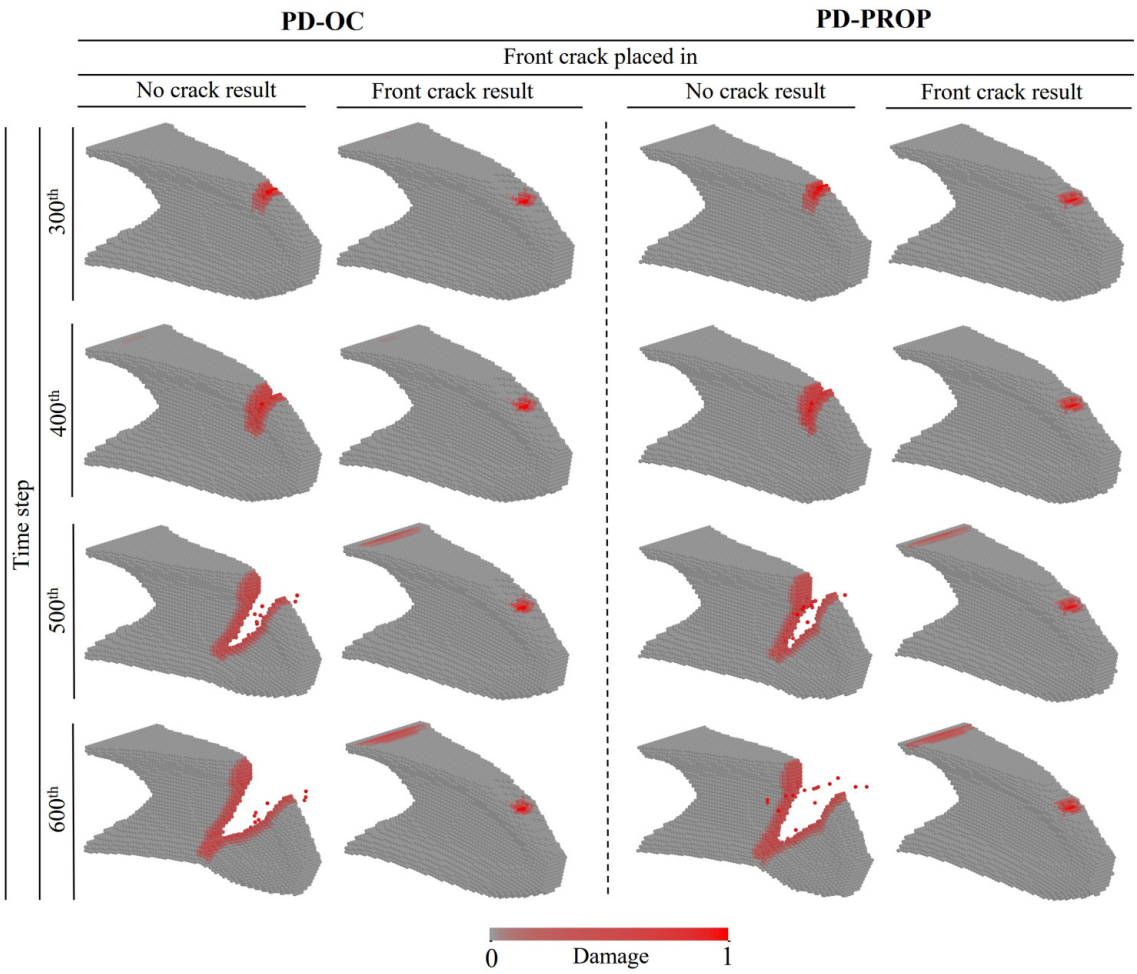


4.2.4.3 Numerical Results: Dynamic Behaviour of the Optimized Structures

After applying dynamic load to the structures for the first strategy, some of the critical time steps (300^{th}, 400^{th}, 500^{th}, 600^{th}) of the analyses are captured to compare the fracture behaviour. In this context, damage contours are given for the selected

instants as shown in Figure 4.58. It can be concluded from Figure 4.58 that both optimizers generate more resistant topologies in the existence of an induced crack in the structure. There is no crack propagation in the front crack results at the parallel time steps (Figure 4.58). It is expected that the crack will propagate after a certain amount of time under the increasing load. Eventually, critical damage accumulation started about the 700^{th} time step as shown in Figure 4.59. This figure shows the maximum total displacement values with respect to the time step.

Figure 4.58 Damage plots at the certain time steps for different optimized PD-OC-TO and PD-PROP-TO results during dynamic PD analysis. Note that total displacements are also reflected in these pictures by the magnification factor of 50.



In Figure 4.59, the displacement regime is linear up to the instant when crack propagation starts. The separation of the material points in the damaged region can be observed as highlighted by zoomed pictures. Moreover, the maximum displacement values of the structures right before the crack propagates are compared to evaluate the load-bearing capacity of the structures. These displacement values right before

the failure are listed in Table 4.8. It is shown that the structures optimized considering the induced crack can deform 85% and 80% more before it fails with PD-OC and PD-PROP, respectively, which can be attributed to the enhanced fracture toughness under the same loading.

Table 4.8 Maximum displacements on cantilever beam just before the crack propagates.

Case	PD-OC-TO		PD-PROP-TO	
	No crack	Front crack	No crack	Front crack
Max disp. (mm)	4.894	9.067	4.897	8.839
Difference (%)	85.27		80.5	

In the second strategy, the demonstrated cracks (Figures 4.57c, d) are embedded in the initial domain for re-optimization. The resultant topologies after the second optimization are tested under the same load, and their dynamic behaviour is depicted in Figure 4.60 together with the results of the initial scenario without crack. As clearly shown in the figure, re-optimized geometries by considering the critical regions become more resilient to breakage. According to damage contours, the re-optimized PD-OC result shows the best performance as compared to the others in the given time interval (Figure 4.60). In addition, PD-PROP brings an improvement in the critical region but fails in another region. Nevertheless, both methods lead to a delay in the failure time when we introduce a crack in a critical region.

The maximum displacement values of the optimized topologies are compared in Figure 4.61 where the failed points are demonstrated in zoomed pictures. It is observed that more resistant structures can be achieved by considering the cracks in critical regions at the optimization stage. Another observation is that the PD-OC reacts more sensitively and produces better results relative to PD-PROP in the context of fracture toughness. Furthermore, the maximum total displacements of the structures just before they fail are compared in Table 4.9. As a result, PD-OC increased the maximum displacement that the structure can resist by 9.24%. The improvement provided by PD-PROP is 7.16% which is relatively lower than what PD-OC offers. Consequently, it is strongly proved that the proposed TO methods would achieve better designs to bear more load.

Figure 4.59 Maximum displacements for cantilever beam during dynamic analysis. The starting point of crack propagation is clarified by showing up the status of critical regions at relevant time steps.

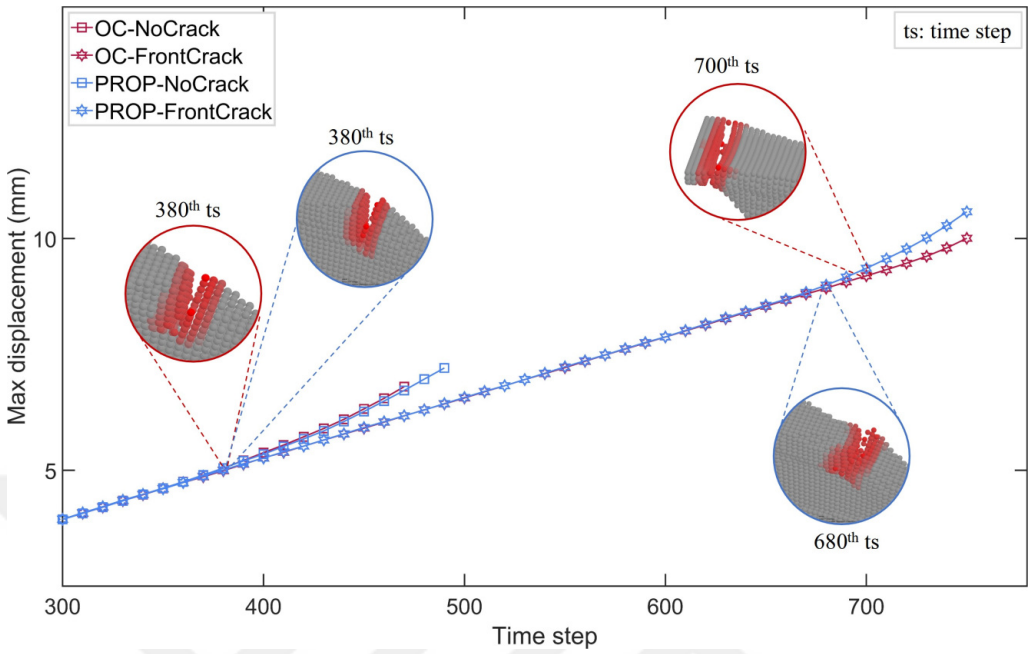


Figure 4.60 Damage plots at the certain time steps for different optimized PD-OC-TO and PD-PROP-TO results during dynamic PD analysis. Note that total displacements are also reflected in these pictures by the magnification factor of 10.

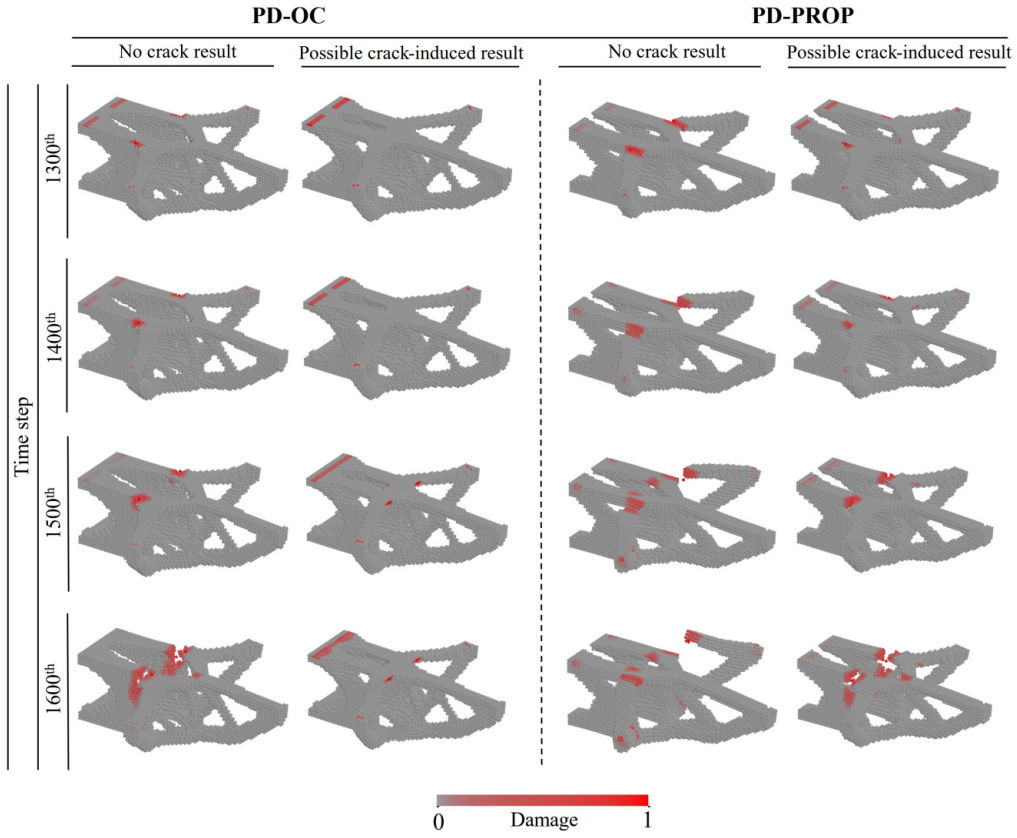


Figure 4.61 Maximum displacements for the hanger during dynamic analysis. The starting point of crack propagation is clarified by showing up the status of critical regions at relevant time steps.

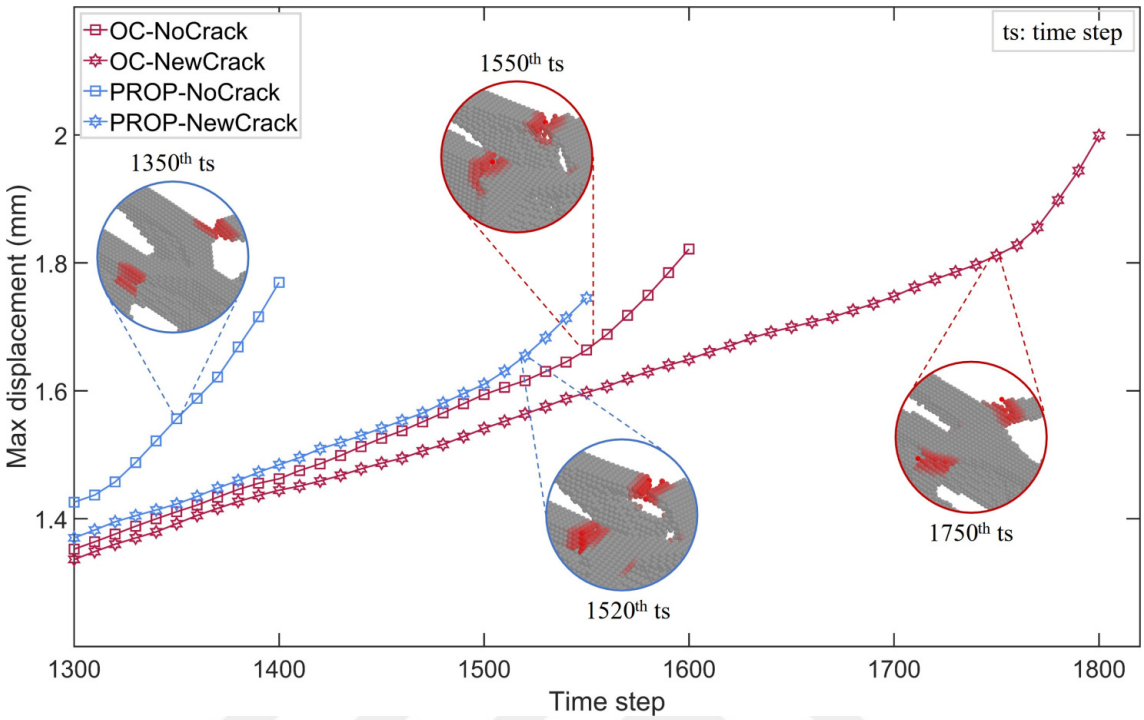


Table 4.9 Maximum displacements on hanger beam just before the crack propagates.

Case	PD-OC-TO		PD-PROP-TO	
	No crack	Front crack	No crack	Front crack
Max disp. (mm)	1.645	1.797	1.522	1.631
Difference (%)	9.24		7.16	

4.2.5 Concluding Remarks

In this research effort, two novel three-dimensional topology optimization methods named PD-OC-TO and PD-PROP-TO are developed for the optimization of structures containing defects. In addition, we present a novel strategy for enhancing the fracture toughness of the topologically optimized structures utilizing the proposed TO methods. Two different benchmark problems are optimized to demonstrate their capabilities. Moreover, various crack locations, numbers, and alignment options are created to investigate the effect of cracking scenarios on the optimized geometries.

Accordingly, two main concluding remarks are obtained:

- The final geometries obtained by PD-OC, and PD-PROP methods for all the scenarios are examined comprehensively. Although both methods show improvement in the optimized results to avoid crack propagation, it is revealed that the OC method is more sensitive to structural discontinuities and PROP creates fewer subbranches between the main support arms.
- The performance of the PD-TO methods in fracture toughness enhancement is investigated. In this regard, the damage contours and fracture patterns of the optimized geometries are compared at certain time steps under dynamic load. These comparisons revealed that the suggested methods would produce superior designs that could support a greater load than the initial TO results by just embedding hypothetical (predicted by simulations) cracks into the regions that are determined to be critical under dynamic loading.

Overall, it is proved that the proposed methods are favourable and practical to be utilized in the lightweight design of various engineering structures. For instance, the defects caused by the thermal-residual stresses during additive manufacturing processes could be modelled by these methods to avoid failures. Moreover, observing the fracture patterns that happen in the operating period of the critical engineering parts would be essential inputs. Hence, these methods would enable a designer to enhance the fracture toughness of the relevant structures through optimized designs. Albeit being generally applicable to many design/optimization problems, the proposed PD-TO methods involve several limitations for specific applications. These can be potentially addressed in future studies. First, the current PD-TO algorithm is based on bond-based formulation, which restricts the Poisson ratio of material to 0.25. This limitation can be addressed by ordinary state-based formulation for the TO problems that Poisson's ratio plays a critical role. Another drawback can be attributed to the uniform particle discretization of the PD-TO, which can be resolved by employing dual horizon peridynamics (DH-PD) in the TO process. This would reduce the computational cost of the present method in optimizing complex geometry with intricate shapes such as holes.

4.3 Enhanced Ship Cross-Section Design Methodology Using Peridynamics Topology Optimization

4.3.1 Introduction

In this section, peridynamics topology optimization (PD-TO) framework is implemented to reduce the total weight of ship structures and increase their structural endurance against cracks. PD-TO is a general nonlocal optimization strategy that performs the minimization of strain energy density as the objective function and uses predefined volume fractions as optimization constraints. To analyze ship structures herein, both the optimality criteria (OC) algorithm and the proportional (PROP) approach are implemented into the PD-TO solver. As the initial design domain, a reference bulkhead geometry of trailing suction hopper dredger (ship) is modeled. This web frame is optimized according to critical wave/loading conditions such as hogging and sagging. Different volume fractions are investigated to obtain lighter designs based on OC and PROP methods. In addition, different cracked scenarios are created by locating the cracks into various positions on the reference ship cross-section. Optimized results for cracked cases shows that the proposed method can create alternative web frames for specific definitions of the possible damaged regions on the board. To prove the efficiency of the proposed method, maximum displacements and compliance of the reference and optimized structures are compared. The results proves that topologically optimized designs offered stiffer structures as compared to conventional designs under the same loading conditions. Finally, some of the optimized results are smoothed to demonstrate the practical utility of the PD-TO for manufacturing. Overall, it is revealed that the PD-TO can be effectively utilized to design marine structures to achieve a higher strength/weight ratio while considering critical operation conditions and possible damaged regions. The provided results in this section is published in the journal of Ocean Engineering (Kendibilir & Kefal (2023a)).

4.3.2 Novelty and Motivation

Albeit its pronounced popularity in other engineering fields, the current state of the art for the design of marine structures includes only a few studies regarding the use of topology optimization methods, i.e., either FEM or PD-based algorithms. For example, Tian, Wang, Liu, Liu, Xie & Deng (2019) utilized the FEM-based MMA topology optimization method for the lightweight design of an offshore jacket platform. Moreover, they applied similar methodologies to the jacket support structure of wind turbines and jack-up platform legs (Tian, Sun, Liu, Deng, Wang, Li & Li (2022), Tian, Wang, Liu, Liu, Deng, Xie & Wang (2022)). According to the results, the optimized leg structure has a higher bearing capacity to support the entire offshore weight while withstanding the external wind and wave loads. Furthermore, Jia & Li (2019) presented the FEM-based topology optimization of a trimaran bulkhead reinforcement. Then, the authors (Jia, Li, Zhang & Li (2019)) applied different loading conditions to bulkhead geometry and optimized the selected area using various volume retention ratios. Besides, Katsuno, Dantas & Silva (2022) utilized the topology optimization based on FEM for identifying the critical regions that need to be surface treated for higher propeller efficiency. In addition, Lu, Long, Zhang, Zhang & Tao (2023) introduced a novel design strategy based on finite element topology optimization for creating a lightweight wind turbine tripod structure with the highest strength.

Most recently, Kendibilir & Kefal (2023b) have applied the PD-TO methodology (i.e., based on the OC method) to investigate the lightweight design of marine structural parts subjected to a basic loading condition. To the authors' best knowledge, there is no detailed study available in the literature regarding topology optimization of marine structures based on non-local mechanics formulation (e.g., peridynamics). Moreover, the study of Kendibilir & Kefal (2023b) did not examine the effect of multiple crack scenarios under critical wave/loading states such as hogging and sagging loads during topological optimization. To address this gap in the literature, there is an urgent need to propose a general application of the PD-TO framework for marine structures by considering different volume constraints, loading conditions, possible crack positions, and optimization algorithms. Hence, the main and novel aim of this study is to develop an effective design methodology based on the PD-TO framework coupled with OC and PROP algorithms for topology optimization of ship cross-sections in case of multiple crack scenarios under critical wave loads.

The remainder of this section is as follows. The problem definition of the selected ship part and its PD model are specified in Section 4.3.3. Topology optimization

results are comprehensively discussed in Section 4.3.4. Major concluding remarks on the current study and recommendations for future studies are given in Section 4.3.5.

4.3.3 Problem Definition and Design Model

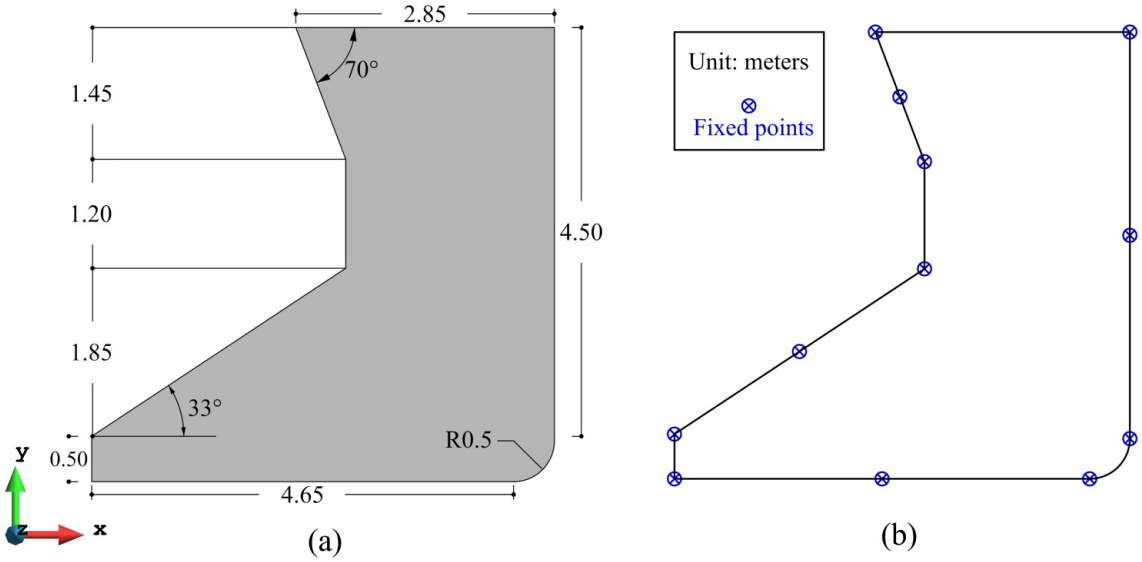
In this section, the design domain of the optimization problem with the relevant constraint and loading conditions is introduced. Moreover, optimization parameters and the PD model are explained in detail.

4.3.3.1 Initial Bulkhead Geometry

Bulkheads are the transverse partition elements in the marine structures for dividing the ship into smaller watertight compartments. Naturally, these plates are designed fully filled to satisfy watertight conditions. However, there are also repeating web frames between the bulkheads which are designed with holes for specific reasons such as inspection and ballast storage. In this study, we selected a reference TSHD (trailing suction hopper dredger) bulkhead geometry as an initial design domain and optimized this geometry to create lighter and stiffer web frames than the conventional one (Vuijk (2020)).

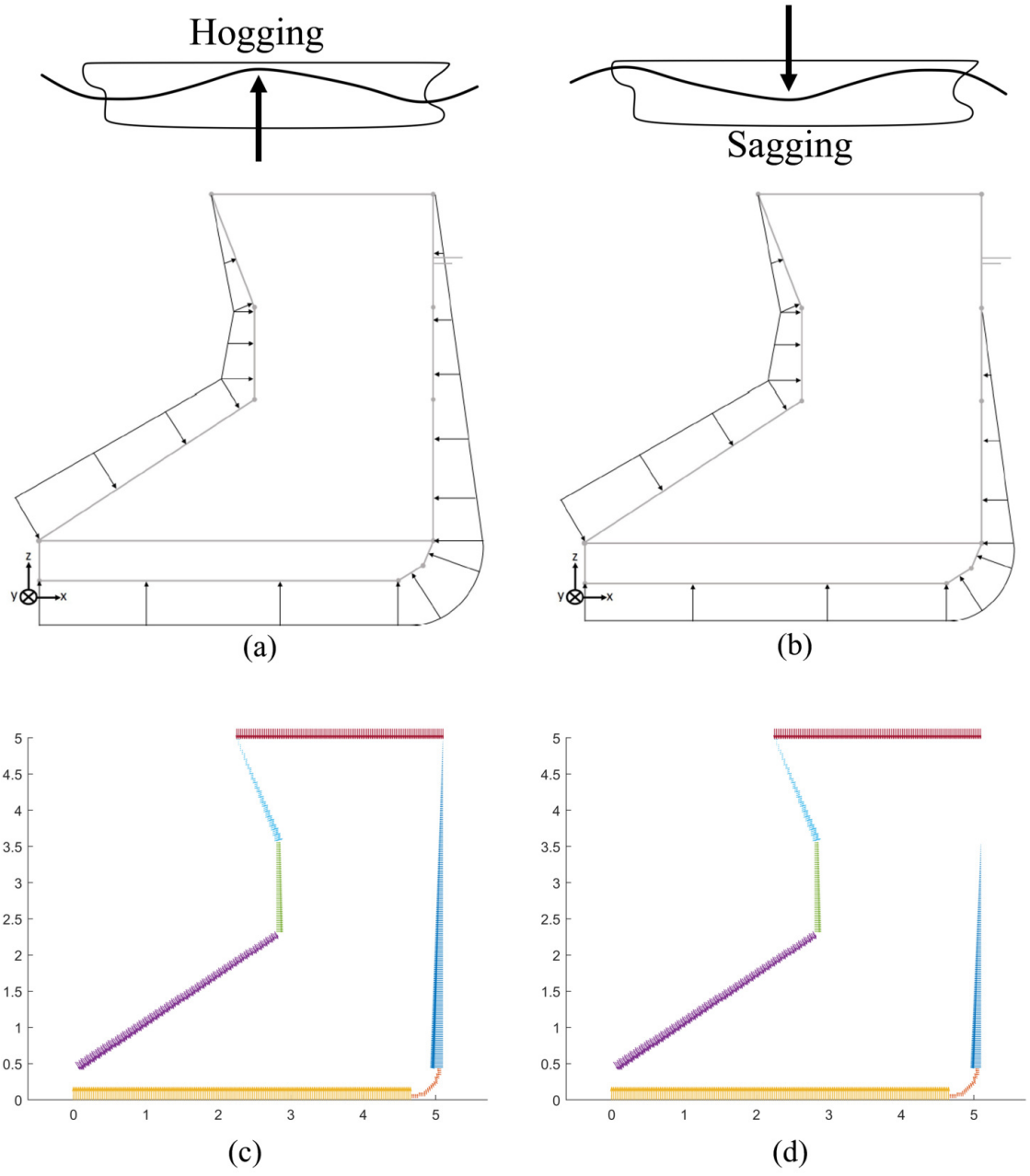
The problem geometry is given with the dimensions in Figure 4.62a. Also, the fixed regions are shown in Figure 4.62b. Constrained locations are determined by considering the points where the longitudinal frames are mainly located according to classification rules to support hull rigidity. As can be seen from Figure 4.62, the bulkhead is a large-scale component of the ship with the highest dimensions of 4.7 m and 5.0 m along the x and y axes, respectively.

Figure 4.62 Problem definition with (a) dimensions of the initial design domain of a reference bulkhead; (b) location of the fixed points in the structures.



The external loads are applied for two different conditions namely hogging and sagging conditions where the shipboard faces different wave profiles. Note that, since the magnitude of the force is not changing the topology, the magnitude of the loads is generic and proportional to each other for providing the hogging and sagging conditions. Accordingly, Figure 4.63(a, b) depict the loads acting on the shipboard and inner walls of the bulkhead for hogging and sagging, respectively. These loads are applied to the relevant PD particles as body force. For clarity, applied forces with respect to positions are shown in Figure 4.63(c, d) where the largest force magnitude is selected as 10 N. It is important to note that we also applied a distributed load on the deck by considering the cranes located on the deck of dredging vessels (Figures 4.63c, d).

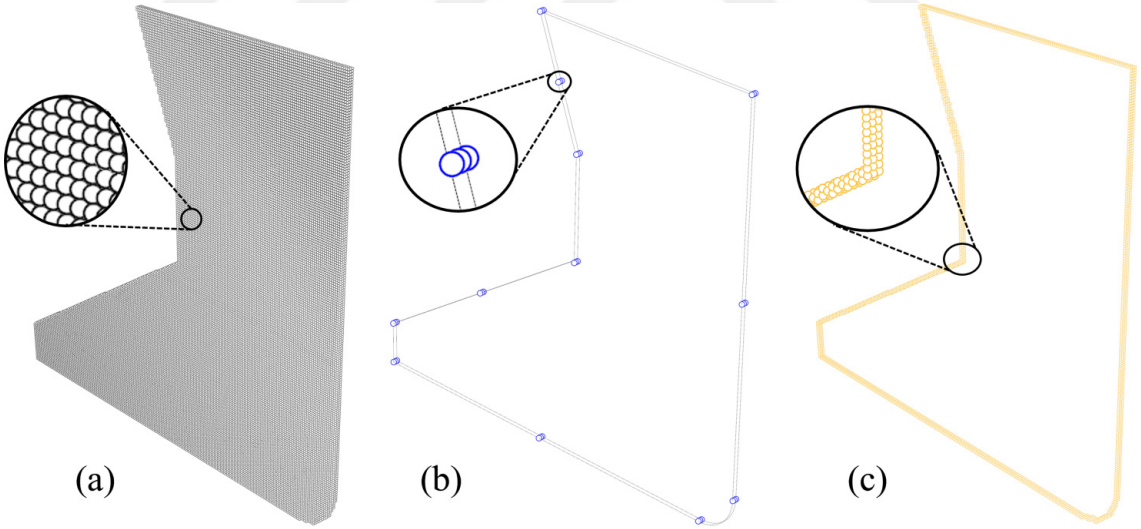
Figure 4.63 Representation of different loading conditions; (a) Typical illustration of hogging condition: wave crest amidships; (b) Typical illustration of sagging condition: wave through amidships, (c) Distribution of force vectors acting on PD particles for hogging condition, (d) Distribution of force vectors acting on PD particles for sagging condition.



4.3.3.2 PD Model and Optimization Parameters

The bulkhead geometry is discretized by 77100 uniformly distributed PD particles which yields the particle spacing of $dx = 0.025m$ in the PD model. Here, there are three particles used in the thickness direction (z-axis) of the model, thus the bulkhead has a total thickness of 75 mm. The total thickness of the bulkhead is just a representative value for satisfying the 2D plane stress condition of the mechanical analysis, thus it can be altered for the manufacturing purpose at the posteriori stage. The fine discretization of the PD model is shown in Figure 4.64a. The boundary condition is employed for the relevant particles that are shown in Figure 4.64b by restricting their displacements. Moreover, we defined the bounding frame of the design domain as passive points during the optimization to keep material continuity in the shipboard (Figure 4.64c). In all PD-TO analyses, the minimum filter radius is set to $R_{min} = 3dx$. Four different volume fractions: 30%, 40%, 50%, and 60%, are defined to compare the effect of target volume on the optimum topology.

Figure 4.64 (a) Particle based PD model of the design domain as a point cloud; (b) fixed PD particles to employ the boundary conditions; (c) passive particles which bound the design domain.

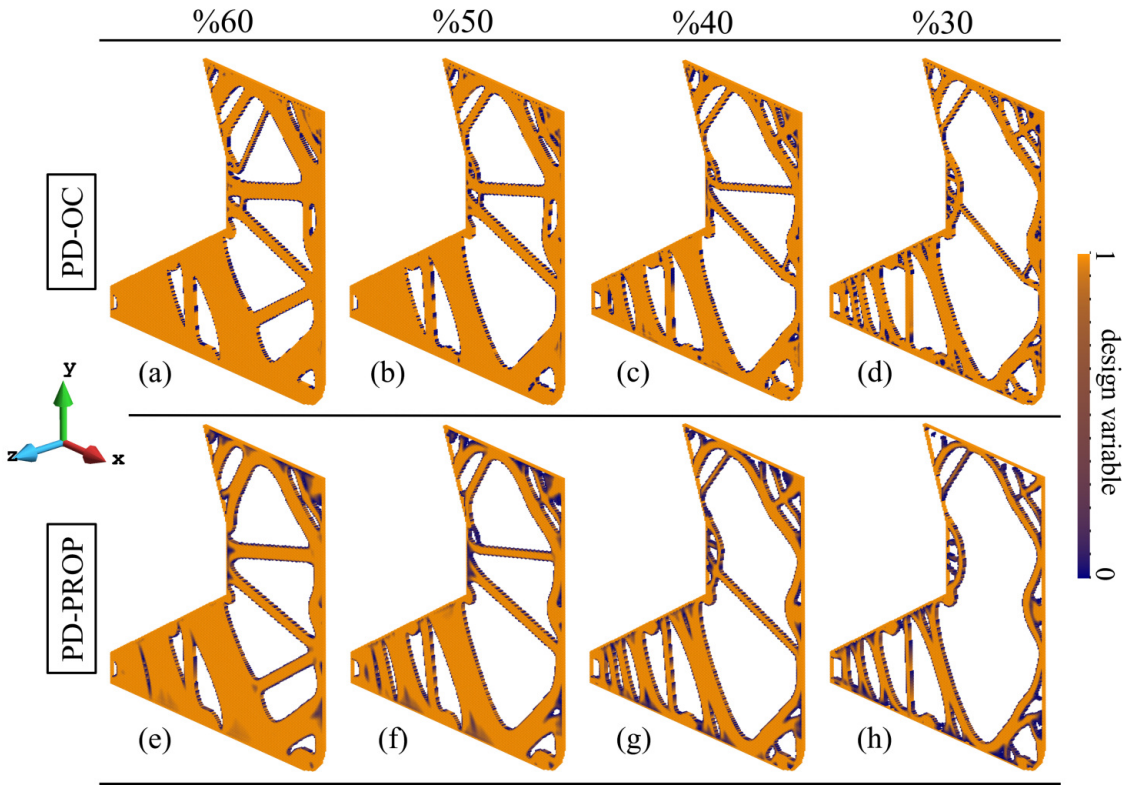


4.3.4 Results and Discussions

4.3.4.1 Optimum Results for Hogging and Sagging Conditions using PD-PROP and PD-OC Methods

In this section, we present the final topologies obtained for the bulkhead design problem by considering two different critical loading conditions, i.e., hogging and sagging. Firstly, Figure 4.65 presents all the results generated by both TO methods for hogging conditions. As can be seen from this figure, the optimum layouts obtained by PD-OC and PD-PROP methods are almost analogous except for slight differences in the local regions of the supports.

Figure 4.65 Isometric view of the final topologies under hogging condition. Four different volume fractions are considered by PD-OC (a, b, c, and d) and PD-PROP (e, f, g, and h).

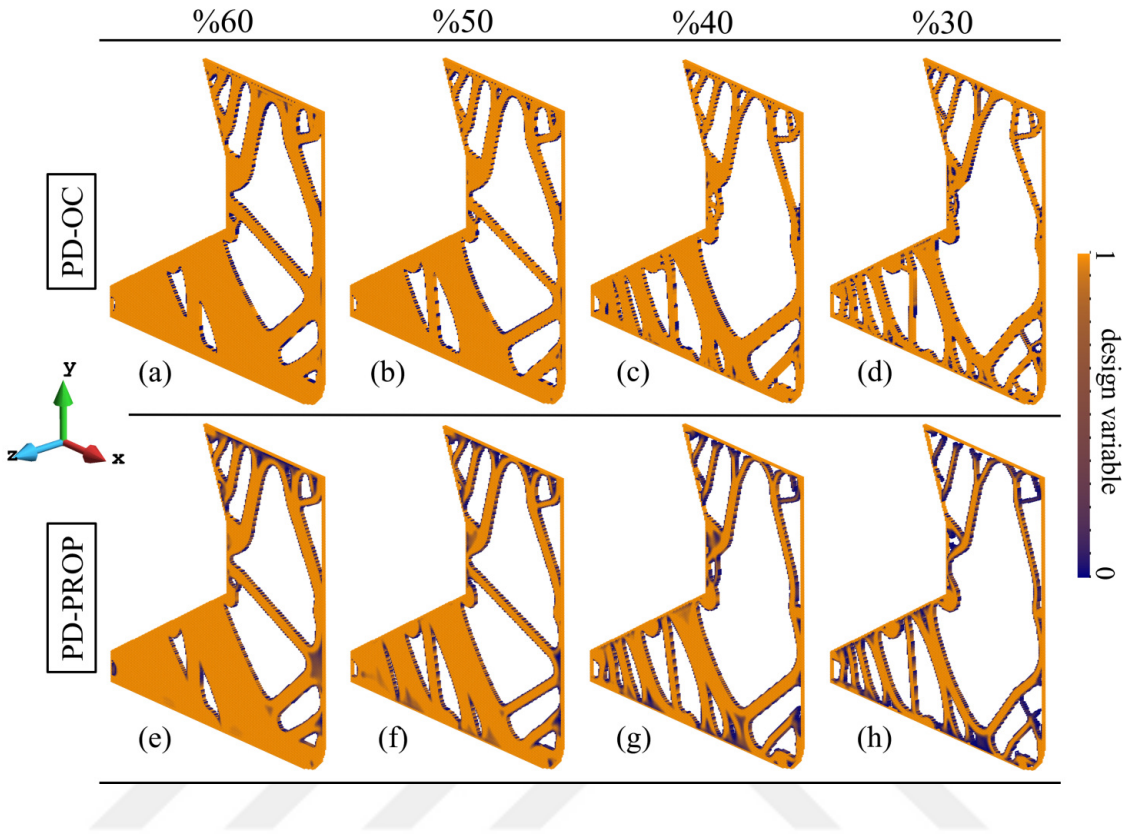


Moreover, the transition of the material density variable has shown a little bit of difference between the two methods in the way that PD-OC results showed a

sharper variance between void and solid materials whereas PD-PROP results offered a smooth transition. The reason for this difference is due to the mathematical background of these methods. In the material density value updating process, the PD-PROP method distributes the whole total material proportionally to the whole design domain which yields to continuous transition. Once the final topologies are obtained, the critical and common frames are observed by varying target volume scenarios. Additionally, it is investigated that the total number of complex and tiny holes is very high which is a negative effect of TO results on the manufacturability of the offered designs. Therefore, these results need to be post-processed (smoothed) to create reliable (high strength) and easily manufacturable geometries.

Moreover, the final topologies for the sagging condition are illustrated in Figure 4.66. Comparison of Figures 4.65 and 4.66 reveal the main differences between the web-frame designs for hogging and sagging conditions. Like the previous loading case, the results of PD-PROP and PD-OC are very close to each other for sagging condition. Moreover, the number of holes between the support arms is still relatively high. From the sagging load results, it can be deduced that there is no need for support in the top portion of the right side. However, the hogging load results in an inclined support arm towards the left to the right side of the design domain (Figure 4.65) to decrease the displacement due to the wave load acting on the highest level of the draft. There is no load in the right-top portion of the shipboard in the sagging condition. Therefore, materials are allocated to create support for the deck side instead of creating supports in the righttop part of the design domain. This variation can be considered one of the major differences between the results of hogging and sagging conditions.

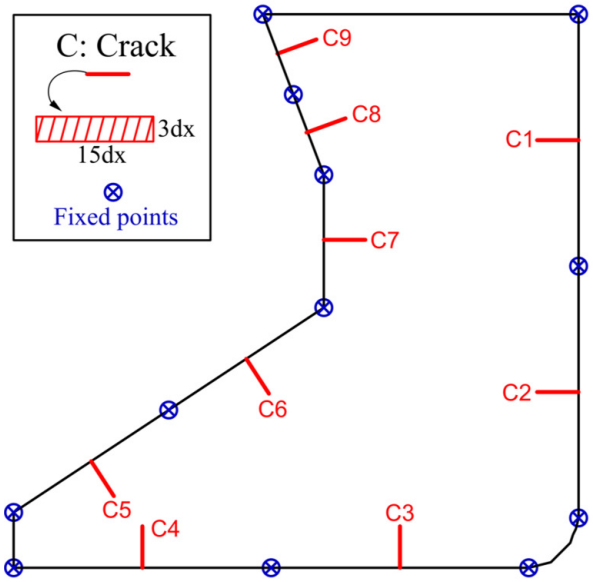
Figure 4.66 Isometric view of the final topologies under sagging condition. Four different volume fractions are considered by PD-OC (a, b, c and d) and PD-PROP (e, f, g, and h).



4.3.4.2 Alternative Optimum Designs for Different Damaged Scenarios

In this section, we will focus on topology optimization of the bulkhead with structural defects/damages. To this end, we add several cracks at different locations of the bulkhead and examine the effect of the number and location of the cracks on the optimum topology. The locations of the possible cracks are shown in Figure 4.67a, where the centers of the unsupported lengths (between constraints) are selected intentionally for positioning the cracks since maximum local deformations are expected therein. In Figure 4.67b, a table is given to classify each multiple crack case for the topology optimization study of the bulkhead.

Figure 4.67 (a) Crack dimension and positions in the design domain; (b) List of the cracked scenarios with relevant crack numbers which are included in the design domain.



(a)

Case No	Cracks included
1	C1, C2
2	C3, C4
3	C5, C6
4	C7
5	C8, C9
6	C1, C2, C3, C4
7	C5, C6, C7, C8, C9
8	All

(b)

In Section 4.3.4.1, ship frame optimization is performed using both PD-OC and PD-PROP methods for two different loading conditions and four different volume fractions. Accordingly, two different methods give rise to similar optimum designs, so we run the analysis herein using the PDOC method only. For conciseness, only the value of 0.4 is considered as the volume constraint. In addition, analyses are conducted only for the hogging condition since it creates a larger load capacity for the design according to the previous results.

The final topologies of the bulkhead for the eight different damage scenarios are presented in Figure 4.68. The reference (no crack) design in Figure 4.68a is given to better observe the differences between the intact condition and alternative designs of the damaged condition. For clarity, these major differences in the optimum topologies of the bulkhead with cracks are marked with circles as illustrated in Figures 4.68(b–i). In these figures, it has been observed that the location and number of cracks cause the topology to evolve differently over the proposed approach. New or alternative support arms and material accumulations are observed in the cracked region to prevent the propagation or further nucleation of cracks in critical regions. This is due to minimizing potential strain energy caused by deformations in the cracked regions. Such physical outcomes agree well with our previous observations for different engineering structures with/without cracks (Kefal et al. (2019),

Kendibilir et al. (2022)). Hence, if the most critical fracture positions or hot spot stress regions are known (either from finite element simulations or classification rules) and used as input to the PD-OC method, one can optimize the topology of bulkheads at the preliminary structural design stage to support them against cracking on pre-defined positions.

4.3.4.3 Final Designs after Smoothing Process

In previous sections, the optimized results of the topologies of structures for undamaged and damaged cases are shown by using only point cloud representations. However, direct manufacturing of these topologies may be difficult due to the intricate shapes available in the optimum designs, therefore, it is always recommended to perform smoothing of these geometries to increase their manufacturability. In this regard, we apply a posteriori smoothing process to the designs obtained with volume constraints of 0.4 and 0.5 under hogging loading. Then, in the next step (Section 4.3.4.4), we will compare them with the reference web-frame design. The main aim of the smoothing process is to reveal the most meaningful (manufacturable) structure from the point cloud provided by the mathematical algorithm. Hence, this hybrid process can prevent stress concentration that may arise from sharp edges and maximize the manufacturability of the bulkheads.

The smoothing processes of the PD-TO results for the undamaged (no crack) condition of the bulkhead with the 0.4 and 0.5 vol constraints under hogging loads are depicted in Figures 4.69(a, b) and 4.69(d, e), respectively. In other words, the smoothed optimum topologies that can be comparable with a conventional web-frame design (i.e., obtained from classification rules) are provided in Figures 4.69b and 4.69e for volume fractions of 40% and 50%, in the given order. As seen from these figures, the holes located very close to the edges of the structure are moved to the inner parts of the bulkhead. Similarly, the small adjacent holes are combined as a single hole. In addition, small gaps near the large support elements are removed for convenience in production. As a result, while structures are smoothed to contain the least possible number of holes and features, gaps are effectively re-designed to eliminate sharp-edged corners.

Figure 4.68 (a) Initial optimum design without crack; Alternative designs and diversified regions for various cracked scenarios: (b) Case 1; (c) Case 2; (d) Case 3; (e) Case 4; (f) Case 5; (g) Case 6; (h) Case 7; (i) Case 8.

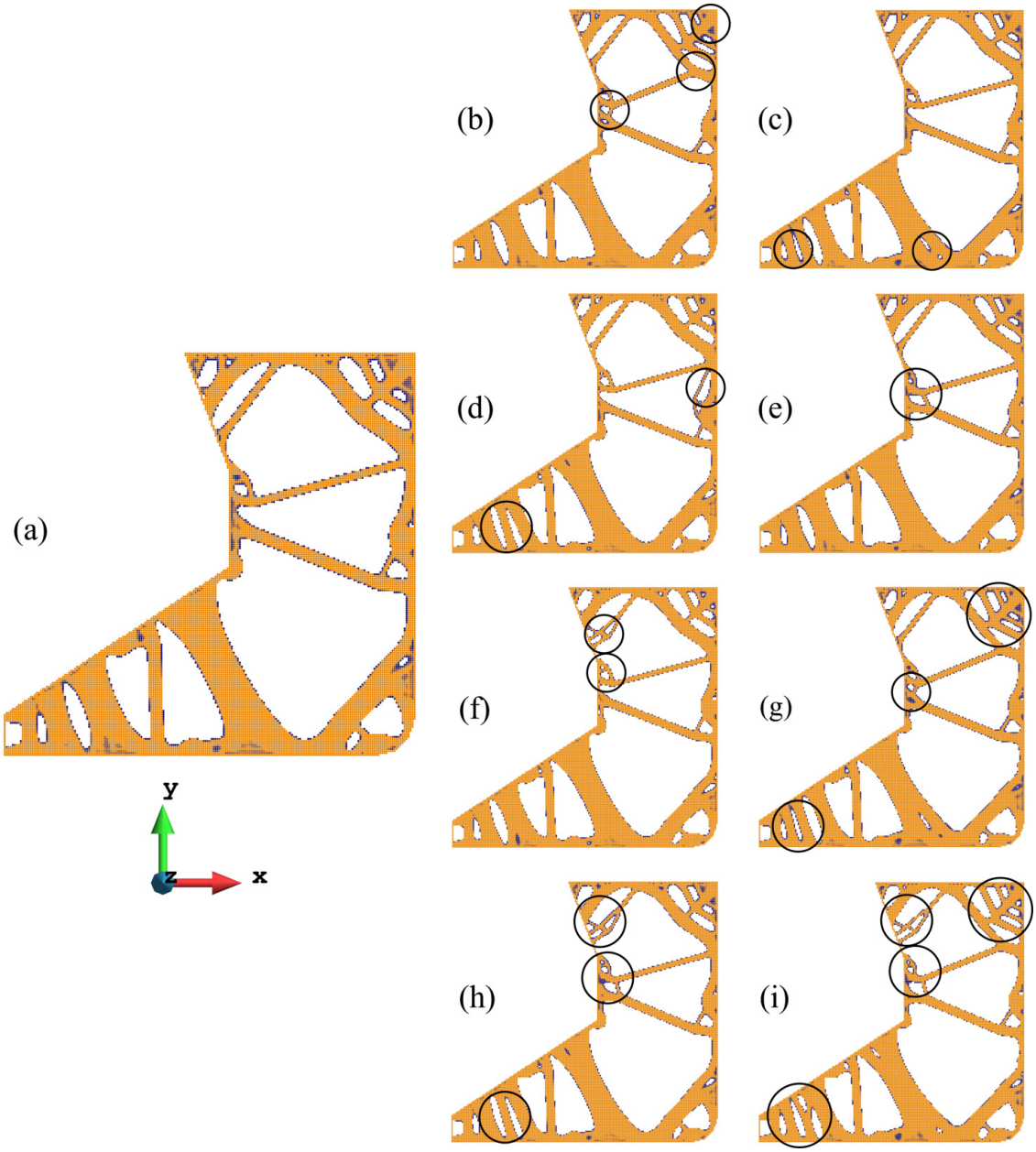
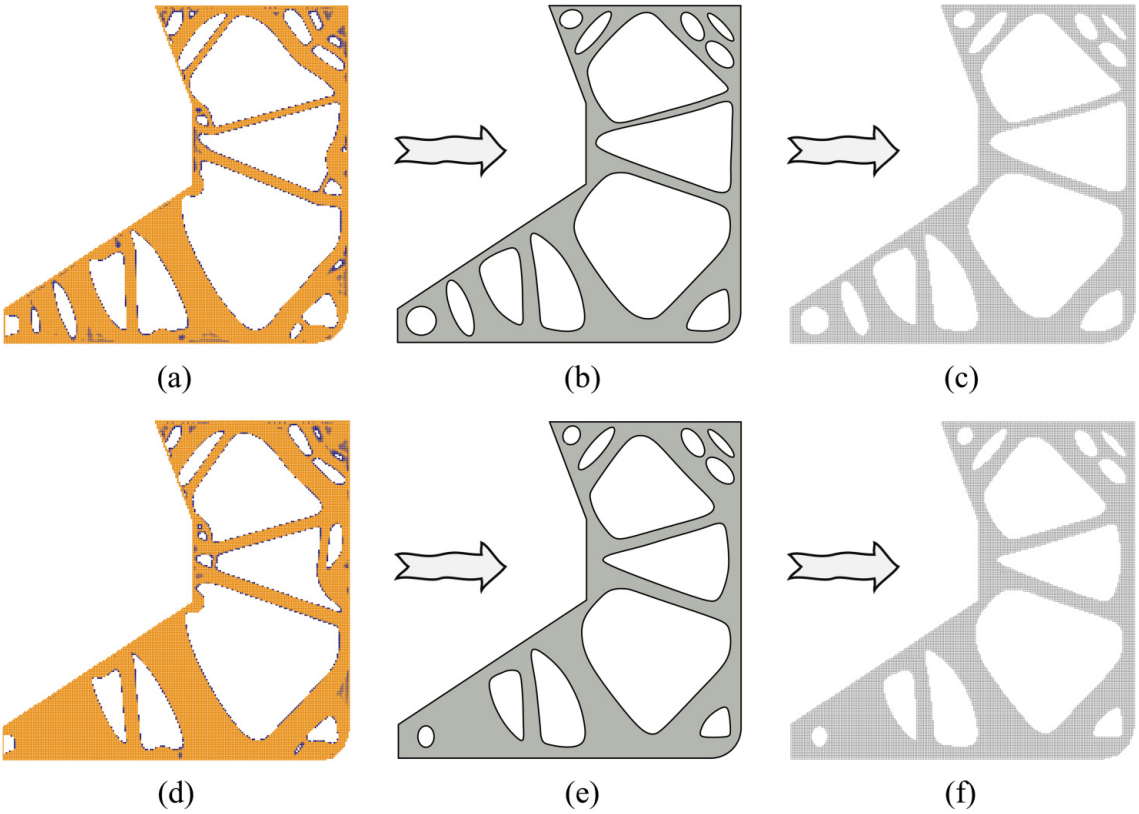


Figure 4.69 (a, c) PD-TO results for the hogging condition; (b, e) smoothed web-frame designs; (c, f) particle model of the smoothed designs (Volume fraction of these results are 0.4 and 0.5, from top to bottom, respectively).

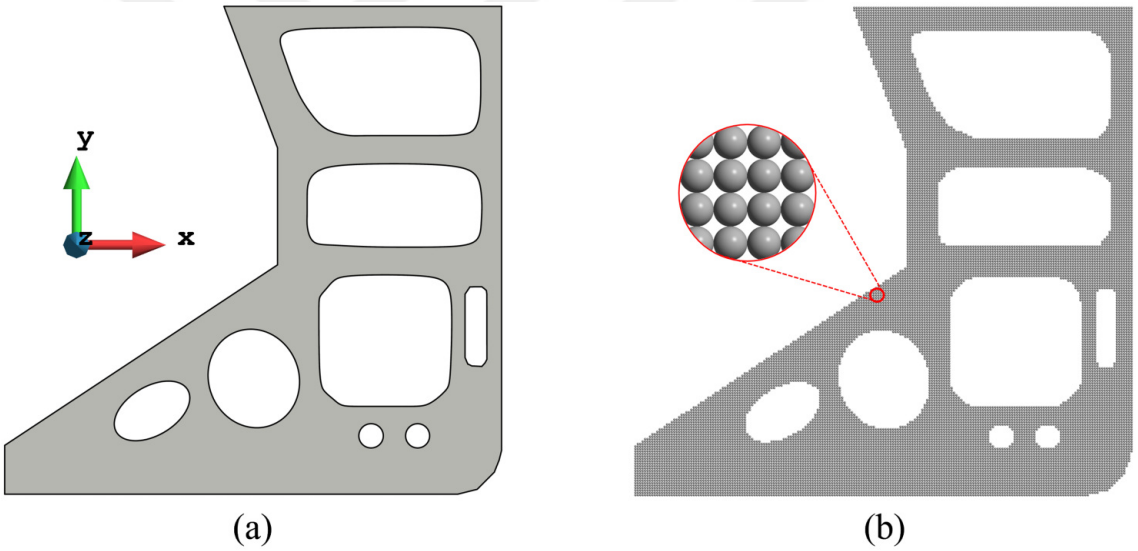


In the next section, these designs will be mechanically compared with the conventional bulkhead design through peridynamics analysis by measuring the structural strength. Therefore, the PD models (same mesh resolution used in previous analyses) of both designs are prepared as depicted in Figures 4.69c and 4.69f. It is worth noting that optimum PD-TO results for no crack case are purposely selected since the conventional web frames are designed without considering any a priori (possible) damage scenarios. According to our previous results (Lahe Motlagh & Kefal (2021)), if the positions of cracks are tailored diligently over the design domain, it is known that the optimum topology with cracks provides higher strength than the one without cracks. Hence, for a fair comparison between conventional bulkhead design methodology and the proposed peridynamics topology optimization method, we run the structural analysis based on the same design conditions (parameters and constraints).

4.3.4.4 Mechanical Assessment of the PD-TO Results against Conventional Web Frame

Figure 4.70a shows a conventional design of a web frame for the TSHD ship type which is generated in accordance with the classification society rules as previously studied by Vuijk (2020). Figure 4.70b presents the particle discretization of this web frame where the particle spacing is the same as the PD models generated for the optimization problems. The volume fraction of this design is calculated by the surface area measurement and obtained approximately 60% of the initial design domain. In contrast, our smoothed optimum PD designs (Figures 4.70b and 4.70e) are 40% or 50% of the initial design domain, thereby being at least 20% lighter than the conventional one.

Figure 4.70 (a) Conventional web frame design; (b) particle-based PD discretization of the design given in (a).



To compare the structural performance of the optimum designs with the conventional one, we run static PD simulations under hogging loading condition. As a result, the displacement contours obtained from these PD analyses are presented in Figure 4.71. The maximum displacement value of optimized structures is relatively much lower than that of a typical web frame. Besides, displacement contours (particularly, for v = 50% design) are uniformly distributed on the optimum geometries whereas the maximum displacement is localized at the deck of the typical web frame. Such a result clearly proves the advantage of the PD-TO approach versus standard design methods for enhanced ship design and structural optimization.

Figure 4.71 Total displacement contours of (a) reference design consisting of 60% material of initial domain; (b) optimized and smoothed design with 50% material; (c) optimized and smoothed design with 40% material.

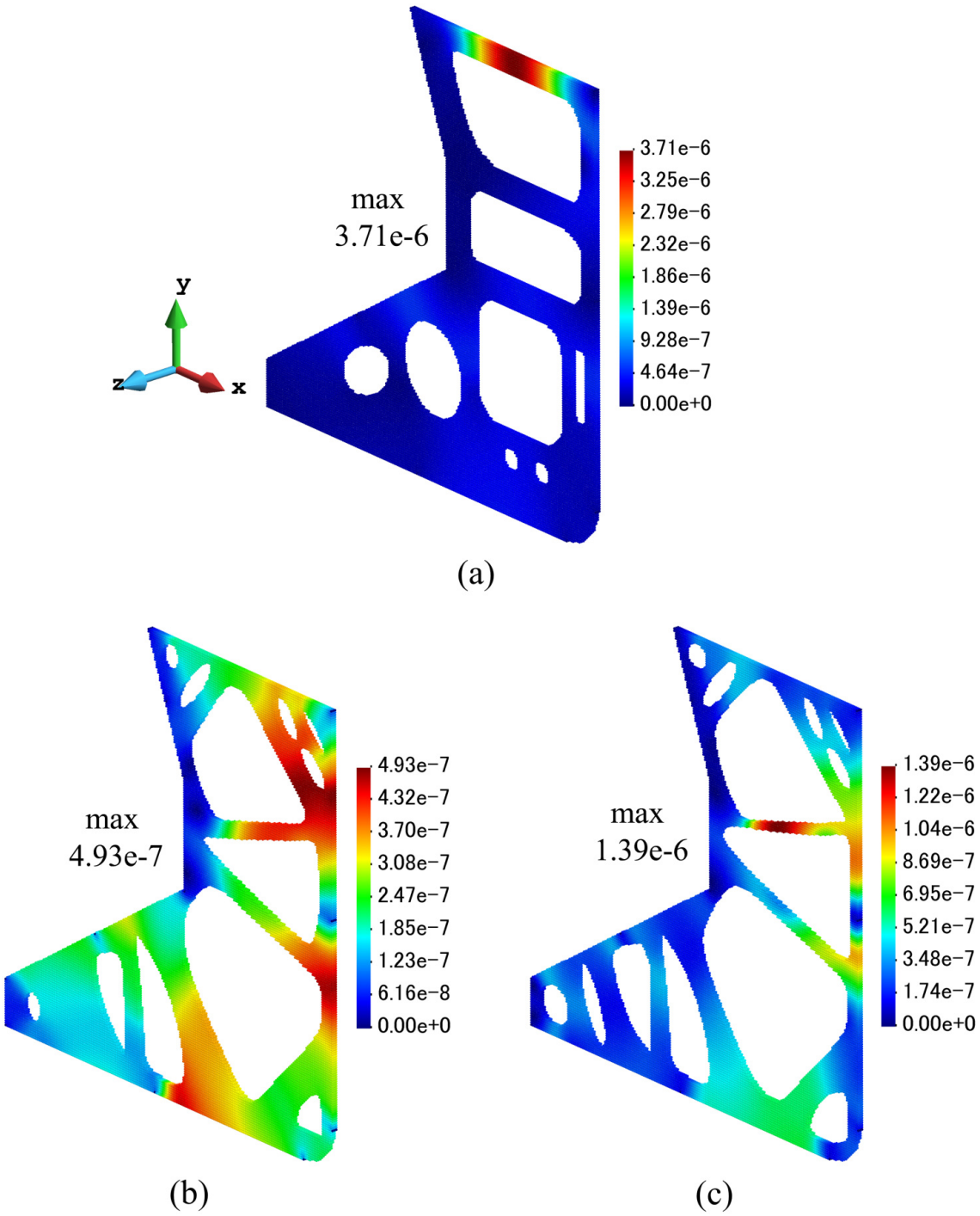
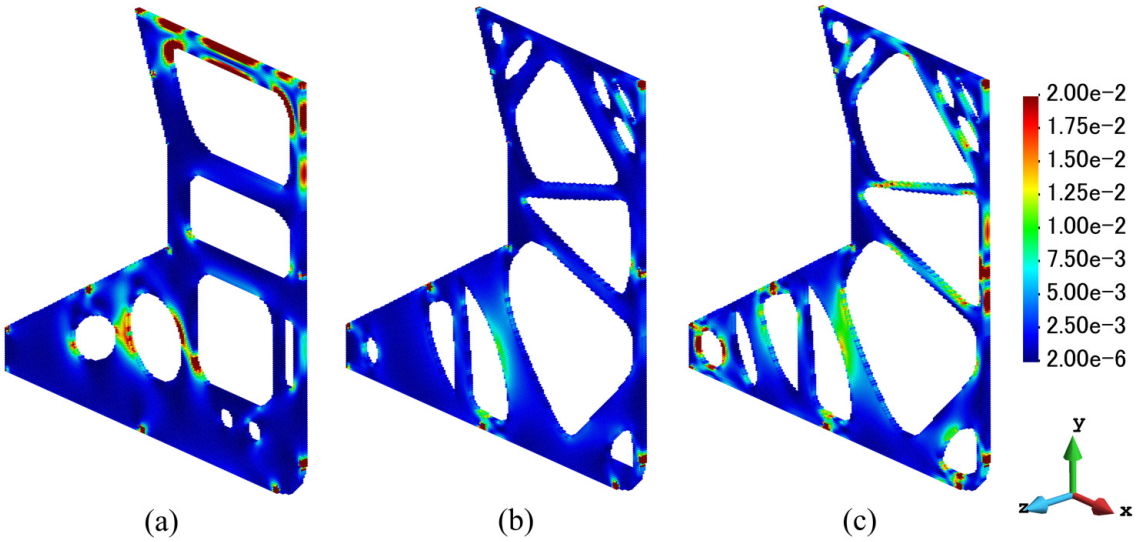


Figure 4.72 Strain energy density distribution for the same energy level, (a) reference design with 60% material of initial domain; (b) optimum design with 50% material; (c) optimum design with 40% material.



In addition to the displacement results, the strain energy distribution over the structures is presented in Figure 4.72. Accordingly, it can be observed that the maximum strain energies are localized on multiple positions of the reference web frame. On the other hand, a couple of regions are found to be experiencing the maximum strain energy in the optimum topologies. To elaborate, the optimum PD topology for the 50% volume fraction contains almost no hotspot region of the strain energy. The strain energy level naturally increases as the material is removed up to 40% (Figure 4.72c). Finally, the compliance values of each design are compared in Figure 4.73 where the advantage of PD-TO is more pronounced albeit the conventional web frame has a higher weight. In Figure 4.73, the structure optimized with 40% material exhibits 17% more rigidity than the reference design whereas this difference increases up to 43% for PD-TO 50% result. For the sake of clearness, the main dimensions of the reference web frame and the optimum topology (PDTO 50%) are compared in Figure 4.74 with Tables 1 and 2. The reference design apparently has less complex hole shapes as compared to the TO results. In this regard, to elevate the ease of manufacturing, some of the holes shown in Figure 4.74b would be eliminated and/or re-designed before production by considering the conservation of total weight. Overall, it can be concluded that the result of PD-TO under 50% volume fraction offers less strain energy, displacement, and weight compared to the conventional one. Hence, for the completeness of this study, by using this frame, a mid-ship compartment of the dredger vessel is generated as depicted in Figure 4.75.

Figure 4.73 Total strain energy (i.e., compliance) values for: reference with 60% volume; optimum design with 50% volume; and optimum design with 40% volume (from left to the right, respectively).

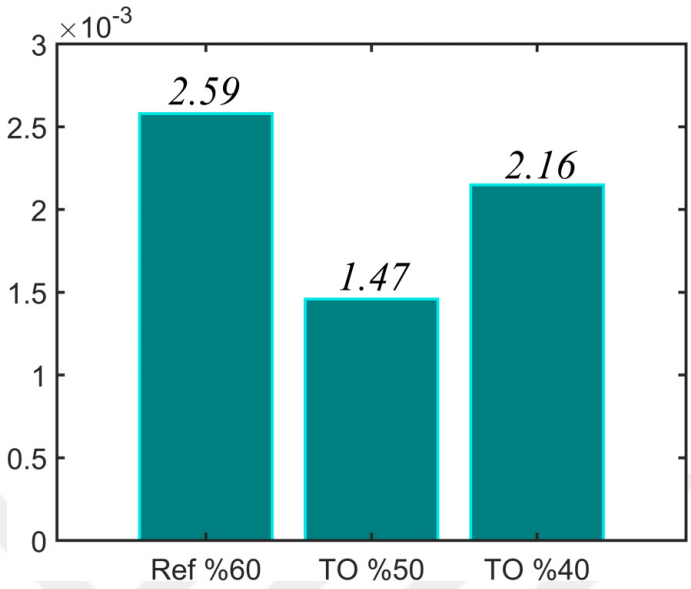
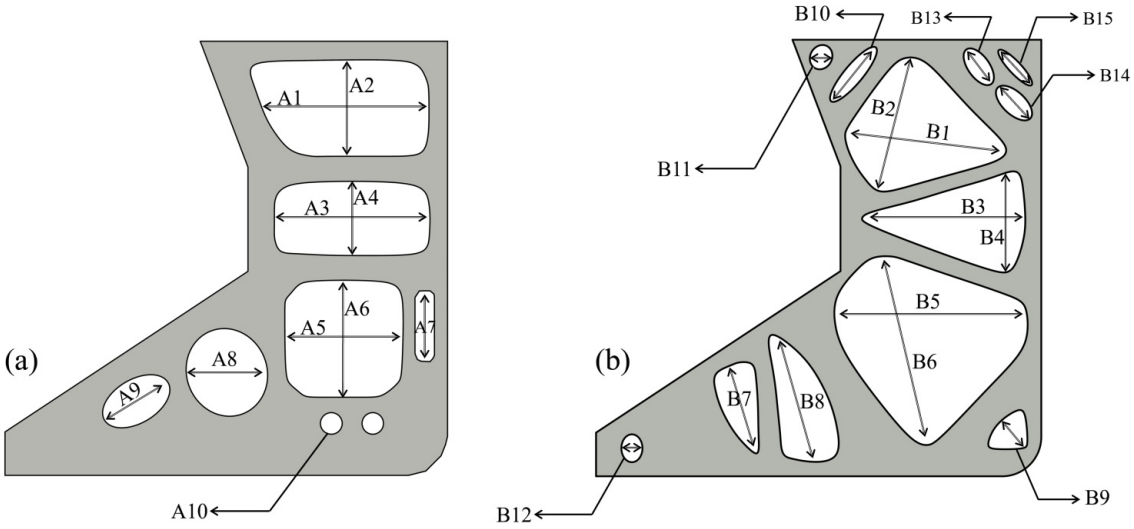


Figure 4.74 The main dimensions of the hole shapes in the (a) reference web frame and, (b) optimum design with 50% volume.

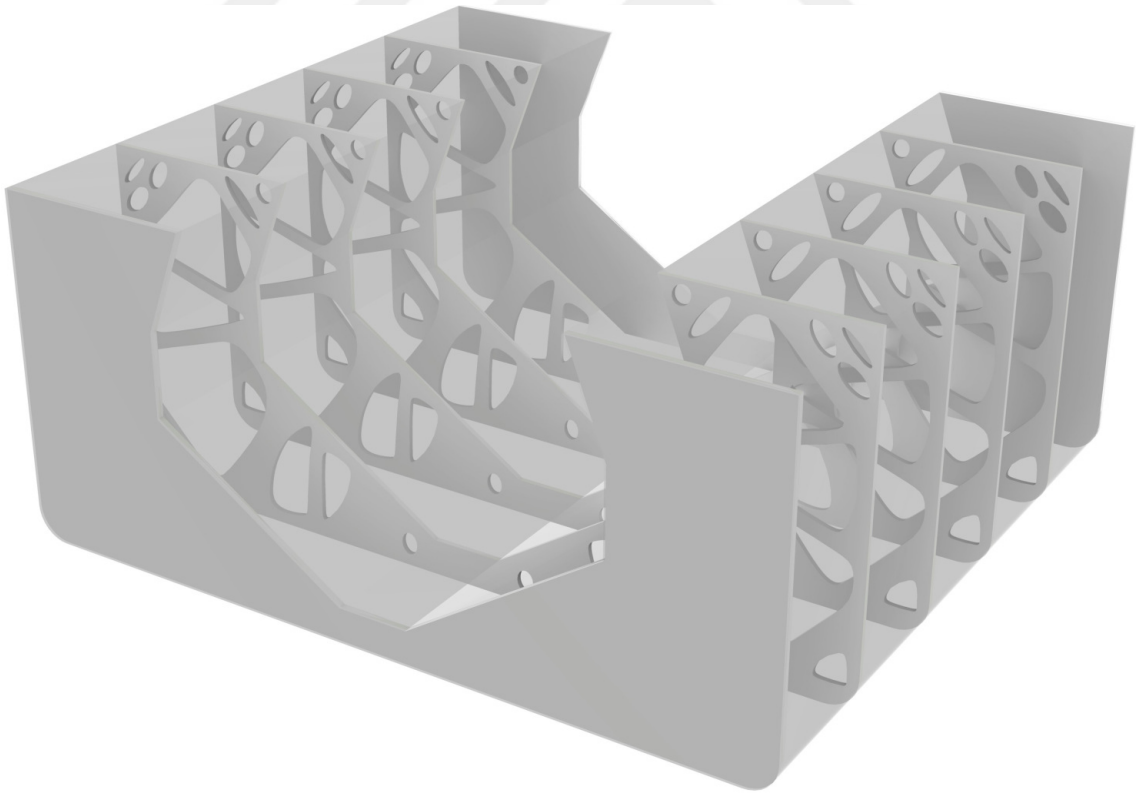


4.3.5 Concluding Remarks

In this research effort, the web frame of a TSHD ship is redesigned by considering different loading and damage conditions and using two different peridynamic-based

topology optimization methods. To this end, volume constraints, loading conditions, and possible damage scenarios on the optimum topologies are thoroughly investigated. It has been observed that both PD-OC and PD-PROP optimization methods produce very close results for similar problems and four different volume constraints. The optimization algorithms have generated alternative web frame designs by minimizing the deformations and strain energies caused by the external pressures of hogging and sagging states. In addition, it is observed that the reduction of volume fractions does not distinctly alter the positions of the main supporting arms formed to maintain the rigidity of the structure whereas it decreases the thickness of these support arms due to the use of less amount of material. For topology optimization of the bulkhead with crack, eight different multiple crack cases are considered, and optimization was performed under hogging conditions. The results of these simulations have revealed that the proposed method demonstrates a sensitive character to any structural discontinuities in the domain, thus effectively altering the optimum topology in the direction of the local cracks as compared to the nocrack case.

Figure 4.75 3D model of the midship compartment consisting of bulkheads and optimized web-frame designs for the hogging condition and 50% volume fraction.



Furthermore, a posteriori smoothing process has been applied to the final geometries by taking into account the manufacturability aspects of the web frames. The structural performance of smoothened and topologically optimized web frames was compared with that of conventional web frame design through peridynamic simulations. According to the results, it has been confirmed that present designs (i.e., corresponding to 0.5 and 0.4 volume fractions) exhibit much less total strain energy (compliance) and maximum displacement compared to the conventional design with approximately 0.6 volume fraction. Such an important outcome unveils the high potential applicability and superiority of the proposed PD-TO method over the conventional design strategies for structural optimization of bulkheads and web frames of ships. Hence, it can be concluded that the PD-TO approach enables the meticulous redesign of conventional bulkheads/web frames to achieve a higher strength with less weight.

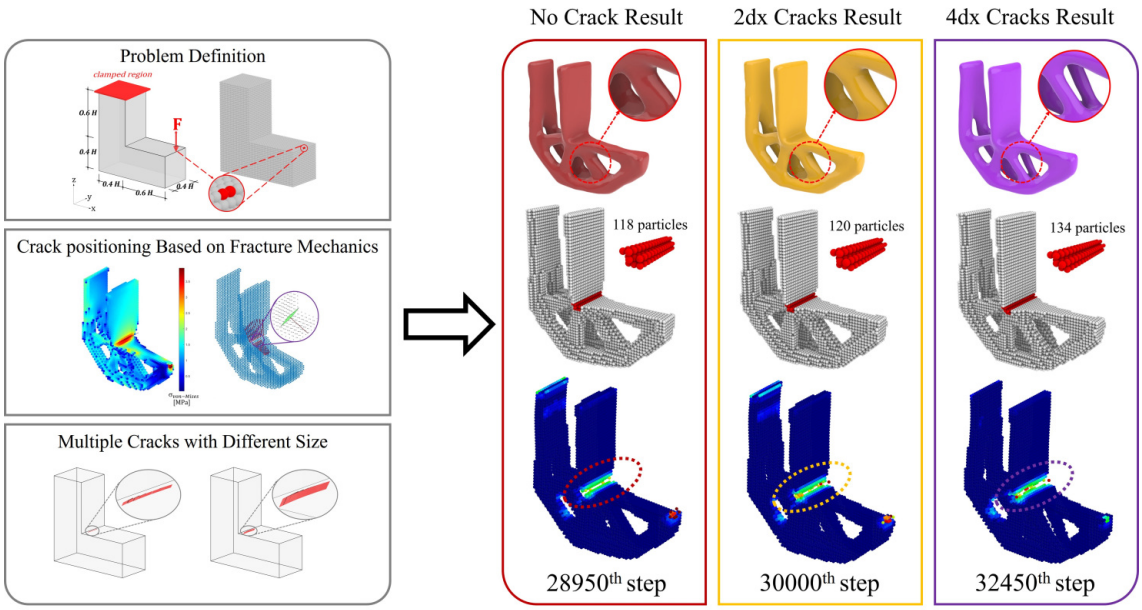
Overall, we believe that the present study establishes a new area for ship structural design and optimization, thus some of the important future studies of the present PD-TO approach are listed as follows.

- Detailed information on different loading and possible damaged/critical areas on different ships can be used as input to this method.
- A more detailed ship section model can be developed by adding other supporting elements to the ship cross-section.
- A study can be conducted to examine the manufacturability in more detail and the proposed geometries can be adapted to the existing production methods.
- Since the acceptance of a design according to class rules is an important necessity so the proposed PD-TO method can be used as an optimization tool for forming new classification rules and calculation methods.
- Lastly, experimental verification of the proposed method considering the class rules in a future study would be a great contribution to the numerical results presented in the current study.

5. APPLICATIONS OF PD-TO FOR MINIMIZING RESIDUAL STRESS ARISES FROM AM PROCESSES

5.1 A Systematic Fusion of Failure Criteria and Peridynamics Topology Optimization for Enhanced Fracture Resistance

Figure 5.1 Graphical abstract of the Section 5.1



5.1.1 Introduction

This section presents a novel systematic optimization process by utilizing a failure criterion embedded within the peridynamics topology optimization (PD-TO) framework to increase the fracture resistance of lightweight engineering structures. In this context, we first optimize the structure without any failure constraint and subsequently determine the high-stress concentration regions to employ the failure criteria for allocating multiple cracks in the initial design domain. Afterward, the design domain with embedded cracks is re-optimized by running a PD-TO simulation to obtain a fracture resistance-enhanced optimum topology. The main benefit of this theoretical advancement is no requirement of any preexisting crack for running PD-TO analyses, automating the TO process to increase the strength of final designs. Thus, the proposed method can be straightforwardly applied to perform the critical design of structures for higher strength even with relatively lower weight as compared to optimized structures with classical TO methods. To prove the efficiency of the proposed method, three benchmark problems are solved and optimized structures are compared against each other through static and dynamic analyses. Comparisons based on static load reveal a reduction in strain energy concentration within critical regions of designs optimized with cracks, indicating the effectively reduced energy levels. The results of dynamic analyses show notable advancements in fracture resistance within optimized designs via the proposed scheme. Hence, we demonstrate an automated practical design tool for engineering applications, offering lightweight structures with increased fracture resistance and reduced strain energy. These research efforts provided in this section are prepared as a journal paper study and submitted to the journal of Structural and Multidisciplinary Optimization (Kendibilir, Lahe Motlagh & Kefal (2024)).

5.1.2 Novelty and Motivation

To the best of the author's knowledge, there is no study presenting a failure criterion-associated peridynamics topology optimization framework to increase the fracture resistance of the topologically optimized structures. The PD-based TO algorithms so far either use an arbitrary position for cracks or easy-to-implement cracks in possible crack positions (i.e. horizontal/vertical surface cracks). Therefore, there is a major need to identify possible weak points based on solid mechanics, so that the optimized structure remains intact under specific loading conditions. At this

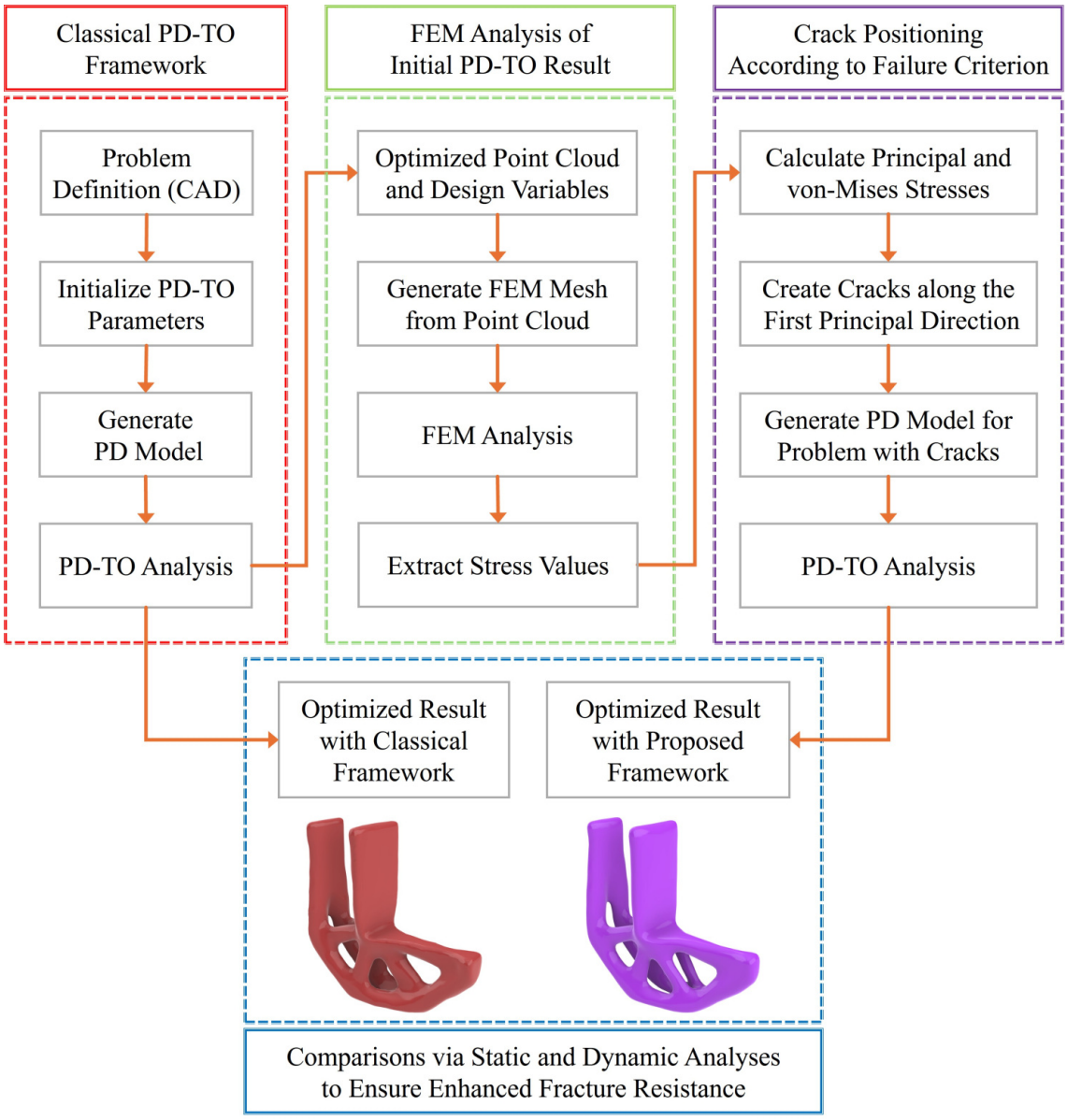
point, we propose an effective topology optimization strategy using failure criteria to locate cracks for designing reliable lightweight structures. The framework proposed herein is generally applicable to different failure criteria available in the literature for various material types. However, we particularly utilize Griffith's criterion for brittle structures in this study. Since the first principal stress as the highest stretching stress can make critical crack openings in most structures, wisely predefining the cracks can prevent possible damages that may happen under operation loads. To this end, the study is focused on determining crack location and orientation based on the first principal stress. Locations are selected where high-stress concentrations occur, and the surface cracks are located perpendicular to the first principal stress. This novel crack identification strategy leads to structures having both maximized stiffness and enhanced fracture resistance to prevent possible future damages.

The remainder of this section is divided to three subsections. Firstly, Section 5.1.3 presents a new algorithm for positioning multiple cracks considering CCM based failure criterion. Moreover, Section 5.1.4 provides the obtained PD-TO results for three benchmark cases. Both static and dynamic analyses performed to comprehensively compare the performance of the classical TO method with proposed TO strategy herein. Lastly, Section 5.1.5 outlines the concluded remarks from the comparisons.

5.1.3 An Algorithm for Failure Criterion Based Crack Definition in PD-TO

In the typical manufacturing process, defects may arise due to various factors such as uncertainties in system control, material strength variations, final machining, and other forms of post-processing. Moreover, even the final topology obtained with an ideal algorithm may experience damage under operation loads or unpredictable excessive loads. At this point, PD-TO can be utilized in a systematic algorithm fed by failure criterion, allowing for iterative processes to ensure the prevention of any catastrophic failure. This section, therefore, explores the potential locations of cracks by leveraging principles from fracture mechanics to address future defect occurrences. The workflow of the proposed PD-TO framework is schematically explained in Figure 5.2.

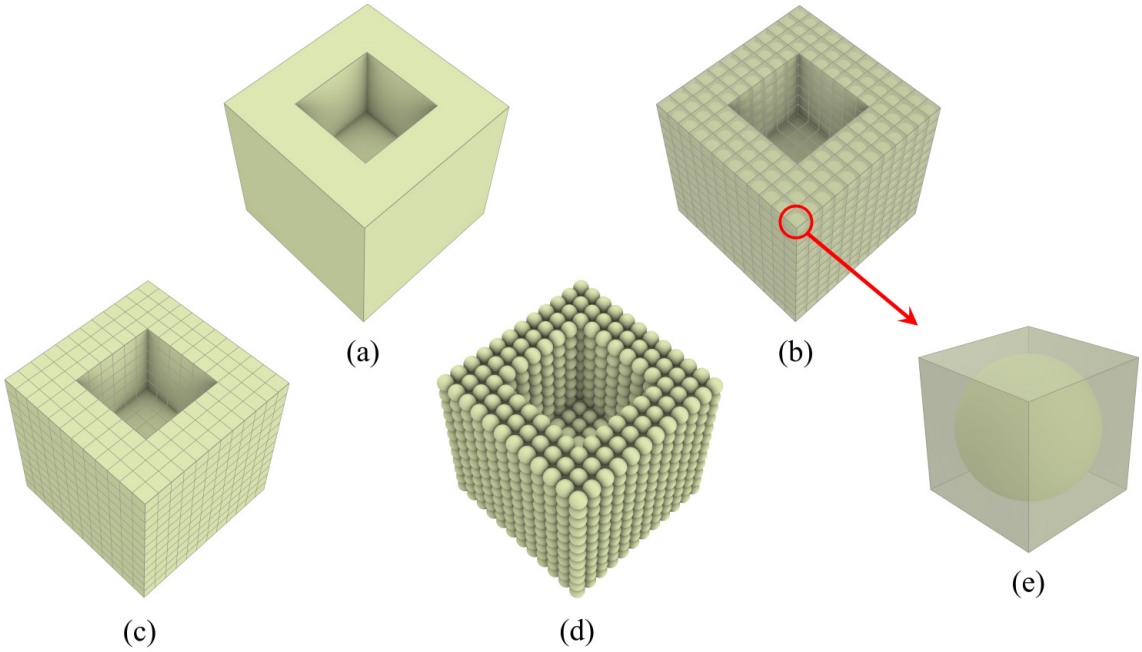
Figure 5.2 The workflow of the proposed failure criterion based crack definition framework.



As a first step, we topologically optimize a structure without considering any damage using the PD-TO method. The obtained particle-based results include the positions of all points in the discretized initial geometry and the optimized design variables. These data serve as the main inputs of the systematic optimization scheme proposed in the paper. Subsequently, stress analysis needs to be performed since the damage criterion definition in the approach is based on the stresses in the structure. At this point, the PD-TO results (point cloud) are prepared for finite element analysis. Figure 5.3 shows the discretized versions of a solid body (Figure 5.3a) for both finite element (Figure 5.3c) and peridynamic (Figure 5.3d) analysis. It can be seen that

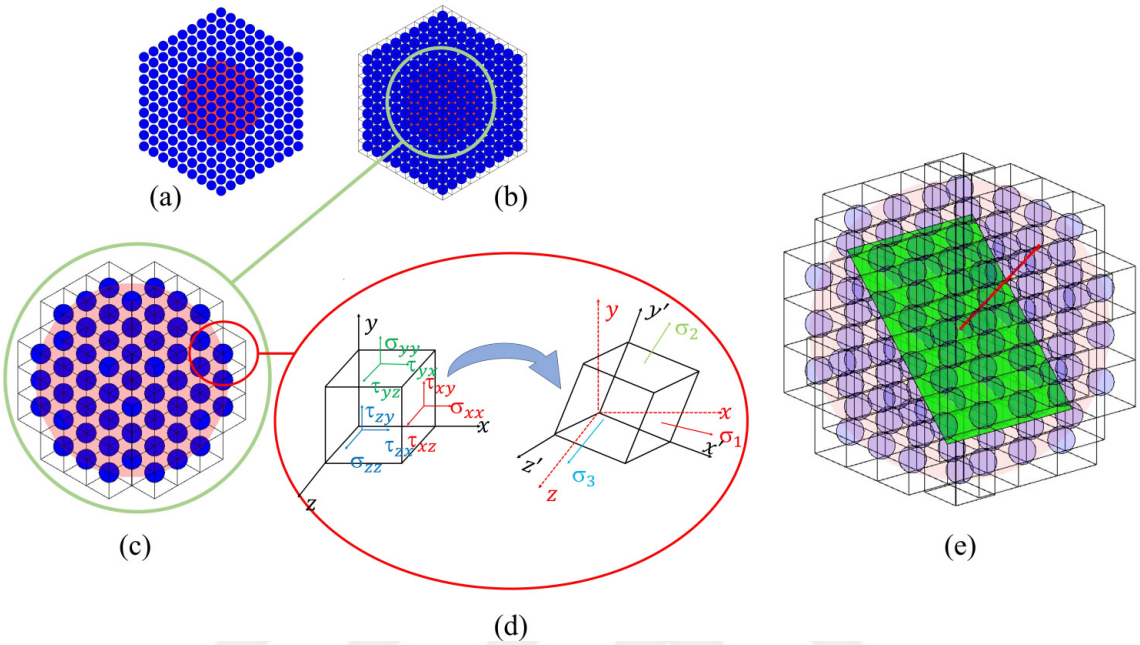
the FEM mesh and PD point cloud are equal in resolution. By creating hexahedral FEM elements for each PD particle with the same size, as shown in Figure 5.3b and Figure 5.3e, PD-TO results are prepared for FEM analysis. Consequently, static analysis is performed by applying loading and boundary conditions to the relevant elements of the problem.

Figure 5.3 (a) Example of a 3D solid body. (b) Illustration of particle and element-based models with the same discretization density. (c) Finite element discretization consisting of eight noded solid elements. (d) PD discretization consisting of equally distanced uniform particles. (e) The center of each PD particle corresponds to the center of each finite element.



Afterwards, the stresses in each element are extracted from FEM analysis and the principal stress values and their corresponding directions are calculated. The first principal stress is always the highest positive value among all principal stresses. Thus, possible crack locations are identified by considering Griffith's criterion to include Mode I cracks and the first principal stress in the positions where von-Mises stress is highest. In this regard, the crack positioning procedure is illustrated in Figure 5.4. The principal stresses and von-Mises stress can be calculated by the following equation:

Figure 5.4 Surface crack positioning. (a) Blue balls are the PD particles, and the pink sphere represents the horizon. (b) FEM elements around particles, transparent cubes are the meshes. (c) Mesh around the horizon. (d) Stress transformation to obtain principal stress. (e) Creating the surface crack (green surface) around the location of maximum stress by using the principal stress (red arrow) direction.



$$\sigma - \lambda\delta_{ij} = \det\begin{pmatrix} \sigma_{xx}-\lambda & \tau_{xy} & \tau_{xz} \\ \tau_{yx} & \sigma_{yy}-\lambda & \tau_{yz} \\ \tau_{zx} & \tau_{zy} & \sigma_{zz}-\lambda \end{pmatrix} \tag{5.1}$$

$$\lambda^3 - I_1\lambda^2 + I_2\lambda - I_3 = 0 \tag{5.2}$$

$$I_1 = \sigma_{xx} + \sigma_{yy} + \sigma_{zz} \tag{5.3}$$

$$I_2 = \sigma_{xx}\sigma_{yy} + \sigma_{yy}\sigma_{zz} + \sigma_{zz}\sigma_{xx} - \tau_{xy}^2 - \tau_{yz}^2 - \tau_{zx}^2 \tag{5.4}$$

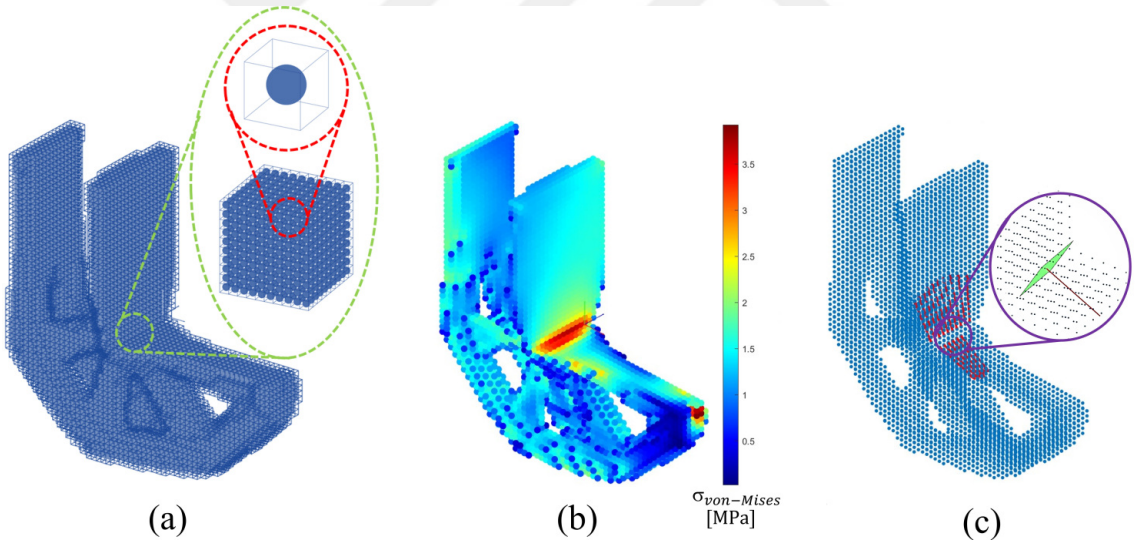
$$\begin{aligned} I_3 = {} & \sigma_{xx}\sigma_{yy}\sigma_{zz} + 2\tau_{xy}\tau_{yz}\tau_{zx} \\ & - \sigma_{xx}\tau_{yz}^2 - \sigma_{yy}\tau_{zx}^2 - \sigma_{zz}\tau_{xy}^2 \end{aligned} \tag{5.5}$$

where σ_{xx}, σ_{yy}, and σ_{zz} are normal stresses, τ_{xy}, τ_{yx}, and τ_{zx} are corresponding to shear stresses. Principal stresses $(\lambda_1, \lambda_2, \lambda_3)$ are the eigenvalues of the stress tensor and I_1, I_2, and I_3 are first, second and third stress invariants, respectively. The von-mises stress can be computed by the values of principal stresses as follows:

$$\sigma_{\text{von-mises}} = \sqrt{\lambda_1^2 + \lambda_2^2 + \lambda_3^2} \tag{5.6}$$

For clarity, the crack positioning procedure is demonstrated on one of the benchmark problems (L-beam) as depicted in Figure 5.5. Here, crack locations and orientations are defined considering Griffith's criterion and von-Mises stress. In this context, firstly the final topology obtained by PD-TO is modeled and analyzed with FEM, and principal stresses are extracted to calculate the von-Mises stresses (Figures 5.5a, b). Hence, the regions with the highest stress values are identified as possible crack locations. At this point, we determine a criterion that the particles carrying the highest 2 percentiles of von-Mises stress should be taken into account to detect the initial position of surface cracks. Moreover, to identify the orientation of surface cracks in point cloud space, a plane perpendicular to the first principal stress is identified and considered as the final form of the crack (Figure 5.5c). Consequently, the possible surface crack perpendicular to its first principal stress orientation is defined by considering the first principal stress.

Figure 5.5 Surface crack positioning on the optimized L-beam structure, (a) FEM mesh around point clouds. (b) von-Mises stress distribution. (c) The embedded surface crack (green surface) according to principal stresses (red arrows) around the location of maximum stress.



5.1.4 Numerical Results and Discussions

In this section, selected benchmark problems are first optimized for reducing the total weight without considering cracks or defects in the initial problem domain. The obtained designs herein are then analyzed by the finite element method under the predefined static loading condition to be able to find the most critical regions

throughout the structure that may initiate the failure. For this purpose, considering the fracture mechanics criteria, we evaluated the high-spot regions. Right after, several rectangular cracks with varying sizes are aligned appropriately and introduced into the initial domain for further optimization. After the second optimization, we achieve alternative designs and compare them with the initial ones, which did not include cracks. All the topology optimization analyses are performed by our in-house MATLAB codes. Poisson's ratio of the material is set as $\nu = 0.25$ to satisfy the bond-based PD formulation for three-dimensional structures.

Figure 5.6 (a) Problem domain for the hanger beam geometry. (b) PD discretization of the given geometry and selected particles for applying the loading condition.

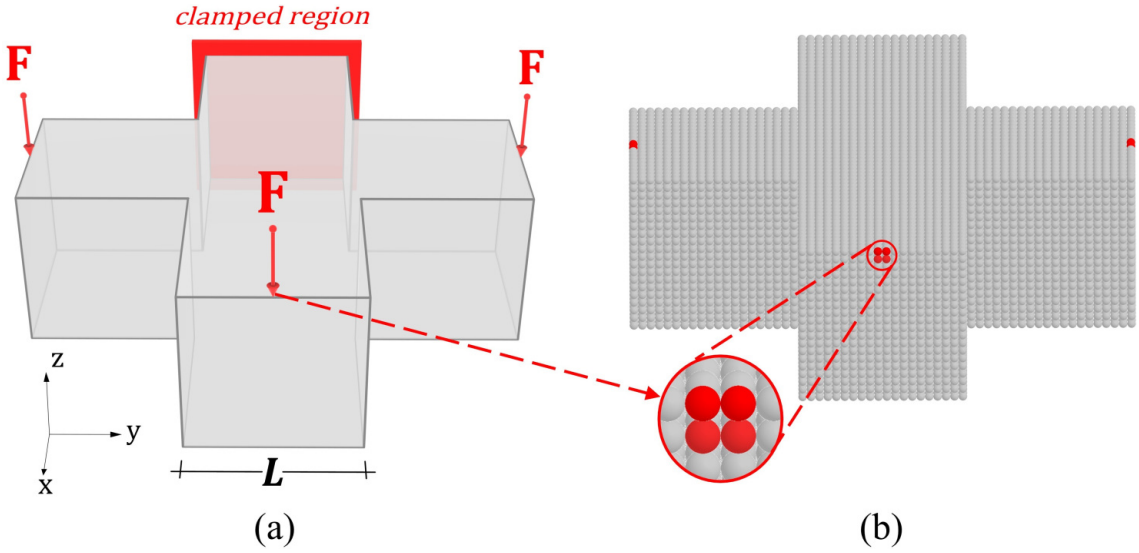
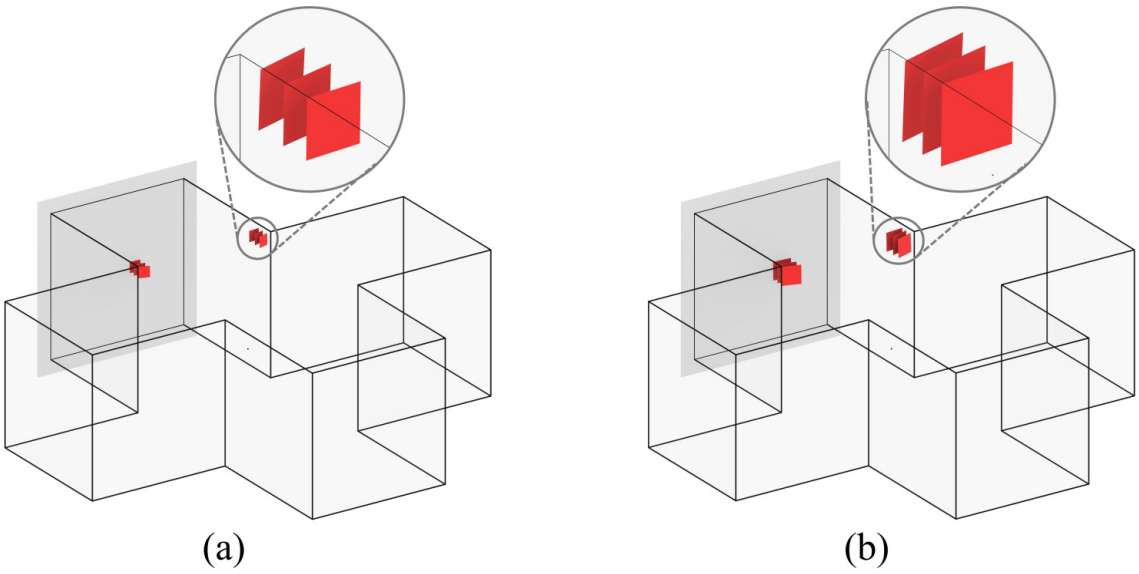


Figure 5.7 Crack positions on hanger-beam geometry for (a) 2dx cracks, and (b) 4dx cracks according to critical von Mises stresses.



Another important parameter for an isotropic material, the elastic modulus, is taken as E=200 Gpa. Moreover, other optimization parameters such as PD horizon size, minimum filter radius, and the penalization factor are defined as: $R_{min} = 3dx$, $\delta = 3.015dx$, and $p = 3$, respectively.

5.1.4.1 Case I: Hanger Beam

For the first optimization problem, we model a hanger beam that is fixed to the face behind it. The problem domain has the same dimensions in the length (180 mm along the x-axis) and width (180 mm along the y-axis) directions and has one-third of the length (60 mm along the z-axis) in the height direction, where all the edges have the same dimension ($L = 60mm$), as shown in Figure 5.6a. The problem geometry is then discretized into 60, 60, and 20 particles in the x, y, and z directions, respectively. Hence, the PD model consists of 40000 elements in a three-dimensional domain. A force load with a magnitude of 500 N is applied to three free edges, meaning that the hanger beam carries the 1500 N force in total. While introducing the force into the middle of the leading edges, four points are picked for each, and load is applied as the body force density in the selected PD particles (Figure 5.6b). The final volume constraint is defined as 20% of the initial volume.

The topology optimization process is performed without including cracks in the initial design domain. Then, we obtain a PD-TO result with high design variable values. Based on the obtained point cloud results, we create a FEM model consisting of uniform eight-noded elements. Once the static structural FEM analysis on the optimized geometry is done, the stress distribution is used to find critical material points so that surface cracks can be found using the criteria set out in Section 5.1.3. In this regard, the embedded surface cracks with edge lengths of 2dx and 4dx are depicted in Figure 5.7a and Figure 5.7b, respectively. The locations, orientations, and number of cracks are the same whereas crack size is the only changed parameter. Here, we intend to understand the effect of the crack size on the optimum design. It would be a guide for the next PD-TO studies for determining the optimum crack size in the initial domain.

Figure 5.8 From top to bottom, the particle-based topology optimization results are transformed into 3D closed meshes utilizing voxel elements, and a final smoothing operation is performed to obtain ready-to-print designs.

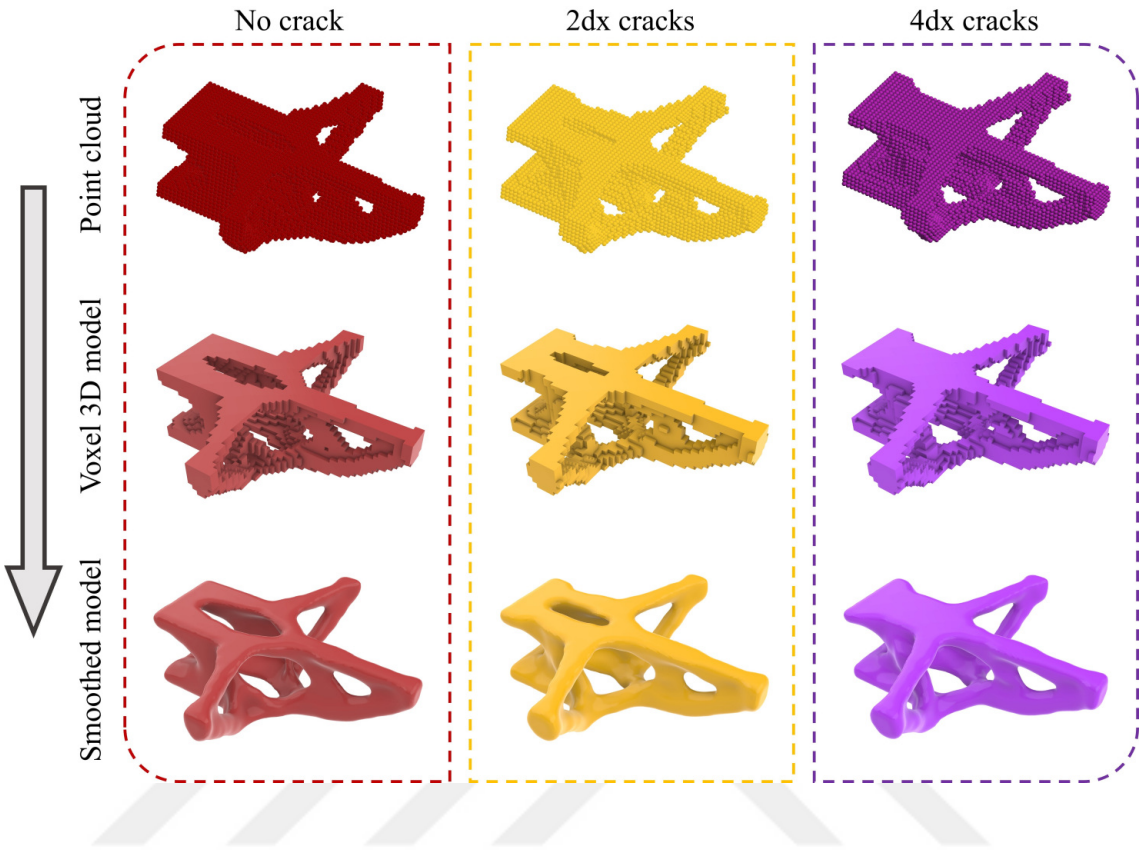
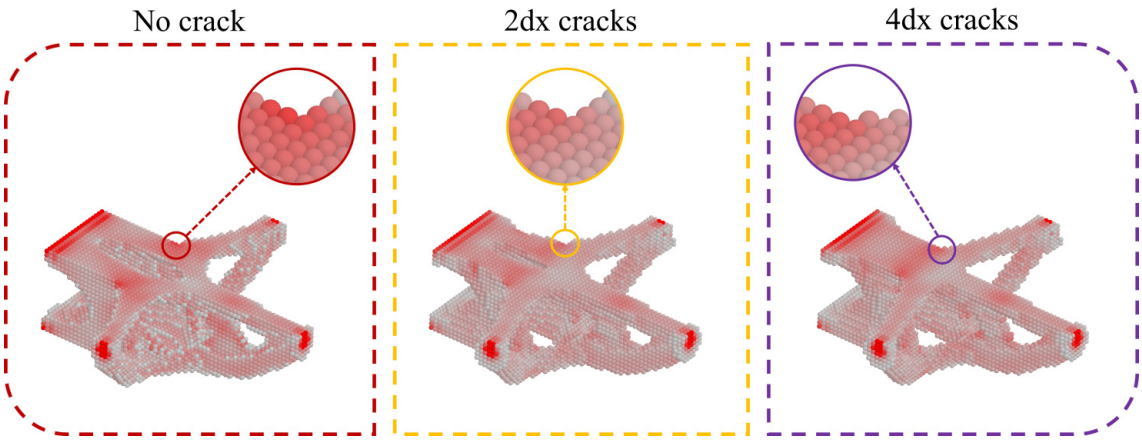


Figure 5.9 Strain energy distribution comparison on particularly cracked regions.



In the second step, we optimize the same geometry, including the 2dx and 4dx cracks in the initial design domain. For clarity, we call the results as "No crack", "2dx cracks", and "4dx cracks" throughout this study. As it says, No crack result is obtained without considering cracks. Moreover, 2dx cracks and 4dx cracks are the

results achieved by optimizing the problem domain with cracks illustrated in Figure 5.7a and Figure 5.7b.

It is not easy to investigate the geometrical detail in these particle-based figures. Therefore, we provide voxel 3D models and smoothed versions of these intricate closed shapes in Figure 5.8. From this figure, geometrical modifications can easily be examined. For example, the hole on the upper back of the No crack result becomes smaller in the 2dx cracks result and is completely filled in the 4dx cracks result. Figure 5.9 shows the optimum designs, including strain energy distributions under static loading, for three different cases. This figure focuses on the critical region (where the cracks are embedded) to compare designs before and after cracks. Here, it can be seen that both design and energy distribution are prominently changed in the results of 2dx and 4dx cracks cases. The zoomed-in circles show the decreased energy in critical region which proves the efficiency of the proposed TO framework.

Further than visual investigation, to compare the strain energy values in three optimum results, we determine a region of interest, a box-shaped region covering embedded cracks (Figure 5.10a) and extract the points inside this region as illustrated in Figure 5.10b. Due to the geometrical variations between designs, the number of particles inside the cracked region is dramatically changed. Hence, there are 94, 82 and 44 particles found in the same region. Table 5.1 presents the strain energy comparison between the three designs, including total, average, and maximum energy values. It is observed that the all values in the critical region are remarkably decreased for the designs optimized with cracks. The decrease in total energy was expected due to the decrease in the number of particles in the region. The main indicators are the average and maximum energy values. As a result, the average energy levels for 4dx and 2dx cracks decreased by approximately 24% and 8%, respectively, through the optimization of cracked structures. Additionally, while a maximum energy value of 195 was observed in the critical region, this value decreased to 134 and 153 in structures optimized with cracks, resulting in an improvement of approximately 31% and 21%, respectively.

Figure 5.10 (a) Extracting the strain energy density values under static loading for the particles inside the interest region of Hanger-beam problem. There are 94, 82, and 44 particles inside the critical region on the optimized structures for the scenario of (b) No crack, (c) 2dx cracks, and (d) 4dx cracks, respectively.

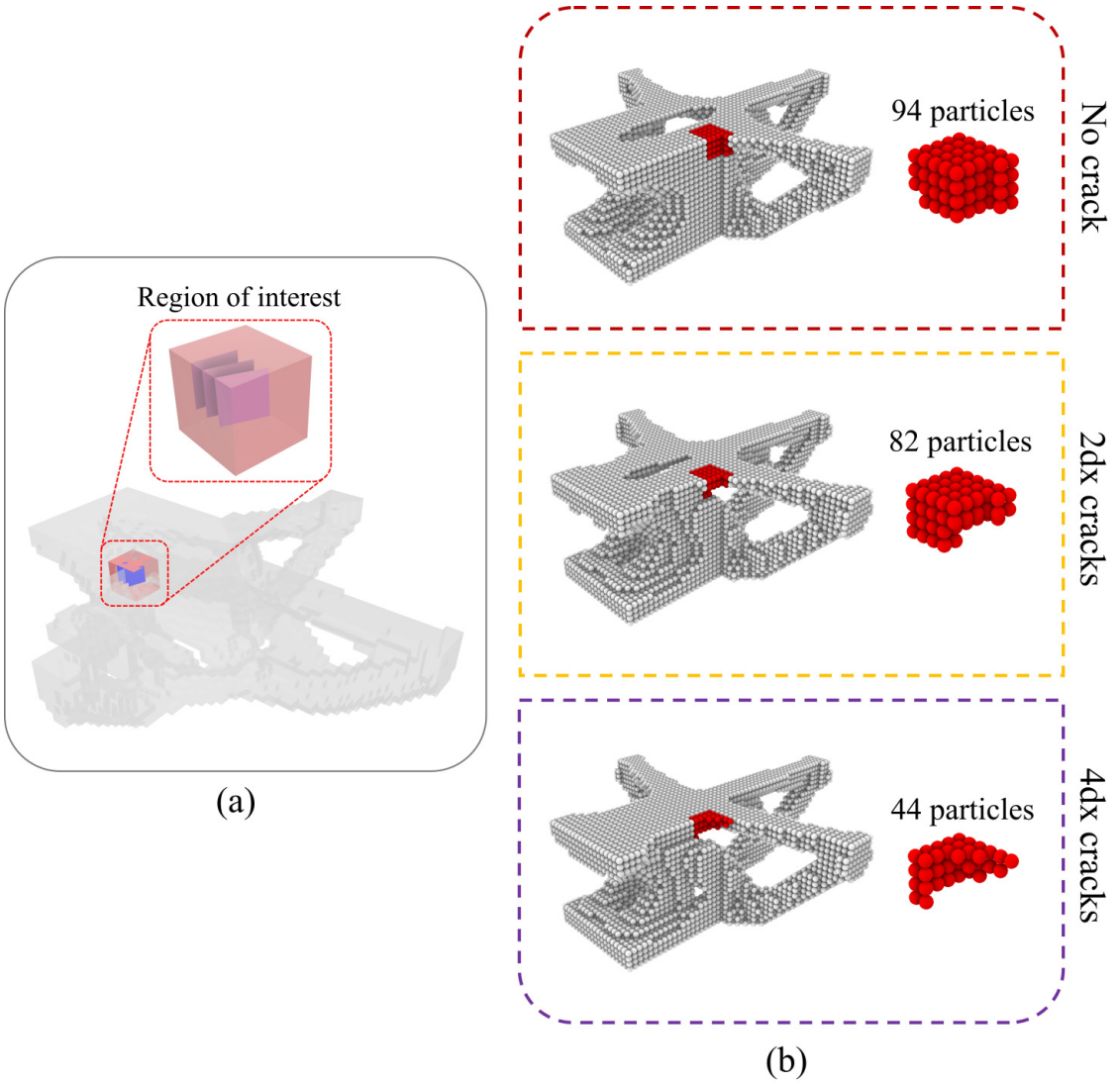
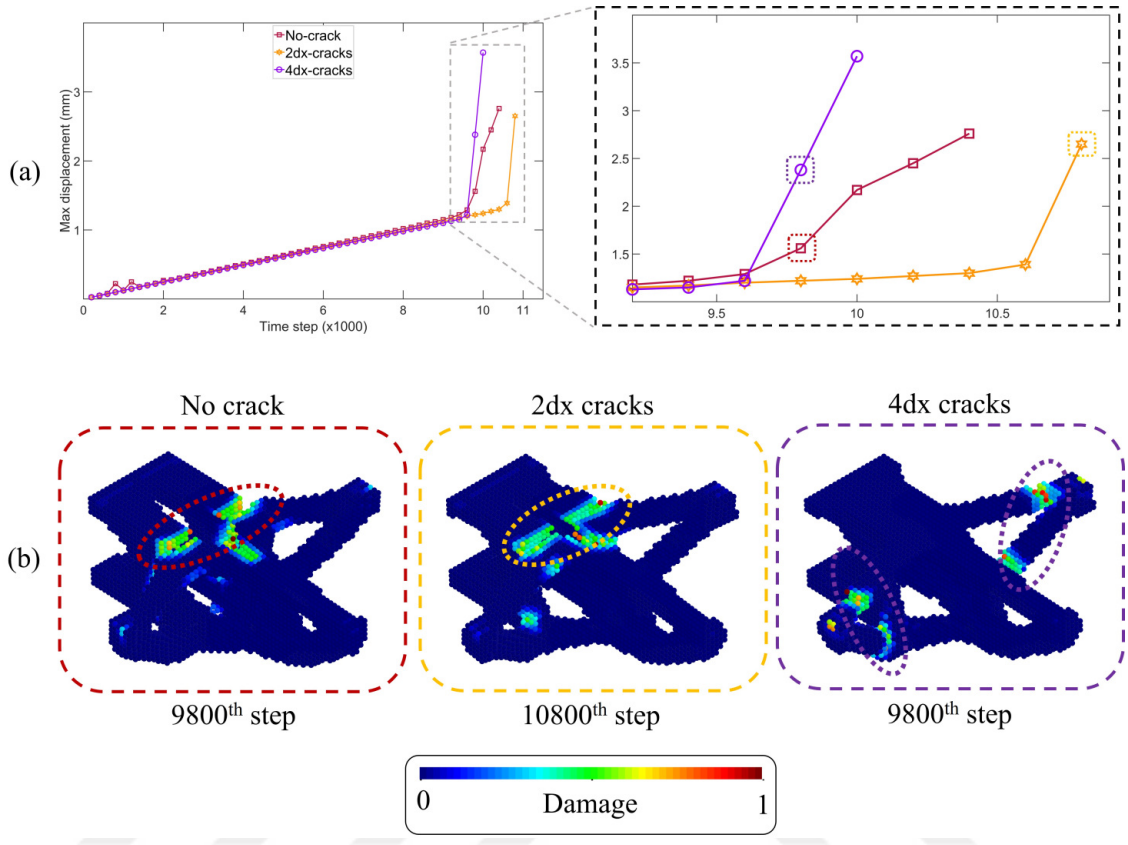


Table 5.1 Total, average and maximum strain energy density comparison in the vicinity of the embedded cracks (region of interest as shown in Fig.5.10) between three optimized Hanger-beam structures under static loading condition

Case	# of part.	Total en.	Diff. [%]	Average en.	Diff. [%]	Max en.	Diff. [%]
No crack	94	7.64E+03	-	81.35	-	195	-
2dx cracks	82	5.06E+03	33.72	61.80	24.02	134.6	30.97
4dx cracks	44	3.30E+03	56.77	75.12	7.65	153.13	21.47

Figure 5.11 (a) Maximum displacements during dynamic analyses on Hanger-beam designs. (b) The damage contours and the failed regions in three designs when the crack starts to propagate.



In addition to comparisons performed under static loading conditions, we also employed dynamic PD analyses under velocity boundary conditions. Accordingly, time-dependent maximum deformation plot (Figure 5.11a), and damage contours plotted during crack propagation (Figure 5.11b) are presented. In the 2dx cracks and No crack results, crack propagation is observed in the same region, while 4dx crack result experiences damage accumulation in the arms located on both sides of the structure. Although the damage accumulation regions are similar for the No crack and 2dx cracks results, the damage evolution under dynamic load was observed 10.2% later in 2dx cracks result, indicating a notable enhancement in the fracture toughness.

Furthermore, when evaluating the performance of the 4dx crack scenario under dynamic load, the absence of any damage formation in the critical region can be considered a positive outcome. However, damage formation in a different region can be interpreted as a negative result. Ultimately, in this specific problem, it was observed that the proposed method increased fracture toughness or prevented potential damage in the critical region with two different crack size configurations.

Eventually, the proposed algorithm should be performed and scrutinized on different problem types.

5.1.4.2 Case II: L-Beam

L-Beam geometry, which is one of the most famous benchmark problems in topology optimization literature, is chosen as the second case for the optimization. Figure 5.12a shows the problem dimensions of the L beam geometry where the $H = 200mm$. The whole domain consists of 32000 PD points where the geometry is discretized into 50 × 20 × 50 particles, in x, y and z directions, respectively. Equal particle distance is set to $dx = 4mm$. PD particles in the highest layer of the L-Beam is fully constrained in all degree of freedoms for assuring the clamped edge condition. Point force, F, is applied to the two particles in the middle of the right edge of the beam, as shown in Figure 5.12b. The target volume of the optimization is selected as 25% of the total volume of the initial domain. This benchmark problem is chosen due to its unique geometrical feature that is having a notch in the design domain.

Figure 5.12 (a) Problem domain for the L-Beam geometry, (b) PD discretization of the given geometry and selected particles for applying the loading condition.

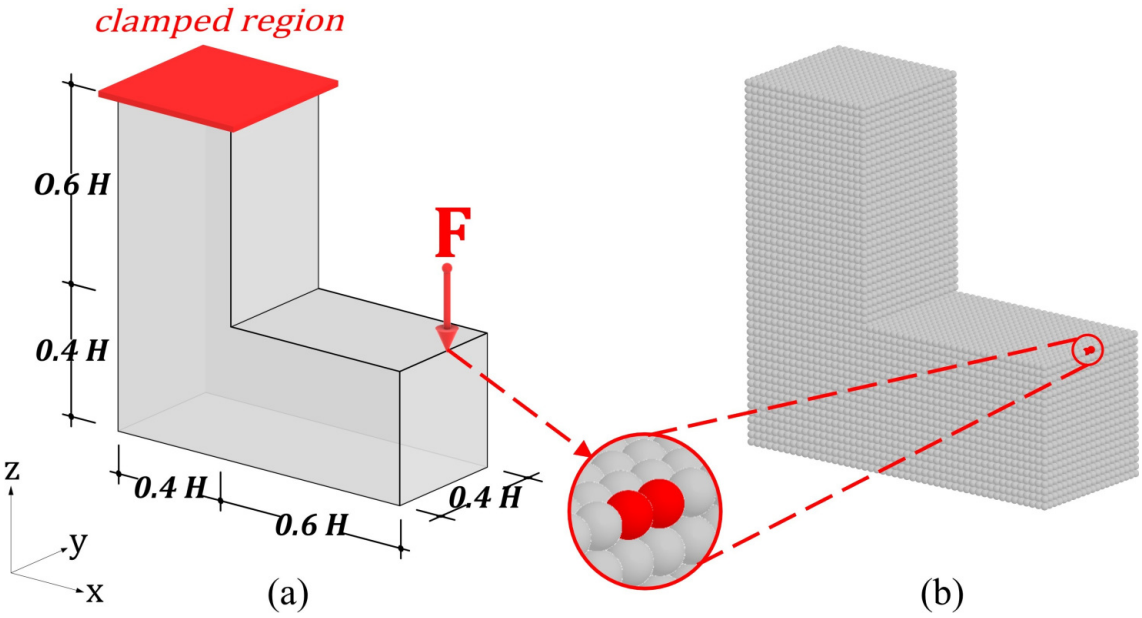
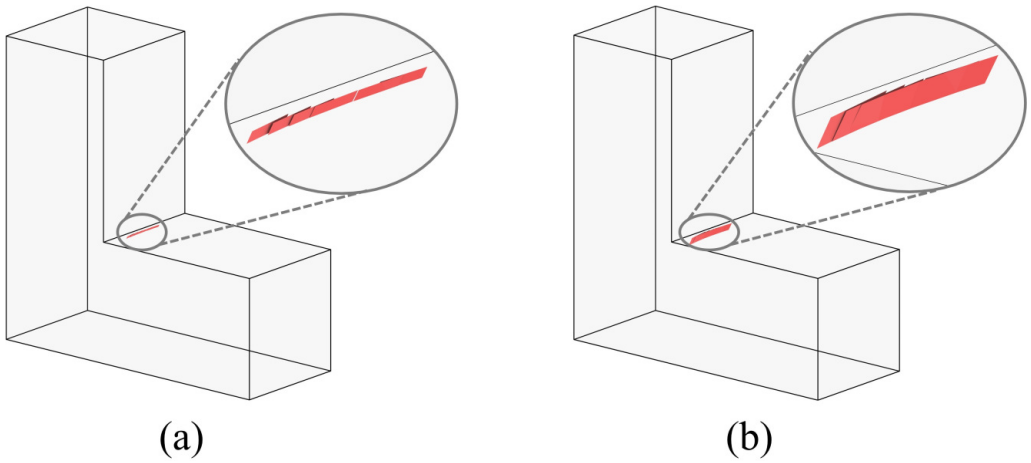


Figure 5.13 Crack positions on L-Beam geometry for (a) 2dx cracks, and (b) 4dx cracks according to critical von Mises stresses.

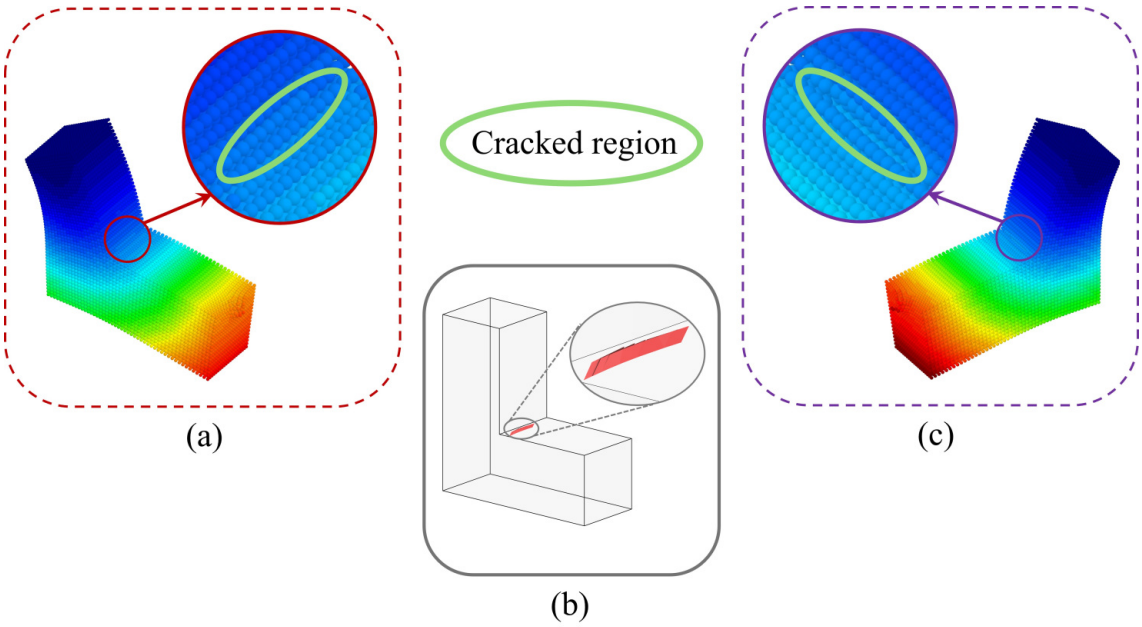


Utilizing the static FEM analysis results of an optimized topology we identify the high-spot regions where the stress values are higher than in other areas. Hence, the multiple surface cracks (with the edge length of 2dx and 4dx cracks) are involved in the design domain, as depicted in Figure 5.13. The effect of crack inclusion with PD can be visually seen in Figure 5.14. Here, the exaggerated displacement contours are given for the L-Beam structures containing cracks or not. It is clear to see the broken bonds result in opening along the cracked region which realistically represents the possible Mode-I crack in such a design problem. In this way, a more robust design will be proposed by minimizing the high-strain energy that will occur in the potential crack zone in the most effective way during optimization.

Table 5.2 Compliance and maximum deformation comparison between three optimized L-beam structures under static loading condition

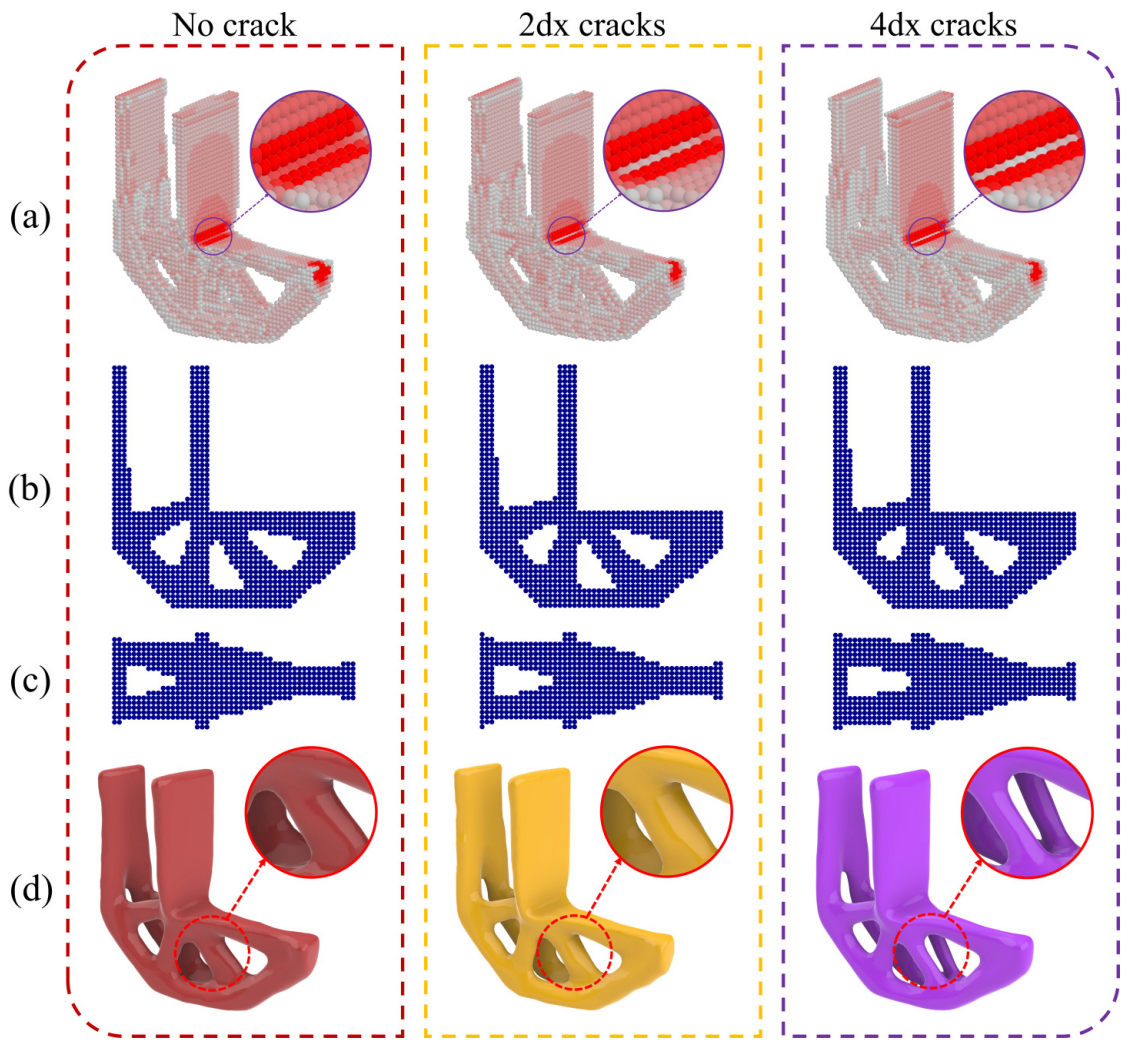
Case	Max. def. [m]	Diff. [%]	Comp. [N.m]	Diff. [%]
No crack	4.81E-05	-	3.60E-02	-
2dx cracks	4.47E-05	7.07	3.26E-02	9.44
4dx cracks	4.58E-05	4.78	3.34E-02	7.22

Figure 5.14 The effect of crack inclusion in PD model. (a) Exaggerated displacement contours before crack. (b) Crack location on structure. (c) Exaggerated displacement contours after crack is modeled.



The optimized L-beam designs are given in Figure 5.15, with strain energy distributions and geometrical details. The stress concentration region of the L-beam problem is the inner turning edge of the beam. Strain energy comparison can be visually examined in this particular region via zoomed pictures in Figure 5.15a. Here, it can be concluded that the strain energy of the particles that are very close to the cracked region is highly reduced in the 2dx and 4dx crack results as compared to the No crack result. Such an observation proves that new particle distributions (2dx cracks and 4dx cracks results) considering proper crack definition provide a better force transmission path by supporting the critical region via alternative ways. This alterations in the design domain are presented in Figures 5.15(b-d) through the plane views of optimization results and an isometric view of smoothed versions. Herein, the most evident difference between the given results is observed in 4dx cracks design. The main supporting arm is divided into two arms which lie to the right and left sides instead of supporting only the center of the critical region as seen in other designs. Furthermore, we compare the compliance and maximum deformations of three designs under static loading in Table 5.2.

Figure 5.15 Final designs of L-beam before and after cracks. (a) Strain energy distribution over the designs. (b) Left view. (c) Top view. (d) Ready-to-print smoothed versions of point cloud results.

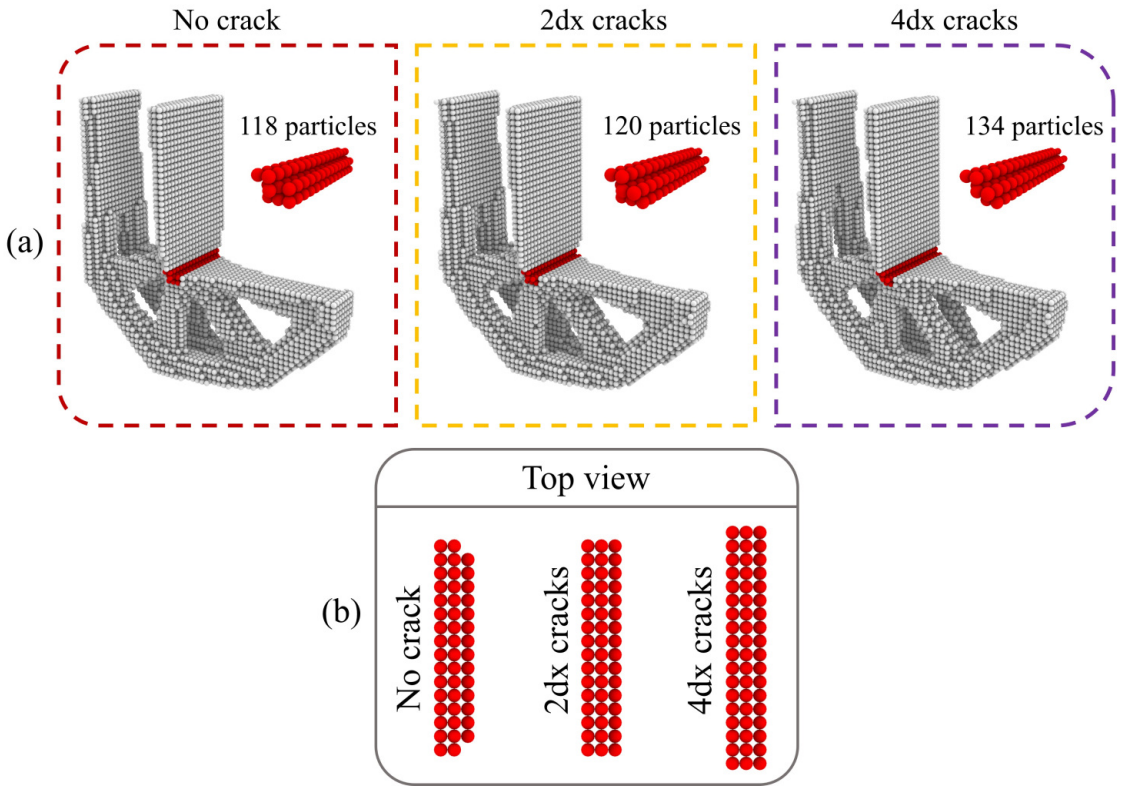


Both maximum deformation and compliance are decreased in the optimized structures considering cracks. 2dx cracks and 4dx cracks results store 9.44% and 7.22% less energy inside the structure against the same load. These are global values providing information about the entire structure. On the other hand, a box-shaped interest region covering embedded cracks is considered and the particles inside this box on the optimized designs are examined to compare their total, average and maximum strain energy values in Table 5.3. The extracted and inspected particles inside the interest region are shown in Figure 5.16. There are 118, 120 and 134 particles found in three optimized designs, respectively. These numbers basically show that the region is supported with more particles after cracks are embedded. Moreover, compared energy values given in Table 5.3 emphasizes the improved performance of the structures considering with cracks.

Table 5.3 Total, average and maximum strain energy density comparison in the vicinity of the embedded cracks between three optimized L-beam structures under static loading condition

Case	# of particles	Total en.	Diff. [%]	Average en.	Diff. [%]	Max en.	Diff. [%]
No crack	118	1.57E+07	-	1.33E+05	-	3.68E+05	-
2dx cracks	120	1.50E+07	4.352	1.25E+05	5.946	3.32E+05	9.783
4dx cracks	134	1.38E+07	12.12	1.03E+05	22.61	2.71E+05	26.27

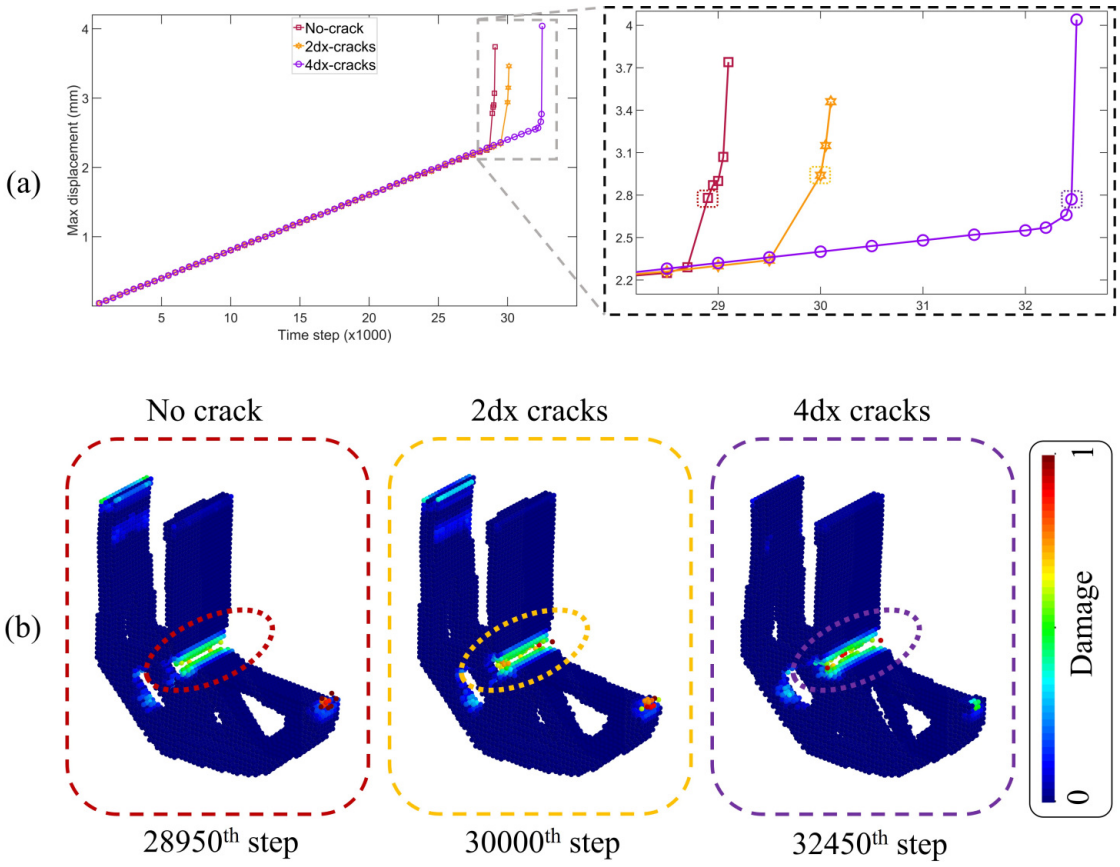
Figure 5.16 (a) The particles inside the interest region that covers embedded cracks of L-beam problem. There are 118, 120, and 134 particles inside the critical region on the optimized structures for the scenario of No crack, 2dx cracks, and 4dx cracks, respectively. (b) Top view of these particles.



Both results obtained by considering cracks have lower total, average, and maximum energy values than the initial result without cracks. However, the 4dx cracks result has a remarkable difference in average and maximum energy, with approximately 23% and 26% improvement, respectively. So far, achieving better improvements with bigger cracks may be attributed to higher geometrical differences in final designs. Such a phenomenon reveals the critical impact of crack size determination. In

the final step of the comparisons, we perform dynamic PD simulations applying the velocity boundary condition to the same particles subjected to static loading during the optimization process. In Figure 5.17a, the time-dependent maximum displacement values obtained for three designs are plotted. The sudden changes in maximum displacements can be examined via a zoomed-in plot. Moreover, the initiation of crack propagation is captured during the dynamic analyses and depicted in Figure 5.17b with the relevant time steps.

Figure 5.17 (a) Maximum displacements during dynamic analyses on L-beam designs. (b) The damage contours and the failed regions in three designs when the crack starts to propagate.



Overall, as can be detected from Figure 5.17, the fracture resistance of the structures optimized with cracks improved. Damage evaluation is started at the 28950^{th} step for No crack result, whereas crack propagation is observed at the 30000^{th} and 32450^{th} time steps for 2dx cracks and 4dx cracks results, respectively. These values correspond to the 4% and 12% fracture toughness enhancements in the 2dx and 4dx crack results against to No crack result, respectively. Similar to static analysis-based comparisons, dynamic analyses also provide a bigger improvement in 4dx cracks results as compared to 2dx cracks. Hence, it can be concluded that the crack size

should be larger than a threshold value to be able to achieve a remarkable increase in the optimized designs with cracks.

5.1.4.3 Case III: Portal frame

In the last benchmark problem, a portal frame geometry is optimized. The problem definition is illustrated in Figure 5.18a. The dimensions shown in the figure are listed in Table 5.4. Uniform pressure load, $P = 0.8MPa$ is applied along -z direction. A quarter part of the portal frame can be modeled by considering symmetry conditions. Hence, the modeled quarter domain is given in Figure 5.18b. To satisfy symmetry condition of the problem, face A and B are fixed along only y and x directions, respectively. The modeled quarter PD domain consists of 39705 particles which means the full domain has 158820 particles in total. The distance between any neighboring particles defined as $dx = 1mm$. Final volume of the optimized structure is set to 15% of the initial volume.

Table 5.4 Dimensions of the portal frame geometry

Name	H1	H2	L	D	W	B
Value [mm]	60	35	120	30	20	5.5

Figure 5.18 (a) Problem domain for the Portal frame geometry. (b) Quarter part of the portal frame for symmetric modelling. (c) PD discretization of the quarter part.

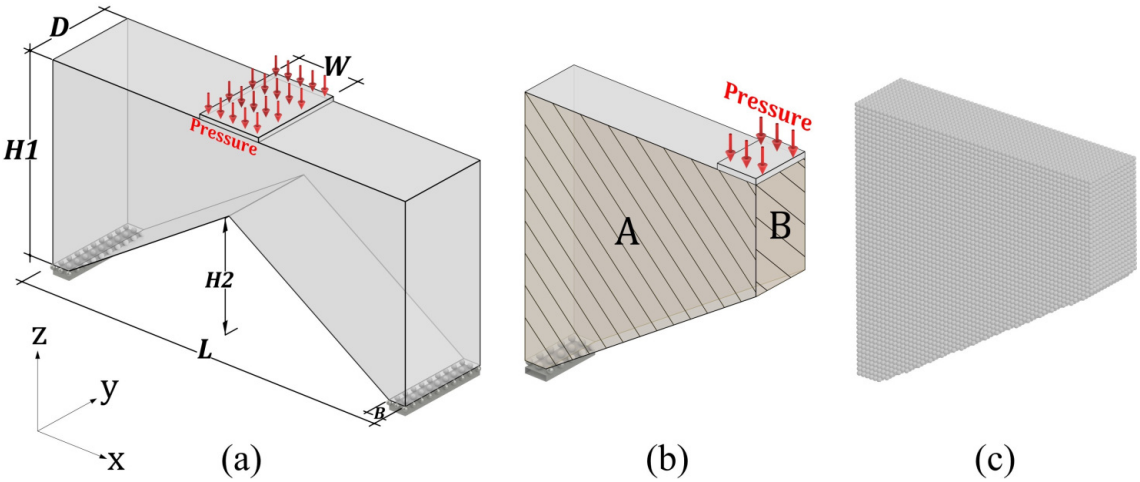
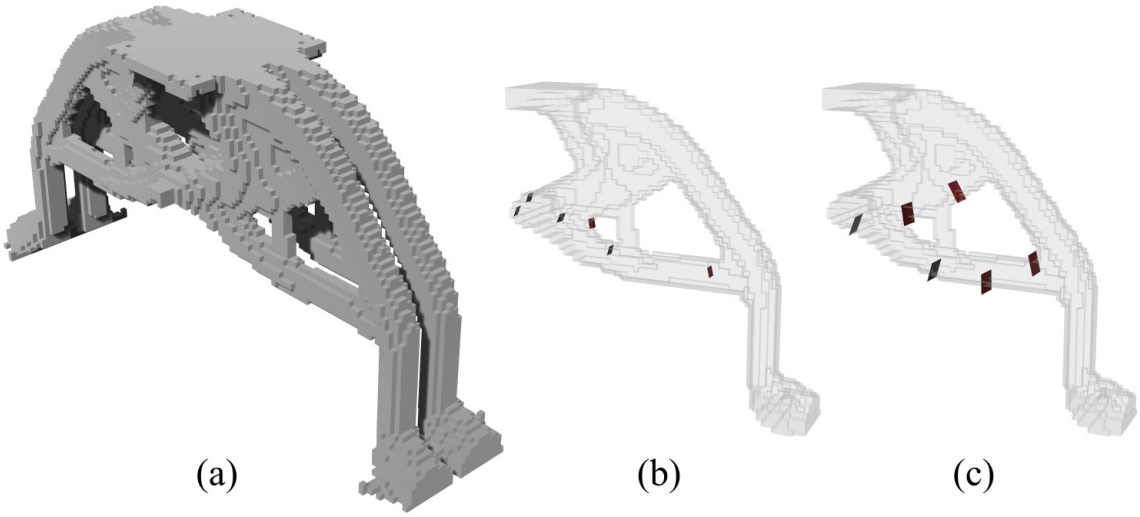


Figure 5.19 (a) The optimum result of portal frame geometry without considering cracks. Locations of the multiple (b) 2dx cracks and (c) 4dx cracks in design domain.



The initial optimization result before embedding the crack is given in Figure 5.19a. Moreover, the locations of multiple surface cracks with the length of 2dx and 4dx on the optimum result are shown in Figure 5.19b and Figure 5.19c, respectively. In this regard, two more topology optimization results are obtained by adding the cracks shown in the figure to the initial design space. The obtained results are provided in Figure 5.20. Here, three plane views of the full geometries (Figure 5.20a) and an isometric view of the quarter of smoothed geometries (Figure 5.20b) are presented to reveal the geometrical differences between optimum designs.

It is obvious that the 4dx cracks result presents a noticeable evolution in final designs compared to others. In detail, the 4dx cracks design creates new supports (check x-z plane view) and removes the links (in the middle and bottom) between two main legs (check y-z plane view). The results of the dynamic analysis of portal frame geometries are presented in Fig. 5.21. The figure depicts damage contours on three geometries at different time intervals. Notably, around the 17200^{th} time step, the initiation of damage becomes evident, primarily attributable to high-stress levels at the joint in the lower-middle section of the structure. Both the No crack and the 2dx crack results experienced damage in this particular region at approximately the same time step. However, the onset of crack formation in the 4dx size cracks result is notably delayed (until the 23000^{th} time step). Consequently, a significant enhancement in fracture resistance, quantified at 34%, is achieved in the optimized structure with 4dx cracks compared to the optimized without cracks. The ability of the structure to endure increased deformation despite damage occurring in a similar region underscores the effectiveness of the design tool.

Figure 5.20 Final designs of Portal frame before and after cracks. (a) Different plane views. (b) Ready-to-print smoothed versions of quarter point cloud results.

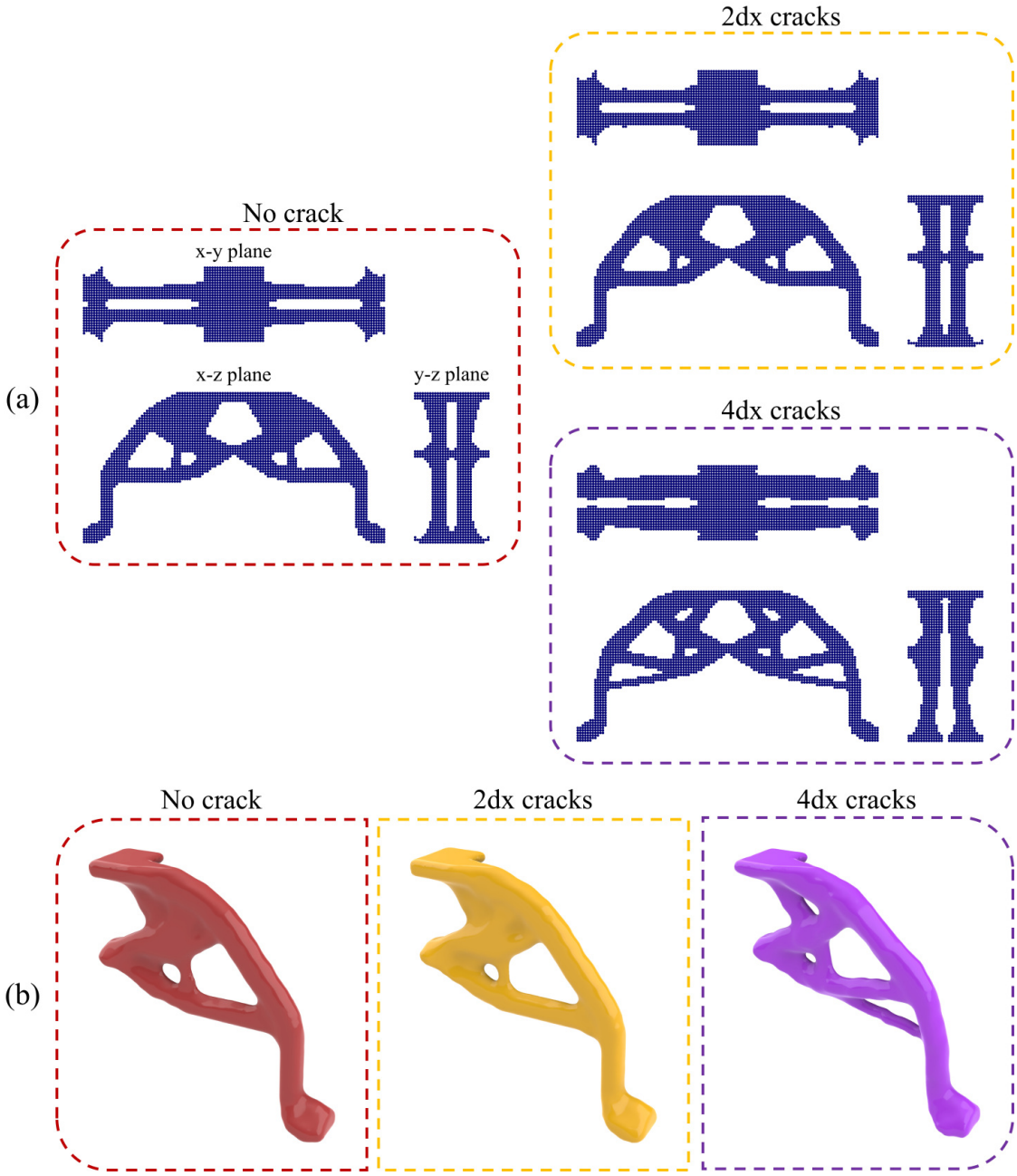
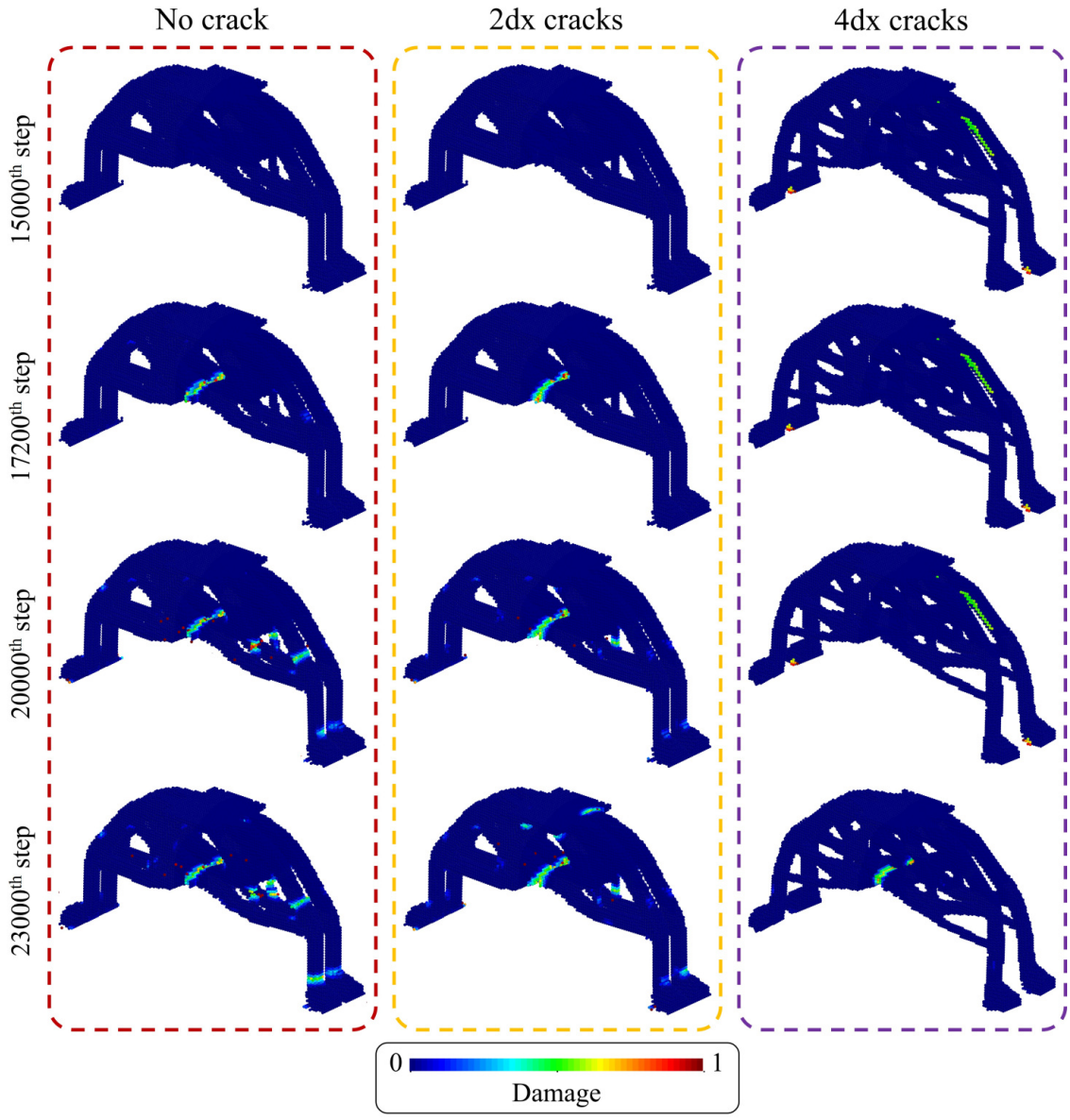


Figure 5.21 The damage contours and the failed regions from some of the selected important time steps in three designs.



5.1.5 Concluding Remarks

This research paper introduces a novel integration of failure criteria with the PD-TO framework to enhance the fracture resistance of lightweight structures during the topology optimization process. The proposed strategy effectively leverages the capabilities of PD-TO by identifying areas of high-stress concentration in the optimized structure and inserting the cracks into the relevant positions during TO. To

demonstrate the advantages of proposed strategy, the study focuses on three benchmark TO problems whereby the final structures optimized with and without cracks are comprehensively compared through static and dynamic analyses. As a result, the following concluding remarks are revealed:

- In static analyses, strain energy values of the particles inside the region of interest are compared. It is observed that the total, average, and maximum values of strain energy in the critical region are reduced in designs optimized with cracks thus indicating smoother energy distribution and decreased strain energy concentration can be obtained via the proposed method.
- In dynamic analyses, the same boundary conditions are applied to final designs (No crack and with crack results) to investigate the enhancement of the damage resistance and crack propagation in the optimum topology. The results indicate that the structures optimized by proposed method either fails later than a classical optimization result. Moreover, it is found that damage nucleation occurs elsewhere than the pre-defined critical region in the enhanced optimum topology.
- In L-beam and Portal frame problems, the fracture resistance of the structure is improved by 12% and 33% where the rectangular surface cracks with an edge length of 4 particle are embedded to the initial design domains.

Overall, the proposed framework is strongly validated by showing the fracture toughness enhancement in optimized designs considering multiple cracks in critical regions. By facilitating the creation of lightweight structures with enhanced fracture resistance and minimized strain energy, the proposed method would serve as a functional design tool for engineering applications. As a future research effort, these theoretical advancements can be validated experimentally, particularly focusing on critical geometries prevalent in industries such as aerospace and automotive engineering.

5.2 On Utilizing Peridynamics Topology Optimization for Residual Stress Minimization in Metal Additive Manufacturing

5.2.1 Introduction

This section of the thesis proposes a novel topology optimization (TO) algorithm that minimizes the residual stresses on the final product manufactured by metal AM process. In this context, peridynamics topology optimization (PD-TO) is utilized to perform TO within an integrated optimization framework, fed by thermal simulations of the L-PBF process. This approach allows us to embed potential cracks precisely in high-stress regions, enhancing the efficacy of structural simulations. The methodology is demonstrated through two case studies: the L-beam and the MBB beam. The optimization process applied to both structures leads to significant improvements in their designs. The promising results are submitted to the journal of Engineering with Computers with the equal contribution of first author (Khalilvandi Behrouzyar, Kendibilir, Cavus, Lahe Motlagh, Oren, Orhangul, Koc & Kefal (2024)). Therefore, only PD-TO results are provided in this section.

5.2.2 Novelty and Motivation

A novel TO procedure integrated with thermo-mechanical analysis is proposed. This method aims at minimizing thermally induced residual stresses in components produced through metal AM processes. Unlike previous research, our approach integrates PD-TO with AM process simulations in a sequential manner. This methodology is driven by the absence of reported studies employing PD-TO and AM process simulations. The justification behind this strategy has two aspects. Firstly, our emphasis on sequential simulations is motivated by the inherent complexity of thermo-mechanical analyses, TO, and PD simulations. Performing these simulations concurrently can be computationally expensive and time intensive. Therefore, our consecutive approach allows for a more efficient and manageable workflow, ensuring a detailed understanding of each stage's results before progressing to the next step. Secondly, this approach is used to strategically introduce hypothetical defects

using PD-TO. The introduction of defects at critical points serves as a powerful design tool, influencing the structure's response to thermally induced stresses. This innovative approach aligns with recent trends in advanced manufacturing research, emphasizing the integration of simulation-driven design methodologies.

This sesction is structured as follows. In Section 5.2.3, we provide numerical PD-TO results for two different condition: (i) before considering cracks, and (ii) considering cracks inside the critical regions in terms of residual stress results obtained for condition (i). Then, concluding remarks are provided in Section 5.2.4, summarizing key findings.

5.2.3 Numerical Results

5.2.3.1 Topology Optimization of L-Beam

Our first subject of study is the L-Beam, a common challenging structure in this field. The L-Beam, a well-established benchmark problem in the field of TO, as shown in Figure 5.22, presents an ideal test case for our framework. The geometry has the length of $L = 200\,mm$. The domain involves 32000 points for particle discretization consisting of 50 $\times$ 20 $\times$ 50 particles along the x, y, and z axes, respectively. The particle spacing is $dx = 4\,mm$. Within the PD model, a point force, denoted as F, is applied at the midpoint of the right edge of the beam. The particles at the uppermost layer of the L-beam are subjected to full constraints. The optimization objective is set to 25% target volume. In the first step, the L-beam geometry is optimized by the PD-TO method without imposing any additional constraints. Optimized topology is given in Figure 5.23. Subsequently, the metal AM process of the obtained design is simulated using the discretization which detailed in (Khalilvandi Behrouzyar et al. (2024)). Obtaining the stress tensor and von Mises stresses due to the heat cycle during the AM process, the critical regions are determined on the produced body.

Figure 5.22 The problem definition of the L-beam.

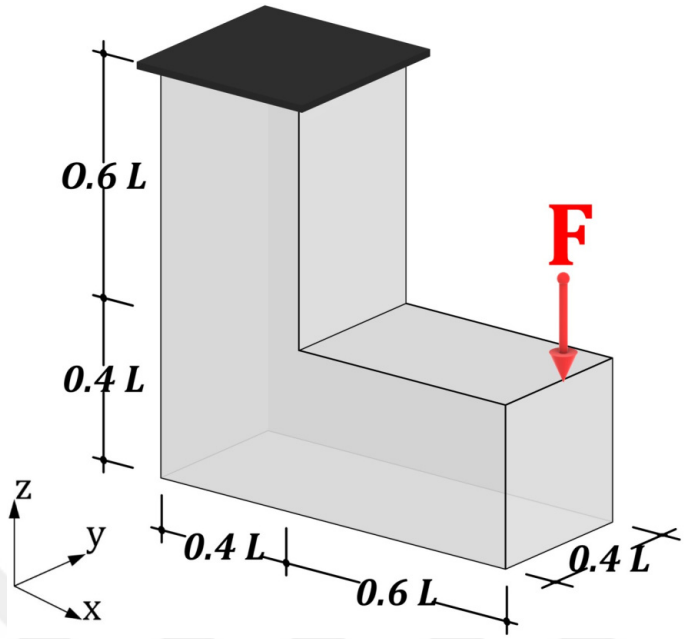


Figure 5.23 Optimum topology for the L-beam problem after the initial optimization without considering cracks. (a) Isometric view of the final geometry, (b) Plane views.

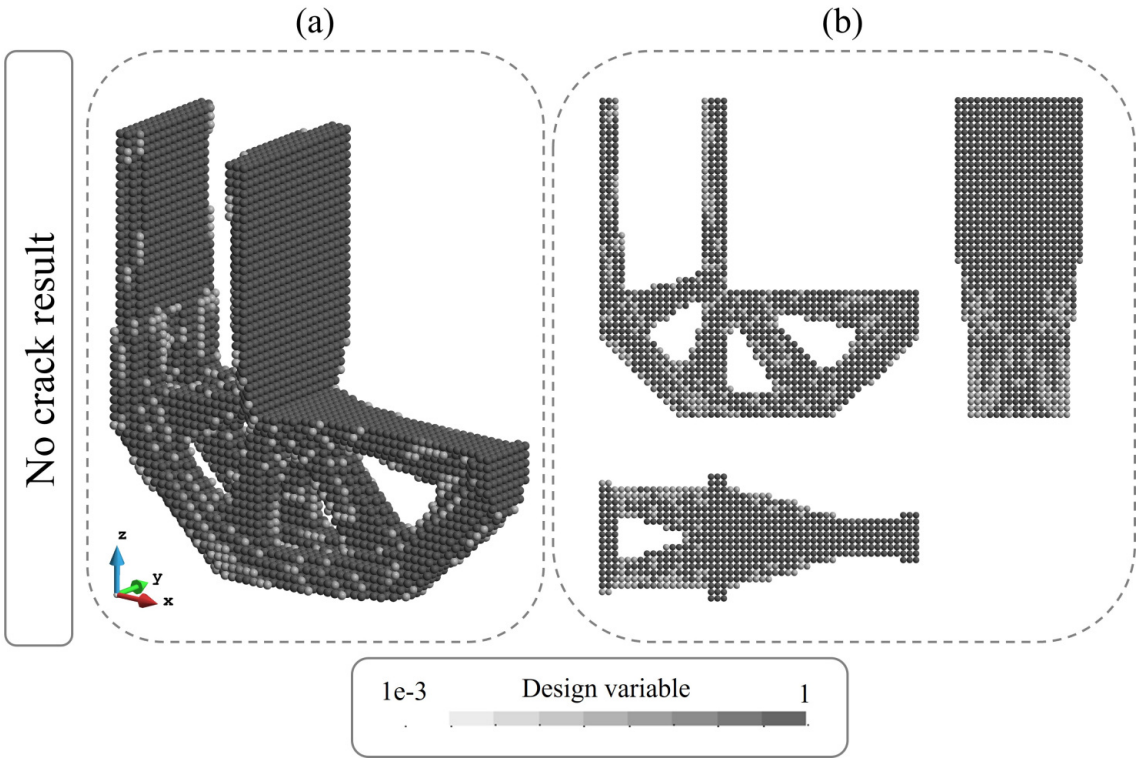
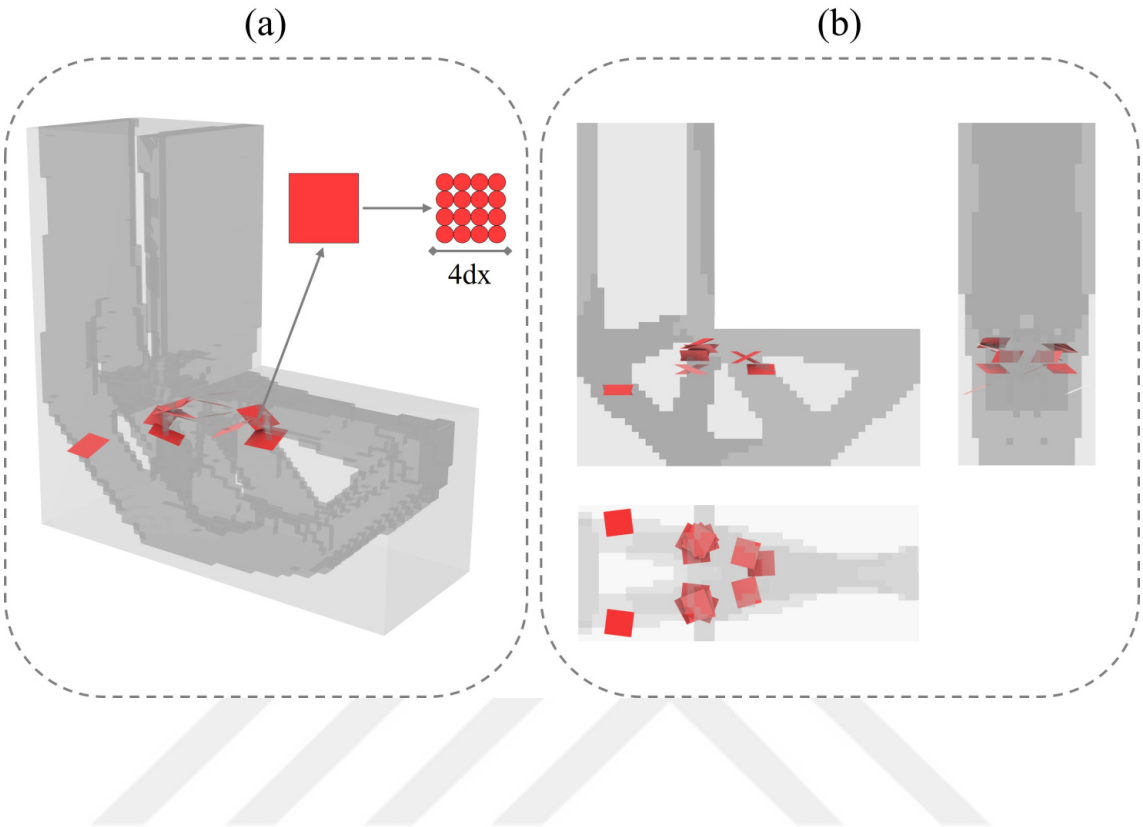


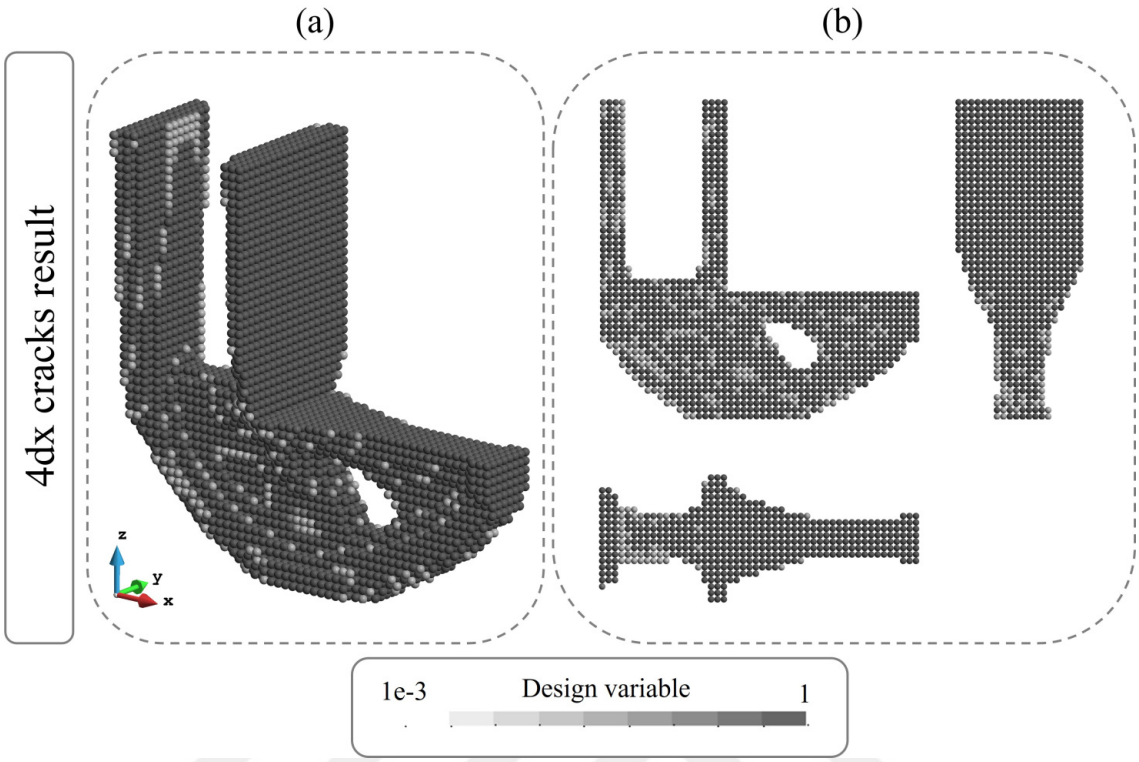
Figure 5.24 Crack locations on the optimized L-beam geometry. (a) Isometric view and (b) plane views are given for the better understanding of location and direction of the surface cracks.



Eventually, utilizing the same problem definition but breaking the intersecting bonds with the surface cracks, the PD-TO is performed once again to create new designs to decrease the residual stresses. The obtained PD-TO results considering the inclusion of 4dx cracks (Figure 5.24) within the domain are presented in Figure 5.25 from various perspectives. It is noticeable that the introduction of multiple cracks significantly impacts the geometry, leading to a reduction in the number of primary support arms when viewed from the planar perspective. Moreover, material allocation in the lower portion of the L-beam along the y-direction is altered by concentrating more particles at the center as compared to the first optimization results. After investigating geometrical differences, the next step involves comparing the outcomes derived from the AM simulation of the re-optimized geometry.

Overall, it can be concluded from the presented results in (Khalilvandi Behrouzyar et al. (2024)) that involving multiple cracks in hot spot regions resulted in a decrease in residual stress. However, the advantages may not be seen easily from the 2D or 3D plots since the stress values are available on the entire structure. In this regard, we also need to analyze the group of material points to ensure that the second optimization provides safer designs with reduced thermally induced residual stresses.

Figure 5.25 Optimum topology for the L-beam problem considering crack (a) Isometric view of the final geometry, (b) Plane views.



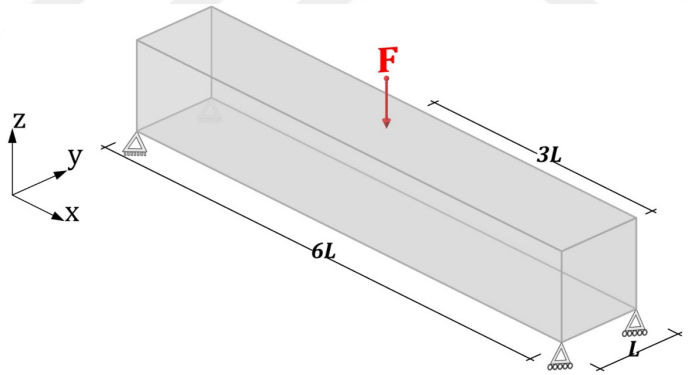
Using the stress results obtained by thermo-mechanical simulations on all points in particular regions, the average equivalent stress values and, the number of points having stress values exceeding the given threshold value in these regions are detailly compared in (Khalilvandi Behrouzyar et al. (2024)). Optimized structure with cracks provides approximately 13% and 10% decrease in the average equivalent stress in investigated two regions. In addition, the number of material points with high stress values also significantly decreased as compared to no crack results. Such revealed outcomes would be interpreted as notable improvements in reducing the undesired effects of the metal AM process. In addition, the number of material points with high stress values also significantly decreased as compared to no crack results. Such revealed outcomes would be interpreted as notable improvements in reducing the undesired effects of the metal AM process.

5.2.3.2 Topology Optimization of MBB-beam Problem

One of the most popular benchmark problems in TO literature, the MBB beam problem, is modeled with the dimensions of $0.18 \times 0.06 \times 0.06$, in three-dimensional space as illustrated in Figure 5.26. Due to the symmetric feature, the problem is analyzed by modeling one-fourth of the whole structure. The quarter part of the problem domain is discretized into $90 \times 15 \times 30$ particles in $x - y - z$ directions, respectively. Thus, the entire geometry is represented by 162000 particles/elements in total. During the material removal operation, the optimizer is set to reach the predefined volume constraint of $\overline{V} = 0.15$.

The optimization results for two distinct radius filter values are presented in Figure 5.27. As depicted in the figure, an increase in the radius value led to a reduction in the number of support arms within the structure, resulting in a simplified geometry. The compliance values for these geometries are $2.328 \times 10^{-4} Nm$ and $2.363 \times 10^{-4} Nm$, respectively. Consequently, the slightly more intricate geometry achieved with the lower radius value exhibits a 1.5% higher stiffness, albeit with a negligible difference.

Figure 5.26 The problem definition of the MBB-beam



The identified crack locations are visually presented in Figure 5.28, emphasizing their precise location and alignment through plane views. It is worth noting that the edge length of the cracks is kept the same as in the previous problem (4dx). A notable observation is the occurrence of cracks in similar areas for both geometries. The results of the second optimization, considering the surface cracks, are illustrated in Figure 5.27.

Figure 5.27 Optimum topology for the MBB-beam problem after the initial optimization without considering cracks. (a) Isometric view of the final geometry, (b) Plane views.

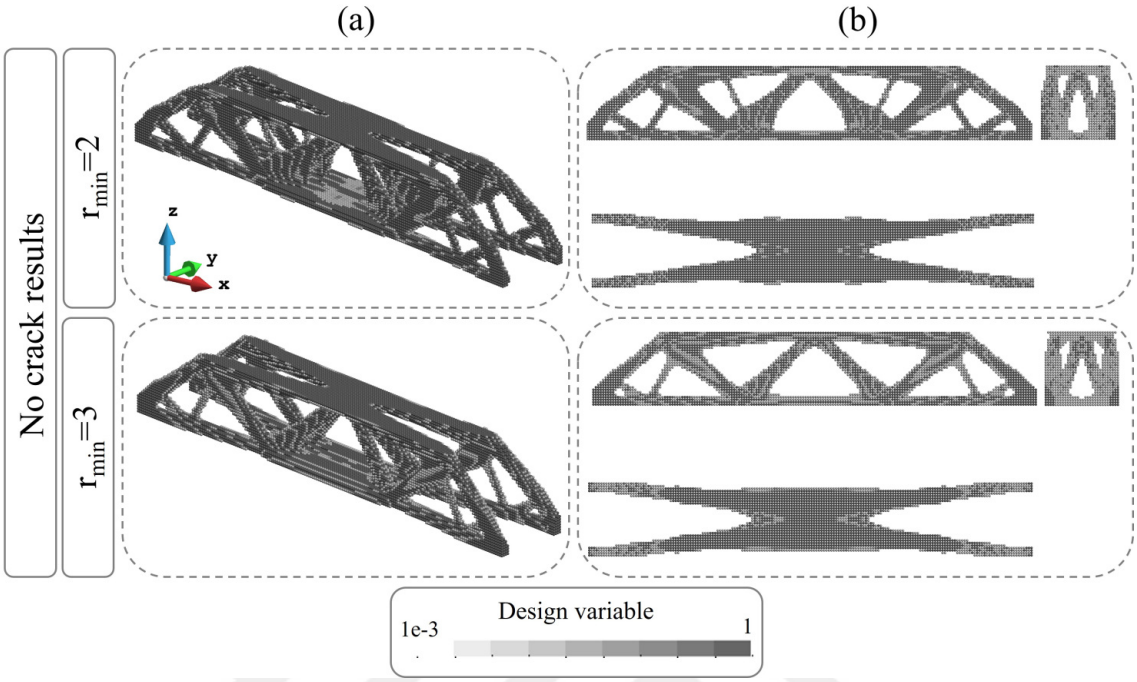
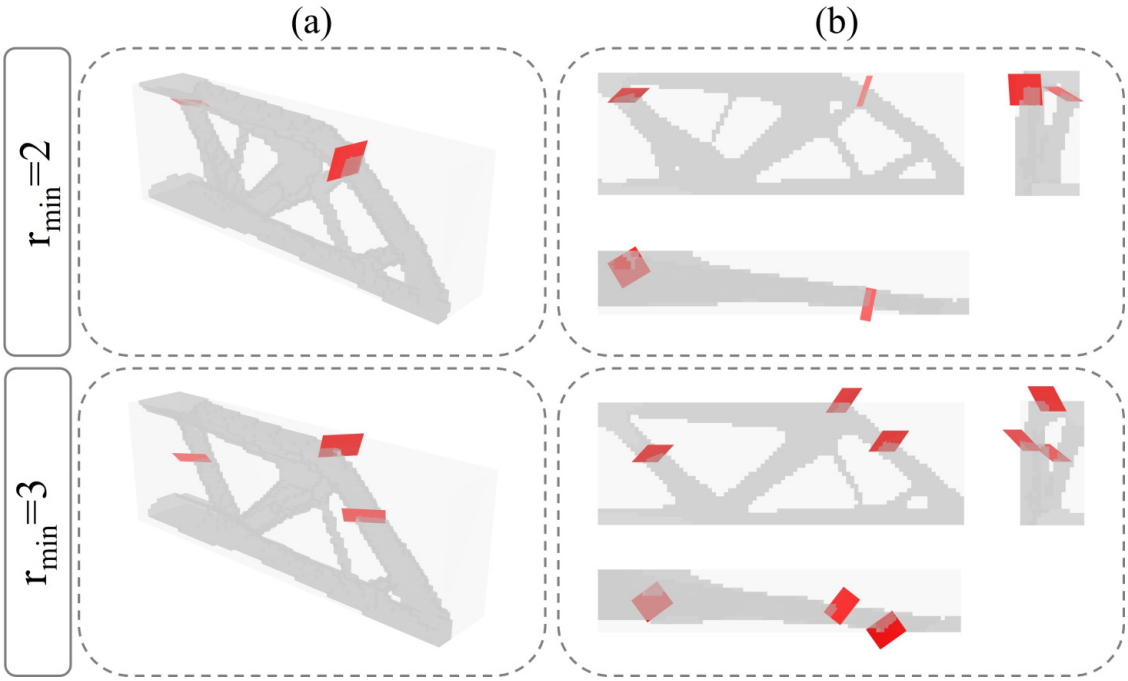
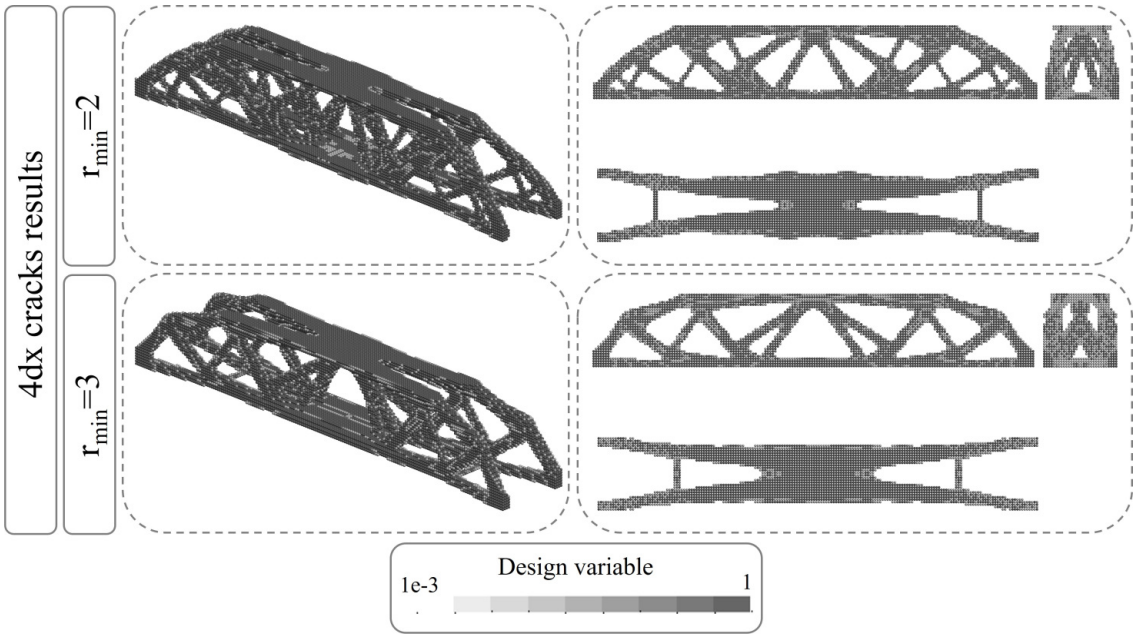


Figure 5.28 Crack locations on the optimized MBB-beam geometry. (a) Isometric view and (b) plane views are given for the better understanding of location and direction of the surface cracks.



Comparing Figure 5.27 and Figure 5.29, it is evident that the final structures achieved through the second optimization have experienced significant geometric modifications compared to those obtained in the initial optimization. Interestingly, this transformation has led to the formation of a greater number of support arms in both structures. Consequently, we anticipate that the increased presence of support arms in critical regions will ensure the uniformity of temperature distribution during production. This enhancement is expected to contribute to a reduction in residual thermal stresses within these specific areas.

Figure 5.29 Optimum topology for the MBB-beam problem considering cracks. (a) Isometric view of the final geometry, (b) Plane views.



The specified regions can be found in (Khalilvandi Behrouzyar et al. (2024)), correspond to the areas where thermal stresses are highly concentrated. Tables given in (Khalilvandi Behrouzyar et al. (2024)) present the average von-Mises values calculated within the interest regions for structures optimized varying R_{min} values. From the provided tables, it is revealed that the stress values in the new geometries are remarkably lower than the results of no crack case. Besides the notable observation of up to a 15% decrease in the average stress value, a significant finding is the significant percent reduction in the total number of points exhibiting high stress values.

5.2.4 Concluding Remarks

This research introduces a sequential topology optimization framework to reduce thermally induced residual stresses in additively manufactured components. By combining thermo-mechanical analyses with the PD-TO method, the framework optimizes temperature distribution in metal AM processes, resulting in more reliable products with lower residual stresses. Case studies on the L-beam and MBB-beam show the method's effectiveness in reducing residual stresses and improving structural performance.

Introducing cracks in the L-beam improved stress distribution by adding material to critical areas, reducing thermal and residual stresses. Though minor localized stress increases were noted, average equivalent stress decreased by about 13% and 10% in specific regions, highlighting the role of varied supporting arms in dissipating thermal stresses. In the MBB-beam, cracks improved stress distribution and significantly reduced residual stresses in two scenarios. The introduction of cracks led to a 15% decrease in average stress and fewer high-stress points.

5.3 Lightweight Engine Bracket Design for Metal Additive Manufacturing: Peridynamics Topology Optimization for Reduction of Thermal Stresses and Improved Structural Performance

5.3.1 Introduction

This section presents the integration of thermo-mechanical simulation of metal additive manufacturing (AM) process with peridynamics based topology optimization (PD-TO) applied to an engine bracket. PD-TO method enables us to consider the formation of cracks at locations with high residual stresses. The PD-TO method is applied both with and without considering the cracks, with crack locations determined based on residual stress calculations during selective laser melting. Both optimization approaches result in a 43% reduction in the weight of the reference model. Experimental studies demonstrate that PD-TO, including crack formation, yields a lightened geometry with significantly similar strain energy to the reference model.

These findings underscore the efficacy of PD-TO in optimizing metal AM structures while considering residual stresses, paving the way for lightweight and structurally robust designs in engineering applications. The research outputs presented in this section are prepared as a journal paper study with the help of co-authors and submitted to the journal of Additive Manufacturing (Kendibilir, Khalilvandi Behrouzyar, Cavus, Lahe Motlagh, Oren, Orhangul, Koc & Kefal (2024)).

5.3.2 Novelty and Motivation

Addressing potential residual stress-induced defects caused by the metal AM process is of great importance considering the increased utilization of AM technologies in the production of lightweight designs created by TO. In this context, the application of thermo-mechanical simulations specific to the metal AM processes, followed by strategic actions to mitigate residual stresses and distortions using the simulation results within the TO framework, emerges as a crucial approach. Therefore, this approach would enhance the final quality and reliability of the high-performance engineering structures by minimizing the undesired effects that may occur due to poor designs that do not consider the production phase sufficiently. To the best of the authors' knowledge, there is no existing research that integrates thermally induced stresses from AM processes into the PD-TO analysis. In this study, we have enhanced the PD-TO method by enabling the integration of residual stress calculations into the optimization processes. We operate under the assumption that cracks may potentially form at points of high residual stresses. Leveraging the peridynamic topology optimization's ability to analyze discontinuities such as cracks, we aim to reduce the weight by accounting for these residual stresses and incorporating structural damages within the optimization process. This advancement is crucial, especially considering the significant impact of high-temperature gradients on mechanical properties during metal AM process. In addition to numerical studies, the effectiveness of the developed optimization strategy is also validated through experimental results.

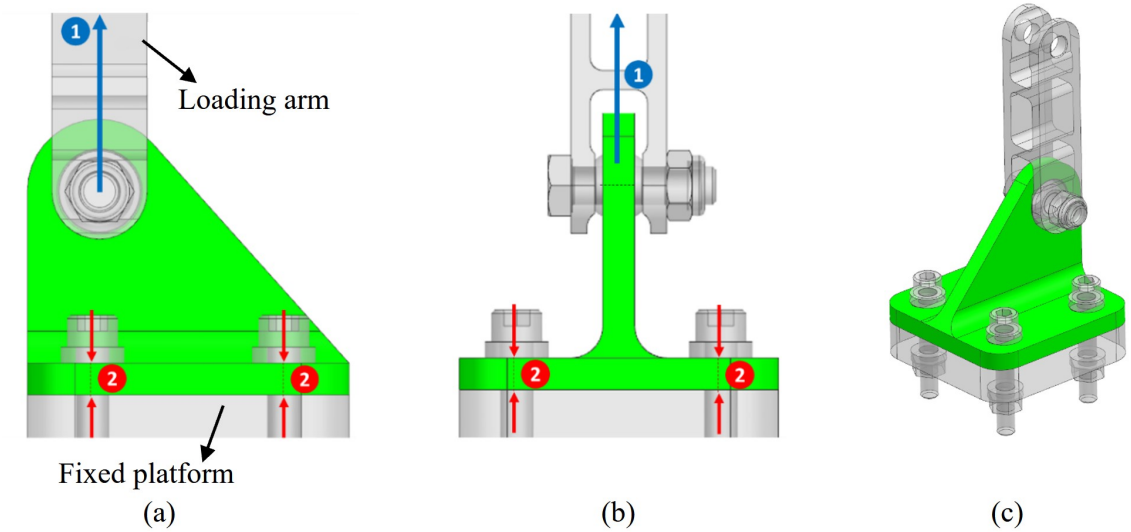
The remainder of this chapter is organized as follows. Sections 5.3.3 and 5.3.4 provide the problem definition and PD model for engine bracket. Then, Section 5.3.5 explains the sequential optimization strategy utilized for the residual stress minimization. Moreover, the numerical results are provided in Section 5.3.6. Furthermore, manufacturing and deformation measurement details of the produced part are explained in Section 5.3.7. Experimental test setup and results are given in Sections

5.3.8 and 5.3.9. Finally, the obtained outcomes are interpreted in Section 5.3.10.

5.3.3 Problem Definition for Engine Bracket

The part to be reduced in weight in this study is a functional bracket. The geometry of the problem is provided by TEI (TUSAS Engine Industries) that operates under static load, enabling the attachment of a turboshaft engine to a fixed platform. The relevant part is responsible for bearing the loads arising from the weight of the engine and is not dynamically stressed. When the geometry is attached to the platform, its relationship with the surrounding components and loading situations are illustrated in Figure 5.30. In this application, the bracket is fabricated using a nickel-based IN718 alloy, while tool steel 1.2344 has been selected for the manufacturing of the fixture. Furthermore, the fixture's durability was enhanced through a surface hardening process via heat treatment, ensuring its hardness surpasses that of the specimen, thereby effectively preventing any crushing of the fixture. To see the material properties of the fixture and bracket, please check the full paper (Kendibilir et al. (2024)).

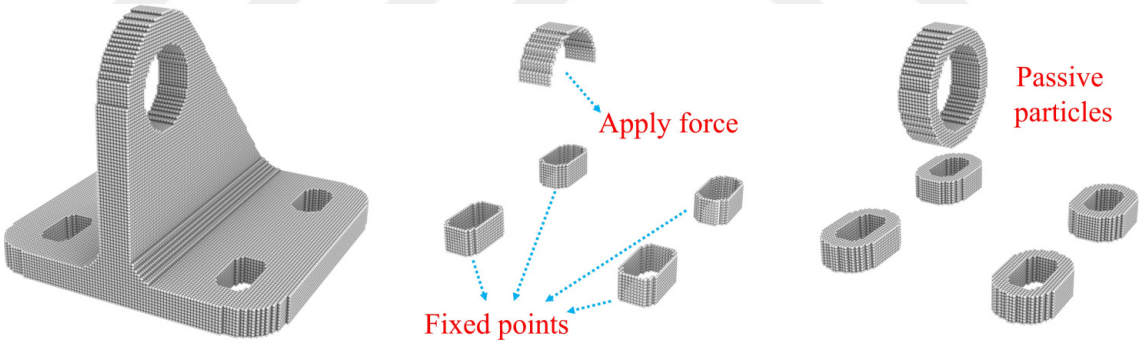
Figure 5.30 Demonstration of fixture assembly, loading and boundary conditions (a) Right view (b) Front view (c) Isometric view.



5.3.4 Particle Model for PD-TO Analyses

The PD model of bracket geometry described in Section 5.3.3 consisting of uniformly distributed particles is shown in Figure 5.31. Considering the dimensions of the geometry, particle size dx is set to $1mm$ for achieving high resolution of discretization. As a result, full PD domain depicted in Figure 5.31a involves 145204 particles in total. In Figure 5.31b, the fixed points around 4 holes and force applying points are shown. We restrict the all components of displacements (along $x-y-z$ axes) for the fixed points inside the holes. Total force is applied as body force density by distributing equally to the loaded points. On the other hand, the design variable of some regions can be kept stable during TO by defining them as passive points. These regions are generally chosen by the vicinity of boundary and loading condition regions due to the high concentration of strain energy. In this regard, we determine the passive particles as shown in Figure 5.31c to constantly support the holes during TO. Minimum filter radius selected as $R_{min} = 3dx$ for PD-TO analyses. Another PD parameter, horizon size (δ), is limited by $\delta = 3.015dx$ for the sake of computational cost.

Figure 5.31 (a) Particle model of the bracket geometry. (b) Selected particles for boundary conditions. (c) Passive particles during topology optimization process.

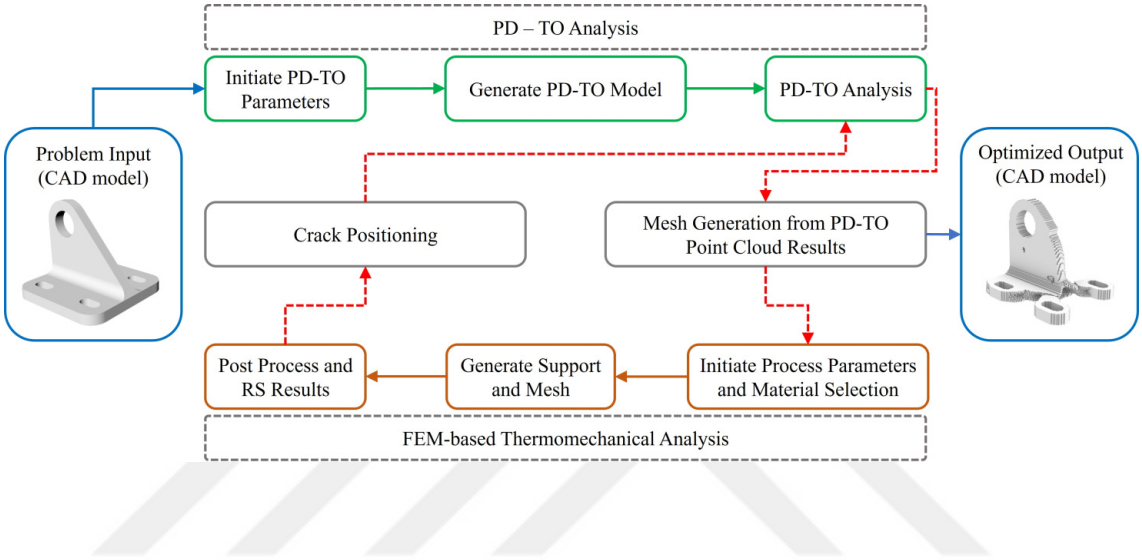


5.3.5 Sequential Optimization Strategy

In our proposed design framework, topology optimization and thermo-mechanical simulation processes follow each other to achieve better designs considering both strain energy and residual stresses on the optimized structure as clarified in Figure 5.32. We first topologically optimize the problem domain via the PD-TO method

and simulate the AM process to calculate the residual stresses, respectively. Hence, the first PD-TO result becomes an input for thermo-mechanical simulation. The full-field residual stress data on optimized geometry obtained from metal AM simulation then can be utilized as an input for creating imaginary defects in the initial design domain for the second PD-TO analysis. As a result, the second PD-TO operation finds another optimum design while counting imaginary crack locations during the TO process.

Figure 5.32 Sequential optimization strategy framework.



5.3.6 Numerical Results

In this section, we provide the numerical results obtained by PD-TO method. Moreover, thermo-mechanical simulations results can be found detailly in which is submitted to a journal with high impact factor. First, the design domain is topologically optimized without considering any additional criteria related to metal AM processes. Here, the optimization results are given in Figure 5.33 providing different views of the particle based material distribution along with the resultant closed polysurface in STL format prepared for simualtions. The thermo-mechanical simulation process encompassed essential steps such as manufacturing simulation, subsequent procedures like cutting from the baseplate, and the removal of supports. Following these manufacturing steps, a meticulous post-processing phase ensued, focusing on the extraction of data related to both residual stresses and the Cauchy stress tensor.

After obtaining the residual stress distributions of the optimized structure without considering any process-induced effect (Fig. 5.33e), the following step is to reveal

the most critical locations that are prone to cause defects or impurities in the final product. In this regard, we identify the possible crack locations by considering Griffith's criterion and the first principal stress in the positions where von-Mises stress values are highest as compared to others. Hence, we consider the elements carrying high stress values in the most critical 15% region, and introduce the imaginary square-shaped cracks with an edge length of 6 particles as depicted in Figure 5.34. The total number of cracks in the problem domain is 20 and these imaginary defects are involved in the PD-TO process for the second optimization by only breaking the bonds between necessary PD particles.

Figure 5.33 PD-TO result without considering any imaginary defects in (a) Isometric, (b)Top, (c) Right, (d) Front views.

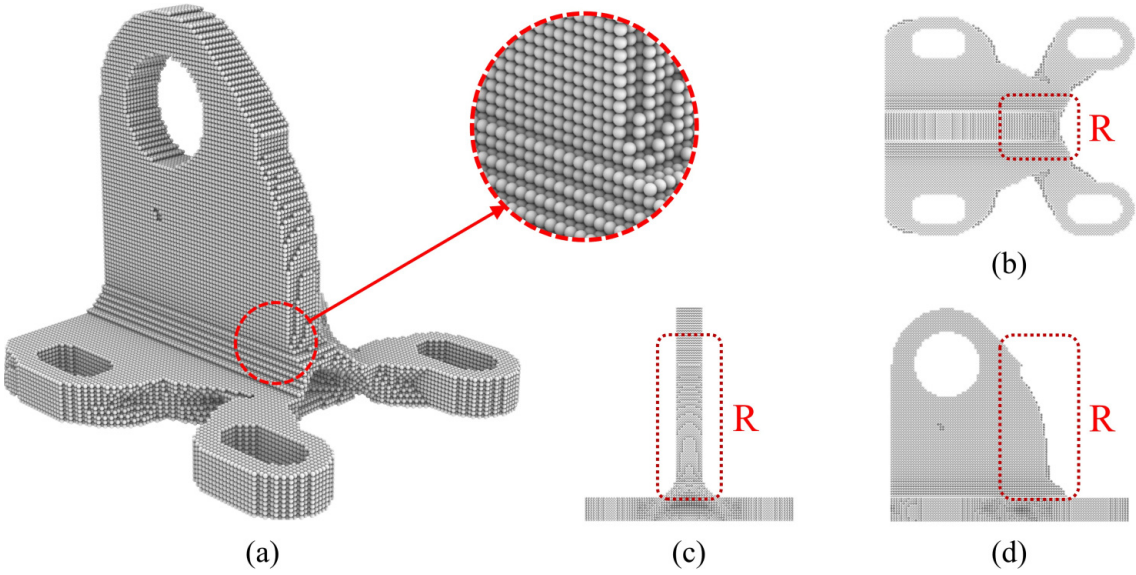
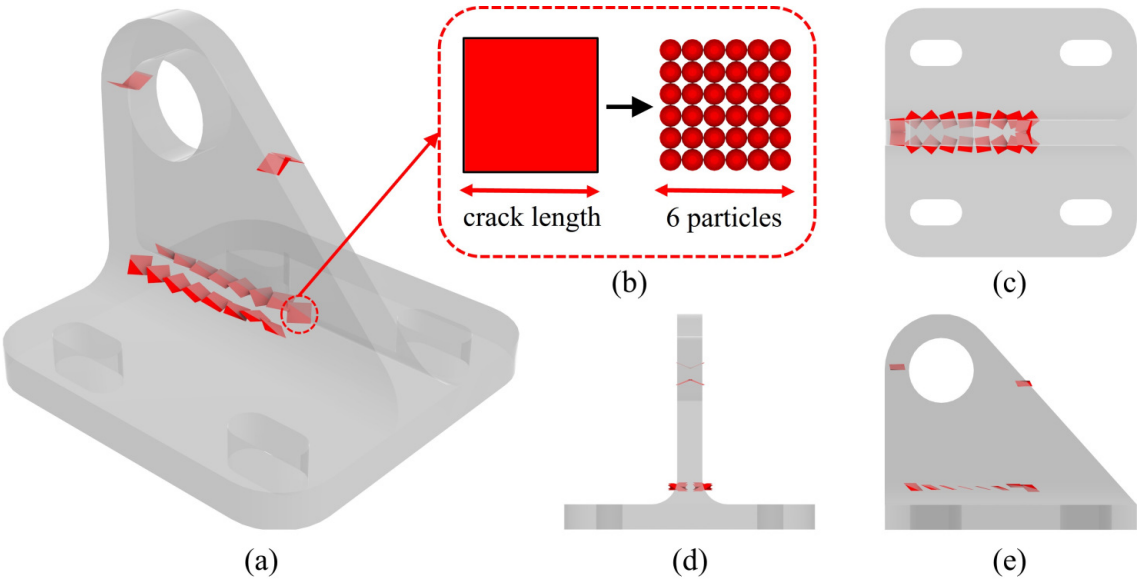


Figure 5.34 (a) Location of the multiple cracks involved in the initial design domain. (b) Dimensions of a square-shaped crack, (c) Top, (d) Right, (e) Front views of the design domain with cracks.



The result of second PD-TO operation where the design domain contains multiple cracks is depicted in Figure 5.35. Note that, the final volume fraction is the same as optimized without considering cracks. Comparing geometrical features between the first and second PD-TO results reveals some visible differences at specific region (highlighted with R in Figures 5.33 and 5.35) of the engine bracket. Especially, isometric and front views depict the modifications on the lowest portion of the region R. In the second result (see Figure 5.35), there is a space at this location while the first result(see Figure 5.33) is fully filled at the same location. Moreover, observing the right view from down to top in the mid-portion of the structure points out the varying the material distribution especially at close regions to the embedded cracks. To gain a more intricate understanding of the variations in residual stress levels at locations where cracks were initiated (refer to Figure 5.34), specific cross sections were selected for analysis.

Figure 5.35 PD-TO result considering imaginary defects in (a) Isometric, (b) Top, (c) Right, (d) Front views.

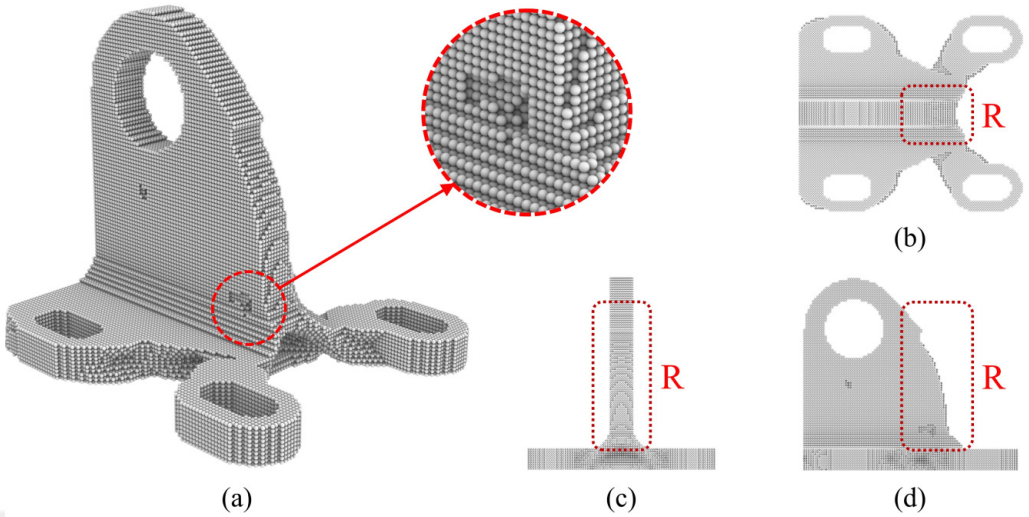


Figure 5.36 Smoothed holes. (a) PD-TO result considering cracks, (b) The final state of the design given in (a) with smoothed holes.

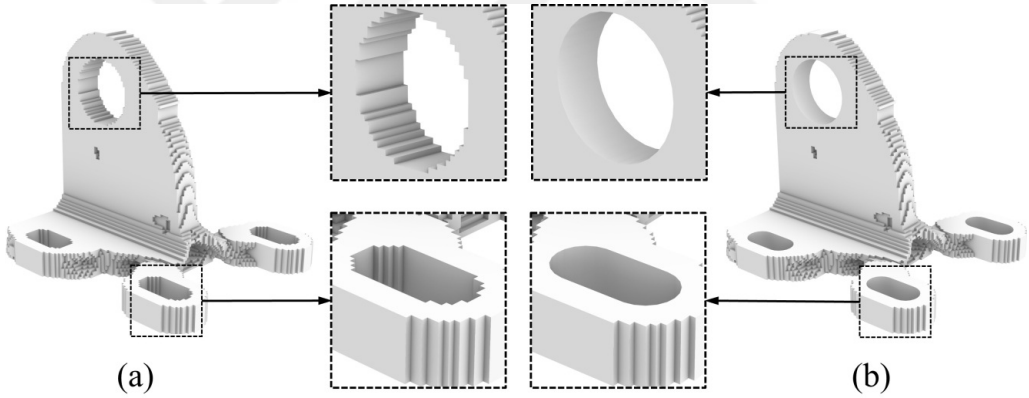
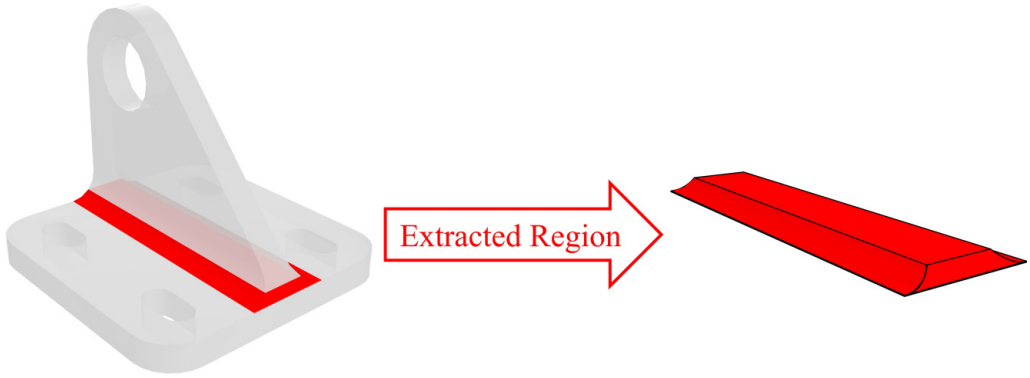


Figure 5.37 The critical region where the residual stress values obtained by thermo-mechanical analyses for two optimized designs are compared.



The numerical stress results are detailly compared in the relevant region. We de-

termine an area of interest to evaluate all points in the 10 - 13 mm height range of the structure. The location of this area of interest on the structure is shown in Figure 5.37. In the thermal results obtained with both the first optimization and the optimization obtained by considering the crack, all points inside this region are separated and the stress values on these points are compared in Table 5.5. Approximately 1800 points were detected in the relevant region for both results. As can be concluded from this table, both the maximum and average stresses are noticeably reduced. In addition, the number of points with higher stress values than certain threshold values is also compared to show how much the number of points with high stress values is decreased. Accordingly, while there were 248 points with stresses higher than 600 MPa, the proposed optimization result reduced this number to 35. For the 700 Mpa threshold value, the difference is even more striking and the number of 90 points is reduced to almost zero. As a result, the comparison of the residual stresses in the similar (critical) region through numerical data provides much more solid evidence that the residual stresses in the structure are reduced.

Table 5.5 Comparison of maximum and average residual stresses as well as the number of high stress carrying points inside the interest region for two optimized results: No crack and With crack results

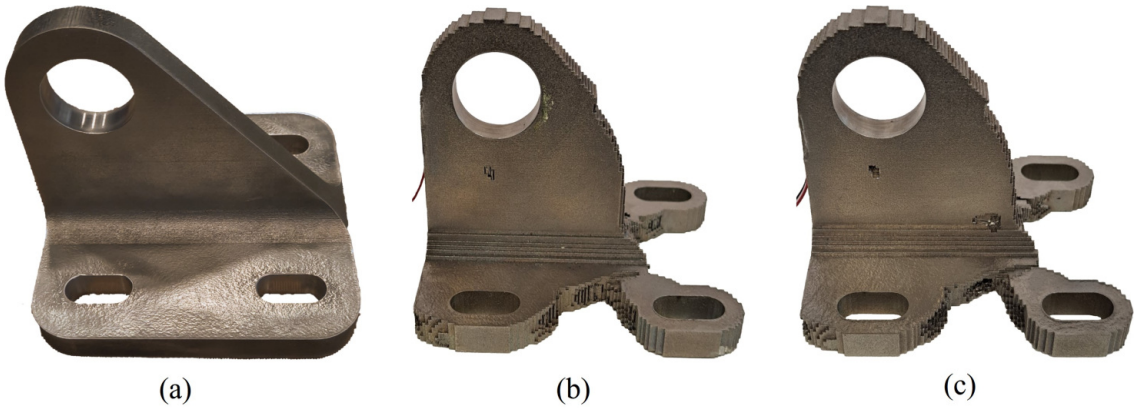
Maximum stress (MPa)			Average stress (MPa)			Threshold	Num. of points	
No crack	With crack	Diff.%	No crack	With crack	Diff.%	(MPa)	No crack	With crack
912.3	869.3	4.7	428.5	389.0	9.2	600 <	248	35
						700 <	90	3

5.3.7 Manufacturing and Deformation Measurements of Manufactured Parts

Considering the boundary and loading conditions and target volume, limited geometrical differences are obtained in the given design domain. Therefore, the practical assessment of the proposed design method can be performed by using appropriate metal 3D printing process simulations and conducting experimental tests under the same loading conditions for the three designs: 1. Initial domain, 2. PD-TO without crack, and 3. PD-TO with crack. In this regard, the two light-weighted designs along with the initial design were produced by an EOS M290 machine using the same laser parameters employed in the thermo-mechanical simulations for the ex-

perimental validation of the study (Figure 5.38).

Figure 5.38 Additively manufactured parts. (a) Initial design. (b) PD-TO result without considering crack. (c) PD-TO optimized considering cracks.



After the parts are manufactured by TEI, these structures were carefully separated from the base plate using Wire-EDM (electrical discharge machining) to minimize any impacts during detachment. Subsequently, all parts were scanned by TEI using the ATOS ScanBox, a 3D optical measurement system, to obtain surface coordinates reflecting the final states of the parts, which have distortions due to the manufacturing process. These surface coordinates were then compared with the original CAD file, which represents the ideal/undeformed state, to accurately calculate the distortions caused by metal AM process. These ATOS measurement results are available in Kendibilir et al. (2024). Since it is a surface measurement technique, this method only allows us to make comparisons on the surface deformations and the residual stresses present on the surface. Therefore, we also designed an experimental test setup in Section 5.3.8 to compare the overall performance of the manufactured designs to ensure that the proposed method offers better designs.

5.3.8 Experimental Test Setup

The location of strain gauges is critical for validating structural analysis results obtained from simulations. The process of placing the strain gauges involved an analysis of the normal strain distribution along the tensile axis, notably the z-axis. We observed that the maximum strains occur in the area where the load is applied. However, it is not practical to install strain gauges in this region for experimental testing. Therefore, we strategically positioned the strain gauges in a

region where strains were observed to be relatively higher compared to other areas. This location is precisely 46 mm above the bottom of the bracket. The test fixture and experimental setup can be found in Kendibilir et al. (2024). Two series of tests were planned. In the first series, the structures were subjected to a linearly increasing load along the z-axis, escalating from 0 to 5 kN over a duration of 60 seconds. The second series involved a linearly increasing load from 0 to 10 kN applied over a period of 120 seconds. Each test series was replicated three times on the specimens, resulting in a total of six tensile tests performed for each individual sample. This methodology was designed to ensure a comprehensive understanding of the material response in a linear region.

5.3.9 Experimental Results for Optimized Brackets

After completing the tests used to determine the behavior in the elastic region, the averages of the data obtained for each geometry were calculated. Subsequently, final load-strain plots were prepared based on these averages (Figure 5.39). As a result, despite a 43% reduction in weight, both optimized geometries exhibited reasonable outcomes in terms of strain energy. However, the geometry optimized without considering any crack (classical TO) stored a 14.5% higher strain energy, an acceptable rise given the significant weight decrease. On the other hand, the geometry optimized with pre-defined cracks (proposed TO framework) demonstrated superior performance, with only a 0.67% increase in strain energy as compared to the initial design. This underlines the effectiveness of the proposed PD-TO framework in balancing weight reduction and structural integrity by considering metal AM-induced residual stress concentration regions.

Figure 5.39 Strain-load plots of the specimens

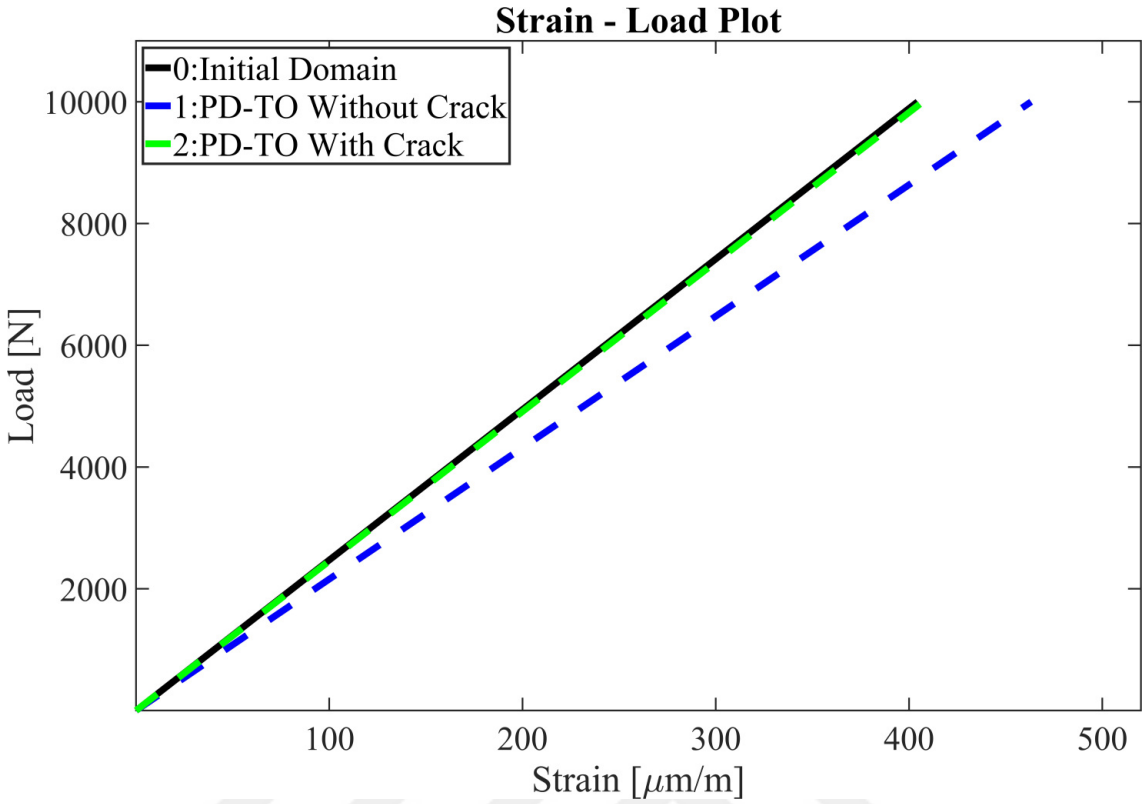


Table 5.6 Comparison of the Strains and Strain Energies

Structure [μm/m]	Compliance [$N\mu$m/m]	Difference [%]
Initial Domain	2.02 $\times 10^6$	–
PD-TO Without Crack	2.32 $\times 10^6$	+14.5%
PD-TO With Crack	2.04 $\times 10^6$	+0.67%

5.3.10 Concluding Remarks

This study performs a PD-TO framework, assisted by thermo-mechanical simulations of metal AM, to mitigate residual stresses in the engine mounting bracket produced via the LBPF process. This framework is experimentally validated by measuring distortions over the surface and comparing elastic deformations under mechanical tests on three designs. The PD-TO method puts multiple cracks into the high-spot regions with high residual stresses found by thermo-mechanical analyses over the structure optimized without considering any manufacturing

process defects. Both the PD-TO and the thermo-mechanical simulations maintain consistent particle/element discretization sizes to facilitate effective communication between the two, enabling precise placement of cracks within the initial design domain to strategically reduce stress concentrations. For the thermo-mechanical simulations of the LBPF process, a single set of process parameters was selected, and the specimens were fabricated using these parameters on an EOS M290 system.

For two lightweight results obtained by PD-TO, residual stress results are extensively compared through stress contour plots over the outer surfaces and some cross-sections extracted from the structures. Similar stress distributions are observed on the surfaces for both designs. However, when the crack-added critical region is deeply investigated by sectional cuts it is revealed that the proposed method provides reduced residual stresses in the most critical region of the manufactured structure. A closed surface covering a point cloud PD result has many sharp corners since we create voxel meshes around the PD particles. However, to remain faithful to the voxel mesh-based numerical analysis results, we do not apply smoothing operations to the geometries produced for the test. Only the inside of the holes are modified to make the assembly of specimens and text fixtures possible. Consequently, three geometries: (a) initial design, (b) PD-TO result without considering crack, and (c) PD-TO optimized considering cracks, are manufactured by the SLM process. The final structures are experimentally compared via surface distortions and mechanical tests for validation purposes.

Accordingly, the final concluding remarks are listed as:

- Linear deformation comparison revealed that the optimized structure by the proposed method has much lower strain energy against conventional optimization results which can be obtained by only considering loading conditions.
- Despite the weight of the structure is 43% decreased, the proposed design shows almost the same performance to initial design in compliance results.

Such outputs reveal the superior advantages of utilization of PD-TO in enhanced metal AM objected optimization algorithms. The following points may be concerned in the future studies:

- An advanced smoothing operation may provide better results in the final product by reducing the stress-concentration possibility around the sharp corners.

- Moreover, different type of AM processes can be studied with PD-TO to mitigate the process induced failures or undesired effects.
- In existence of computationally cheap large scale thermo-mechanical analysis methods, PD-TO can be fully coupled with these methods and optimization would consider thermo-mechanical results during TO process works.

6. GENERAL CONCLUSIONS

6.1 Achievements against the Objectives

The objectives of the research efforts provided in this thesis are listed in Section 1.3. Accordingly, the achievements of this research against the pre-defined objectives can be listed as follows:

- Three different density-based TO algorithms including (1) bi-directional evolutionary structural optimization (BESO); (2) optimality criteria (OC); and (3) proportional approach (PROP) is coupled with peridynamics method in Kendibilir et al. (2022) and Kendibilir et al. (2024) for the optimization of three-dimensional structures with/without cracks.

- The proposed methods in Kendibilir et al. (2024,2) are comprehensively validated by solving different benchmark problems available in TO literature. It is shown that one can easily embed crack/cracks into the 3D problem domain and optimize the structure to achieve better designs in terms of the structural performance under both static and dynamic loading.

- The proposed continuous density based PD-TO methods in Kendibilir et al. (2024) is utilized for the structural optimization of large-scale engineering structures by simulating their most critical loading conditions and avoiding crack formations in some regions via apriori knowledge of damaged regions. In this context, light weighted ship cross-section designs are achieved in a research paper published in the Journal of Ocean Engineering (Kendibilir & Kefal (2023a)).

- Additionally, the PD-OC-TO method is systematically utilized considering a CCM based failure criteria for increased the fracture toughness in TO designs.

Achieved results indicated that the proposed method provides the designs with better performance under both static and dynamic loading conditions. The proposed PD model can include a lot of smaller cracks that are aligned according to first principle directions to reflect the mode-1 cracks in the initial design domain. These outputs are submitted to the journal of Structural and Multidisciplinary Optimization (Kendibilir et al. (2024)).

- Furthermore, these PD-TO methods are utilized to work with thermo-mechanical AM simulations in order to decrease the residual stresses on the manufactured structures by metal AM processes. Regardingly, with the help of colleagues from SU-IMC and Sabancı University, the obtained promising results submitted to a respected journal in AM and TO fields (Khalilvandi Behrouzyar et al. (2024)).

- After all the listed achievements and developments of PD-TO methods and optimization strategies, a real life engineering structure, engine mounting bracket, is topologically optimized while considering AM process induced residual stresses by utilizing the strategy proposed in (Kendibilir et al. (2024)) and (Khalilvandi Behrouzyar et al. (2024)). According to the numerical results, the final thermally induced residual stresses on the procuded structure is minimized by PD-TO method. In addition to the numerical results, the metal AM productions and mechanical tests of the designs are performed to experimentally validate the proposed algorithm. Experimental results proved that precise crack modeling ability of PD-TO would enable the optimizer to create a final design with decreased strain energy over the full domain thereby providing more load-bearing capacity under the same boundary conditions. Hence, the promising results are submitted to the journal of Additive Manufacturing (Kendibilir et al. (2024)).

6.2 Gaps and Future Studies

Albeit being generally applicable to many design/optimization problems, the proposed PD-TO methods involve several limitations and future plans for specific applications. Some of them can be potentially addressed in future studies:

- The current PD-TO algorithm is based on a bond-based formulation, which restricts the material's Poisson ratio to 0.25. This limitation can be over-

come by using an ordinary state-based formulation for topology optimization problems where the Poisson ratio plays a critical role.

- The uniform particle discretization of the PD-TO is another drawback which can be addressed by employing dual horizon peridynamics (DH-PD) in the topology optimization process. This approach would reduce the computational cost of the current method when optimizing complex geometries with intricate shapes, such as holes.
- For large-scale engineering structures, detailed information on various loading conditions and potential damaged or critical areas can be utilized as input for this method in future applications.
- Future research endeavors may involve applying this innovative methodology for optimizing functional parts, and validating the results with more and more case studies.
- The proposed methodology holds promise for diverse applications, ranging from aerospace to medical implants, where reducing residual stresses is crucial for ensuring mechanical integrity and durability.
- An advanced smoothing operation could yield better results in the final product by reducing the likelihood of stress concentration around sharp corners.
- With the availability of computationally efficient large-scale thermo-mechanical analysis methods, PD-TO can be fully integrated with these methods, allowing the optimization process to consider thermo-mechanical results during topology optimization.

6.3 Research Outputs

This section outlines all of the author's research outputs related to the 3D PD-TO research study presented in this thesis. During PhD period, I have contributed to the following research projects which are supported by the Scientific and Technological Research Council of Turkey (TUBITAK):

2022-2025

- Computational Design and Topology Optimization Platform for Additive Man-

ufacturing, TUBITAK-3219504, Developing and preparing back-end topology optimization codes for graphical user interface. Writing and reviewing technical reports for TUBITAK

2020-2023

- Development and Experimental Verification of Innovative Topology Optimization Algorithms, TUBITAK-218M713, Developing peridynamics-based topology optimization algorithms for three-dimensional structures with cracks. Numerical analysis for verification and demonstration of the proposed methods. Writing research papers for increasing the impact of the developed methods within the TUBITAK project

The financial support provided by the Scientific and Technological Research Council of Turkey (TUBITAK) under the grant No: 3219504 and No: 218M713 are greatly acknowledged. Thanks to the research and development effort I put into these projects, I had the opportunity to publish scientific papers. These include 6 journal papers and 8 conference presentations and are listed below chronologically from newest to oldest.

Journal Publications

2024

- **Kendibilir, A.,**, Khalilvandi Behrouzyar, S., Cavus, O.S., Lahe Motlagh, P., Oren, S., Orhangul, A., Koc, B., and Kefal, A., 2024. Lightweight engine bracket design for metal additive manufacturing: peridynamics topology optimization for reduction of thermal stresses and improved structural performance*, Submitted to the Journal of Additive Manufacturing*

- Khalilvandi Behrouzyar, S., **Kendibilir, A.,** Cavus, O.S., Lahe Motlagh, P., Oren, S., Orhangul, A., Kefal, A. and Koc, B., 2024. Minimizing Thermally Induced Residual Stresses in Metal Additive Manufacturing Through Peridynamics Topology Optimization*, Submitted to the Journal of Engineering with Computers* (equally contributed)

- **Kendibilir, A.,** Lahe Motlagh, P. and Kefal, A., 2024. A Systematic Fusion of Failure Criteria and Peridynamics Topology Optimization for Enhanced Fracture Resistance*, Submitted to the Journal of Structural and Multidisciplinary Optimization*

- **Kendibilir, A.,** Bilgin, M. H. and Kefal, A., 2024.Coupling of bond-based peridynamics and continuous density-based topology optimization methods for

effective design of three-dimensional structures with discontinuities. *Engineering with Computers, pp.1-22.*

2023

- **Kendibilir, A.** and Kefal, A., 2023. Enhanced ship cross-section design methodology using peridynamics topology optimization. *Ocean Engineering, 286,* p.115531.

2022

- **Kendibilir, A.,** Kefal, A., Sohouli, A., Yildiz, M., Koc, B. and Suleman, A., 2022.Peridynamics topology optimization of three-dimensional structures with surface cracks for additive manufacturing. *Computer Methods in Applied Mechanics and Engineering, 401,* p.115665.

Conference Presentations

2024

- **Kendibilir, A.,** and Kefal, A.,2024. Systematic Integration of Failure Criteria and Peridynamic Topology Optimization for Enhancing Fracture Resistance *iCONSOM 2024, Cagliari, Sardinia, Italy,* physical presentation at Conference
- **Kendibilir, A.,** Khalilvandi Behrouzyar, S., Lahe Motlagh, P., Koc, B. and Kefal, A.,2024. Topology optimization using peridynamic approach for minimizing residual stresses in additive manufacturing. *AMCTURKEY 2024, Antalya, Turkey,* physical presentation at Conference
- Yildiz, R., **Kendibilir, A.,** Varoglu, H., Koc, B. and Kefal, A., 2024. Development of peridynamics topology optimization software for additive manufacturing-oriented designs *AMCTURKEY 2024, Antalya, Turkey*, will be published in Journal of Additive Manufacturing Technologies.

2023

- **Kendibilir, A.** and Kefal, A., 2023. Lightweight design and topology optimization of marine structures using peridynamics. *9th International Conference on Marine Structures, MARSTRUCT 2023, Gothenburg, Sweden,* published in Advances in the Analysis and Design of Marine Structures.

2022

- **Kendibilir, A.,** Bilgin, M. H. and Kefal, A., 2022. Peridynamic investigation of surface cracks in optimality criterion-based topology optimization for additive manufacturing. *The 3rd Additive Manufacturing Conference in Turkey, AMCTURKEY 2022, Aydın, Turkey,* published in Journal of Additive Manufacturing Technologies.

- **Kendibilir, A.,** Polat, M.F., Cavus, O.S., Khalilvandi Behrouzyar, S., Lahe Motlagh, P., Koc, B. and Kefal, A.,2022. Combination of peridynamics and genetic algorithm based topology optimization methods for AM-friendly designs. *The 3rd Additive Manufacturing Conference in Turkey, AMCTURKEY 2022, Aydın, Turkey,* published in Journal of Additive Manufacturing Technologies.

2021

- **Kendibilir, A.,** Lahe Motlagh, P. and Kefal, A.,2021. Three-dimensional topology optimization for marine structure components using non-local methods. *The 34th Asian-Pacific Technical Exchange and Advisory Meeting on Marine Structures TEAM 2020/21, Istanbul, Turkey.*

- Lahe Motlagh, P., **Kendibilir, A.** and Kefal, A., 2021. Peridynamics-informed effect of micro-cracks on topology optimization of lightweight structures. *The 2nd Additive Manufacturing Conference in Turkey, AMCTURKEY 2021, Istanbul, Turkey*, published in Journal of Additive Manufacturing Technologies.

BIBLIOGRAPHY

Allaire, G., Dapogny, C., Estevez, R., Faure, A., & Michailidis, G. (2017). Structural optimization under overhang constraints imposed by additive manufacturing technologies. *Journal of Computational Physics*, *351*, 295–328.

Allaire, G. & Jakabčin, L. (2018). Taking into account thermal residual stresses in topology optimization of structures built by additive manufacturing. *Mathematical Models and Methods in Applied Sciences*, *28*(12), 2313–2366.

Allaire, G., Jouve, F., & Michailidis, G. (2016). Thickness control in structural optimization via a level set method. *Structural and Multidisciplinary Optimization*, *53*, 1349–1382.

Atluri, S. N. & Zhu, T. (1998). A new meshless local petrov-galerkin (mlpg) approach in computational mechanics. *Computational mechanics*, *22*(2), 117–127.

Bartlett, J. L. & Li, X. (2019). An overview of residual stresses in metal powder bed fusion. *Additive Manufacturing*, *27*, 131–149.

Becker, T. H., Kumar, P., & Ramamurty, U. (2021). Fracture and fatigue in additively manufactured metals. *Acta Materialia*, *219*, 117240.

Belhabib, S. & Guessasma, S. (2017). Compression performance of hollow structures: From topology optimisation to design 3d printing. *International Journal of Mechanical Sciences*, *133*, 728–739.

Belytschko, T., Lu, Y. Y., & Gu, L. (1994). Element-free galerkin methods. *International journal for numerical methods in engineering*, *37*(2), 229–256.

Bendsøe, M. P. (1995). *Optimization of structural topology, shape, and material*, volume 414. Springer.

Bendsøe, M. P. & Kikuchi, N. (1988). Generating optimal topologies in structural design using a homogenization method. *Computer methods in applied mechanics and engineering*, *71*(2), 197–224.

Bendsøe, M. P. & Sigmund, O. (1999). Material interpolation schemes in topology optimization. *Archive of applied mechanics*, *69*, 635–654.

Bendsoe, M. P. & Sigmund, O. (2013). *Topology optimization: theory, methods, and applications*. Springer Science & Business Media.

Biyikli, E. & To, A. C. (2015). Proportional topology optimization: a new non-sensitivity method for solving stress constrained and minimum compliance problems and its implementation in matlab. *PloS one*, *10*(12), e0145041.

Brackett, D., Ashcroft, I., & Hague, R. (2011). Topology optimization for additive manufacturing.

Briot, S. & Goldsztejn, A. (2018). Topology optimization of industrial robots: Application to a five-bar mechanism. *Mechanism and Machine Theory*, *120*, 30–56.

Buchbinder, D., Meiners, W., Pirch, N., Wissenbach, K., & Schrage, J. (2014). Investigation on reducing distortion by preheating during manufacture of aluminum components using selective laser melting. *Journal of laser applications*, *26*(1).

Bureerat, S. & Limtragool, J. (2008). Structural topology optimisation using simulated annealing with multiresolution design variables. *Finite Elements in Analysis and Design*, *44*(12-13), 738–747.

Burger, M. & Stainko, R. (2006). Phase-field relaxation of topology optimization

with local stress constraints. *SIAM Journal on Control and Optimization*, *45*(4), 1447–1466.

Cavazzuti, M., Baldini, A., Bertocchi, E., Costi, D., Torricelli, E., & Moruzzi, P. (2011). High performance automotive chassis design: a topology optimization based approach. *Structural and Multidisciplinary Optimization*, *44*, 45–56.

Chen, Q., Liang, X., Hayduke, D., Liu, J., Cheng, L., Oskin, J., Whitmore, R., & To, A. C. (2019). An inherent strain based multiscale modeling framework for simulating part-scale residual deformation for direct metal laser sintering. *Additive Manufacturing*, *28*, 406–418.

Cheng, L., Liang, X., Bai, J., Chen, Q., Lemon, J., & To, A. (2019). On utilizing topology optimization to design support structure to prevent residual stress induced build failure in laser powder bed metal additive manufacturing. *Additive Manufacturing*, *27*, 290–304.

Cotteleer, M. & Joyce, J. (2014). 3d opportunity: Additive manufacturing paths to performance, innovation, and growth. *Deloitte review*, *14*(1), 3–19.

Deaton, J. D. & Grandhi, R. V. (2014). A survey of structural and multidisciplinary continuum topology optimization: post 2000. *Structural and Multidisciplinary Optimization*, *49*, 1–38.

Fergani, O., Berto, F., Welo, T., & Liang, S. (2017). Analytical modelling of residual stress in additive manufacturing. *Fatigue & Fracture of Engineering Materials & Structures*, *40*(6), 971–978.

Fernandez, E., Ayas, C., Langelaar, M., & Duysinx, P. (2021). Topology optimisation for large-scale additive manufacturing: generating designs tailored to the deposition nozzle size. *Virtual and Physical Prototyping*, *16*(2), 196–220.

Fu, Y.-F., Rolfe, B., Chiu, L. N., Wang, Y., Huang, X., & Ghabraie, K. (2019). Design and experimental validation of self-supporting topologies for additive manufacturing. *Virtual and Physical Prototyping*, *14*(4), 382–394.

Gaynor, A. T. & Guest, J. K. (2016). Topology optimization considering overhang constraints: Eliminating sacrificial support material in additive manufacturing through design. *Structural and Multidisciplinary Optimization*, *54*(5), 1157–1172.

Gibson, I., Rosen, D. W., Stucker, B., Khorasani, M., Rosen, D., Stucker, B., & Khorasani, M. (2021). *Additive manufacturing technologies*, volume 17. Springer.

Gu, D. D., Meiners, W., Wissenbach, K., & Poprawe, R. (2012). Laser additive manufacturing of metallic components: materials, processes and mechanisms. *International materials reviews*, *57*(3), 133–164.

Guidault, P.-A., Allix, O., Champaney, L., & Cornuault, C. (2008). A multiscale extended finite element method for crack propagation. *Computer Methods in Applied Mechanics and Engineering*, *197*(5), 381–399.

Guo, X., Zhang, W., & Zhang, L. (2013). Robust structural topology optimization considering boundary uncertainties. *Computer Methods in Applied Mechanics and Engineering*, *253*, 356–368.

Guo, X., Zhou, J., Zhang, W., Du, Z., Liu, C., & Liu, Y. (2017). Self-supporting structure design in additive manufacturing through explicit topology optimization. *Computer Methods in Applied Mechanics and Engineering*, *323*, 27–63.

Gusarov, A., Yadroitsev, I., Bertrand, P., & Smurov, I. (2009). Model of radiation and heat transfer in laser-powder interaction zone at selective laser melting.

Habashneh, M. & Rad, M. M. (2024). Optimizing structural topology design through

consideration of fatigue crack propagation. *Computer Methods in Applied Mechanics and Engineering*, *419*, 116629.

Habibian, A., Sohouli, A., Kefal, A., Nadler, B., Yildiz, M., & Suleman, A. (2021). Multi-material topology optimization of structures with discontinuities using peridynamics. *Composite Structures*, *258*, 113345.

Hassani, B. & Hinton, E. (1998). A review of homogenization and topology optimization iii—topology optimization using optimality criteria. *Computers & structures*, *69*(6), 739–756.

Heigel, J., Michaleris, P., & Reutzel, E. W. (2015). Thermo-mechanical model development and validation of directed energy deposition additive manufacturing of ti–6al–4v. *Additive manufacturing*, *5*, 9–19.

Huang, X. & Xie, M. (2010a). *Evolutionary topology optimization of continuum structures: methods and applications*. John Wiley & Sons.

Huang, X. & Xie, Y.-M. (2010b). A further review of eso type methods for topology optimization. *Structural and Multidisciplinary Optimization*, *41*, 671–683.

Huang, X., Xie, Y. M., & Burry, M. C. (2007). Advantages of bi-directional evolutionary structural optimization (beso) over evolutionary structural optimization (eso). *Advances in Structural Engineering*, *10*(6), 727–737.

Jia, D. & Li, F. (2019). Design of bulkhead reinforcement of trimaran based on topological optimization. *Ocean Engineering*, *191*, 106498.

Jia, D., Li, F., Zhang, C., & Li, L. (2019). Design and simulation analysis of trimaran bulkhead based on topological optimization. *Ocean Engineering*, *191*, 106304.

Jihong, Z., Han, Z., Chuang, W., Lu, Z., Shangqin, Y., & Zhang, W. (2021). A review of topology optimization for additive manufacturing: Status and challenges. *Chinese Journal of Aeronautics*, *34*(1), 91–110.

Joshi, S. C. & Sheikh, A. A. (2015). 3d printing in aerospace and its long-term sustainability. *Virtual and physical prototyping*, *10*(4), 175–185.

Kang, Z., Liu, P., & Li, M. (2017). Topology optimization considering fracture mechanics behaviors at specified locations. *Structural and Multidisciplinary Optimization*, *55*, 1847–1864.

Katsuno, E. T., Dantas, J. L. D., & Silva, E. C. N. (2022). Topology optimization of low-friction painting distribution on a marine propeller. *Structural and Multidisciplinary Optimization*, *65*(9), 269.

Kefal, A., Sohouli, A., Oterkus, E., Yildiz, M., & Suleman, A. (2019). Topology optimization of cracked structures using peridynamics. *Continuum Mechanics and Thermodynamics*, *31*, 1645–1672.

Keller, N. & Ploshikhin, V. (2014). New method for fast predictions on residual stress and distortion of am parts.

Kendibilir, A., Bilgin, M., & Kefal, A. (2024). Coupling of bond-based peridynamics and continuous density-based topology optimization methods for effective design of three-dimensional structures with discontinuities. *Engineering with Computers*, 1–22.

Kendibilir, A. & Kefal, A. (2023a). Enhanced ship cross-section design methodology using peridynamics topology optimization. *Ocean Engineering*, *286*, 115531.

Kendibilir, A. & Kefal, A. (2023b). Lightweight design and topology optimization of marine structures using peridynamics. In *Advances in the analysis and design of marine structures* (pp. 827–834). CRC Press.

Kendibilir, A., Kefal, A., Sohouli, A., Yildiz, M., Koc, B., & Suleman, A. (2022).

Peridynamics topology optimization of three-dimensional structures with surface cracks for additive manufacturing. *Computer Methods in Applied Mechanics and Engineering*, *401*, 115665.

Kendibilir, A., Khalilvandi Behrouzyar, S., Cavus, O. S., Lahe Motlagh, P., Oren, S., Orhangul, A., Koc, B., & Kefal, A. (2024). Lightweight engine bracket design for metal additive manufacturing: peridynamics topology optimization for reduction of thermal stresses and improved structural performance. *Submitted to the Journal of Additive Manufacturing*.

Kendibilir, A., Lahe Motlagh, P., & Kefal, A. (2024). A systematic fusion of failure criteria and peridynamics topology optimization for enhanced fracture resistance. *Submitted to the Journal of Structural and Multidisciplinary Optimization*.

Khalilvandi Behrouzyar, S., Kendibilir, A., Cavus, O. S., Lahe Motlagh, P., Oren, S., Orhangul, A., Koc, B., & Kefal, A. (2024). Minimizing thermally induced residual stresses in metal additive manufacturing through peridynamics topology optimization. *Submitted to the Journal of Engineering with Computers (equal contribution from first two authors)*.

Kim, D.-J., Pereira, J., & Duarte, C. (2010). Analysis of three-dimensional fracture mechanics problems: A two-scale approach using coarse-generalized fem meshes. *International journal for numerical methods in engineering*, *81*(3), 335–365.

Lahe Motlagh, P. & Kefal, A. (2021). Comparative study of peridynamics and finite element method for practical modeling of cracks in topology optimization. *Symmetry*, *13*(8), 1407.

Langelaar, M. (2016). Topology optimization of 3d self-supporting structures for additive manufacturing. *Additive manufacturing*, *12*, 60–70.

Langelaar, M. (2017). An additive manufacturing filter for topology optimization of print-ready designs. *Structural and multidisciplinary optimization*, *55*, 871–883.

Lapidus, L. & Pinder, G. F. (1999). *Numerical solution of partial differential equations in science and engineering*. John Wiley & Sons.

Lazarus, V. (2011). Perturbation approaches of a planar crack in linear elastic fracture mechanics: a review. *Journal of the Mechanics and Physics of Solids*, *59*(2), 121–144.

Leuders, S., Thöne, M., Riemer, A., Niendorf, T., Tröster, T., Richard, H. a., & Maier, H. (2013). On the mechanical behaviour of titanium alloy tial6v4 manufactured by selective laser melting: Fatigue resistance and crack growth performance. *International journal of fatigue*, *48*, 300–307.

Li, C., Fu, C., Guo, Y., & Fang, F. (2016). A multiscale modeling approach for fast prediction of part distortion in selective laser melting. *Journal of materials processing technology*, *229*, 703–712.

Li, C., Lei, H., Zhang, Z., Zhang, X., Zhou, H., Wang, P., & Fang, D. (2020). Architecture design of periodic truss-lattice cells for additive manufacturing. *Additive Manufacturing*, *34*, 101172.

Li, D., Qin, R., Xu, J., Zhou, J., & Chen, B. (2022). Topology optimization of thin-walled tubes filled with lattice structures. *International Journal of Mechanical Sciences*, *227*, 107457.

Li, L., Liu, C., Zhang, W., Du, Z., & Guo, X. (2021). Combined model-based topol-

ogy optimization of stiffened plate structures via mmc approach. *International Journal of Mechanical Sciences*, *208*, 106682.

Liang, X., Cheng, L., Chen, Q., Yang, Q., & To, A. C. (2018). A modified method for estimating inherent strains from detailed process simulation for fast residual distortion prediction of single-walled structures fabricated by directed energy deposition. *Additive Manufacturing*, *23*, 471–486.

Liu, J., Gaynor, A. T., Chen, S., Kang, Z., Suresh, K., Takezawa, A., Li, L., Kato, J., Tang, J., Wang, C. C., et al. (2018). Current and future trends in topology optimization for additive manufacturing. *Structural and multidisciplinary optimization*, *57*(6), 2457–2483.

Liu, J. & Ma, Y. (2018). A new multi-material level set topology optimization method with the length scale control capability. *Computer Methods in Applied Mechanics and Engineering*, *329*, 444–463.

Liu, J. & Ma, Y. S. (2015). 3d level-set topology optimization: a machining feature-based approach. *Structural and Multidisciplinary Optimization*, *52*, 563–582.

Liu, J., Zheng, Y., Ahmad, R., Tang, J., & Ma, Y. (2019). Minimum length scale constraints in multi-scale topology optimisation for additive manufacturing. *Virtual and Physical Prototyping*, *14*(3), 229–241.

Liu, W. K., Jun, S., & Zhang, Y. F. (1995). Reproducing kernel particle methods. *International journal for numerical methods in fluids*, *20*(8-9), 1081–1106.

Lu, F., Long, K., Zhang, C., Zhang, J., & Tao, T. (2023). A novel design of the offshore wind turbine tripod structure using topology optimization methodology. *Ocean Engineering*, *280*, 114607.

Maute, K. & Allen, M. (2004). Conceptual design of aeroelastic structures by topology optimization. *Structural and Multidisciplinary Optimization*, *27*, 27–42.

Megahed, M., Mindt, H.-W., N'Dri, N., Duan, H., & Desmaison, O. (2016). Metal additive-manufacturing process and residual stress modeling. *Integrating Materials and Manufacturing Innovation*, *5*, 61–93.

Mercelis, P. & Kruth, J.-P. (2006). Residual stresses in selective laser sintering and selective laser melting. *Rapid prototyping journal*, *12*(5), 254–265.

Mezzadri, F., Bouriakov, V., & Qian, X. (2018). Topology optimization of self-supporting support structures for additive manufacturing. *Additive Manufacturing*, *21*, 666–682.

Misiun, G., van de Ven, E., Langelaar, M., Geijselaers, H., van Keulen, F., van den Boogaard, T., & Ayas, C. (2021). Topology optimization for additive manufacturing with distortion constraints. *Computer methods in applied mechanics and engineering*, *386*, 114095.

Moës, N., Dolbow, J., & Belytschko, T. (1999). A finite element method for crack growth without remeshing. *International journal for numerical methods in engineering*, *46*(1), 131–150.

Mohan, S. R. & Simhambhatla, S. (2019). Adopting feature resolution and material distribution constraints into topology optimisation of additive manufacturing components. *Virtual and Physical Prototyping*, *14*(1), 79–91.

Monaghan, J. J. (2012). Smoothed particle hydrodynamics and its diverse applications. *Annual Review of Fluid Mechanics*, *44*(1), 323–346.

Motlagh, P. L., Kendibilir, A., Koc, B., & Kefal, A. (2021). Peridynamics-informed effect of micro-cracks on topology optimization of lightweight structures. *Journal of Additive Manufacturing Technologies*, *1*(3), 610–610.

Nejat, S. A., Changizi, N., Tootkaboni, M., & Asadpoure, A. (2021). Topology optimization of lightweight periodic lattices under stiffness and stability constraints. *International Journal of Mechanical Sciences*, *209*, 106727.

Neugebauer, F., Keller, N., Ploshikhin, V., Feuerhahn, F., & Köhler, H. (2014). Multi scale fem simulation for distortion calculation in additive manufacturing of hardening stainless steel. In *international workshop on thermal forming and welding distortion, Bremen, Germany*.

Parry, L., Ashcroft, I., & Wildman, R. D. (2016). Understanding the effect of laser scan strategy on residual stress in selective laser melting through thermo-mechanical simulation. *Additive Manufacturing*, *12*, 1–15.

Pereira, J., Kim, D.-J., & Duarte, C. A. (2012). A two-scale approach for the analysis of propagating three-dimensional fractures. *Computational Mechanics*, *49*, 99–121.

Prabhakar, P., Sames, W. J., Dehoff, R., & Babu, S. S. (2015). Computational modeling of residual stress formation during the electron beam melting process for inconel 718. *Additive Manufacturing*, *7*, 83–91.

Qian, X. (2017). Undercut and overhang angle control in topology optimization: a density gradient based integral approach. *International Journal for Numerical Methods in Engineering*, *111*(3), 247–272.

Querin, O. M., Young, V., Steven, G., & Xie, Y. (2000). Computational efficiency and validation of bi-directional evolutionary structural optimisation. *Computer methods in applied mechanics and engineering*, *189*(2), 559–573.

Rabczuk, T. & Ren, H. (2017). A peridynamics formulation for quasi-static fracture and contact in rock. *Engineering Geology*, *225*, 42–48.

Rabczuk, T., Ren, H., & Zhuang, X. (2019). A nonlocal operator method for partial differential equations with application to electromagnetic waveguide problem. *Computers, Materials & Continua 59 (2019), Nr. 1*, 31–55.

Ren, H., Zhuang, X., Cai, Y., & Rabczuk, T. (2016). Dual-horizon peridynamics. *International Journal for Numerical Methods in Engineering*, *108*(12), 1451–1476.

Ren, H., Zhuang, X., & Rabczuk, T. (2017a). Dual-horizon peridynamics: A stable solution to varying horizons. *Computer Methods in Applied Mechanics and Engineering*, *318*, 762–782.

Ren, H., Zhuang, X., & Rabczuk, T. (2017b). Implementation of gtn model in dual-horizon peridynamics. *Procedia engineering*, *197*, 224–232.

Ren, H., Zhuang, X., & Rabczuk, T. (2020). A nonlocal operator method for solving partial differential equations. *Computer Methods in Applied Mechanics and Engineering*, *358*, 112621.

Rosen, D. W. (2016). A review of synthesis methods for additive manufacturing. *Virtual and Physical Prototyping*, *11*(4), 305–317.

Rozvany, G. I. (2009). A critical review of established methods of structural topology optimization. *Structural and multidisciplinary optimization*, *37*, 217–237.

Rozvany, G. I., Zhou, M., & Birker, T. (1992). Generalized shape optimization without homogenization. *Structural optimization*, *4*, 250–252.

Safonov, A. A. (2019). 3d topology optimization of continuous fiber-reinforced structures via natural evolution method. *Composite Structures*, *215*, 289–297.

Sames, W. J., List, F., Pannala, S., Dehoff, R. R., & Babu, S. S. (2016). The metallurgy and processing science of metal additive manufacturing. *International*

materials reviews, *61*(5), 315–360.

Schevenels, M., Lazarov, B. S., & Sigmund, O. (2011). Robust topology optimization accounting for spatially varying manufacturing errors. *Computer Methods in Applied Mechanics and Engineering*, *200*(49-52), 3613–3627.

Schoinochoritis, B., Chantzis, D., & Salonitis, K. (2017). Simulation of metallic powder bed additive manufacturing processes with the finite element method: A critical review. *Proceedings of the Institution of Mechanical Engineers, Part B: Journal of Engineering Manufacture*, *231*(1), 96–117.

Sethian, J. A. & Wiegmann, A. (2000). Structural boundary design via level set and immersed interface methods. *Journal of computational physics*, *163*(2), 489–528.

Sharma, A. & Maute, K. (2018). Stress-based topology optimization using spatial gradient stabilized xfem. *Structural and Multidisciplinary Optimization*, *57*, 17–38.

Shiomi, M., Osakada, K., Nakamura, K., Yamashita, T., & Abe, F. (2004). Residual stress within metallic model made by selective laser melting process. *CIRP annals*, *53*(1), 195–198.

Sigmund, O. (2001). A 99 line topology optimization code written in matlab. *Structural and multidisciplinary optimization*, *21*, 120–127.

Sigmund, O. (2009). Manufacturing tolerant topology optimization. *Acta Mechanica Sinica*, *25*, 227–239.

Sigmund, O. & Maute, K. (2013). Topology optimization approaches: A comparative review. *Structural and multidisciplinary optimization*, *48*(6), 1031–1055.

Silling, S. A. (2000). Reformulation of elasticity theory for discontinuities and long-range forces. *Journal of the Mechanics and Physics of Solids*, *48*(1), 175–209.

Silling, S. A. & Askari, E. (2005). A meshfree method based on the peridynamic model of solid mechanics. *Computers & structures*, *83*(17-18), 1526–1535.

Silling, S. A., Epton, M., Weckner, O., Xu, J., & Askari, E. (2007). Peridynamic states and constitutive modeling. *Journal of elasticity*, *88*, 151–184.

Sohouli, A., Kefal, A., Abdelhamid, A., Yildiz, M., & Suleman, A. (2020). Continuous density-based topology optimization of cracked structures using peridynamics. *Structural and Multidisciplinary Optimization*, *62*, 2375–2389.

Stazi, F., Budyn, E., Chessa, J., & Belytschko, T. (2003). An extended finite element method with higher-order elements for curved cracks. *Computational Mechanics*, *31*(1), 38–48.

Svanberg, K. & Werme, M. (2007). Sequential integer programming methods for stress constrained topology optimization. *Structural and Multidisciplinary Optimization*, *34*, 277–299.

Talebi, H., Silani, M., Bordas, S. P., Kerfriden, P., & Rabczuk, T. (2013). Molecular dynamics/xfem coupling by a three-dimensional extended bridging domain with applications to dynamic brittle fracture. *International Journal for Multiscale Computational Engineering*, *11*(6).

Tang, Y., Kurtz, A., & Zhao, Y. F. (2015). Bidirectional evolutionary structural optimization (beso) based design method for lattice structure to be fabricated by additive manufacturing. *Computer-Aided Design*, *69*, 91–101.

Tay, Y. W. D., Panda, B., Paul, S. C., Noor Mohamed, N. A., Tan, M. J., & Leong, K. F. (2017). 3d printing trends in building and construction industry: a review. *Virtual and physical prototyping*, *12*(3), 261–276.

Tian, X., Sun, X., Liu, G., Deng, W., Wang, H., Li, Z., & Li, D. (2022). Optimization design of the jacket support structure for offshore wind turbine using topology optimization method. *Ocean Engineering*, *243*, 110084.

Tian, X., Wang, Q., Liu, G., Liu, Y., Xie, Y., & Deng, W. (2019). Topology optimization design for offshore platform jacket structure. *Applied Ocean Research*, *84*, 38–50.

Tian, X., Wang, Z., Liu, D., Liu, G., Deng, W., Xie, Y., & Wang, H. (2022). Jack-up platform leg optimization by topology optimization algorithm-beso. *Ocean Engineering*, *257*, 111633.

Travieso-Rodriguez, J. A., Jerez-Mesa, R., Llumà, J., Traver-Ramos, O., Gomez-Gras, G., & Roa Rovira, J. J. (2019). Mechanical properties of 3d-printing polylactic acid parts subjected to bending stress and fatigue testing. *Materials*, *12*(23), 3859.

Ueda, Y. & Yuan, M. (1993). Prediction of residual stresses in butt welded plates using inherent strains.

Van Belle, L., Vansteenkiste, G., & Boyer, J. C. (2013). Investigation of residual stresses induced during the selective laser melting process. *Key engineering materials*, *554*, 1828–1834.

Van Dijk, N. P., Maute, K., Langelaar, M., & Van Keulen, F. (2013). Level-set methods for structural topology optimization: a review. *Structural and Multidisciplinary Optimization*, *48*, 437–472.

Vrancken, B., Cain, V., Knutsen, R., & Van Humbeeck, J. (2014). Residual stress via the contour method in compact tension specimens produced via selective laser melting. *Scripta Materialia*, *87*, 29–32.

Vuijk, W. (2020). Shape and topology optimized tshd midsection.

Wang, M. Y., Wang, X., & Guo, D. (2003). A level set method for structural topology optimization. *Computer methods in applied mechanics and engineering*, *192*(1-2), 227–246.

Wang, Y., Gao, J., & Kang, Z. (2018). Level set-based topology optimization with overhang constraint: Towards support-free additive manufacturing. *Computer Methods in Applied Mechanics and Engineering*, *339*, 591–614.

Wildman, R. A. & Gaynor, A. T. (2017). Topology optimization for reducing additive manufacturing processing distortions. *Weapons and Materials Research Directorate, United States*, 1–32.

Wu, C., Fang, J., Zhou, S., Zhang, Z., Sun, G., Steven, G. P., & Li, Q. (2020). Level-set topology optimization for maximizing fracture resistance of brittle materials using phase-field fracture model. *International Journal for Numerical Methods in Engineering*, *121*(13), 2929–2945.

Wu, J., Sigmund, O., & Groen, J. P. (2021). Topology optimization of multi-scale structures: a review. *Structural and Multidisciplinary Optimization*, *63*, 1455–1480.

Wu, Y., Yvonnet, J., Li, P., & He, Z.-C. (2022). Topology optimization for enhanced dynamic fracture resistance of structures. *Computer Methods in Applied Mechanics and Engineering*, *394*, 114846.

Xia, L., Da, D., & Yvonnet, J. (2018). Topology optimization for maximizing the fracture resistance of quasi-brittle composites. *Computer Methods in Applied Mechanics and Engineering*, *332*, 234–254.

Xie, Y. M. & Steven, G. P. (1993). A simple evolutionary procedure for structural

optimization. *Computers & structures*, *49*(5), 885–896.

Xu, D., Chen, J., Tang, Y., & Cao, J. (2012). Topology optimization of die weight reduction for high-strength sheet metal stamping. *International Journal of Mechanical Sciences*, *59*(1), 73–82.

Xu, J., Gao, L., Xiao, M., Gao, J., & Li, H. (2020). Isogeometric topology optimization for rational design of ultra-lightweight architected materials. *International Journal of Mechanical Sciences*, *166*, 105103.

Yang, G., Xie, Y., Zhao, S., Qin, L., Wang, X., & Wu, B. (2022). Quality control: Internal defects formation mechanism of selective laser melting based on laser-powder-melt pool interaction: A review. *Chinese Journal of Mechanical Engineering: Additive Manufacturing Frontiers*, *1*(3), 100037.

Yang, R. & Chahande, A. (1995). Automotive applications of topology optimization. *Structural optimization*, *9*, 245–249.

Yang, X. Y., Xie, Y. M., Steven, G. P., & Querin, O. M. (1999). Bidirectional evolutionary method for stiffness optimization. *AIAA journal*, *37*(11), 1483–1488.

Zaeh, M. F. & Branner, G. (2010). Investigations on residual stresses and deformations in selective laser melting. *Production Engineering*, *4*(1), 35–45.

Zerbst, U., Bruno, G., Buffiere, J.-Y., Wegener, T., Niendorf, T., Wu, T., Zhang, X., Kashaev, N., Meneghetti, G., Hrabe, N., et al. (2021). Damage tolerant design of additively manufactured metallic components subjected to cyclic loading: State of the art and challenges. *Progress in materials science*, *121*, 100786.

Zhang, K. & Cheng, G. (2020). Three-dimensional high resolution topology optimization considering additive manufacturing constraints. *Additive Manufacturing*, *35*, 101224.

Zhang, K., Cheng, G., & Xu, L. (2019). Topology optimization considering overhang constraint in additive manufacturing. *Computers & Structures*, *212*, 86–100.

Zhang, Q., Liu, Y., Nguyen-Thanh, N., Li, W., Li, S., & Zhou, K. (2024). Adaptive topology optimization for enhancing resistance to brittle fracture using the phase field model. *Computer Methods in Applied Mechanics and Engineering*, *431*, 117237.

Zhang, Z.-D., Ibhadode, O., Ali, U., Dibia, C. F., Rahnama, P., Bonakdar, A., & Toyserkani, E. (2020). Topology optimization parallel-computing framework based on the inherent strain method for support structure design in laser powder-bed fusion additive manufacturing. *International Journal of Mechanics and Materials in Design*, *16*, 897–923.

Zhou, M., Lazarov, B. S., Wang, F., & Sigmund, O. (2015). Minimum length scale in topology optimization by geometric constraints. *Computer Methods in Applied Mechanics and Engineering*, *293*, 266–282.

Zhou, Z., Shen, H., Liu, B., Du, W., Jin, J., & Lin, J. (2022). Residual thermal stress prediction for continuous tool-paths in wire-arc additive manufacturing: A three-level data-driven method. *Virtual and Physical Prototyping*, *17*(1), 105–124.

Zhu, J.-H., Zhang, W.-H., & Xia, L. (2016). Topology optimization in aircraft and aerospace structures design. *Archives of computational methods in engineering*, *23*, 595–622.